UNIVERSITY OF SOUTHAMPTON

FACULTY OF ENGINEERING AND THE ENVIRONMENT

Engineering Materials & Surface Engineering Group

Infrared thermography for test machine control and material characterisation

by

James Edward Thatcher

Thesis for the degree of Doctor of Philosophy

February 2018

UNIVERSITY OF SOUTHAMPTON

ABSTRACT

FACULTY OF ENGINEERING AND THE ENVIRONMENT

Engineering Materials & Surface Engineering Group

Thesis for the degree of Doctor of Philosophy

INFRARED THERMOGRAPHY FOR TEST MACHINE CONTROL AND MATERIAL CHARACTERISATION

James Edward Thatcher

The aim of the PhD is to develop Infrared thermography (IRT) so that it can be used to detect and assess damage growth in metallic and composite materials. A key component is to demonstrate that cheaper and more robust microbolometers could be used to replace the expensive photon detectors that are used currently in most laboratory settings, particularly for thermoelastic stress analysis (TSA). The possibility of using IRT, not just for monitoring and assessment of material behaviour, but additionally, for test machine control is investigated. The building blocks for a new approach to test machine control known as ‘damage evolution control’ are defined, using IRT based on the application of a microbolometer, presented as an alternative to the standard load, strain or displacement control methods incorporated in to modern test machine control systems.

The thesis contains a detailed review of the literature associated with the application of IRT in material assessments. As TSA and IRT are well established techniques only an overview of the underlying physics is provided. A detailed appraisal of the two infrared detector types (microbolometers and photon detectors) is provided alongside an overview of their architecture, advantages and

limitations. The performance of each detector type is evaluated using a temperature controlled blackbody to evaluate the noise levels and sensitivity of the bolometer system in comparison with that of the photon detector and incorporated into a camera model framework. The model is then used to demonstrate the limitations of using a bolometer based system for TSA using a metallic notched specimen.

It is demonstrated that IRT can be used to monitor and evaluate a growing crack in the metallic notched specimen and in particular that the bolometer temperature data is sufficiently accurate to determine the crack length. It is also demonstrated that IRT could be used to control a fatigue test. The IRT results from the photon detector were post processed for thermoelastic stress analysis (TSA), the output of which provide two other means to determine the crack length and confirmed the validity of the bolometer data. The TSA data was further post processed to calculate the stress intensity factor (SIF) to provide a further verification of the findings.

The design and implementation of a fatigue test on composite open hole tension (OHT) and un-notched specimens is described which characterises the temperature change generated in damaged composites and how the damage and the temperature evolves. The difference between the photon detector and microbolometer are reviewed and discussed, concluding that IRT may be used to monitor and assess damage evolution.

Integration of the IRT monitoring into the Instron test machine control system is described with an overview of the test machine control system and a variety of implementation strategies. A feasibility study of one of the integration techniques is presented, that demonstrates the microbolometers temperature output could be connected to Instron’s WaveMatrix software via an analogue input.

Table of Contents

Table of Tables

Table of Figures

Academic Thesis: Declaration of Authorship

I, James Edward Thatcher, declare that this thesis and the work presented in it are my own and has been generated by me as the result of my own original research.

Infrared thermography for test machine control and material characterisation

I confirm that:

1. This work was done wholly or mainly while in candidature for a research degree at this University;
2. Where any part of this thesis has previously been submitted for a degree or any other qualification at this University or any other institution, this has been clearly stated;
3. Where I have consulted the published work of others, this is always clearly attributed;
4. Where I have quoted from the work of others, the source is always given. With the exception of such quotations, this thesis is entirely my own work;
5. I have acknowledged all main sources of help;
6. Where the thesis is based on work done by myself jointly with others, I have made clear exactly what was done by others and what I have contributed myself;
7. Parts of this work have been published as:

    - **Damage evolution test machine control based on thermography,**

      J.E. Thatcher, D.A. Crump, P.B.S Bailey and J.M. Dulieu-Barton,

      ECCM 17 - 17th European Conference on Composite Materials, Munich, Germany (2016).

- **Characterising the infrared signature of damaged composites for test control,**

  J.E. Thatcher, D.A. Crump, P.B.S Bailey and J.M. Dulieu-Barton,

  SEM XIII – Society for Experimental Mechanics, 13th International Congress Conference, Florida, USA (2016), &

  Mechanics of Composite and Multi-functional Materials, Volume 7, ed: Springer (2017) 277-281.
- **Control of composite fatigue damage evolution using infrared thermography and thermoelastic stress analysis,**

  J.E. Thatcher, D.A. Crump, P.B.S Bailey and J.M. Dulieu-Barton,

  ICCM 21 – 21st International Conference on Composite Materials, Xi'an, China (2017).

Signed: ....

Date: ....

Acknowledgements

I would like to recognise the support and guidance of my academic supervisors, Professor Janice Barton, Dr Duncan Crump, and my industrial supervisor Dr Peter Bailey. Along with Dr Cedric Devivier for his guidance and assistance with his Matlab codes, and Dr Andrew Robinson for the training on composite manufacture and specimen preparation. Finally, I would like to thank, Instron Division of ITW Ltd., UK, and the EPSRC for funding this research.

Notation and Abbreviations

Notation

Symbol	Meaning
Upper case Roman symbols	
B	Specimen thickness
C	Paris law constant
C	Geometric shape function
C_1	First radiation constant
C_2	Second radiation constant
C_p	Materials specific heat capacity
F	Load
K	Thermoelastic constant
K_1	Stress intensity factor
$\mathrm{K}_{1\mathrm{C}}$	Critical stress intensity factor
T	Absolute temperature
T_o	Mean temperature
T_{ch}	Change in temperature
T_{i}	Incremental temperature change
W	Specimen width
Lower case Roman symbols	
a	Crack length
c	Speed of light
f_0	Frequency
g	Specimen geometry factor
h	Planck’s constant
m	Paris law constant
m	Gradient
r	Radius
t	Time
Greek symbols	
α	Coefficient of thermal expansion
ΔT	Change in temperature
$\Delta\mathrm{K}$	Change in elastic stress intensity factor range

ΔK_{1c}	Change in critical stress intensity factor
ΔK_{th}	Change in threshold stress intensity factor
ϵ	Strain
Φ	Phase angle
θ	Angle
∞	Infinite
λ	Wavelength
ρ	Materials mass density
σ_1	First principal stress
σ_2	Second principal stress
$\Phi_{\lambda,b}$	Spectral radiant emittance

Abbreviations

3D DIC	3 dimensional Digital image correlation
AC	Alternating current
ACPD	Alternating current potential drop
ADC	Analogue to digital converter
ASTM	American Society for Testing and Materials
BNC	Bayonet Neill-Concelman
BS	British Standards
BVID	Barely visible impact damage
C#	C# programming language
CCD	Charge coupled device
CCT	Centre cracked tension
CFRP	Carbon fibre reinforced polymer
COD	Crack opening displacement
CSA	Cross sectional area
CT	Compact tension
DAC	Digital to analogue converter

DC	Direct current
DCPD	Direct current potential drop
DIC	Digital image correlation
DL	Digital levels
EBSD	Electron backscatter diffraction
EN	European standard
EPD	Electric potential drop
ERCM	Electric resistant change method
FBG	Fibre Bragg grating
FE	Finite element
FEM	Finite element method
FLIR	FLIR® Systems Inc.
FOV	Field of view
FPA	Focal plane array
GigE	Gigabit Ethernet
GPIB	General purpose interface bus
GFRP	Glass fibre reinforced polymer
IAC	Integrated axis controller
InSb	Indium Antimonide
IR	Infrared
IRT	Infrared thermography
IS1	Implementation Strategy 1
IS2	Implementation Strategy 2
IS3	Implementation Strategy 3
IS4	Implementation Strategy 4
ISO	International organisation for standardisation
K	Kelvin
LHS	Left hand side
LSM	Least square method
LT	Lock in thermography
LVDT	Linear variable displacement transducer
LWIR	Long-wave infrared
MMI	Man machine interface
MWIR	Mid-wave infrared
NDE	Non-destructive evaluation

NETD	Noise equivalent temperature difference
NR	Noise reduction
NUC	Non uniformity correction
NNUC	Numerical NUC
OH	Open hole
OHT	Open hole tension
OTS	Off the shelf
PC	Photon counts
PID	Proportional-integral-derivative
PIF	Process interface
PT	Pulsed thermography
R	Radiance
R^2	Correlation coefficient
RHS	Right hand side
ROIC	Read-out integrated circuit
SD	Standard deviation
SDK	Software development kit
SENT	Single edge notched tensile
SIF	Stress intensity factor
SSD	Sum of squared differences
SSHC	Specimen self-heating control
SWIR	Short-wave infrared
TSA	Thermoelastic stress analysis
UFPA	Uncooled focal plane array
USB	Universal serial bus
UTS	Ultimate tensile stress
VI	Virtual instrument
X-ray CT	X-ray computed tomography

Chapter 1 Introduction

1.1 Background and motivation

Infrared thermography (IRT), is based on the use of an infrared detector camera system and is a practically real-time, full-field, non-contact method of monitoring the surface temperature of a component or system. It has been used as a non-destructive technique to detect cracks in welded metallic specimens [1], to monitor damage evolution in composites [2] and as a general condition monitoring technique [3]. IRT is based on the principle that infrared energy is radiated from all objects above 0 K. As the temperature increases, the amount of infrared radiation emitted by the specimen also increases according to Planck's Law [4] of black body radiation.

Infrared camera systems are based on two generic devices: microbolometers or photon detectors. Microbolometers detect the infrared energy in the wavelength range 7-14 μm, referred to as long-wave infrared (LWIR). Photon detectors generally measure IR energy either in the wavelength range 0.9-1.7 μm, short-wave infrared (SWIR), or 3-5 μm, mid-wave infrared (MWIR). In general photon detectors are much more sensitive, and are cryogenically cooled. Microbolometers are uncooled and are not as sensitive as photon detectors, but cost roughly a tenth of a photon detector system. The uncooled detectors are usually more robust as they do not containing a cooling system and are much smaller lending themselves to remote monitoring. Photon detectors are usually confined to laboratory type research and development work.

Alongside evaluating temperature changes in a component for condition monitoring purposes, IRT has been developed as an active NDE (non-destructive evaluation) technique using external stimulus to identify subsurface damage and defects and to evaluate stresses. Pulsed and lock-in thermography (PT, LT) [5], use a heating device to excite the structure and subsequent heat diffusion to identify defects. When a specimen or component is cyclically loaded in the material elastic region, a technique known as thermoelastic stress analysis (TSA) [6] is used to relate the temperature change resulting from the cyclic loading to the change in the surface stresses. It is clear that IRT offers many opportunities for rapid inspection of components and structures in a non-contact non-destructive fashion. However, there are many as yet unexplored areas of research that could make advantage of IRT but these have not been studied due to the relative expense and cumbersome nature of photon detectors that are necessary for the active thermography techniques, such as PT, LT and TSA. Application of bolometers to active thermography has been limited to a few investigations of the use of a specific bolometer for TSA [7] [8]. A key part of the work described in the current thesis is to study the applicability of bolometers for monitoring structural tests, to enable the use of TSA and develop test machine control. Hence providing a robust and cheap alternative to photon detectors with systems that can be applied in the field, production line or in laboratory conditions.

A frequently used method for detecting damage (and monitoring damage growth) during a fatigue test is to stop the test and use NDE, e.g. ultrasound. If IRT is developed to monitor a fatigue test, a live display can be used to detect the evolution of damage growth. Controlling the test machine with IRT can, therefore, be considered as the next step in the evolution of materials testing. The motivation is to enable the rate of damage evolution in composite material testing to be controlled in a similar manner to the current techniques used for crack growth monitoring in metallic materials [9] [10]. This damage evolution control would complement and enhance the current methods of displacement, strain and load control of the test machine.

At present strain gauges are used throughout structural testing to provide strain values at single points within a test component or structure. Installation of strain gauges is a highly skilled and costly process. TSA has the potential to reduce the number of strain gauges required by providing full-field measurements that are related to the stresses. After the initial purchase of the imaging equipment, IRT would supplant the cost of purchasing and installation of strain gauges, along with reducing the time involved in processing the data. Moreover using the microbolometer devices, instead of the expensive photon detectors, would reduce the upfront equipment purchase cost considerably. A typical cost for a photon detector with a similar specification to that used in the research is approximately £75,000, whereas the microbolometer was purchased for approximately £15,000.

In addition the time required to conduct a test would also be reduced, by removing the current method of stopping and starting a test to allow for NDE of the damage growth using techniques such as manual ultrasound inspection. The largest benefit in upscaling the use of IRT is in component, element and substructure testing, which is gaining more interest, particularly in composite structures, e.g. [11] [12] to reduce the number of coupon tests required for material certification. As this implies an increase in specimen manufacturing costs, fewer specimens would be tested with the requirement to extract more data on the material behaviour and failure initiation from each test, to offset the increased cost. IR imaging techniques will provide a key enabler in this process, if developed in such a way that they can be applied to large structural tests both in the context of measurement and test control. The work described in the thesis sets out to develop the underpinning technical advances to allow bolometers to be deployed for TSA and for test machine control, as well as developing a fundamental understanding of how to relate temperature measurement to material condition.

1.2 Aim and objectives

The overarching aim of the PhD is to develop IRT so that it can be used to monitor and assess damage growth in metallic and composite materials. A key component is to demonstrate that a cheaper microbolometer can be used for monitoring damage evolution and have the potential to be used in test machine control. The building blocks for a new approach to test machine control known as 'damage evolution control' are defined, using IRT, based on the application of a microbolometer, presented as an alternative to the standard load, strain or displacement control methods incorporated in modern test machine control systems.

To achieve the project aim the following objectives must be addressed:

1. Evaluate the suitability of using IRT in structural testing, by designing a series of verification studies that can be used to confirm that an IR detector can detect and monitor damage evolution in metallic and composite specimens.
2. Compare and contrast the differences between the performance of a microbolometer and photon detector in terms of noise and sensitivity from experiments using a temperature controlled blackbody.
3. Use a camera modelling approach to assess if it is possible to use a microbolometer for TSA and compare with experimental results around the crack tip in a single edge notch tensile (SENT) metallic specimen.
4. Use the SENT specimen to demonstrate that temperature changes due to damage, can be obtained using IRT with sufficient fidelity to control a test machine.
5. Create a framework for implementing IRT into test machine control.

1.3 Novelty

There are currently no British Standards for using IRT as a method for monitoring and assessing material damage growth during testing. Although not the aim of this project, the methodology developed during the course of this research could provide the basis of a composite damage evolution standard.

The use of a microbolometer for TSA has been investigated before [7], but was limited to metallic materials and purely elastic loading to give adiabatic conditions required for TSA. This research differs, in that metallic and composite specimens are being cyclically loaded to grow damage within the specimen, therefore each specimen contains regions of elastic and plastic deformation.

Currently there appears to be a limited number of publications on the integration of IRT into test machine control, e.g. [13]. This may be due to the expense of purchasing suitable equipment. Although there is a software package called "Specimen Self-Heating Control", available from Instron [14]. The software is an add-on module within the WaveMatrix™ control system, which utilises a simple USB connected Infrared camera, to monitor and control a test. The camera monitors the temperature of the test specimen. As the temperature changes, the software changes the test frequency, within a set temperature and frequency window. This project proposes to control, not only the test frequency, but the specimen stress levels. Aiming to control the damage evolution rate of the specimen, from indicators such as, temperature threshold levels and area measurements. There are publications where TSA has been used to monitor damage in fatigue testing of composite materials, e.g. [15]. However, a TSA approach that is integrated into a test control and monitoring methodology that informs on the damage type and identifies the point of failure does not exist.

1.4 Thesis content and structure

This thesis covers an assessment of the equipment that was used, a comparison between the two types of IR detector, how the equipment works together, with some feasibility trials, along with some testing and research outcomes to confirm that a microbolometer can monitor and assess damage evolution within metallic and composite test specimens, and perform TSA. Hence, Chapter 2 reviews current methods of damage evolution control in metallic and composite materials and the use of IRT and TSA in the detection and monitoring of damage evolution. As test machine control is a goal for the research, Chapter 2 starts with an overview of the Instron 8800 test machine and controller used throughout the work described in the thesis to apply the loading.

Chapter 3 provides a description of the two types of infrared detector that are used in the experimental work of the PhD project. The performance of each camera is evaluated using a temperature controlled black body to evaluate the noise levels and sensitivity of the bolometer system and compare with that of a photon detector. Tests were conducted over a range of black body temperatures and detector frame rates. The results from the experimental trials were then input into a Matlab camera model, created by Dr Cedric Devivier in a parallel project, to better understand the camera performance.

An introduction and overview of TSA is provided in Chapter 4. The chapter also describes the design of an experiment on a SENT metallic test specimen. The specimen is used as a basis for evaluation of the suitability of using bolometer for TSA using the camera model approach described in chapter 3. It is demonstrated that for a known stress field the camera model can provide a useful basis for assessment of the validity of results. In this case it is shown that the model can be used to identify the region ahead of the crack tip that is dominated by non-adiabatic effects resulting from local plasticity and dissipation. The model also demonstrated that a microbolometer is not suitable for TSA for the experimental parameters used in the thesis.

The experimental results for a SENT specimen are described in Chapter 5. Both types of detector were used to monitor crack growth, in two loading scenarios, using the IR, TSA, and TSA phase data to determine the crack length. The TSA data was further post processed to calculate the stress intensity factor (SIF) throughout the test. Resulting in the confirmation that a microbolometer has the fidelity to detect and monitor damage evolution within the specimen.

Chapter 6 describes the implementation of the IRT techniques on open hole tension (OHT) and un-notched fibre reinforced polymer specimens. It is demonstrated that the temperature evolutions can be used to monitor damage progression and that the thermoelastic response can characterise the damage type. An approach is suggested that uses temperature evolution that occur as the damage progresses in the composite material might be used to control the test machine.

An overview of the various implementation strategies to integrate the IRT monitoring technique into the test machine control system can be found in Chapter 7. Concluding with feasibility demonstration trials of two integration techniques. The first trial utilises the Optris PI450 camera software, to output temperature data, into Instron’s WaveMatrix software via an analogue input. The second trial uses LabVIEW to control the image capture and output the required temperature data.

Finally, Chapter 8 discusses the outcomes of the previous chapters and summarises the conclusions from the work undertaken for this thesis. Areas for future study are also suggested.

Chapter 2 Literature review

2.1 Introduction

To facilitate the integration of an infrared detector system for damage evolution control a thorough understanding of the test machine control system has been developed. In the present work a servo hydraulic test machine is used to provide the necessary cyclic loading on the test specimens. An over view of servo hydraulic test machines functionality is provided in the next section of this review.

This chapter then considers the current state of the art in detection and damage control techniques for use in the mechanical testing of metallic and composite materials, and then compares the different techniques used for each type of material. Particular focus is given to the control of damage evolution in cyclic testing, detecting and monitoring damage in composite materials, and the use of full field imaging techniques. Three full field measurement techniques have been selected as potential approaches for test machine control, namely infrared thermography (IRT), thermoelastic stress analysis (TSA), and digital image correlation (DIC). IRT theory is introduced and the two damage detection techniques, active and passive IRT, where the active techniques use an external heat source, when the specimens are stationary, and the passive technique using temperature changes generated during testing. The equipment used for TSA is described and a review of using TSA for crack and damage evolution in a selection of materials. The use of DIC for damage detection in both material types, is investigated and discussed in section 2.6. The chapter concludes with an overview of the literature review and down selection of the techniques to be further assessed in this research.

2.2 Servo hydraulic test machine

A servo hydraulic test machine is shown in Figure 2.1 and is comprised of the following main parts: a rigid frame; load cell; displacement transducers; hydraulic actuator; and a control system. The actuator is a hydraulic ram that moves to impart a load or displacement onto the test specimen. One end of the actuator is connected to the specimen via a mechanical gripping arrangement and on the other end is a linear variable displacement transducer (LVDT) which feeds the actuator displacement into the control system. On the other end of the specimen is another mechanical gripping device, connected to a load cell. The load cell's output is also fed back into the control system. The specimens are gripped into the load string via a variety of gripping mechanisms, depending on the type of specimen being tested. They include pneumatic pistons and wedge grips, hydraulic pistons and wedge grips and manually operated wedge grips. In some cases the specimens can be bolted directly to the actuator and load cell.

The movement of the actuator is controlled by a digital controller, which has standard control regimes of displacement, load and strain. Displacement control utilises the data from the displacement transducer and encoders, and adjusts the speed of the actuator or crosshead (electromechanical test machines), to achieve the required displacement over a given time period, e.g. 2 mm min^{-1}. Load control employs the information from the load cell to move the actuator at a speed to achieve a specified load change per time period, e.g. 2 kN min^{-1}. Strain control uses either a strain gauge or an extensometer. Both of these instruments measure displacement over a given gauge length, ranging from 0.5 mm to 150 mm for a strain gauge and 10 mm to 750 mm for a extensometer. The displacement rate of the actuator or crosshead is then adjusted to achieve the required strain over time period, e.g. 1 min^{-1}. This method is used to disregard any test machine or jig compliance issues that may result from the use of displacement control.

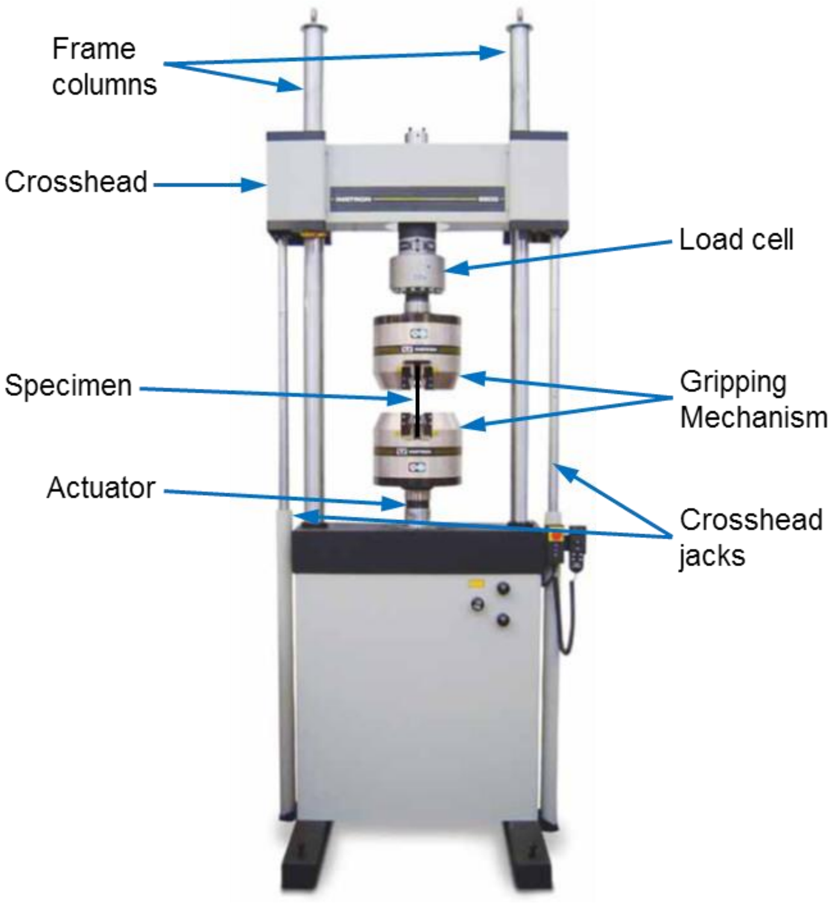

Figure 2.1. Instron 8802 servo hydraulic test machine [16]

The Instron servo hydraulic test machine used in this work is controlled by the Instron 8800 digital controller. This controller consists of three major systems, the hardware, firmware and software. The hardware (Section 2.2.1) commands the actuator. The firmware controls the functions of the test machines, such as limits, proportional-integral-derivative (PID) feedback loop (Section 2.2.2), amplitude control (during cyclic loading), adaptive control and data logging. The software, WaveMatrix™, provides the test conditions and data storage (Section 2.2.3).

2.2.1 Hardware - 8800 Tower

The 8800 controller tower consists of (at a minimum) an integrated axis controller (IAC) card, that controls the test machine in position or load control, and an operator interface connection. Two connections are available for the operator interface. The first connection is used to connect a man machine interface (MMI).

The second connection is a high speed general purpose interface bus (GPIB) port that connects the tower to a computer running the software suites.

External inputs available to connect the imaging systems to the controller tower are limited to:

- Up to six, 25 way D-type analogue connections ("Strain channels" used to attach extensometers, other Instron devices and the Optris PI450 IR camera discussed later in section 3.3.3).
- Four digital logic connections.
- One BNC (Bayonet Neill-Concelman) analogue input.

As the digital inputs are logic (i.e. 0/1), they can only be used to switch actions within the software. The actions available are "limit" actions: No action, actuator off, stop and hold (in current control mode), stop and transfer to position control, transfer, log data and reset. Therefore the only channels available for input to the tower are the analogue inputs.

When using the analogue input, it is necessary to convert the digital output from any imaging equipment, into an analogue signal for the test machine, which will then convert back into the digital format that the controller requires. The digital to analogue, and analogue to digital, conversions take time and introduces an error source to any calculations. The error is created by the discrete steps of the digital resolution, when compared with the analogue. For example an analogue output of 0 to 10 volts, with a digital resolution of 12 bits, giving 4096 discrete steps. When the voltage range is divided by the number of steps, the digital resolution is 2.44 mV. Then when the voltage is converted back to analogue the error is compounded.

2.2.2 PID control

PID feedback loops are used to control and minimise the error value between the command value (displacement, load or strain) and the value achieved. The proportional value is the current error, the integral is the past error values summed together, and the derivative is the possible future error, based on the current rate of change. Software within the controller uses these values to adjust the test machine as required. Each manufacturer that utilises PID control often develop their own algorithms, which results in the software remaining proprietary information. Occasionally the software is patented [17], and licensed to other manufacturers.

Instron digital controllers have the ability to “Autotune” the PID control loop in all three control modes, displacement, load and strain. The tuning ensures that the test machine accurately responds to the commands given to it by the control system. If there is a difference between the command value and the output value from the displacement, load or strain transducers there is an error. Autotuning minimises or removes the error. The errors can be caused by inertia or slack within the load train, specimen compliance, servo valve response or drag within the actuator. Before starting a test, any jig or fixtures must be installed into the test machine and tuned in the same control mode as the test. In displacement control a specimen does not have to be installed. For the load and strain control modes a specimen has to be installed as the load and strain values refer to those applied to the specimen.

Before autotuning is initiated, the mean and amplitude in load and strain control must be specified so that the specimen installed, stays within its elastic limit. In displacement control the amplitude is usually set to be half of the expected maximum displacement of the test. When the tuning is started a square wave is used, with the proportional gain automatically reduced (to prevent an unstable response). The autotune algorithm then increases the proportional gain in steps to achieve a specific overshoot. The derivative gain is then adjusted in steps to reduce the overshoot. Next a triangular wave is used and the integral gain is adjusted. When this process is complete the waveforms stop and the new PID values are displayed.

During cyclic testing in load and strain control, the specimen compliance can change significantly, resulting in the peak loads or strains not being achieved. To overcome these differences, Instron controllers have an amplitude control option available. The amplitude control option monitors the peak values of the waveform and when the required peak values are not achieved, the command value is increased until the required values are achieved.

2.2.3 WaveMatrix™ software

WaveMatrix has been developed for dynamic and fatigue testing, with the capability to run a static test, through to spectrum loading fatigue test on single and multiple actuator systems. There is also the ability for additional software or calculation channel, to be added for standard fatigue test programs, customising the control and data logging output as required.

Creating a test sequence requires the waveform to be selected for each step, along with the data logging requirements, the method is saved and then the test can be started. If the waveform required is not available within the software, the operator can import their own waveform profile. More than one channel is available, so others can be specified to control a second actuator (torque or multiaxial loading), or control a heating chamber.

An additional self-heating control software [14] is available for WaveMatrix. This module was developed to reduce the time to create a fatigue life curve (S-N curve) for composite specimens. Composite specimens increase in temperature when they are fatigue loaded. They are also sensitive to temperature increase, so the tests are run at lower frequencies to prevent this increase in temperature. Instron’s specimen self-heating control (SSHC) monitors the specimen using a thermocouple or a USB infrared thermometer. A target temperature is set, along with a maximum frequency and then the test is started. The module runs the test at the maximum frequency unless the limit temperature is surpassed. If the temperature goes beyond that limit, the frequency is automatically adjusted so that the temperature remains constant throughout the test.

2.3 Current approaches to detect the evolution of damage in fatigue testing

There are a variety of test methods and standards, dedicated to fatigue loading of notched metallic specimens, monitoring and controlling the damage growth rate (BS ISO 12108 [9] & ASTM E647 [18]). Composite specimens are currently limited to fatigue testing to obtain material fatigue properties only, without damage growth rate control (BS ISO 13003 [19] & ASTM D3479 [20]). This section is presented in three parts. The first is dedicated to the detection of damage within a metallic specimen, followed by the listing and discussion of testing techniques used for the monitoring and control of a metallic fatigue test. The second section reviews the monitoring techniques used during the fatigue of composite test specimens. This section concludes with a comparison between the techniques applied to tests on metallic and composite materials and the feasibility of applying them to the current research.

2.3.1 Metallic specimens

Current non-destructive evaluation techniques used for the detection of damage within metallic materials include, ultrasonic [21], and radiographic testing [22]. These techniques do not require a change in specimen stress, or damage evolution within the specimen to allow detection and monitoring. Utilising these evaluation techniques during a fatigue test requires the test to be stopped so that the inspection can be conducted, before the test is restarted. For metallic specimens other, contacting, techniques are available that enable the evolution of damage in a pre-cracked specimen to be monitored, and measured, during a fatigue test. [9]. This type of approach is well established for crack propagation in metals, using controlled level and variation in crack tip stress intensity factor (SIF). The SIF is a function of the applied stress, crack length, specimen size and geometry. The approaches that can be used to monitor and measure the crack growth from initiation through to failure, include the use of crack opening displacement (COD) gauges, attached to either side of the notch, and electric potential drop (EPD) methods. EPD uses alternating current potential drop, or direct current potential drop (ACPD & DCPD), which measure the change in potential drop during the test sequence. All three methods convert the measured values to crack length, and do not require the test to be stopped or paused, for the inspection to be carried out.

BS ISO 12108 [9] states that stopping a fatigue test to visually monitor the crack growth “is discouraged and shall be avoided when possible” and that the crack growth rate may be altered after a test pause, therefore an automated method of crack measurement is preferred. The standard also states that the crack has to grow within a narrow corridor across the specimen from the notch and the uniformity of the crack length on both sides of the specimen. Both of these constraints are suitable for a metallic specimen, but not a composite specimen. The reasons for the unsuitability of these crack monitoring techniques for composite materials are discussed at the end of this section.

2.3.2 Composite specimens

Current non-destructive evaluation techniques used for detecting, locating and quantifying damage within unstressed composite materials include ultrasound

[23], radiography [24] and pulse thermography (PT) [25]. The current accepted techniques are not suitable for continuous inspection throughout a fatigue test, instead requiring the test to be paused for the inspection to be conducted. Two alternate techniques for monitoring quasi-statically and fatigue loaded specimens are DIC and IRT. These two techniques are the subject of large areas of research and are discussed individually in sections 2.4 and 2.6 respectively. There are currently no British standards for the monitoring of damage evolution in a composite specimen. The only standard available for composite specimen fatigue testing is BS ISO 13003 [19], which gives guidelines on fatigue tests, based on quasi-static test standards and does not include an approach for testing using damage growth rate control.

The specimen geometry for damage evolution rate control can be considered critical for the successful outcome of the test. A standard composite test coupon is rectangular in shape with no obvious stress concentrations to initiate damage, except at the end of the specimen close to the gripped area or endtabs. According to the test standard, failure of the specimen at these points is considered invalid. For a valid test the specimen has to fail within the gauge section of the specimen. Although two full field imaging techniques are being considered, and the whole of the specimen can be observed, to improve the detail of the damage in the images captured, a more focused region of interest is preferred. To ensure that the observed area contains the damage initiation and growth, a stress concentration is required to initiate the failure. Two common stress raisers used in composite testing are an open-hole (OH) and barely visible impact damage (BVID). OH specimens [26] are a rectangular specimen with a hole machined through the centre of the coupon, and used for tension and compression testing. BVID tests were designed and developed for aviation industry certification. Boeing [27] and Airbus [28] both employ similar test standards for compression after impact testing using specimens, 150 x 100 mm, nominally 4 mm thick with a BVID in the centre.

OH specimens, are the preferred method of introducing a stress raiser for the work in the current thesis, due to the repeatability of the damage introduction. The OH specimen is prepared by machining a single hole through the centre of the specimen and is then tested in tension using standard test machine jaws. Whereas the BVID specimen requires an additional testing step where the specimens are impacted via an instrument drop weight tower, introducing more variability to the size, type and location of the induced damage. Additionally, the BVID specimens are usually tested in compression using an anti-buckling loading fixture, which may introduce more experimental errors and hide parts of the specimen from the imaging technique.

Broughton *et al.* [25], undertook an assessment of glass fibre reinforced polymer (GFRP) OH tension specimens to evaluate the measurement techniques available to monitor and quantify material damage and specimen fatigue life, thus aiding and improving finite element (FE) models of fatigue damage in quasi-isotropic composite materials. In particular, [9] considered PT, DIC and multiplexed fibre Bragg grating (FBG) system to assess the damage evolution. The FBG was successfully used to measure strain while the specimen was subjected to quasi-static and cyclic loading, and exhibited superior fatigue endurance when compared to standard foil strain gauges. To apply the PT and DIC techniques the test was paused. The PT, using two xenon flash lamps pulsed for 31 ms and the cooling recorded for 30 seconds, was used to observe damage growth around the hole once the test had been stopped at pre-determined points within the test to provide a measurement of the size/location of the damage. The DIC measurement was applied every 10,000 cycles. The specimen was unloaded, and then statically reloaded whilst the DIC recorded the surface strains. The paper concluded that DIC was successful in monitoring of strain distribution around a hole due to damage evolution, and that longitudinal strain and stiffness could possibly be used for predicting fatigue life of notched composites. The paper also concluded that stopping the tests at pre-determined points, resulted in some of the damage evolution during final failure of the specimen being missed or difficult to measure.

X-ray computed tomography (X-ray CT) has also been utilised for monitoring damage development in a fatigue loaded OH composite specimens [29]. Both quasi-static and cyclic loading was applied to 51 open-hole composite specimens. To monitor damage evolution, each specimen was stopped at a prescribed stress level or number of cycles to allow the X-ray images to be taken. The X-ray CT images have shown initial damage propagating from the hole by matrix cracks or delamination. Additionally, for selected tests, IRT was used to measure temperature change during the test, and it was concluded that the increase in temperature corresponds well with the damage evolution. Similar damage monitoring using DIC and X-ray CT was used [30] for interrupted static and fatigue tests. It was concluded that damage detected by X-ray CT, corresponded well with regions of high strain concentrations, recorded by the DIC.

2.3.3 Comparison between metallic and composite techniques

The largest difference between metallic and composite fatigue damage detection techniques is that metallic techniques have matured over many decades, and are now well established, that specific test standards [9], [18] have been created for the variety of monitoring and controlling of an uninterrupted fatigue test. Whereas for composite test techniques, the damage detection technology is predominantly used in the research environment, until such time a robust and repeatable technique is developed, a test standard cannot be created. Hence, there is not a technique approved for use in design approval and certification testing. The monitoring technology often requires the fatigue test to be paused, for example to allow DIC to be applied during a quasi-static test, or the specimen removed to enable X-ray CT to be applied. DIC has the potential for monitoring and control, with recent advances in the data processing, and is described and discussed further in Section 2.6. Infrared thermography, discussed in [29], does not require the fatigue test to be paused, and is considered suitable for the monitoring and control of damage evolution rate in a composite material. The depth of this area of research, requires this full field imaging technique to be reviewed in a separate section, Section 2.4.

It is not feasible to adapt many of the techniques currently used for metallic notched specimens and crack propagation monitoring techniques for testing of composite materials. Composite materials are subjected to a variety of failure mechanisms e.g. fibre breakage, ply splitting, delamination and shear failure, all of which may be present in a single damaged area. Therefore a single crack growing across the width of the specimen, that allows a COD gauge to be used to monitor crack length, is not viable. Some studies have been conducted using the compact tension (CT) specimen geometry on the intralaminar fracture toughness of woven composite laminates. A thick laminate was manufactured, with the notch machined to align with the plies of the laminate. Blanco *et al.* [31] summarised previous work in this field and investigated the use of modified CT specimen geometries by finite element analysis (FEA), to determine a suitable specimen to achieve crack propagation for intralaminar fracture toughness characterisation. A preferred specimen geometry was selected that best ensured intralaminar crack progression, but it was noted that the specimen might still fail by other, non-desired, mechanisms. In part 2 of the paper [32], the selected specimen geometry was investigated experimentally. The experiment applied DIC to measure the crack growth instead of a COD gauge. The geometry was a success in measuring intralaminar fracture toughness and DIC measured the surface strains around the crack tip.

Techniques utilising electric potential drop are also not suitable for composite crack growth monitoring due to the electrical insulating properties of polymer matrices and some fibres, such as glass. An adaption of EPD called electric resistance change method (ERCM) has been developed [33], allowing the size and location of delamination's in CFRP beams to be estimated, but it requires the use of an array of sensors and "learning data" from FEA and a large number of experiments on the same material and ply orientation.

2.4 Infrared Thermography

Infrared thermography (IRT) is a real-time, non-contact, approach used to measure the surface temperature of objects. Essentially an optical system comprising lenses is used to focus infrared radiation onto a temperature sensitive electronic chip or detector array. The detector response or voltage output is converted to digital level (DL) using an analogue to digital converter also on the electronic chip to enable output to a computer.

Infrared energy is radiated from all objects above 0 K. As the temperature increases, the amount of infrared radiation emitted by the specimen also increases according to Planck's Law [4] of black body radiation as follows:

$$\Phi_{\lambda,b} = \frac{C_1}{\lambda^5\left(\exp^{C_2/\lambda T} - 1\right)} \tag{3.1}$$

where $\Phi_{\lambda,b}$ is the spectral radiant emittance, C_1 is the first radiation constant, C_2 is the second radiation constant, λ is wavelength and T is the absolute temperature.

A plot of the spectral radiant emittance against wavelength is shown in Figure 2.2 for the temperature range applicable to the experimental work described in the thesis. The coloured areas in Figure 2.2 indicate the wavelength ranges for the two detector types: photon detectors and microbolometers, which are described in detail in Chapter 3. Microbolometers detect the infrared energy in the wavelength range 7-14 μm, referred to as long-wave infrared (LWIR). Photon detectors measure IR energy either in the wavelength range 0.9-1.7 μm, short-wave infrared (SWIR), or 3-5 μm, mid-wave infrared (MWIR).

The calibration process for an IR detector consists of a series of measurements from the surface of a black body at a range of accurately controlled temperatures. The information from this process is used to create a three dimensional calibration curve of temperature versus DL versus integration time/thermal time constant. These curves are then used to convert the DL or uncalibrated output into temperature. Chapter 3 explains the detectors integration time (photon detector) and thermal time constant (microbolometer).

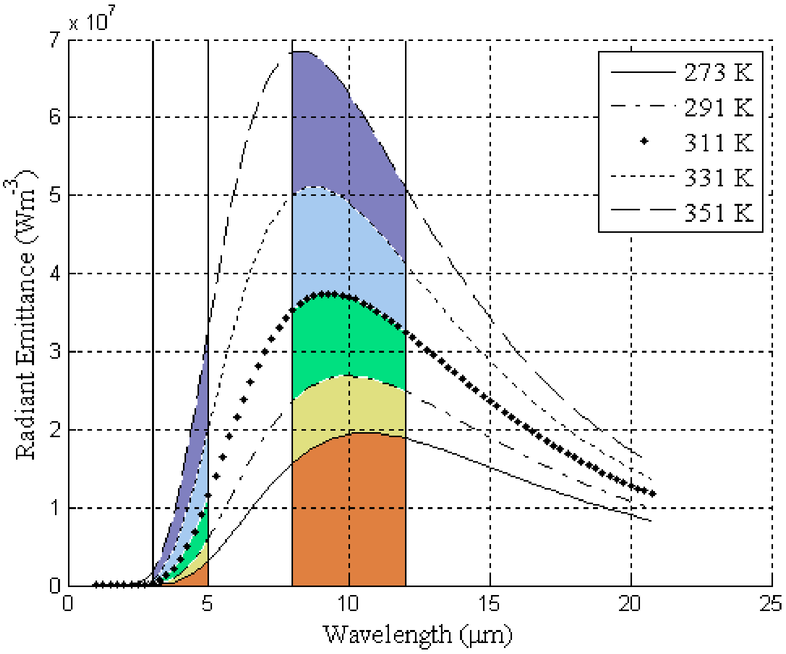

Figure 2.2. Electromagnetic radiation curves for some representative temperatures [34].

It is common in thermography applications to improve emissivity of the surface to be measured by applying a thin layer of matt black paint. This is used to provide a uniform surface finish and reduce reflections that may occur from polished surfaces. Infrared energy from external sources such as lights or the camera can be correlated into the response from a reflective surface, and provide an incorrect measure of temperature.

There are two types of IRT used experimentally, active and passive. Active thermography uses an external source to heat the specimen, then the temperature decay rate is monitored. In [25] two xenon camera flashes, pulsed for 31 ms, emitting a flash of approximately 276 lux, were used. Passive thermography monitors the surface temperature of a specimen. Harizi, *et al*, have undertaken two studies using active, PT, [35] and passive [36] thermography to characterise the damage in GFRP during static tensile loading. In the passive tests, there was no indication of damage at low stress states. However at higher stress states, above 250 MPa, interfacial disbonding and delamination was detected. A second set of tests were conducted where specimens were subjected to step-wise static loading. At each load step the test was paused allowing active thermography to be performed whilst the specimen was held at the specified load. Two halogen lamps were used to heat the specimen for 30 seconds, before the cooling phase was recorded using IRT for 125 seconds. The paper does not provide any full-field images from the IRT measurements to indicate the damage detected. Instead cooling rate graphs from an undefined area of interest are shown, demonstrating that the measured cooling rate is different for the specimen once damage is initiated. The authors conclude that if a cooling rate can be associated with a damage state, then the global damage state of a specimen could be quantified.

A similar study using passive thermography, recorded the temperature evolution of the specimen throughout a continuous static tensile loading of a GFRP specimen [37]. The paper reported the use of passive thermography for damage assessment of different material lay-ups, comparing the thermographic output with microscopic analysis of specimen sections, loaded to predefined stress levels and then unloaded. After failure the specimens were sectioned, to determine the specimen failure mechanisms. It was concluded [37] that analysis of the specimen thermal maps and profiles, permitted the detection of three regions: the initial thermoelastic region, when the material is within its elastic behaviour region, the second region of decreasing temperature, due to micro cracking and the third region of increasing temperature due to damage growth beyond micro cracking.

The suitability of passive IRT as a method of monitoring damage evolution in a composite material was also confirmed in [38], where IRT was compared with digital image stereo-correlation (3D DIC) and X-ray CT. The X-ray CT was used after the specimens had failed, to confirm findings of the IRT and 3D DIC. Two material lay-ups were used during testing, type A $[0/90]_6$ and type B $[+/-45]_6$, and were subjected to interrupted quasi-static testing. Each specimen was loaded in displacement control, to a predefined load level and then returned to zero load. The loading was repeated with a higher predefined load, returned to zero load, then repeated, with increasing load levels, until failure. Using 3D DIC and IRT for tests on type A specimens did not identify any damage prior to failure, and therefore it was not possible to forewarn before sudden specimen failure. However at failure the IRT measured a sudden increase in temperature. X-ray CT confirmed that the failure of the type A specimen was orthogonal to the tension axis, through the 0° fibres as expected. For tests on type B specimens the DIC measurement detected changes in longitudinal and transverse strains localised around the resulting failure point and IRT detected changes in temperature, correlating with the changes in strain. It was noted that the type B specimen was warmer at failure than the type A which was attributed to the matrix shearing mechanisms present in the type B specimen, and that IRT was better at monitoring the damage initiation (earlier detection) and evolution during the test. The X-ray CT confirmed the localised heat zone corresponded with fibre-matrix disbonding and delamination.

Usamentiaga, *et al* [39] proposed a method for using PT to automatically detect impact damage in a CFRP (carbon fibre reinforced polymer), primarily to remove operator interpretation of the results. Specimens were heated by three 1000 W halogen lamps for 15 s and the cooling captured, using an IR detector, for 15 s. It was reported that while damage was successfully detected, with the areas measured and quantified to the pixel level, there were drawbacks with the time required to process the data. The specimens were heated for 15 seconds, the temperature decay recorded for 15 seconds, and then the data processing of 10 seconds. This process was repeated 4 times, as the specimen was rotated 90° between inspections, at 0°, 90°, 180° and 270°. These timescales and the requirement to rotate the specimen, make this process unsuitable for test machine control, but may prove suitable as an automated quality control inspection technique. A further development of the technique, to locate the damage depth through the thickness is proposed in [40]. The authors demonstrated that damage at different depths within the specimen have different temperature decay times, the actual depth calculation requires 3D numerical models of heat dissipation within the material, which may also be used to confirm defect size and thickness. Although the defect thickness accuracy would improve with a double sided inspection, instead of a single sided inspection.

The application of IRT to fatigue testing of metallic and composite specimens is also the subject of numerous papers. For example, in [41] active and passive IR techniques were used to monitor damage evolution during tension-tension fatigue tests of rectangular CFRP specimens. The passive technique was applied during the fatigue test, at predefined cycle counts, to measure the hysteretic heating effect. Whereas the active testing was undertaken at predefined cycle counts, alternating with the passive technique, during fatigue testing, when the waveform was paused. Once the active scan was completed the specimens were subjected to an ultrasonic C-scan inspection to compare with the damage detected using active IRT. The results show that the thermal images allow the identification of damage initiation and evolution and that the active thermography technique allows damage to be detected by variations in heat conductivity. When the thermal images were compared with the C-scans, it was noted that while there was a small difference between the thermal images taken at each cycle count at the lower damage state, the C-scans showed significant differences. The authors concluded that passive monitoring was suitable for monitoring heat dissipation through the specimen during the fatigue tests, and active thermography required further investigation to improve the reliability of damage detection at the lower damage states.

Metallic specimens subjected to cyclic loading, have been monitored using passive IRT, where it was noted that as a metallic specimen is fatigued beyond it elastic limit the temperature of the specimen increases e.g. [42]. It was reported that when an aluminium alloy specimen is subjected to fatigue loading where the maximum stress value is higher than the yield stress of the material, a sudden increase in temperature is observed. If the specimen has a stress concentration such as a notch or cracks, the temperature around these defects changes more than the undamaged parts of the specimen, due to localised material plasticity. The temperature evolution due to localised material plasticity, has been associated with the fatigue limit and fatigue life of cylindrical and rectangular metallic specimens [43], where IRT was used to locate the areas of plastic deformation and then monitor the temperature evolution of its hot-spot, along with the fatigue damage propagation. The paper confirmed that the hot-spot was associated with the subsequent fracture locations, and that the temperature evolution rate of the hotspot may be used to calculate the materials fatigue stress limit.

IRT has also been used on damaged composite materials to monitor damage evolution in fatigue specimens subjected to barely visible impact damage (BVID) [44]. IRT was used to monitor the damage evolution during compression fatigue testing, under load control. The global change in specimen compliance was used to estimate the damaged area, and then measured the damage area using the IR temperature profiles around the damage, subtracting an initial image recorded at the start of the test, from the images recorded at various cycle counts. The type of damage sustained during the fatigue test was not investigated and the data was processed after the test had finished. It should be noted that the IR camera was not synchronised with the fatigue test, and the method of recording the IR images during the fatigue test is not stated. The paper concludes that it is possible to correlate the change in specimen stiffness with the change in damaged area and that IRT is a useful method for tracking damage evolution in composite materials.

Using passive thermography with fatigue loading of composite materials appears to be the way forward in the research in the present work to detection of damage initiation and evolution. In [45] it was concluded that the infrared images obtained, were capable of establishing local high-temperature regions, which corresponded to damage within the specimen. The authors also concluded that for the braided CFRP specimens they were testing, the damage state could be identified (braider yarn cracks i.e. cracks developing in the woven tow), although future work suggested using X-ray CT of the damaged specimens, to confirm the findings of the study.

2.5 Thermoelastic stress analysis (TSA)

Thermoelastic stress analysis (TSA) is based upon the theory reported by Lord Kelvin, in the 1850's, that there is a relationship between the elastic deformation of a material and the thermal energy change within the specimen [46]. This relationship is known as the thermoelastic effect. The thermoelastic equation that has been derived from this theory, for an isotropic, homogeneous material, is as follows:

$$\Delta T = -KT(\Delta\sigma_1 + \Delta\sigma_2) \tag{2.1}$$

where ΔT is the change in temperature, K is the thermoelastic constant, T is the absolute temperature of the specimen, and $\Delta\sigma_1$, $\Delta\sigma_2$, are the changes in the principal stresses.

The theoretical thermoelastic constant (K) of a material is:

$$K = \frac{\alpha}{\rho C_p} \tag{2.2}$$

where α is the coefficient of thermal expansion, ρ is the density and C_p is the specific heat capacity at constant stress.

For a composite/orthotropic material, the thermoelastic equation has been derived and validated [47] to give:

$$\Delta T = -\frac{T}{\rho C_p}(\alpha_1 \Delta\sigma_1 + \alpha_2 \Delta\sigma_2) \tag{2.3}$$

To obtain K, experimentally for an isotropic material a strip loaded in uniaxial tension is used; here the applied stress, $\Delta\sigma$, is known so K is obtained as follows:

$$K = \frac{\Delta T}{T \Delta\sigma} \tag{2.4}$$

Thermoelastic stress analysis assumes that the specimen is tested under adiabatic conditions. Adiabatic conditions are such that there is no heat transfer within the specimen or with its surroundings. Under laboratory conditions this is met by cyclical loading of the specimen in a test machine, within the elastic region of the test material.

In practice, TSA is applied using a ‘lock-in’ algorithm to improve the signal to noise ratio and enable the small temperature change resulting from the thermoelastic effect to be detected. When a specimen is undergoing cyclic loading in a test machine, the load measurement is recorded from the load cell via an analogue voltage output alongside the infrared images (see Figure 2.3). The frame rate and duration are specified, so that a sufficient amount of data is recorded over a loading cycle, and over a sufficient number of loading cycles. The NETD (Noise Equivalent Temperature Difference) and recording frequency of the photon detector, allow the small change in temperature, i.e. the thermoelastic response (ΔT) during cyclic loading to be recorded.

The SC5500 records infrared images into a ".ptw" video file for post processing using proprietary software known as Altair LI. The software applies a "lock in" algorithm on the infrared image series using the recorded load signal as the reference. The post processing creates three images, the specimen's mean temperature (T), change in temperature due to load (ΔT) and phase (ϕ). The phase image provides the phase angle difference between the ΔT output and the load signal. An in-phase response means that the test is conforming to equation (2.2). It should be noted that an in-phase response has a 180° phase angle, due to the temperature of the specimen decreasing as the stress increases. An out of phase response indicates, non-adiabatic conditions, such as heat generated due to plastic deformation of the specimen.

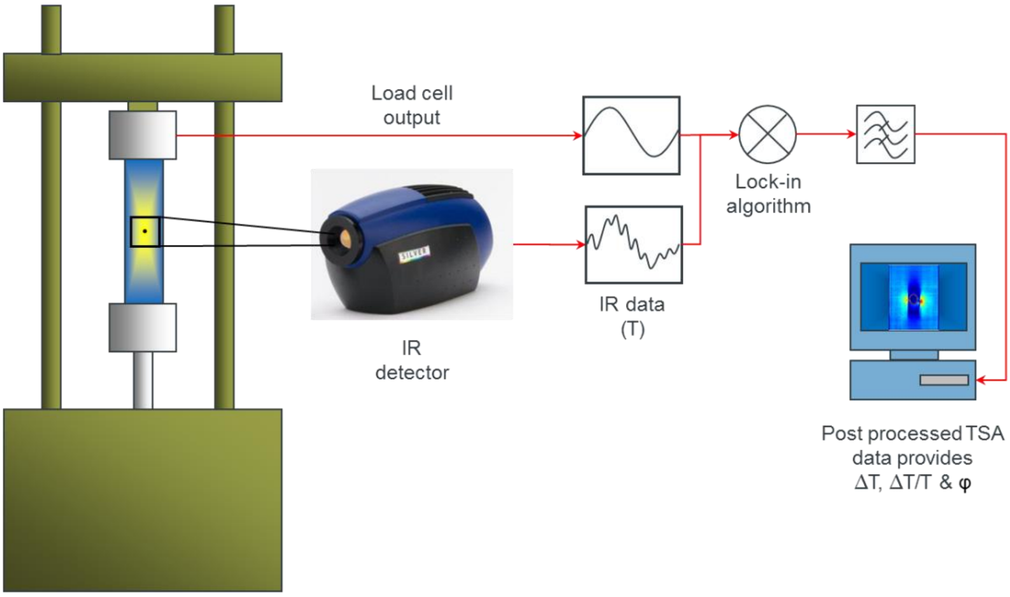

Figure 2.3 Typical TSA experimental set-up.

2.5.1 TSA of crack and damage evolution

TSA is a useful tool for analysing the stress field around crack tips in metallic materials. From a review of published work in [48] which focused on using TSA for analysing crack tip stress fields and deriving SIFs directly from TSA, it can be concluded that there are a variety of approaches to deriving the SIFs from TSA. Furthermore the high resolution nature of the data, which since the publication of [48] has improved enormously, make TSA an attractive technique for assessing cracks. Other advantages included, minimal specimen preparation and the ability to directly obtain the stress intensity factor (SIF), from the TSA data. In the present work the original approach devised by Stanley *et al* [47]is used; a detailed overview is provided in Chapter 4. A study comparing the use of TSA and the conventional compliance method to measure crack growth in a metallic specimen was conducted in [49]. The study used CT specimens, manufactured from a silicon carbide particle-reinforced aluminium alloy (A359/SiCp). Four equally spaced vertical lines were marked on the specimen in front of the crack, where the TSA stress values were monitored. The idea was that the stress would increase as the crack approached the line and then peak when the crack tip reached the line. The study concluded that TSA showed a good match with the compliance method, and then suggests the suitability of TSA for in-service monitoring of cracks in aircraft wings and turbine engines, using the normal loading conditions to produce a thermoelastic response. Experimental results from TSA for a CT specimen, have been compared with computational modelling and finite element method [50]. The study concluded that the computational modelling and the finite element method produced encouraging results, verifying validity with the experimental results from TSA.

The calculation of stress intensity factors (SIFs) during fatigue crack growth [51], from TSA measurements, was validated against compliance measurements and numerical analysis for mode 1 SIFs, confirming that crack closure ahead of the crack can be experimentally identified. IRT has been used to locate fatigue crack initiation and then for monitoring the crack growth [52]. This was achieved by monitoring the temperature field on the specimen and post processing the data to compute the spatial standard deviation of the temperature. It was shown that a sudden increase in the standard deviation value corresponded to a crack initiation. TSA has also been used for monitoring the crack growth rate in metal matrix composites [53]; where it was shown that TSA is a good match with a conventional compliance method. The paper also states that surface and subsurface cracks were detected, allowing them to be monitored. Vieira, *et al* [8] used TSA measurements, to obtain crack tip location and SIF in a polycarbonate specimen, and concluded that TSA can determine the crack tip location, crack growth rate and SIF simultaneously with their algorithm, and that the raw temperature measurement near the crack tip directly relate to the crack growth rate. These conclusions agree with the results presented in Chapter 5 that monitored crack growth in a metallic specimen.

A system for automated crack growth detection using TSA [54] has been developed and validated, using a microbolometer. The software and algorithms developed allowed the microbolometer and a microscope to move on an X-Y linear slider, keeping the crack tip in the centre of the image. It was noted that at crack growth rate below 10^{-7} m/cycle, there was measurement scatter due to the limited spatial resolution of the IR detector. A similar result was also noted during this research and is reported in Chapter 5. The software and algorithm developed to move the linear slider, could be developed further to feedback crack length into the test machine control, and then control the test in a similar fashion when using COD gauges and EPD measurements, for a metallic crack growth specimen. Some issues with the results is that to validate the TSA crack length measurement, the test was paused, the maximum load applied and a photograph of the crack recorded. The article did not state the algorithm processing time or when the microbolometer and microscope were moved.

The impact damage of GFRP samples has been detected using active and passive IRT and TSA [55] . Passive monitoring was used when the specimen was subjected to an impact and cyclic loading (TSA). Active, PT, monitoring was used after cyclic loading to compare the damage area detected with the TSA stress distribution. The authors concluded that the TSA results depict damaged fibres, while the active thermography depicted regions of delamination. Suggesting that the two methods should be used together to give the best overview of damage in the composite. It should be noted that this conclusion that TSA depicted only damaged fibres, goes against the results of this research, where fibre breakage was detected, along with matrix cracking, delamination, and interlamina shear; see Chapter 7. Furthermore, Emery, *et al* [6] utilised three different GFRP material lay-ups to initiate different damage types. A cross ply laminate was used to initiate matrix cracks in the transverse fibre direction and longitudinal splits in the loading direction, an angle ply laminate to introduce matrix cracking due to shear between plies, and a quasi-isotropic lay-up to replicate an in-service engineering application, introduced delamination's. The specimens were fatigue tested at constant load and interrupted after 3000 cycles, to carry out the TSA at a constant displacement cyclic loading. The TSA images were compared with the macroscopic images taken off the specimens. The study concluded that TSA can be used to identify the different types of damage within the material, but it was noted that the specimen design was optimised for specific damage types within the specimens. The author stated that this was an initial step requiring further work to investigate different materials, lay-ups, and loading conditions. It should be noted that, while TSA is a surface temperature measurement, subsurface defects were detected and confirmed with the macroscopic inspection of the backlit transparent material.

Hussain, *et al* [56] investigated the use of TSA as a microscopic damage inspection technique, on a thermoplastic material (PEEK). To detect the microscopic defects, a high magnification lens was used, and it was noted that TSA went from a full field imaging technique, to a focused technique. It was also noted that spraying the specimens matt black to improve emissivity, obscured some of the defects, therefore requiring some tests to be carried out on unpainted specimens. The painted specimens displayed uniform stress fields, whereas the un-painted specimens displayed stress gradients due to surface marks from the manufacturing process. The primary goal of the work was to investigate defects caused by the conditioning of the specimens, but it was noted that the majority of the defects detected were present from the specimen manufacturing technique and not the specimen conditioning. The study concluded that TSA was able to detect microscopic defects, but was unable to determine the defect size, primarily due to the change in size due to the changing load. Two challenges encountered during the study were summarised as, achieving the correct focus on the specimen surface, and locating the defects in the narrow field of view.

2.6 Digital image correlation

DIC compares an image of the test specimen, unloaded, at the start of the test, with images taken, under load, at various points through the testing process to obtain specimen deformations. The correlation software requires a random pattern on the surface of the specimen to allow it to uniquely identify each region of the specimen. If the specimen does not have a random pattern on its surface, the specimen is prepared by having contrasting coloured speckles spray painted onto it, either black speckles on a white background or white speckles on a black background. The images are converted to greyscale images and then, using the post processing software the movement of the unique pattern is tracked to obtain the surface displacement of the specimen. The in-plane displacements can be calculated using a single camera. For 3D displacements, two cameras have to be used. DIC can be used on static [57] as well as fatigue tests [58].

Typically, a charge coupled device (CCD) camera is used to take images of the test specimen. A CCD camera operates and collects images in a similar method as the photon detector, except the cameras are not usually cooled. The substrate that the photons strike in the sensor is manufactured from silicon. Photons, striking the silicon, create electrons by the photoelectric effect and this charge is then processed from a charge to an analogue greyscale. This information is then processed through an analogue to digital converter and recorded on a computer.

To process the images into displacement and then strain values the image is first divided up into interrogation windows. The number of pixels per window is specified by the operator. Each window should have a unique pattern within it and can then be used to calculate the displacement of the surface. The movement of greyscale peaks within the window is measured by the number of pixels they have moved between images. The more pixels within a window the greater the greyscale averaging or smoothing, so the greyscale peaks lose definition. The lower the number of pixels within a window, the spatial resolution increases along with image noise. The displacement is converted to strains by obtaining the strain gradient over multiple windows, essentially a numerical differentiation, which also introduces noise.

Monitoring the peaks movement and the patterns they create, is done using a variety of different algorithms. The algorithms are Cross-correlation, Cross-correlation in the Fourier domain and Variation (Sum of squared differences (SSD) or alternatively called least square difference (LSM) [59]. New algorithms are being developed constantly to minimise measurement errors and increase accuracy [60], [61]. Alongside the correlation algorithm DIC potentially contains a large amount of measurement error sources including the camera with image noise and lens distortion [62], the size and distribution of the random speckle pattern on the specimen [63], out of plane movement when using a single camera, and the alignment of the camera perpendicular to the surface being inspected [64].

Instron supply a video extensometer that can be used for DIC, the software is called DIC replay [65]. The extensometer can supply live strain data (between two marked points on the specimen) during a test, but the DIC full field information, requires post processing after the test has finished. Images are recorded at a maximum of 50 Hz, with an accuracy in the 60mm field of view (FOV) of ±1 μm and ±5.5 μm for the 500mm FOV. The DIC accuracy for the 60mm FOV is ±200 με and the 500mm FOV is ±1000με.

The lack of an instant full-field displacement output is the largest barrier for using DIC as a damage evolution control technique. The images are taken in steps during the test sequence and the differences between the images have to be correlated. Fayolle *et al* [66] applied DIC to a quasi-static tensile test and used the resulting strain data to control the test machine. The specimen was loaded with the test machine controlled in an inner and outer loop control system. The inner loop used the standard displacement control in the test machine controller, while the DIC strain data is provided to the system to act as an outer loop control. The specimen was loaded in 5 steps to pre-set strain values, the test was then stopped, the load was reduced, the DIC data was processed and then the loading was restarted. The test used a single camera, so only in-plane measurements were taken. Fayolle et al [67] followed up the work in [66] applying the procedure to a cracked specimen controlling stress intensity factor. The paper does not specify the test frequency, the specimen was only loaded across four cycles and the procedure requires almost three seconds per control cycle. The author’s noted that future work should consider crack propagation and once some other processing issues have been resolved, trial monitoring and ‘real time’ control of high cycle fatigue tests. It was highlighted that the longer time required for crack propagation will assist by allowing time for the correlation process.

S. Vanlanduit *et al* [58] investigated applying DIC to monitor crack growth during a fatigue test, using stroboscopic illumination to freeze the image at the maximum and minimum displacement. The technique was successfully applied to a fatigue test at 1Hz, providing the global specimen displacement. However it was necessary to post-process the images to measure the crack length automatically. This extra post-processing step means the approach in this form would not allow live control of a test machine.

Using DIC as a uniaxial or biaxial strain gauge for strain control of a test machine has been shown to work by Tao and Xia [68] for uniaxial and biaxial cyclic loading using strain control, but again the cyclic frequency is not recorded. It was noted that the maximum camera frame rate of the DIC system was 10 Hz and that the processing time did cause the maximum and minimum strain levels to exceed the pre-set limits as the actuator continued to move whilst the data was processed. This delay also caused a fluctuation of the maximum and minimum strain values throughout the test. Future work that was suggested, including the use of a higher resolution camera or increase the camera frame rate, which are two conflicting requirements as more sensors in the detector array reduces readout rates. A further suggestion was to use a computer with a faster processing speed, which cannot help if the frame rate is insufficient.

Wu *et al* [69] reported applying DIC to achieve a strain measurement refresh rate of 60 Hz by using an improved image processing algorithm and improved computer technology. The work was validated by computer simulation and experimental results. The experimental analysis was conducted on a steel specimen subjected to a fatigue load at 2 Hz & 4 Hz. It should be noted that although a full field image was taken, the actual strain measurement were between two predetermined points on the specimen. A single strain measurement would not be suitable for damage evolution control of the composite specimens considered in the current research.

Full field monitoring and crack growth control of a metallic SENT specimen using DIC has been successfully trailed by Durif *et al* [70] the results of which were compared with the results of a DCPD method of crack measurement. An algorithm, based on the displacement field around the crack tip, was developed to estimate the crack length in real time, and to calculate the SIF. When the SIF had been calculated, it was compared to the target value, and the fatigue load was adjusted to return to the required value. When the estimated crack length was compared with the DCPD values, there was good agreement, validating the DIC crack length estimates. The paper discusses the synchronisation of the camera with the cyclic load, the algorithms used, specimen geometry, etc. outlining its potential to control a fatigue test, but, it does not mention the tests cyclic frequency or the processing time required, and it was estimating the crack length, not measuring it, thus limiting its potential in the detection and control of damage evolution within a material.

In the future it is possible that once the delays due to data processing have been overcome or significantly reduced, the full potential of DIC full field imaging, can be used to monitor and control the damage evolution within a test specimen. Damage evolution within a metallic specimen is usually the monitoring of a crack, initiated from a notch on the edge (SENT or compact tension CT) or in the centre of the specimen (Centre cracked tension CCT) [9]. Such specimens lend themselves well to the standard crack monitoring and control processes previously mentioned, but, there are strict parameters that permit assumptions within the standards, to be made. When these parameters cannot be met, such as a non-standard specimen geometry, the monitoring of crack growth by DIC permits full field data to be acquired. Fagerholt *et al* [71] used DIC to investigate fracture of a SENT specimen, manufactured from a welded structure. The specimen was instrumented with both a COD gauge and DIC, the DIC data was used to measure crack length, crack path and, the displacement and strain fields at the crack tip. When the data from the COD gauge was compared with the DIC data they correlated well providing confidence that the COD measurement could be extracted from the DIC data. The paper concluded that the DIC analysis provided valuable input into their numerical models, but it was noted that DIC only provides surface measurement and that typical fracture mechanisms usually initiate from the centre of the specimen.

High resolution DIC has been utilised by Carroll *et al* [72] to provide full-field strain measurements near a growing fatigue crack. The high resolution strain measurement were compared with electron backscatter diffraction (EBSD) measurements of grain size and shape, by overlaying the grain pattern over the strain map. This comparison permitted the strain across individual grains and between grains to be measured. Allowing a better understanding of crack growth at a micro-structural material level. It should be noted that the test was stopped after approximately 0.5 mm of crack growth, to permit the EBSD measurement to be taken and a DIC image. Therefore the DIC measurements were of the plastic deformation strain measurement due to the crack growth, and not the strain created during the cyclic loading. Using high resolution DIC would permit the investigation of composite damage evolution at the fibre level and the understanding of damage mechanisms.

Understanding damage and failure mechanisms of composite materials used in the aviation industry is vitally important during the design of the aircraft. DIC has been used to monitor composite structural tests by Laurin *et al* [73] along with standard measurement techniques of strain gauges and LVDTs. The work presented in the paper evaluated the use of DIC on three specimen types, an open holed tensile specimen, compression after impact and a four point bend test on an L-shaped specimen. Using DIC permitted the authors to validate the boundary conditions of the test when anti-buckle and four point bend fixtures were used, compare the measurements with the LVDT and strain gauge results, improved their ability to distinguish local buckling (due to damage) from global buckling, and validate FE predictions.

Development of composite damage assessment has been undertaken by Caminero *et al* [74] who tested open-hole tensile specimen, in addition to some external bonded patch repairs to open holes, and a thicker specimen with a bonded scarfed repair. Different material lay-ups were tested and the unrepaired open-hole specimens were subject to X-radiography to determine damage evolution and compare with the DIC results. It was reported that the DIC strain and displacement measurements were in good agreement with FE predictions for all specimen types, the high localised strains around the holes corresponded with the damage detected by the radiography, and, that it was a challenge to accurately identify internal damage from surface strains.

The two previous examples of DIC evaluation of composite materials, were only subject to quasi-static loading. Giancane *et al* [75] demonstrates a method of capturing DIC images during a fatigue test, and then proposes that calculating the specimens change in stiffness and absorbed energy from the DIC data corresponds to damage evolution of the specimen. The method used to capture the images required the specimen to be cycled at 9.5 Hz and the images to be captured at 5 Hz. The camera and test machine were synchronised to record 18 images, starting from a trigger at the mean load, and capturing images extremely close to the minimum and maximum stress. Synchronised capture of DIC and IR images [76] was used to record DIC images at the minimum and maximum points of a cyclic load, whilst recording a sequence of IR images that were used for TSA, without the need for pausing a fatigue test. The results from the data generated were used to identify different types of damage evolution in a composite material, which was verified by X-ray CT. A similar technique called lock-in DIC [77], has also been developed that applies a lock-in amplifier to the strain data recorded from the DIC, therefore allowing data to be recorded without interrupting a fatigue test.

DIC has the ability to monitor damage evolution in metallic and composite materials, and, depending on the resolution, in extreme detail. Unfortunately for this research, the requirement for significant data post-processing is a shortcoming. The papers mentioning real time strain outputs are for pre-determined points on the specimen, therefore missing the adaptability of a full-field imaging technique. The aim of this research is to identify, monitor and control damage evolution within a composite material. When an undamaged or un-notched specimen is tested, the location of damage initiation is not known, therefore the requirement to pre-define the strain measurement points may miss the damage location. Therefore, for DIC to be a suitable method for composite fatigue damage evolution control, the post processing of the full-field images need to be eliminated or reduced significantly.

2.7 Conclusions

Current standardised methods of damage detection and monitoring in metallic materials, during cyclic loading, require a physical connection to the specimen, or the test stopped, to allow ultrasonic or X-ray CT to be carried out. There are no standardised methods of damage detection in composite materials. All of the methods currently used are based in a purely research environment, requiring a combination of highly skilled operators, long equipment set-up times and data processing, and expensive equipment. Making a full field imaging technique that is robust and repeatable, to detect and monitor damage evolution in any material, is desirable.

IRT has the capability to detect damage, using active IRT when the specimen is stationery, or passive, when the specimen is undergoing cyclic loading. If a lock-in signal is available from the test machine, TSA can also be undertaken. The benefit of passive IRT is that it is practically real time because it is not necessary to post processing the image data. Therefore the IR image created can be considered instantaneous or ‘live’. DIC has been discounted, as a damage detection and measurement technique, predominantly due to the processing time required to output measurements. As previously mentioned, research into increasing the processing speed of full field measurement, and the instant output of predetermined or global strain measurement has been undertaken and is ongoing. Unfortunately the techniques and processes are immature and will require significant development to create a real time damage detector and measurement process.

IRT, with the additional benefit of recording data for TSA, is the technique that will be developed further in the thesis for full field imaging, damage detection, and damage measurement. The benefits of the system are;

- Real time full field temperature output, which can detect damage evolution and failure.
- The recording, at predetermine cycle counts, of the temperature data over a specified number of cycles, for later TSA. To assist in identifying the damage mechanisms.

To make the IRT approach affordable it is necessary to use a bolometer IR device; full details are provided in Chapter 3. Its applicability for TSA is determined in Chapter 4 using a novel camera model approach. In Chapter 5 it demonstrated that a bolometer can be used to monitor crack growth effectively and used as the basis for test machine control. It is then shown in Chapter 6 that a bolometer can be used on composite materials as well as metallic materials to monitor damage evolution. In Chapter 7 different approaches for test machine control are suggested. The literature review shows that the use of IRT in both monitoring damage evolution and in test machine control has not been fully explored hence the overall aim of the thesis and the key research question is ‘Is IRT suitable for assessment of damage and can it be used as a new form of test machine control’.

Chapter 3 Infrared thermography: detector types and capability

IRT has been used as a non-destructive technique to detect cracks in welded metallic specimens [1], to monitor damage evolution in composites [2] and as a general condition monitoring technique [3]. In this chapter the two different types of IR detector are examined: the microbolometer detector and the photon detector. A description of microbolometers and photon detectors can be found in sections 3.1 and 3.2 respectively. Three IR detectors are used in the experiments described in the thesis. In section 3.3, an overview of the two microbolometers and the photon detector is given. To compare the performance of different IR cameras a means of constructing a camera model has been developed in a parallel project. To compare the performance of a microbolometer against that of a photon detector the approach is used in section 3.4. Data is gathered from an accurate black body source at known temperatures to develop the models for each camera type. The camera models are then used in Chapter 4 to determine the suitability of using a bolometer for TSA.

3.1 Microbolometers

A microbolometer is made up from a series of sensing elements to form a detector array; each sensing element has an IR radiation absorbing surface layer, manufactured from metal or a semiconductor material, which changes resistance in accordance with the amount of energy absorbed. As the temperature increases, the resistance of the sensor decreases exponentially. The resistance change is converted into a voltage, which is then converted from an analogue to a digital signal. The recorded digital level (DL) is converted into temperature through calibration. A microbolometer camera collects information over a given time period, known as the thermal time constant which is typically between 7 and 12 ms; the thermal time constant is fixed in the design of the Read-out Integrated Circuit (ROIC) [78]. The detector response time is usually about 3 times the time constant where around 95% of the final value is achieved and 99% after 6 times the time constant [79].

The detectors used in microbolometers are uncooled focal plane arrays (UFPA). The lack of cooling leads to simpler, and less expensive detectors, but typically with lower sensitivities than the cooled chips used in photon detectors. A typical microbolometer has a thermal sensitivity (Noise Equivalent Temperature Difference, NETD) of ~ 0.05°C. The frame rate or rate of image capture is also determined by the detector ROIC. Most bolometers are capable of achieving frame rates around 60 Hz although some can be increased to 200 Hz when windowing is applied. Windowing is when the number sensors in the detector array is reduced and therefore the spatial resolution is reduced, this is often undertaken to increase framing rates by reducing the data transfer load. A typical microbolometer detector with an UFPA is shown in Figure 3.1, with the main components labelled.

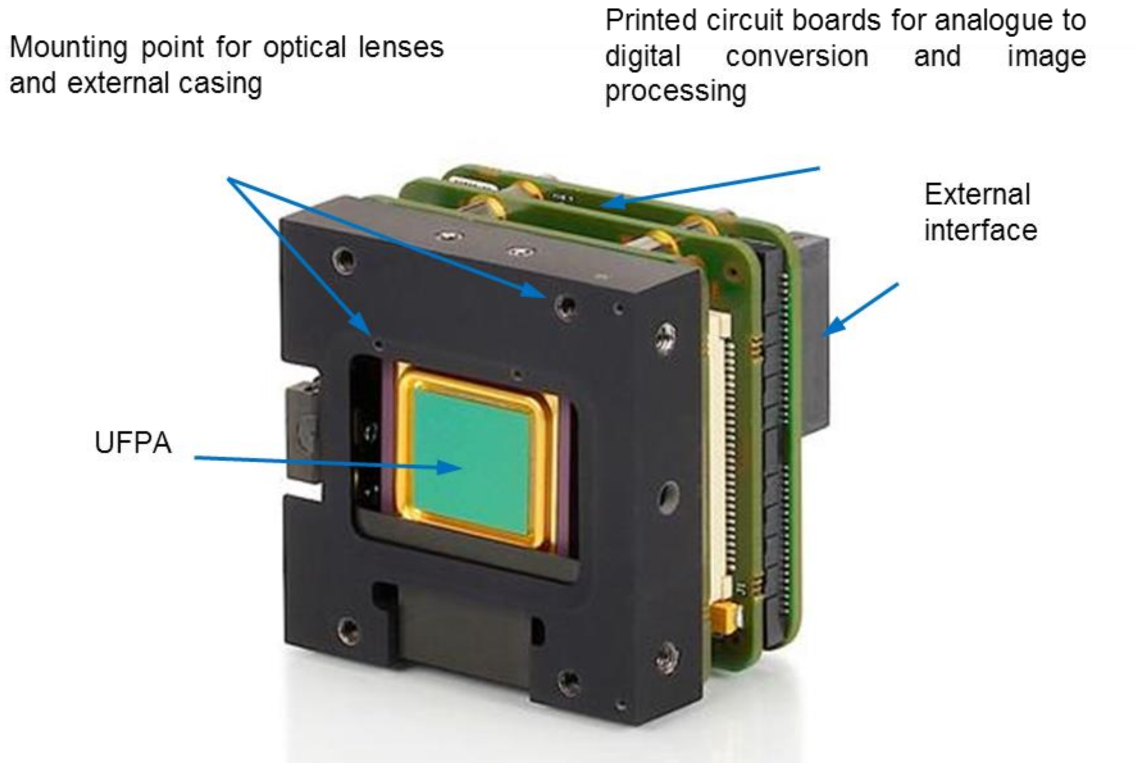

Figure 3.1. A typical microbolometer with UFPA detector [80].

3.2 Photon detectors

Photon detectors use a semiconductor device that is photovoltaic. When excited by photons in the wavelength window in which the device is sensitive, an electric current is generated across the band gap in the semiconductor. The voltage output from the device essentially allows the photons to be counted in the form of an analogue signal that is converted to a digital signal using an analogue to digital convertor to create a response in DL. The DL values are then converted into temperature, using the calibration procedure described in Section 2.4. Unlike microbolometers, where the device has a fixed thermal time constant, photon detectors have an adjustable electronic shutter, which allows the number of photons to be counted over a prescribed period, more commonly referred to as integration time. As the number of photons counted for a given temperature is proportional to the integration time, the calibration is dependent on the integration time.

Photon detectors are cryogenically cooled which provide improved NETD when compared with an uncooled microbolometer. The extra sensitivity means photon detectors are often preferred in research and development applications. Most photon detectors have a temperature resolution of ~ 20 mK. As a photon detector provides a practically instantaneous response when excited by photons much higher frame rates can be achieved than those available with microbolometers. Depending on the number of elements in the detector array frame rates are of the order of hundreds of Hz into the KHz range. A FLIR photon detector and cooling system can be seen in Figure 3.2 [81].

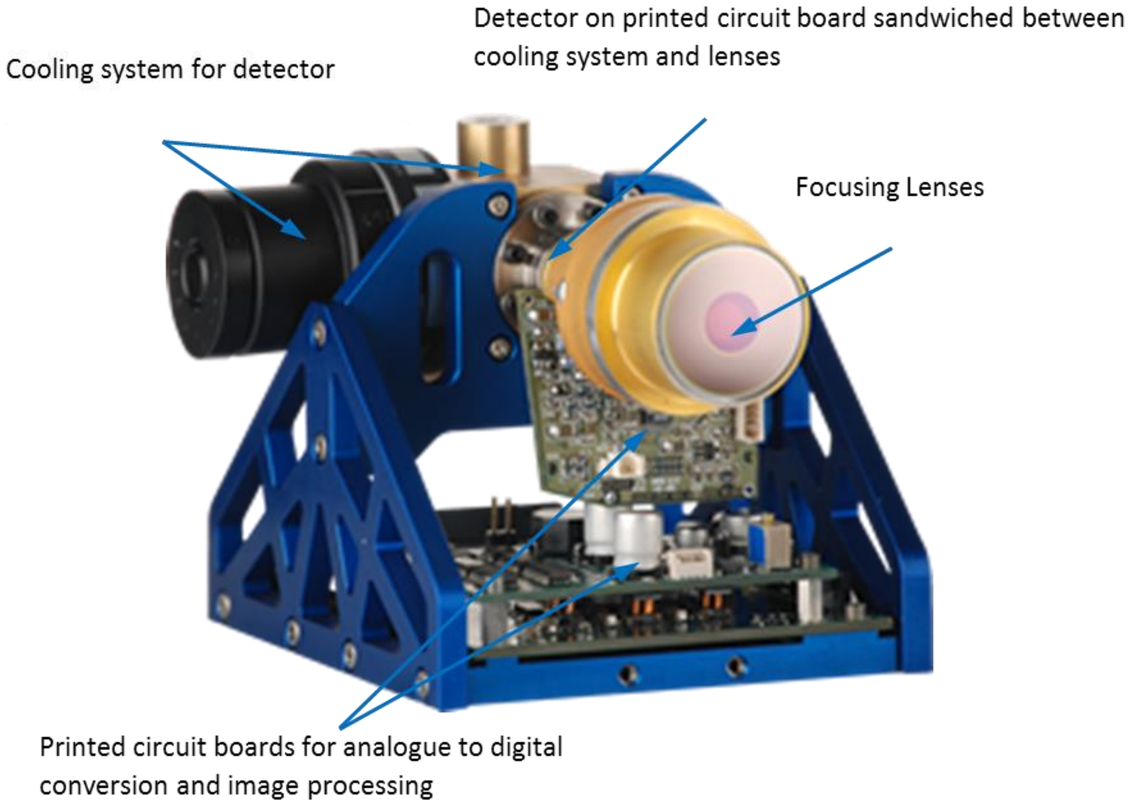

Figure 3.2. FLIR photon detector and cooling system [81].

3.3 Detector systems

The work in this thesis was conducted using three camera/detector systems. A FLIR SC5500 photon detector was used as the benchmark, for comparison purposes during the damage characterisation trials, in chapters 5 and 7, and the numerical model, section 3.4. The microbolometer that was compared to the photon detector, in all instances was a FLIR A655SC. A second microbolometer, an Optris PI450, was only used in a test control trial at Instron's UK headquarters in High Wycombe. All three detectors are described in this section.

3.3.1 FLIR SC5500

A FLIR SC5500 series photon detector [82] was used in the damage propagation studies reported in Chapters 5 and 7, as well as in the following chapter as a benchmark with which to compare the suitability of using a bolometer for TSA. The system comprises a camera with a 320 x 256 cryogenically cooled Indium Antimonide (InSb) photon detector focal plane array (FPA), with a spectral range of 3-5 μm, a NEDT of 0.02 K and an integration time (Electronic shutter speed) adjustable between 3 μs to 20ms. The detector has a maximum frame rate of 383 Hz and a standard temperature range of 5 °C to 300 °C (optional -20 °C to 3000 °C). It has been reported [83] that the capture frequency can be increased to 15 kHz, with a window size of 64 x 12 pixels and in-house pixel by pixel calibration procedure. There are three types of video output, 1 analogue and 2 digital. The analogue output uses a BNC connection, and the digital outputs uses Camera Link and a Gigabit Ethernet connections. There are also three analogue inputs that can be used for embedding external measurements, such as the reference load signal used for applying the lock-in in TSA, into the image data. FLIR photon detectors can all be operated by the software suite called Altair [84]. A photograph of the detector is provided in Figure 3.3 [82]. The dimensions of the camera are 141 mm x 159 mm x 320 mm and a mass of 3.8 kg.

Figure 3.3. A FLIR SC5500 photon detector [82].

3.3.2 FLIR A65SC

The microbolometer used in most of this study was a FLIR A655SC. It is available with one of three permanently attached lens options and two additional macro lenses. A vanadium oxide (VoX) UFPA detector, is used in the camera, with a spectral range of 7.5-14 μm, and a resolution of 640 x 480 pixels. The thermal time constant is described as typically less than 8 ms and the NETD as less than 30 mK [85]. The maximum recording frequency, using the full detector, is 50 Hz. When the windowing mode is applied, the maximum frame rate for 640 x 240 pixels is 100 Hz, and 640 x 120 is 200 Hz. The standard temperature ranges for the detector are -40 °C to 150 °C, and 100 °C to 650 °C (optional up to 2,000 °C) with an accuracy of +/-2 °C or +/-2 % of the reading. A Gigabit Ethernet (GigE) port is used to connect the camera to the control and recording computer, and a 6-pole digital input/output, for data recording start/stop triggers. Unlike the photon detector, there is no facility to embed external data into the captured images. To operate the camera and record the data a software suite called ResearchIR [86] is used. The dimensions of the camera are 216 mm x 73 mm x 75 mm and a mass of 0.9 kg. A photograph of the camera is shown Figure 3.4 [85].

Figure 3.4. A FLIR A655SC Microbolometer [85].

A typical set-up of the Research IR software is shown in Figure 3.5. The figure shows the back face of a metallic SENT specimen, described in Chapter 4. On the specimen image a rectangular area (red box) and a line plot (green line) have been drawn on the area of interest. The statistics of the plots can be found in the “Stats” box on the right hand side of the display. In the box a variety of statistics are available to view, including the areas mean, maximum and minimum temperature. The pixel co-ordinates of the maximum and minimum temperature can be seen in the bracket preceding the temperature.

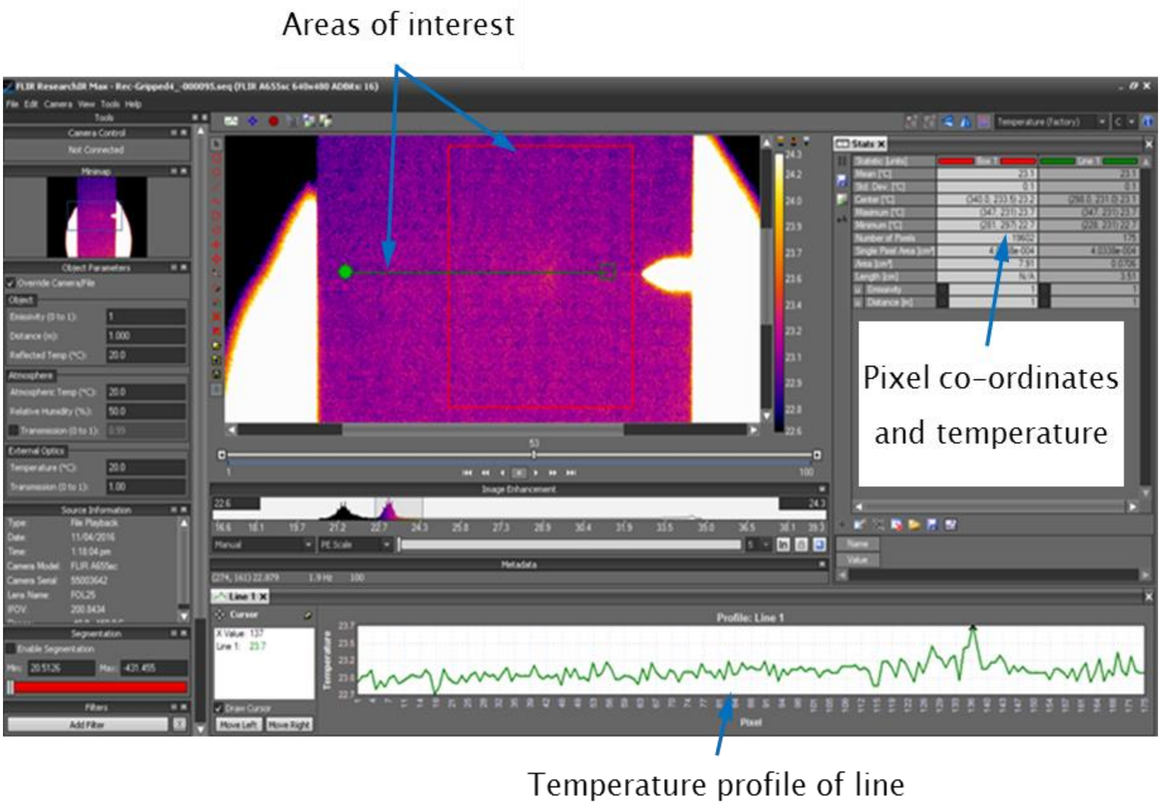

Figure 3.5. A typical set-up of Research IR software.

3.3.3 Optris PI450

The Optris PI450 is a microbolometer, with an interchangeable lens. Four lenses are available. The detector is a vanadium oxide (VoX) UFPA 382 x 288 pixels, with a spectral range of 7.5-13 µm and a NETD of 0.04 K using the 38° x 29° field of view (FOV) lens. The camera has a maximum frame rate of 80 Hz, and a temperature range of -20 to 900 °C. The software controlling the camera is called Optris PI Connect (release 2.9.2147.0) and is compatible with Windows XP, Vista and 7. The camera is shown in Figure 3.6 and has dimensions of 46 mm x 56 mm x 90mm and a mass of 0.32 kg.

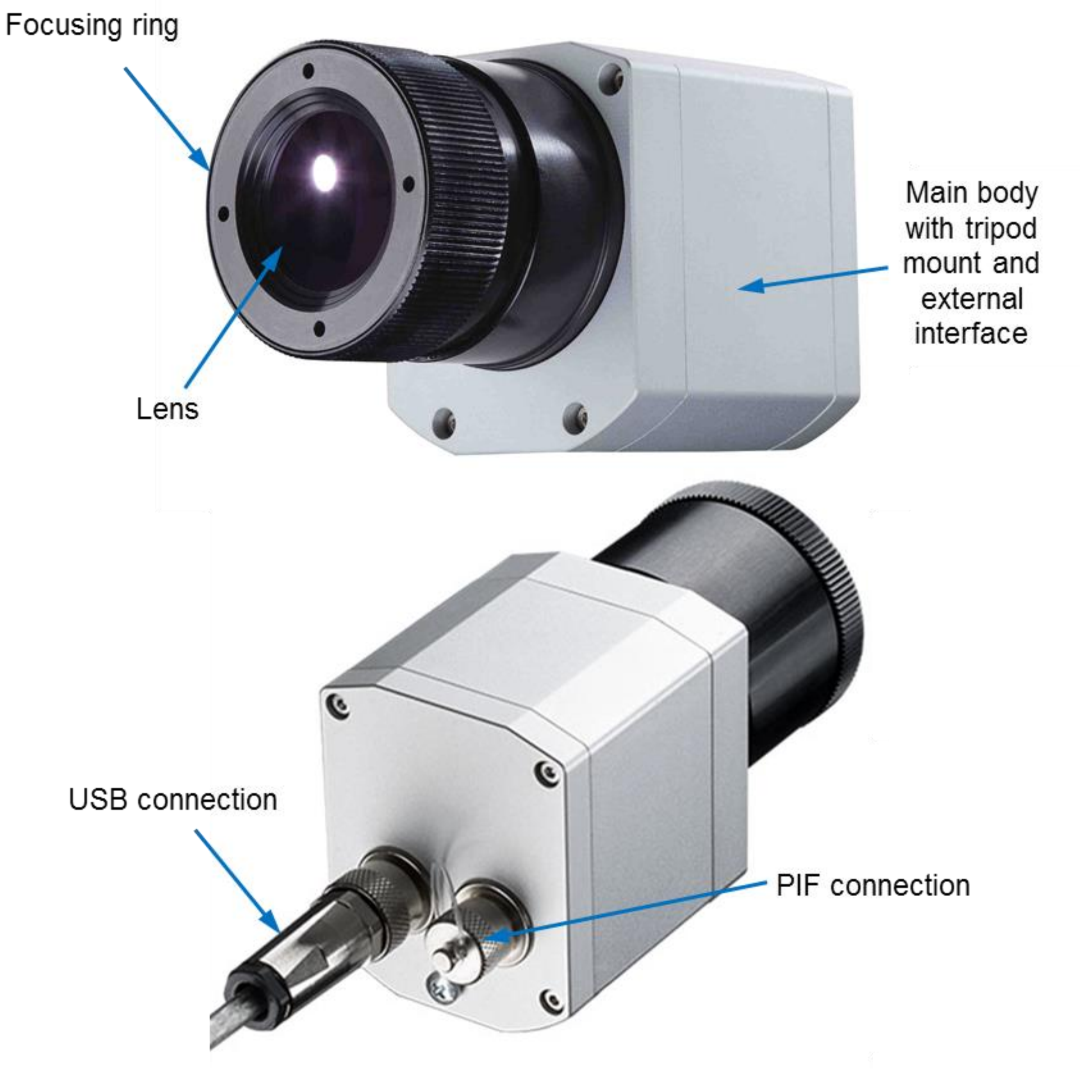

Figure 3.6. An Optris PI450 camera [87].

The Optris PI connect software remotely operates the camera via a USB interface, displaying a live image when the software is open. Options within the software allow the user to define areas within the image that can be masked from measurement or defined as the measurement area. The area size options have three predefined sizes of 1x1, 3x3 or 5x5 pixels, and a user defined rectangle. Each area can output, to a visual display, one of the following options:

- Maximum temperature.
- Minimum temperature.
- Average temperature.

A hotspot and cold spot tracking is also available over the whole specimen or specified areas. A single output can be transmitted to the test machine via the process interface (PIF) cable. When a measurement area has been prescribed, temperature maximum and minimum limits, within the area, can be defined. Once a limit has been tripped a variety of actions are available:

- Record the output image (.ravi file), over a user defined period of time.
- Take a snapshot of the image (.tiff).
- Trigger an audible alarm on the computer.
- Send an alarm via the PIF.

The alarm via the PIF is either on or off and prevents the use of the temperature output of a defined area. It is not possible to interrogate the images and obtain an exact location for the hot/cold spots. Figure 3.7 shows a typical software set-up.

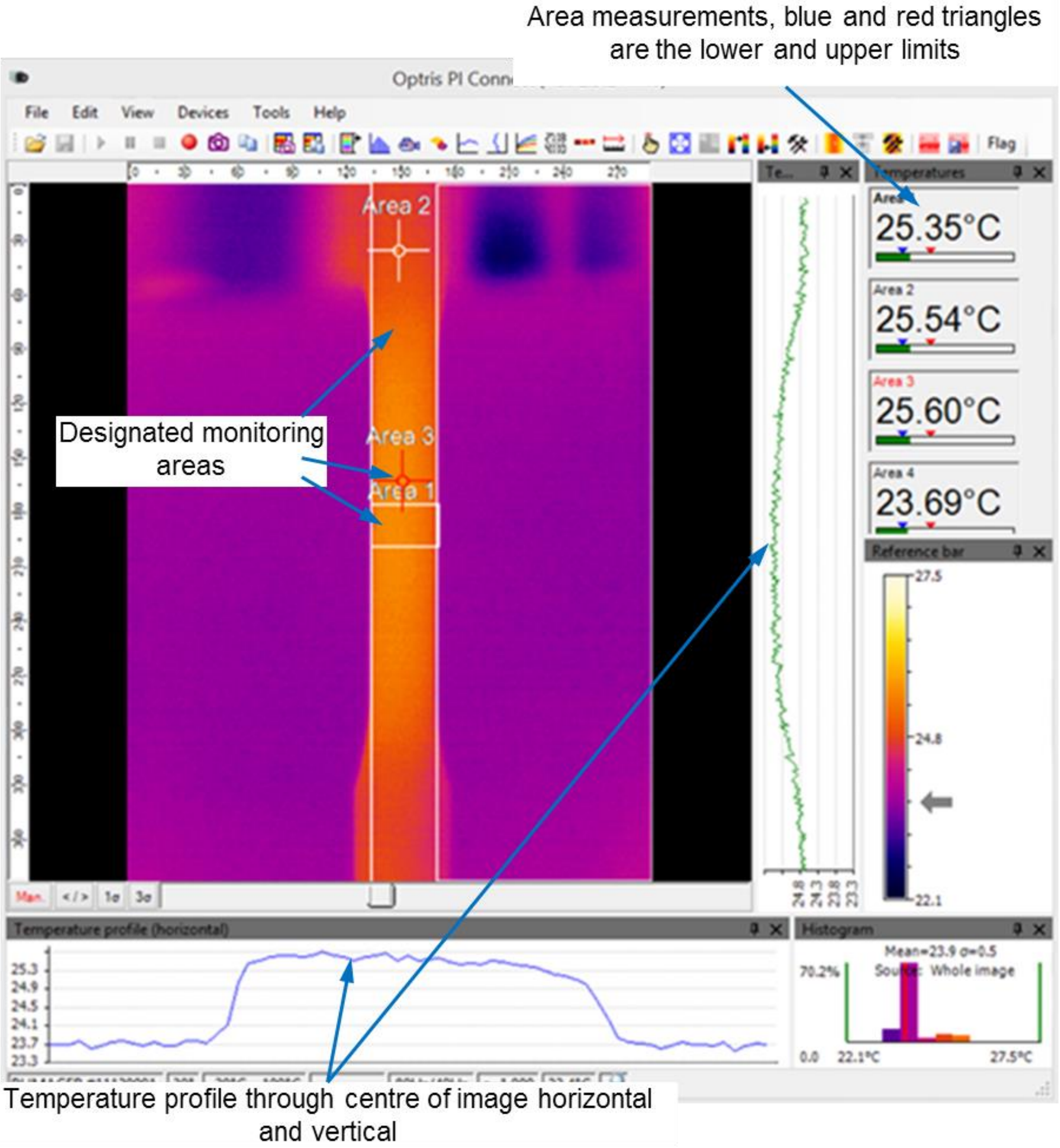
Area measurements, blue and red triangles are the lower and upper limits

Designated monitoring areas

Temperature profile through centre of image horizontal and vertical

Figure 3.7. Typical software set-up for Optris PI450 Microbolometer.

Alternatively, the operator can manually start recording the temperature image as a moving image or snapshot. The moving image file is a .ravi file, recording the temperature output of each pixel or an .avi file recording the colour of each pixel. Snapshots can record the image as either a .tiff or .csv file, both recording each pixels temperature.

The limitation of the Optris microbolometer is the smaller detector size, and the lack of data on the temperature accuracy/calibration and thermal time constant. The benefit of the Optris detector is the cheaper price (approximately £6000) and the analogue temperature output of user defined area. Compared with the FLIR microbolometer, it is supplied with a calibration certificate and has the ability to be user calibrated, but the microbolometer costs approximately £15,000 and does not have the facility (analogue output) to output a live temperature.

3.4 Camera model

An objective of the PhD is to compare the performance of a low cost microbolometer to that of a photon detector. The system characteristics according to the manufacturer of the A655SC microbolometer and SC5500 photon detector are provided above. However, it was considered useful to carry out a detailed performance analysis of each system using a camera modelling approach developed in a parallel project. The camera model enables different characteristics to be examined without additional experimentation and has been especially useful in assessing if a bolometer can be used for TSA. This section of work was carried out with the additional supervision of Dr Cedric Devivier who devised the camera modelling approach in a parallel project. The basis of the camera model is knowing the camera response in terms of inherent noise and its sensitivity to a given input.

3.4.1 Experimentation to derive camera model

To build the camera model it is necessary to use a temperature controlled black body, to generate a variety of temperatures for the detectors to record their response in DL, using a variety of different detector settings. An Infrared Systems Development Corporation, black body IR-2106/301plate source was used. It has a temperature range of 5 to 150 °C, with a wavelength range of 1 to 99 µm, and an emissivity of 0.96 +/- 0.02. The emitter size is 152 mm x 152 mm, a temperature resolution of 0.1 °C and a temperature stability of +/- 0.1 °C short term and +/- 0.2 °C long term. Temperature control is maintained by an IR-301 P.I.D controller, with a resolution of 0.1 C, and a sample rate of 10 Hz, digitally filtered to eliminate noise.

For each test the detectors lens was placed 30 cm from the black body plate, ensuring the detector was viewing the majority of black body plate. To prevent the possible reflection of the heat generated by the detector, it was offset from the perpendicular by approximately 5°. In an effort to minimise the effect of any localised hot or cold spots on the black body plate, the cameras were defocused. Finally, a black shroud was used to cover the gap between the detector and the black body, ensuring that the heat from the black body heating/cooling vents was not directed under the shroud. This guaranteed that there were no external influences or reflections visible to the detector. A schematic plan view of the experimental set-up is shown in Figure 3.8.

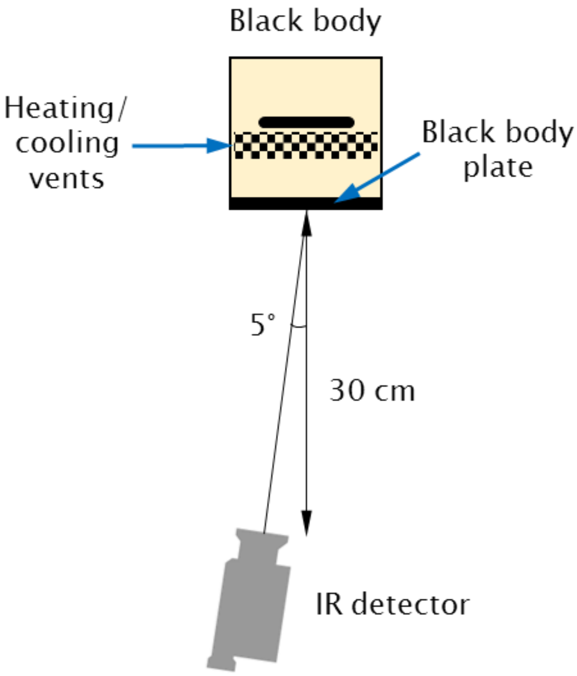

Figure 3.8. Schematic black body experimental test set-up.

For each experiment, a range of temperatures was observed, using a range of frame rates, a constant integration time for the photon detector, and both the on and off conditions of the microbolometer's inbuilt noise reduction (NR) facility. The temperatures chosen covered the typical range seen during previous tests. Table 3.1 provides the experimental parameters. The microbolometer used its full frame, at the five available recording frequencies, whereas the photon detector was windowed down, to permit higher recording frequencies, which were used for comparison with another detector in a parallel project, and required the shorter than normal (1332 μs) Integration time. The number of frames recorded for the microbolometer, was lower than the photon detector, due to the slower frame rate. In normal operation, using the detectors full frame, at its fastest frame rate, 50 Hz and 383 Hz for the microbolometer and photon detector respectively, data were recorded for approximately 2 seconds.

Table 3.1. Experimental parameters.

	Frame size (Pixels)	No. of frames recorded	Test temps (°C)	Frame rate (Hz)	Integration time (μs)	Noise reduction (NR)
SC5500	160 x 128	1000	15, 20, 40, 50, 60, 70	25, 100, 200, 500, 1000, 1253	500	NA
A655SC	640 x 240	100	15, 20, 30, 40, 50, 60, 70	3.13, 6.25, 12.5, 25, 50	NA	On, off

It is standard practice when taking measurements using IR detector arrays to apply a ‘Non Uniformity Correction’ (NUC). This is essentially an adjustment to the offset and gain values for each sensor in the detector to compensate for the differences in the response of the individual sensors. In general the photon detector is shown a black body at two temperatures and a linear fit is performed pixel by pixel to determine the response of and adjust the settings for each sensor accordingly. To eliminate any inbuilt software correction factors associated with the NUC procedure, the photon detector also recorded the data without performing the NUC. The microbolometer has an internal facility to carry-out a NUC, which can be switched off, but only after at least one correction has been carried out, when the camera is switched on. During the data processing it was noted that there was a bias in the standard deviation (SD) in the noise and sensitivity, therefore a numerical NUC was carried out. A full description of the numerical NUC process can be found in section 3.4.3.

In all experiments described in this section only the camera DL was recorded to negate any effect of the temperature calibration procedure. It should be noted that as the devices are different, working in a different wavelength window, temperature range, and the microbolometer measures radiance, whereas the photon detector counts photons, the DL values for the microbolometer and the photon detector are not directly comparable. Radiance is measured in watt per steradian per square meter (W.sr^{-1}.m^{-2}). Planck's law for radiance *(R)* over the microbolometer detector operating wavelengths, is as follows:

$$R = \int_{7500}^{14000} \frac{2hc^2\lambda^{-5}}{e^{\frac{hc}{k\lambda T}} - 1} d\lambda \tag{3.1}$$

where h is Planck's constant, c is the speed of light, λ is the wavelength, k is Boltzmann constant, and T is temperature.

Planck's law is adjusted to give the photon count for the photon detector:

$$PC = \int_{2500}^{5100} \frac{2hc\lambda^{-4}}{e^{\frac{hc}{k\lambda T}} - 1} d\lambda \tag{3.2}$$

The detectors also have different dynamic ranges as the ADCs incorporated in each system have different resolutions. The microbolometer has a 16 bit ADC, giving a dynamic range of 65536 DL, and a 14 bit ADC, with dynamic range 16384 DL, is used for the photon detector.

3.4.2 Camera noise and sensitivity

To calibrate an IR detector, a known temperature is generated in a blackbody, and data is captured by the detector in DL. This process is repeated at a variety of different temperatures across the detector's operating range, and a variety of detector settings (recording frequency, integration times, etc.). A spline fit is then produced for the measured values and the equation of that calibration line is created for all the different parameters, therefore allowing interpolation of the detector response to temperatures that were not physically recorded. Alongside the calibration curve, each camera has a sensitivity, i.e. the DL produced for a given temperature (DL/K) or radiance/photon count, and a resolution, i.e. the smallest value of DL that can be obtained without being masked by the camera noise. To develop the camera model it is necessary to obtain both the sensitivity and the noise. The camera model then applies a similar interpolation process, in that the noise and sensitivity of the detectors obtained over a range of frame rates are input into the model.

A flow diagram of the modelling process can be found in Figure 3.9. Starting at the top, the temperature required to be modelled is converted into radiance or photon counts (DL), the derived camera sensitivity relationship (described in section 3.4.3) are then referenced for the required temperature, giving the new DL for each pixel. The results from this step are refered to as DL1. Next the camera noise reletionships (described in section 3.4.3) are incorporated into DL1, resulting in each pixel having new DL value, called DL2. These values are then mapped to the numerical NUC values, DL3, and finally convert from the numerical values to a pictorial representation, Img. The approach for deriving the noise and sensitivity reletionships is described in the next section.

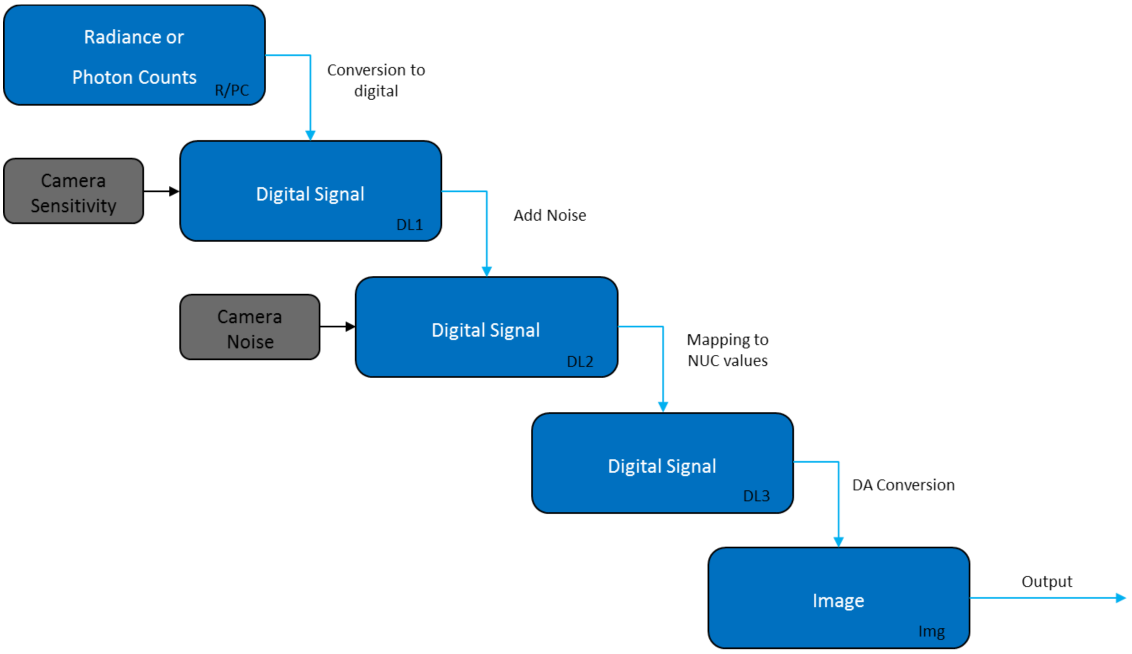

Figure 3.9. Flow diagram of blackbody modelling process.

3.4.3 Noise and sensitivity evaluation

From the images recorded, in an individual experiment, it is possible to calculate the mean and standard deviation (SD) of the DL recorded for every camera setting (see Table 3.1), both temporally (i.e. frame by frame) and spatially (i.e. across the whole detector array for each image captured). From this data, images can be produced that show the pixel by pixel temporal mean and temporal standard deviation of DL as shown in Figures 3.10 and 3.11. A spatial mean of DL can be provided from the first frame of each temperature/frame rate recording sequence. Likewise spatial standard deviations of the DL values from this image can be calculated. To calculate the detector noise the spatial SD of DL from the first frame is plotted against the spatial mean of DL from the same image. The detector sensitivity is obtained by plotting the spatial mean of DL, against the radiance, for the microbolometer, and the photon counts for the photon detector.

To compare images of pixel by pixel temporal mean and temporal SD from the two detectors and the effect of using the microbolometers noise reduction facility the data collected using a frame rate of 25 Hz at 40°C is used as an example. A comparison between the noise reductions (NR) facility of the ResearchIR switched on and off is shown in Figure 3.10. On the left of the figure the temporal mean (in DL) is displayed, where it can be seen that the NR facility has no effect on this result. The right hand side of the figure displays the temporal SD. Switching on the NR facility, reduces the SD, from a maximum value of 18 DL, NR off, to just over 8 DL, NR on.

The temporal mean for the photon detector is shown the left hand side of Figure 3.11. Unlike the temporal mean images seen in Figure 3.10, where the mean is constant across the whole image frame, there appears to be some vignetting at the corners of the frame and some damaged pixels, as well as trace of the detector construction shown as vertical lines in the image. A NUC would remove these effects from the image, which is performed automatically on the microbolometer on power up.

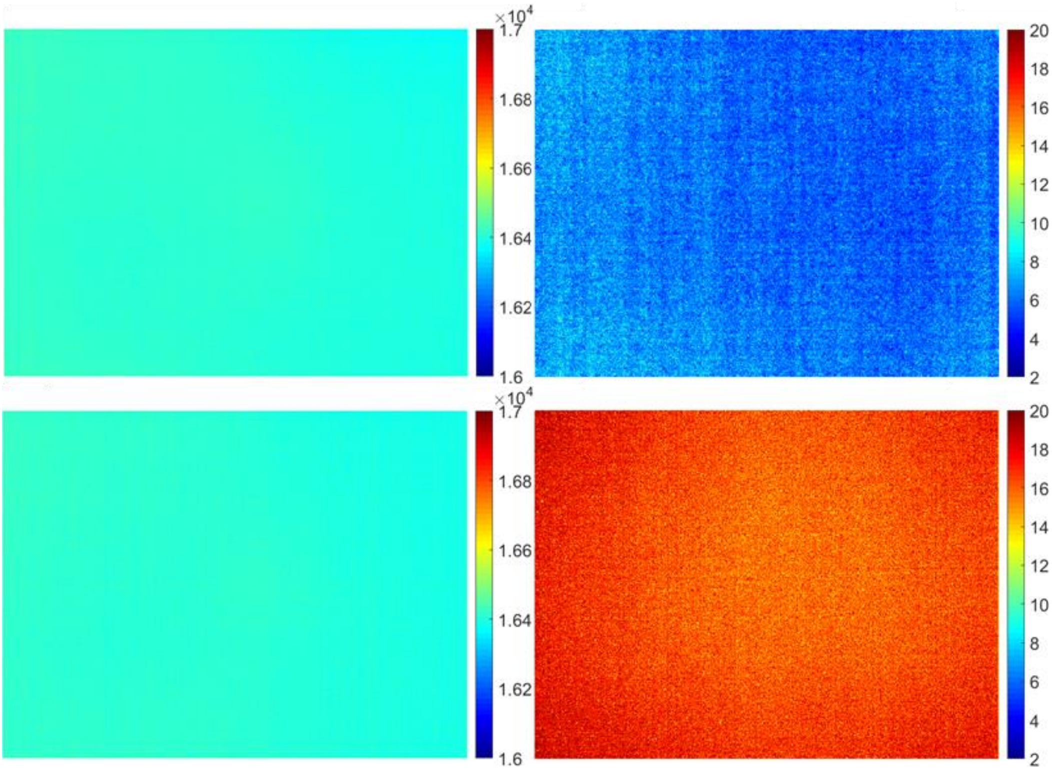

Temporal Mean Temporal SD

Figure 3.10. Comparison between the NR facility on the microbolometer, switched on (top) and off (bottom).

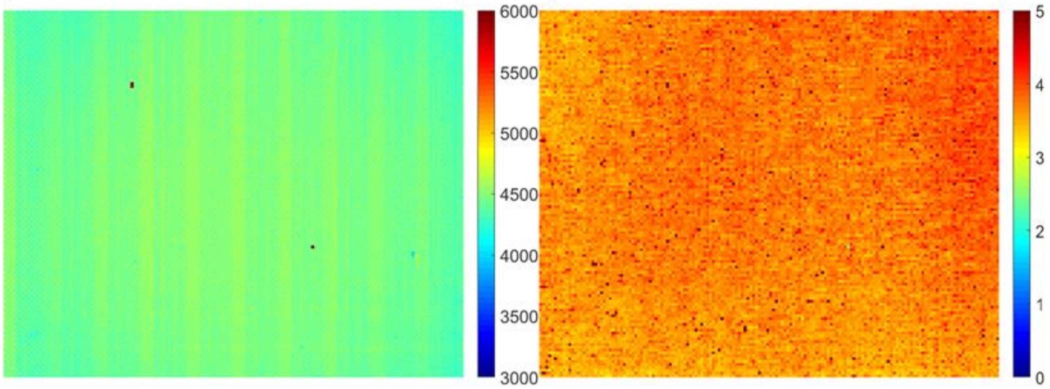

Temporal Mean Temporal SD

Figure 3.11. Temporal mean and SD for the photon detector.

When the data was processed to calculate the detector's noise and sensitivity it was noted that the lack of NUC led to a bias in the spatial SD, particularly with the photon detector, which had no previous NUC, unlike the microbolometer that had an initial NUC at start up. Therefore, a numerical NUC (NNUC) was performed, where each frame image had the temporal mean value subtracted from it. The results of the subtraction were then referred to as NNUC. Figure 3.12 displays the ‘before’ and ‘after’, NNUC for the photon detector, with a frame rate of 25 Hz. The ‘before’ numerical NUC can be seen on the top of the figure, where the spatial SD ranges from 128 to 146 DL, compared with 2.7 to 5.5 DL, after the NNUC, shown at the bottom of the figure. The numerical NUC has also linearised the relationship between the spatial mean and the spatial SD.

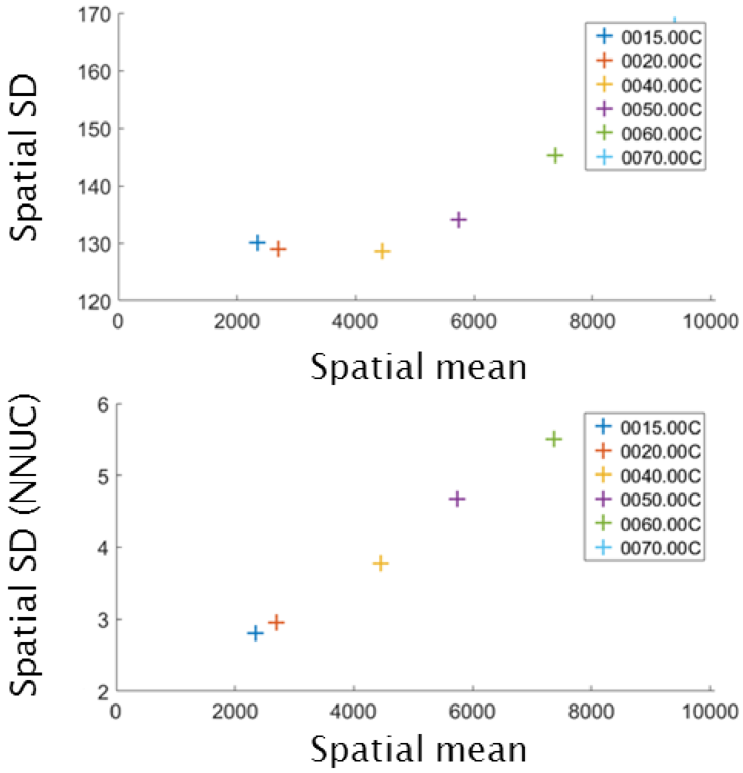

Figure 3.12. Spatial SD before (top) and after (bottom) numerical NUC for the photon detector. All values DL.

Once the NNUC had been performed, plots of spatial SD against spatial mean were produced, from which the relationship to determine the camera noise for each frame rate, over the range of black body temperatures can be seen. A linear relationship was assumed, between the spatial mean and the SD so that slope, intercept and correlation coefficient R^2 were obtained; these are given in Figure 3.13 for the bolometer with the NR on and off and Figure 3.14 for the photon detector. In Figure 3.13 it can be seen that the software NR facility reduces the spatial SD significantly from around 17 DL to 8. The almost horizontal trend lines indicate that the microbolometer's noise, is insensitive to the recording frame rate, and may also be considered insensitive to temperature, for the range tested. The photon detector results can be seen in Figure 3.14, where it is shown that the noise increases with temperature. It is not possible to make a quantitative comparison of the noise levels produced by each IR system when using DL.

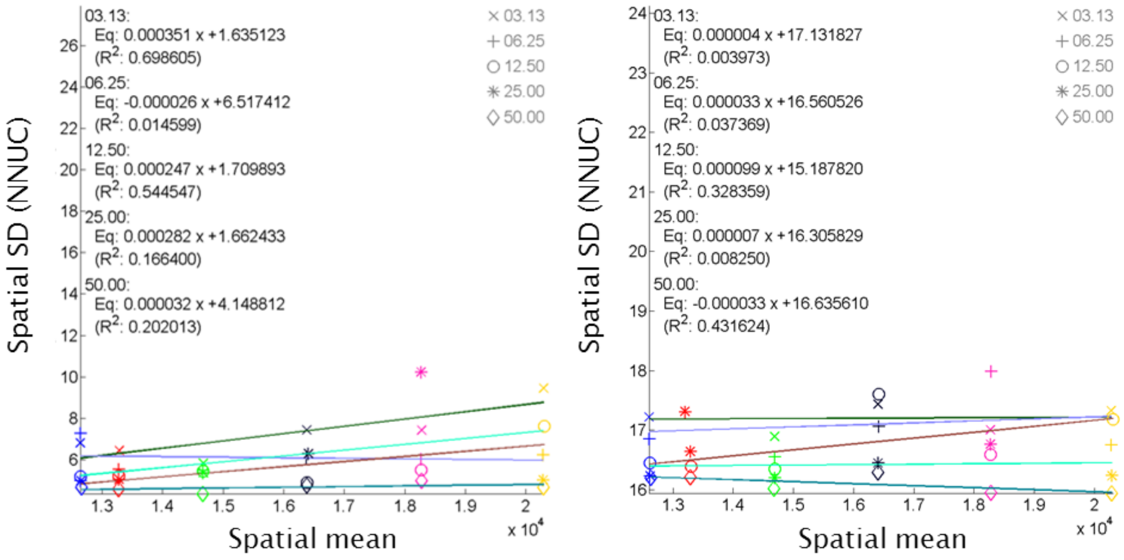

Figure 3.13. Spatial SD NR 'on' (left) and NR 'off' (right) for the microbolometer.

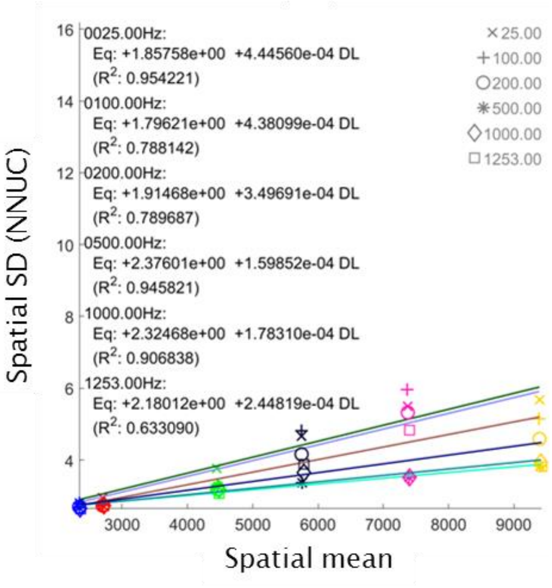

Figure 3.14. Spatial SD for the photon detector.

The detector sensitivity is obtained from plots of the spatial mean of DL against radiance of the blackbody for each recording frequency. A linear fit was also applied and a trend line was plotted and displayed, along with the R^2 value. In contrast to the noise plots the R^2 values of these lines are very close to 1 and confirms that the for both systems the detector responds linearly to increases in radiance. The NR facility has little effect on the detector’s sensitivity, and the detector’s sensitivity does not change with the frame rate. Figure 3.15 displays the microbolometers results with the NR on and off. Figure 3.16 shows that the photodetector behaves in a similar manner to the microbolometer, in that the sensitivity does not depend on the frame rate.

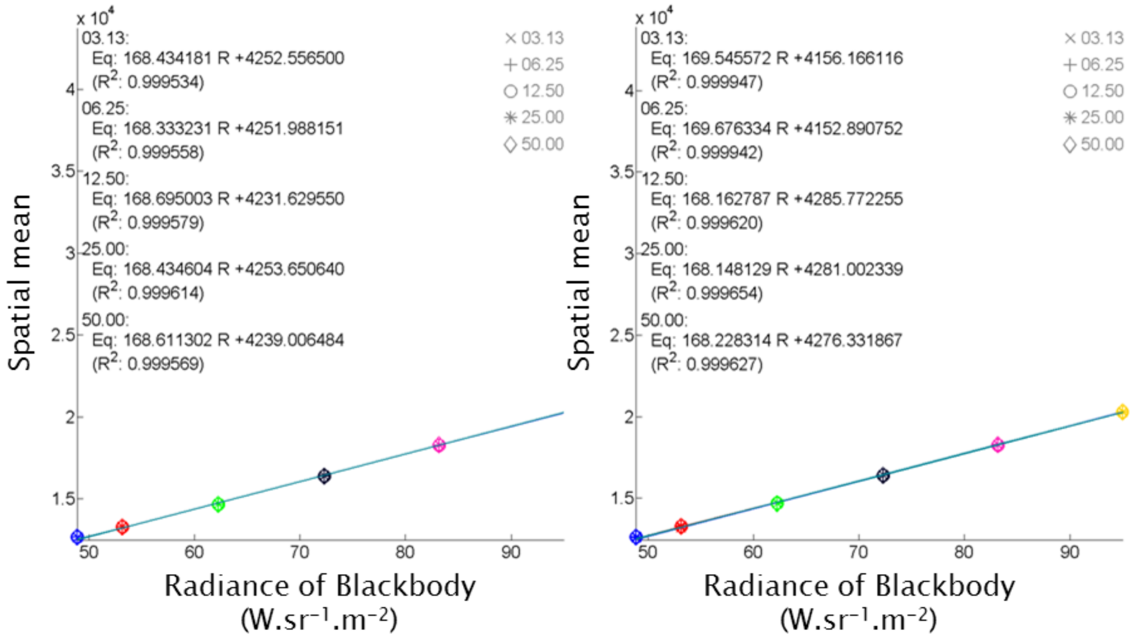

Figure 3.15. Spatial mean NR on (left), and NR off (right) vs blackbody radiance for the microbolometer.

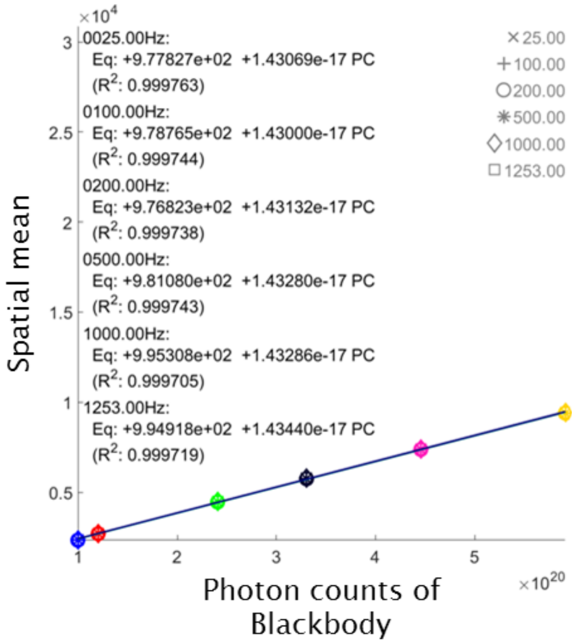

Figure 3.16. Spatial mean vs blackbody radiance for the photon detector.

After the curve equations from graphs had been calculated, they were integrated into the Matlab code (written by Devivier) to obtain the camera models. The model results for the microbolometer are presented first. Figures 3.17 and 3.18, compares the experimental data with the modelled results, for 15 °C and 50 °C, at a frame rate of 25 Hz. The experimental results are on the left hand side of the image. The pair of images displayed in Figure 3.17, are identical, unlike Figure 3.18, where there model results are slightly lower than the experimental results.

Figure 3.17. Comparison between the microbolometer blackbody experiment NR on (left) and model at 15 °C.

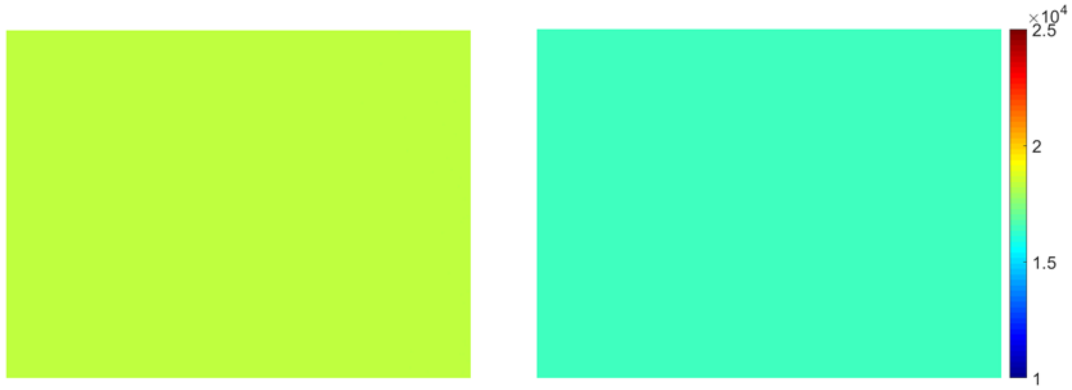

Figure 3.18. Comparison between the microbolometer blackbody experiment NR on (left) and the model at 50 °C.

The photon detector model used the same process as the microbolometer, except that two models for each temperature were created. An average model used the noise trend line equation, the same as the microbolometer model, along with a max model that used the maximum noise value recorded at each temperature. Figure 3.19, displays the experimental result (left hand image), the average model (centre) and max model (right hand side) for 15 °C and 25 Hz frame rate.

Figure 3.19. Comparison between the photon detector blackbody experiment, average model (centre) and max model (right) at 15 °C.

The same sequence is also used in Figure 3.20, where the parameters are 50 °C at 25 Hz frame rate. Apart from the vignetting seen in the experimental data, the images are basically identical, the difference between the average and max model are insignificant at the temperatures tested. Again, when all of the experimental conditions were compared with their model, the differences were not significant.

Figure 3.20. Comparison between the photon detector blackbody experiment, average model (centre) and max model (right) at 50 °C.

3.5 Conclusion

The blackbody experimental analysis has shown that the cooled photon detector has less noise, and a greater sensitivity than the microbolometer, which was as expected, from the manufacturer supplied data. The modelling of the blackbody is the first step to determining if a microbolometer can be used for TSA. In Chapter 4, a metallic specimen with a notch is used for comparison between the photon detector, microbolometer, and camera models for both detector types.

Chapter 4 Application of camera model to thermoelastic stress analysis

4.1 Introduction

The chapter provides a comparison of the thermoelastic response obtained using the Flir SC5500 photon detector IR system and the thermoelastic response from the A655SC bolometer based IR detection system. The comparison is carried out on a metallic SENT specimen, to investigate if a less expensive microbolometer type detector can be used to perform TSA as effectively as a photon detector. The general equipment set-up for the photon detector is detailed in Chapter 2. A key difference, highlighted in Chapter 3, is that there is no facility for the microbolometer to accept the 'reference signal' and hence provide a synchronisation between the applied cyclic load and the thermal signal from the detector. Therefore the lock-in approach necessary for TSA must be applied separately and the loading frequency input manually to perform the lock-in. The annotated MATLAB script used to process the microbolometer data, is shown in Appendix A, which was developed with the support of Dr Cedric Devivier.

To provide a more detailed insight into the camera performance, cracks are grown in the SENT specimens to a specific length and then linear elastic fracture mechanics [88] is used in conjunction with the relationship between the sum of the principal stresses and the thermoelastic temperature change to provide a simulation of the thermoelastic response using the camera models developed in Chapter 3. The theory underlying the application of TSA to a stationary crack to determine the stress intensity factor (K_I) [89] is recapped in the chapter and then it is demonstrated how this is applied to create the simulated data from each camera. The SENT test specimen is described in detail, alongside the loading regime to obtain two different length cracks and different stress intensity factors (SIFs). The results of the model, for both detectors, are compared with the experimental results from a SENT specimen with two different crack lengths. It is shown that the bolometer system has the potential to be used for TSA; the key limitation of the response time of the detector is highlighted as a barrier for a straightforward deployment of bolometers for TSA.

4.2 Determining the SIF using crack length and thermoelastic data

There are several approaches for determining SIFs from thermoelastic data; these are overviewed in Chapter 2. The first report of determining the SIF from thermoelastic data is reported in [89], where only K_I is obtained from the thermoelastic data around the crack tip. This is the most straightforward approach and hence will be used here to build the simulated response from the detectors. For clarity a detailed recap of the approach is provided. The starting point is to define the coordinate system used to develop the theory, which is as shown in Figure 4.1. The origin of the coordinate system is the tip of the crack. In linear elastic fracture mechanics it is usual to define a point in the crack tip stress field in terms of polar coordinates, (r, θ). In the thermal images it is natural to use a Cartesian coordinate system, i.e. pixel by pixel, so it is necessary to convert the polar system into a grid to use the data array, hence the inclusion of the Cartesian coordinate system in Figure 4.1. It is important to note that the datum of the θ-coordinate is the crack line, with anti-clockwise being positive.

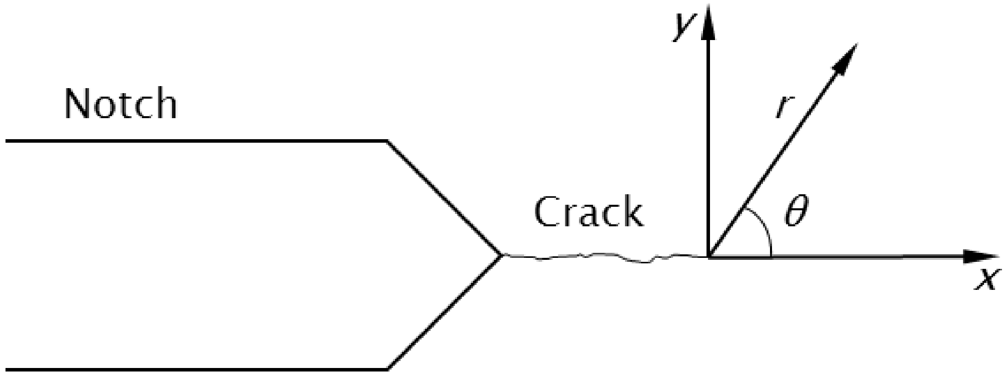

Figure 4.1. Coordinate system around the crack tip

Firstly it is necessary to combine an expression for the thermoelastic response with an expression for the crack tip stress field. Here equation (2.1) is combined with the first-order or singular term of the Westergaard equation [89] that includes the mode 1 SIF only, as follows:

$$\frac{\Delta T}{TK} = \frac{2K_1}{\sqrt{2\pi r}}\cos\left(\frac{\theta}{2}\right) \tag{4.1}$$

Rearranging gives:

$$\frac{\Delta T}{T} = \frac{2KK_1}{\sqrt{2\pi r}}\cos\left(\frac{\theta}{2}\right) \tag{4.2}$$

Equation 4.2 gives the thermoelastic response from all points in the vicinity of the crack-tip in terms of the SIF, as the IR data is collected in a Cartesian framework (x, y) then it is convenient to introduce the y ordinate to replace r in Equation 4.2 as follows:

$$sin\theta = \frac{y}{r}, r = \frac{y}{\sin\theta} \tag{4.3}$$

This results in the following equation:

$$\frac{\Delta T}{T} = \frac{2KK_1}{\sqrt{2\pi y}}(\sin\theta)^{\frac{1}{2}}\cos\left(\frac{\theta}{2}\right) \tag{4.4}$$

Equation 4.4 is then differentiated by parts and equated to zero to identify the maximum *ΔT/T*:

$$\frac{\delta\frac{\Delta T}{T}}{\delta\theta}=\frac{2KK_1}{\sqrt{2\pi y}}\left(-\frac{1}{2}(\sin\theta)^{\frac{1}{2}}.\sin\frac{\theta}{2}+\frac{\frac{1}{2}\cos\frac{\theta}{2}.\cos\theta}{\sqrt{\sin\theta}}\right) \tag{4.5}$$

to give:

$$\frac{2KK_1}{\sqrt{2\pi y}}\left[\frac{1}{2}\sqrt{\sin\theta}.\sin\frac{\theta}{2}\right]=\frac{2KK_1}{\sqrt{2\pi y}}\left[\frac{\frac{1}{2}\cos\frac{\theta}{2}.\cos\theta}{\sqrt{\sin\theta}}\right] \tag{4.6}$$

which simplifies to:

$$\sqrt{\sin\theta}.\sin\frac{\theta}{2}=\frac{\cos\frac{\theta}{2}.\cos\theta}{\sqrt{\sin\theta}} \tag{4.7}$$

Rearranging Equation 4.7, puts all the variables on one side of the equation:

$$\frac{\sin\theta.\sin\frac{\theta}{2}}{\cos\frac{\theta}{2}.\cos\theta}=1 \tag{4.8}$$

Equation 4.8 can be reduced further because:

$$\tan\theta=\frac{\sin\theta}{\cos\theta} \tag{4.9}$$

Substituting Equation 4.9 into 4.8, produces:

$$\tan\theta.\tan\frac{\theta}{2}=1 \tag{4.10}$$

Utilising the half angle rule, Equation 4.10 can be written:

$$\frac{2\tan\frac{\theta}{2}}{1-\tan^2\frac{\theta}{2}}.\tan\frac{\theta}{2}=1 \qquad (4.11)$$

Rearranging Equation 4.11, produces:

$$2\tan^2\frac{\theta}{2}=1-\tan^2\frac{\theta}{2} \qquad (4.12$$

which gives:

$$\tan\frac{\theta}{2}=\frac{1}{\sqrt{3}} \qquad (4.13)$$

Therefore the $(\Delta T/T)_{\max}$ occurs at the intersection of each horizontal line image where $\theta = 60^\circ$. The θ value is substituted into Equation 4.4, and both sides of the equation squared, giving the expression relating the maximum response in the image to its y coordinate only:

$$\left(\frac{\Delta T}{T}\right)^2_{\max}=\frac{4K^2K_1^2}{2\pi y}.\frac{\sqrt{3}}{2}.\frac{3}{4} \qquad (4.14)$$

Equation 4.14 is the key to extracting K_I from the thermoelastic data as this is the only unknown. By inspection it can be seen that all the constants in Equation 4.14 can be gathered to give:

$$\left(\frac{\Delta T}{T}\right)^2_{\max}=\left[\frac{4K^2K_1^2}{2\pi}.\frac{\sqrt{3}}{2}.\frac{3}{4}\right]\frac{1}{y} \qquad (4.15)$$

Equation 4.15 is takes the form of a straight line relationship, $\left(\frac{\Delta T}{T}\right)^2_{\max}$ can be identified along any horizontal line (of value y) and a plot made. However when $y = 0$, $1/y=\infty$, hence it is more convenient to express Equation 4.15 as follows:

$$y = \left[\frac{3\sqrt{3}K^2 K_1^{\;2}}{4\pi} \right] \frac{1}{\left(\frac{\Delta T}{T} \right)^2_{\max}} \tag{4.16}$$

If $\frac{1}{\left(\frac{\Delta T}{T} \right)^2_{\max}}$ is plotted against y then the gradient of the line, *m*, can be used to extract K_I:

$$m = \frac{3\sqrt{3}K^2 K_1^{\;2}}{4\pi} \tag{4.17}$$

By rearranging Equation 4.17, K_1 is obtained as:

$$K_1 = \sqrt{\frac{4\pi m}{3\sqrt{3}K^2}} \tag{4.18}$$

The specimen geometry then has to be considered, and Equation 4.18 is multiplied by a shape function, *C*, [88]:

$$K_1 = C\sqrt{\frac{4\pi m}{3\sqrt{3}K^2}} \tag{4.19}$$

4.3 Test specimen and loading arrangements

As the ultimate aim of the PhD is to demonstrate that IRT can be used to monitor damage growth and use this to control the test machine it was decided to commence investigations with a specimen that had a known single damage initiation point. Hence a standard specimen geometry from BS ISO 12108:2012 [9], a British Standard for monitoring crack growth within metallic specimens was chosen. The standard offers a variety of different specimen designs, which are, compact tension (CT), centre cracked tension (CCT), and single edge notch tensile (SENT), see Figures 4.2, 4.3 and 4.4 taken from the standard.

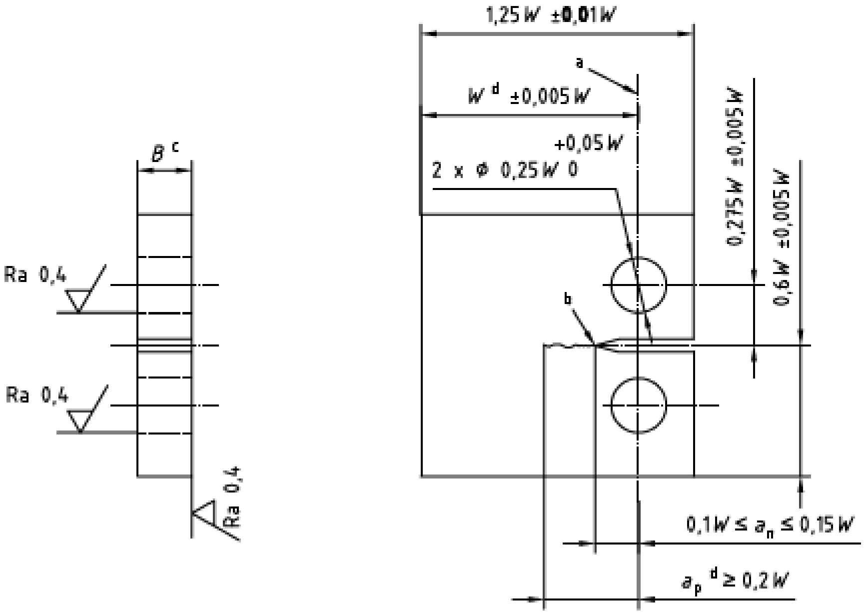

Figure 4.2. A CT specimen with dimension ratios [9].

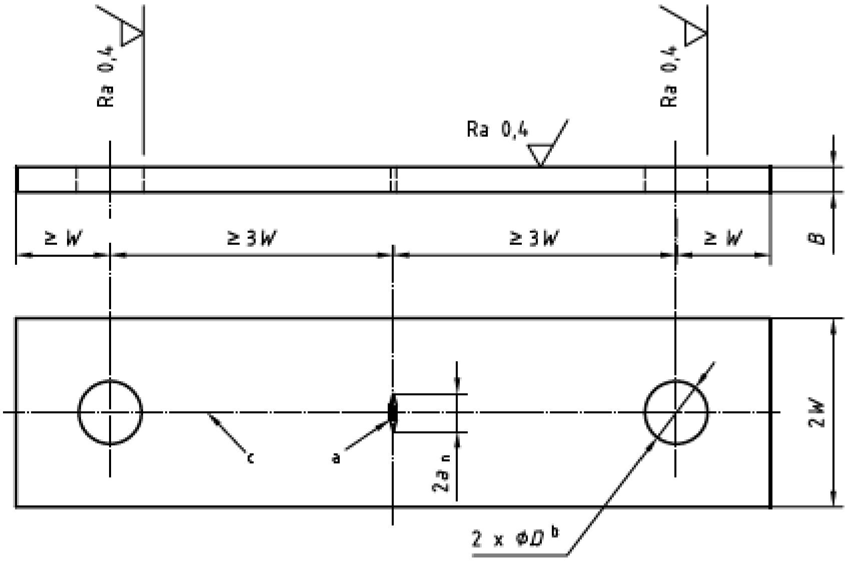

Figure 4.3. A CCT specimen with dimension ratios [9].

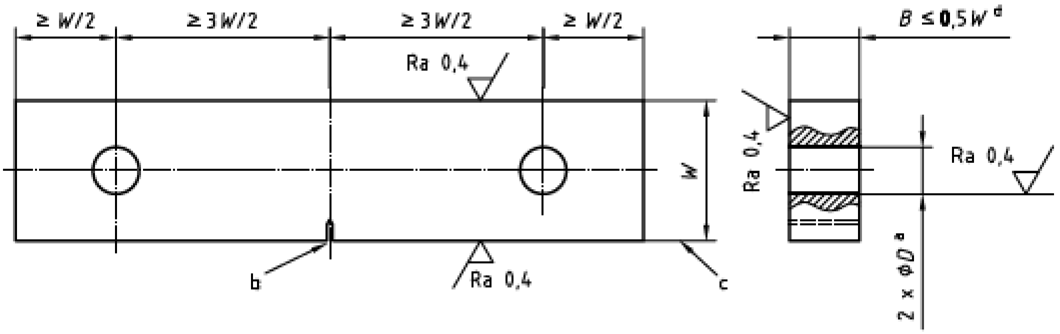

Figure 4.4. A SENT specimen with dimension ratios [9].

The different specimen designs allow for various test materials, geometries, available test fixtures and test machine capacity. The SENT specimen was chosen as it produces:

- a single crack from the sharp notch tip.
- allows unimpeded visual access to the specimen gauge section.
- a specimen thickness of only a few mm is required, ensuring that the crack front is perpendicular to the direction of travel.
- the location and direction of travel of the initial crack are known, allowing the IR detector to focused on the damaged area.

The test standard also specifies the ratios of specimen length, width, thickness, and notch dimensions, as seen in Figures 4.2 – 4.4. The material chosen for the test specimen was 316L stainless steel. 316L has well understood material and thermoelastic properties [90] [91], the fine grain structure ensures steady and consistent crack growth and the material stress intensity factor (K_{1C}) is known. The material properties for 316L stainless steel are provided in Table 4.1.

Table 4.1. 316L Stainless steel material properties [90] [92].

Material Property	**Value**	**Units**
Tensile strength	485	MPa
Yield strength	170	MPa
Elastic modulus	193	GPa
Thermoelastic constant (K)	4.73	MPa^{-1}
Critical mode 1 SIF (K_{1C})	230	MPa $m^{1/2}$
Coefficient of thermal expansion	15.9	(mm/m/°C)
Density	8000	kg/m^3

Initial trial tests were conducted on metallic SENT specimens directly gripped in the jaws of an Instron test machine, and specimens with a pinned connection. It was hypothesised that the pinned connection would be required to account for small misalignments of the loading chain and ensure crack growth aligned with the initial notch. However during the initial trials the tested pin loaded SENT specimen resulted in a crack tip that did not travel horizontally across the specimen. This was confirmed by the use of TSA to show the stress concentration was rotated away from the horizontal at the crack tip. This was due to the specimen rotating around the loading pins. Therefore, a clamped end specimen geometry was chosen to prevent the rotation at the loading pins, and force the crack to grow perpendicular to the loading direction. The clamped-end specimen is defined with a gauge section four times the specimen width. The nominal gripping geometry for the servo hydraulic test machine used for the experiments was 50 mm wide and 50 mm deep. Therefore, with these dimensions known, the rest of the specimen and notch geometry, was determined (see Figure 4.5). Therefore, only results from the clamped end SENT specimens are presented in this thesis. The dimensions of the two specimens, can be found in Table 4.2.

Table 4.2. SENT specimen dimensions.

Specimen No.	Width (mm)	Thickness (mm)	Notch (mm)	
			Width	Depth
1	50.04	2.44	3.13	6.96
2	50.03	2.44	3.10	6.93

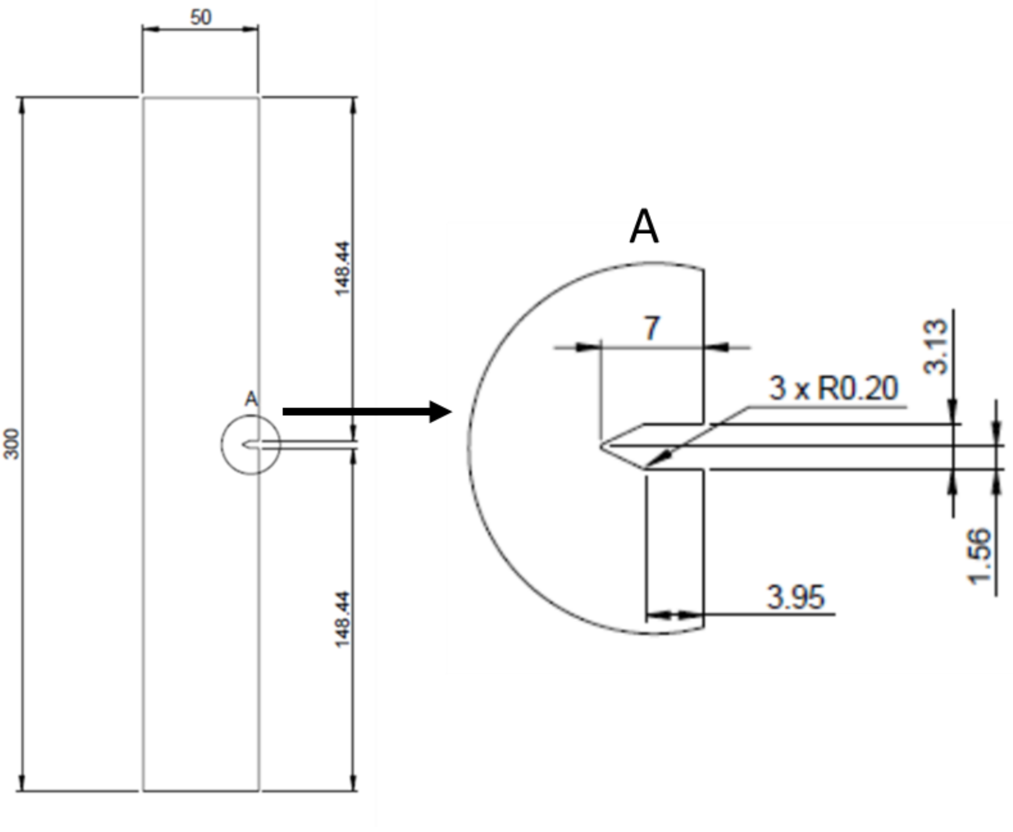

Figure 4.5. Calculated dimensions of specimen.

4.4 Test arrangement

Two IR detectors were used to monitor and record the full-field temperature of the test specimen in the area around the notch. The FLIR SC5500 photon detector was setup to view the "front" face, approximately 25mm above and below the notch, with the notch on the left hand side of the image and the FLIR A655SC microbolometer, was set-up to view the "back" face, approximately 50mm above and below the notch, with the notch on the right hand side of the image. The height of each detector was set to be level with the centre of the notch, but to avoid the reflection of the cameras affecting the measurement the camera was not set perpendicular to the surface of the specimen, it was instead slightly angled to the left hand side. A schematic plan of the test set-up can be seen in Figure 4.6. This set-up is referred to throughout the thesis as back to back observation. To ensure a uniform emissivity across the specimen and to minimise the reflective nature of the material, the specimens were painted with a thin layer of RS matt black on both the front and back surfaces. From a previous study [90] the paint thickness should be between 15 and 25 μm. This paint thickness is achieved by a number of thin even coats of paint and measured using an Elcometer 456 coating thickness gauge, at three points across the specimen gauge section. The photon detector was set to record 1000 frames at a frequency of 383 Hz and the microbolometer was set to 100 frames at 50 Hz. To prevent other external sources of heat being seen either directly or indirectly, reflected on the specimen, a black curtain was mounted around the test machine and camera. See Figure 4.7 for a photograph of test arrangement.

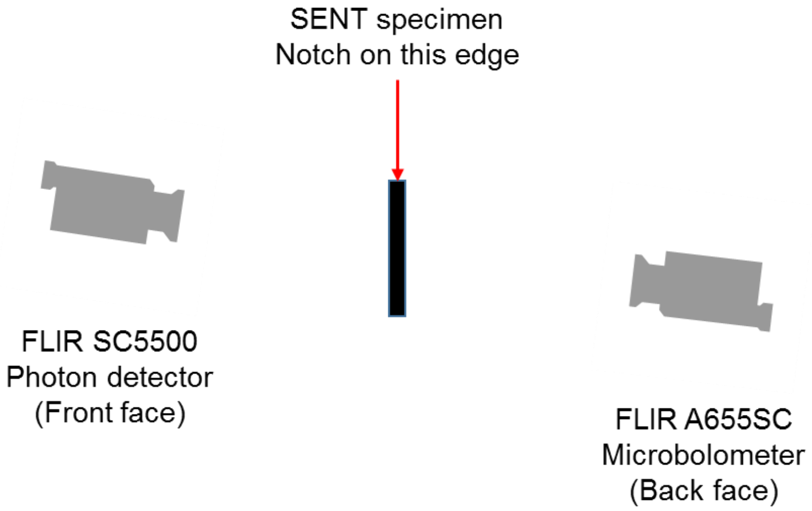

Figure 4.6. Plan view of SENT specimen test arrangement.

Figure 4.7. SENT specimen test arrangement.

4.5 Derivation of K_I from thermoelastic data

Application of Equation 4.19 requires that a graph of $\frac{1}{\left(\frac{\Delta T}{T}\right)^2_{\max}}$, to be plotted against the y coordinate of the horizontal row it is extracted from. To achieve this a number of steps have to be taken to convert the measured temperature into the required format. First the sequence of temperature images is processed using Altair

LI (see chapter 2) to obtain the mean temperature *(T)*, change in temperature *(ΔT)* and phase *(Φ)* image data. All of the temperature measurements are in Kelvin (K). Next, the ΔT data is divided by T data, to give the new image of $\Delta T/T$ data of the thermoelastic response. An example of the three IR data images can be seen in Figure 4.8, from specimen 1 after 24,000 cycles, a constant load test, cycling with a mean load of 11.55 kN, amplitude of 9.55 kN and a frequency of 10 Hz. The total crack length (including the initial notch) at this point was 10.92 mm.

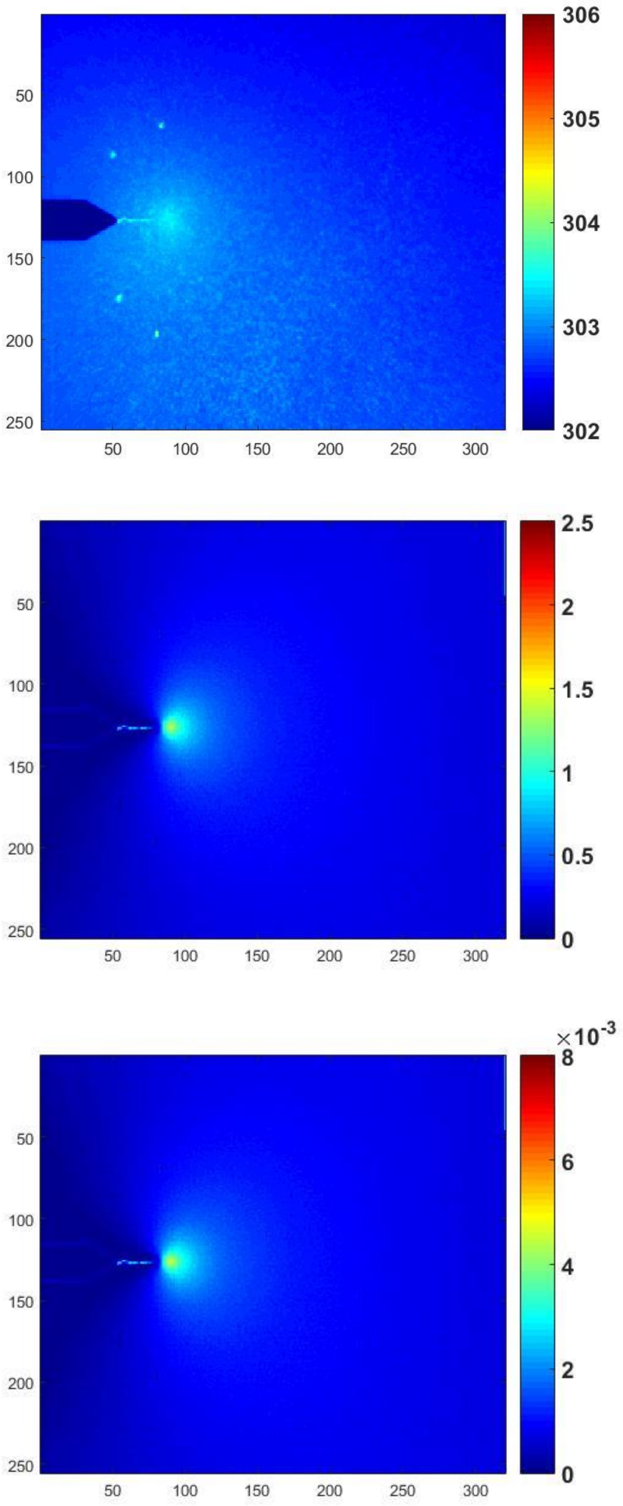

Figure 4.8. Example IR data from a specimen with crack growth from a constant load test, using the photon detector images, mean temperature (T_0) in Kelvin (top), change in temperature ΔT (middle), and the $\Delta T/T$ (bottom).

A Matlab script was developed (Appendix B) so that $(\Delta T/T)_{max}$ is identified in each horizontal row, along with the row number to create a two column matrix, containing row numbers and $(\Delta T/T)_{max}$. Each value of $(\Delta T/T)_{max}$ is then squared and inverted. The row numbers are converted into a position value in metres from the row containing the crack tip, e.g. for the data shown in Figure 4.8, the crack tip was in row 127. The conversion from pixels to length unit is achieved by knowing the spatial resolution of the image, which in this example is 0.135 mm per pixel. Figure 4.9 plots an example of the resulting data for the specific example of the image data shown in Figure 4.8. It can be clearly seen that the data has an approximately linear behaviour with similar gradients above and below the crack tip, defined as 0 m.

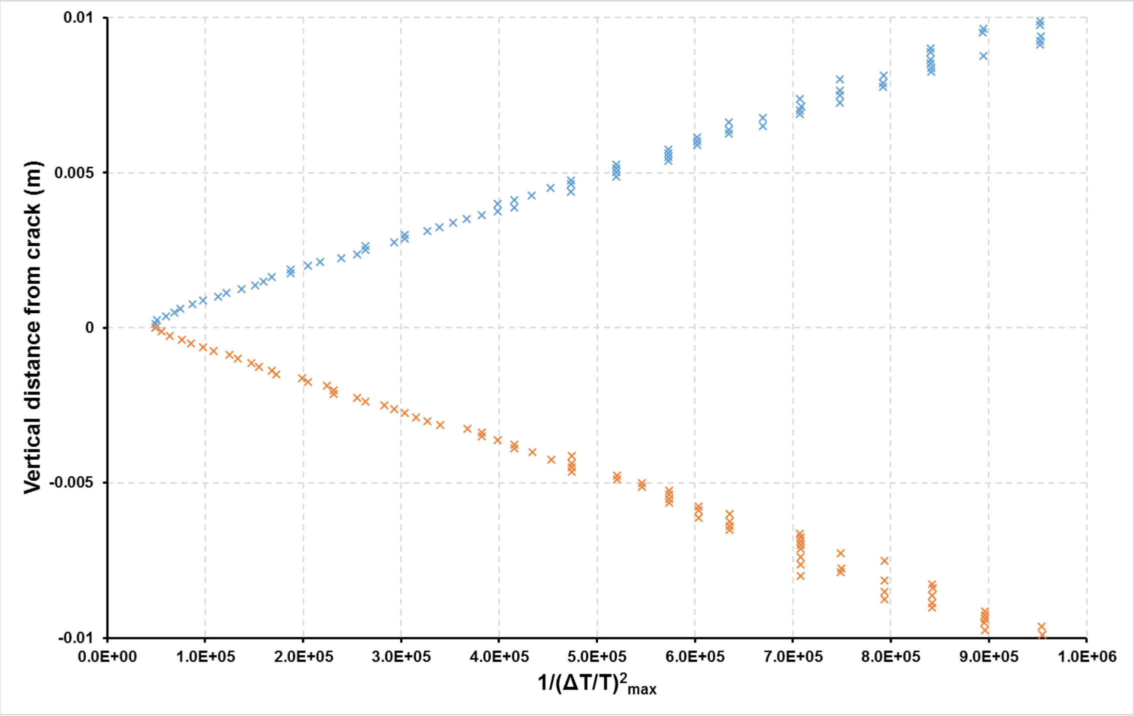

Figure 4.9 Graph of $\dfrac{1}{\left(\dfrac{\Delta T}{T}\right)^2_{\text{max}}}$ *against distance from crack tip (m).*

The Matlab script then uses linear regression to obtain the gradient of $\dfrac{1}{\left(\dfrac{\Delta T}{T}\right)^2_{\text{max}}}$ against position. It should be noted that the Westergaard equation assumes only elastic deformations in the material, therefore the regions of plastic deformation at the crack tip need to ignored, and only the linear portions of the graph should be considered. The code was written to only consider data between 0.0005 m and 0.004 m away from the crack tip to ensure that only the linear portion of the graph was included, e.g. Figure 4.10 plots these regions for the specific example in Figure 4.8.

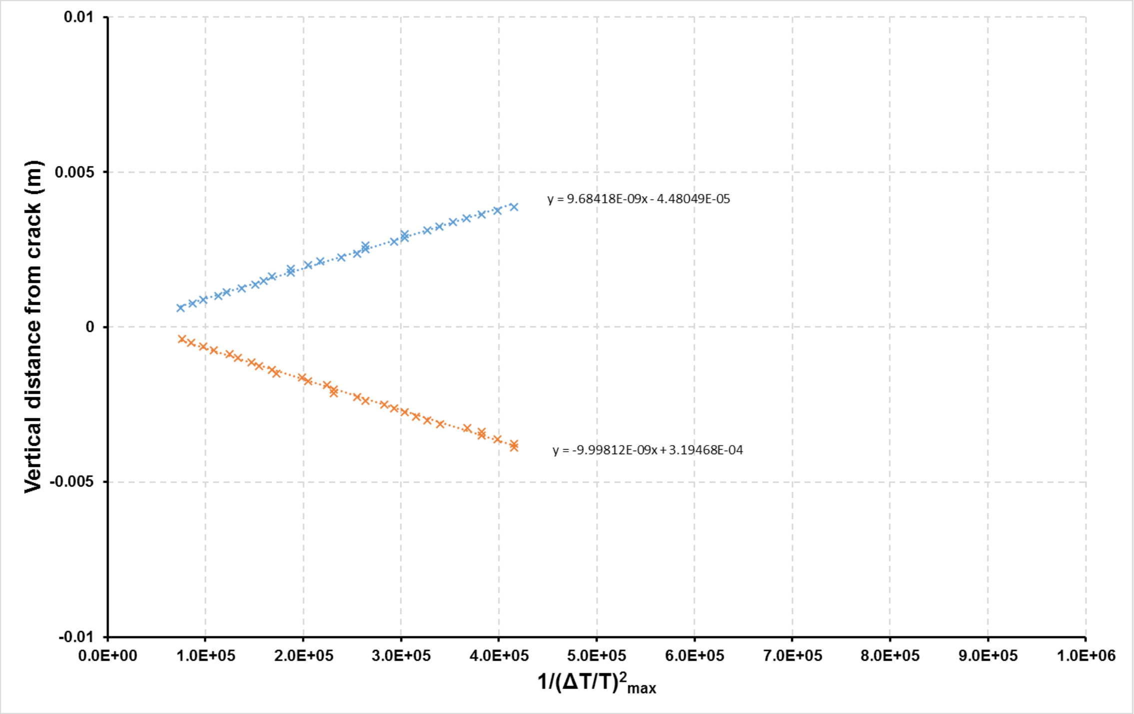

Figure 4.10. Graph of $\frac{1}{\left(\frac{\Delta T}{T}\right)^2_{\max}}$ *against distance from crack tip (m), displaying only the relevant region, and the trend line equations.*

The output from the Matlab script provides directly the gradients of the lines (m), both above and below the crack tip. To calculate K_I, the gradient values were then used with Equation 4.19, along with the SENT specimen shape function C [88]:

$$C = 1.12 - 0.2318\left(\frac{a}{W}\right) + 10.55\left(\frac{a}{W}\right)^2 - 21.72\left(\frac{a}{W}\right)^3 + 30.39\left(\frac{a}{W}\right)^4 \qquad (4.20)$$

where *a* is the total crack length (including the initial notch) *W* is the specimen width.

Finally, the thermoelastic constant, *K*, was calculated using the test data. To calculate *K*, for this specimen, the TSA data is required. A row of pixels, across the centre third of the specimen, and as far from the notch as possible and the average ΔT and T along the row was obtained in Kelvin. It was assumed that there was uniform stress through the specimen cross section at the location, allowing the stress range to be calculated from the applied cyclic loading. The following equation is then used to give *K*:

$$K = \frac{\Delta T}{T \Delta \sigma} \tag{4.21}$$

Additionally, K_I is also obtained using the crack length as follows [9]:

$$K_1 = C\sigma\sqrt{\pi a} \tag{4.22}$$

where K_I is the calculated SIF, C is the SIF geometry function, σ is the stress, and a is the total crack length (including the initial notch).

Table 4.3 lists the K_I values obtained from the thermoelastic data, above and below the crack tip, and the crack length for the particular snap shot of data considered here. The TSA calculated SIF compare well with each other, and have slightly greater values than using the measured crack length. The approaches to obtaining the crack length to derive the SIF are described in Chapter 5.

Table 4.3. K_I SIF (MPa.m$^{1/2}$) values using TSA and crack length.

TSA SIF above crack tip	TSA SIF below crack tip	SIF from crack length measurement
46.07	46.49	44.93

4.6 Detector model of thermoelastic response

The noise and sensitivity models, of the two detector types, described in Chapter 3, were built upon to formulate a camera model, which simulates the TSA data that would be obtained from the SENT specimens. The model required the location of the crack tip to be defined. Therefore, a Cartesian coordinate system was defined, with the origin in the bottom left hand corner of the region of interest of the specimen. For each camera model, the size of the image was the same as the detectors pixel count, to ensure a direct comparison. The crack tip location was obtained using the procedure described in Chapter 5 and positioned in the image using the Cartesian coordinates system, and then used as the origin for a polar coordinate system centred at the crack tip as follows:

$$r = \sqrt{(x - x_{CT})^2 + (y - y_{CT})^2} \tag{4.23}$$

$$\theta = tan^{-1}\frac{y - y_{CT}}{x - x_{CT}} \tag{4.24}$$

where r and θ are defined in Figure 4.1 and the subscript CT indicates the location of the crack tip.

A polar coordinate system is developed around the crack tip and then equation (4.3) is rearranged into following expression to obtain ΔT:

$$\Delta T = \frac{2KK_1T_0}{\sqrt{2\pi r}} cos\frac{\theta}{2} \tag{4.25}$$

T_0 is used to indicate the mean temperature in the cycle and for the model is set to 293 K.

A cyclic variation of temperature, T, is then created, using the following equation:

$$T(x,y,t) = T_0 + 0.5\Delta T(x,y)\cos(2\pi f_0 t + \phi + \pi) \tag{4.26}$$

where the additional variables of t is time, f_0 is the specimen loading frequency and Φ is the phase angle.

Finally, the temperature is converted into radiance for the microbolometer and photon counts for the photon detector. Equations 3.1 and 3.2 are written to include the pixel coordinates and time:

$$R(x,y,t) = \int_{7500}^{14000} \frac{2hc^2\lambda^{-5}}{e^{\frac{hc}{k\lambda T(x,y,t)}} - 1} d\lambda \tag{4.27}$$

$$PC(x,y,t) = \int_{2500}^{5100} \frac{2hc\lambda^{-4}}{e^{\frac{hc}{k\lambda T(x,y,t)}} - 1} d\lambda \tag{4.28}$$

Two ‘snap shots’ of the thermoelastic response from a stationary crack taken from the propagating crack are used in the model described in this chapter. The first snap shot was taken after 26,000 cycles, where the total crack length (including the initial notch) was 9.64 mm. The second snap shot was after 82,000 cycles, with a total crack length of 17.16 mm. The crack length was obtained from the TSA phase plots; a detailed explanation of how this was done is given in Chapter 5.

For the first “snap shot” taken at 26,000 cycles, the SENT specimen was subjected to a mean load of 11.55 kN, with an amplitude of 9.55 kN and a frequency of 10 Hz. Then the load amplitude reduction, to maintain a constant crack growth rate, as described in Chapter 5. Therefore the second “snap shot” at 82,000 cycles, the mean load was 11.55 kN, with an amplitude of 5 kN and a frequency of 10 Hz.

First the results of the numerical model and the experiments are compared, for each crack length. It should be noted that the bolometer experimental results have been mirrored horizontally, so that the notch is on the left hand side of the image, and spatially rescaled, to give the same size field of view as the photon detector. For each of the two crack lengths presented, the specimen’s mean temperature (T), change in temperature (ΔT), both expressed in terms of DL, and phase (Φ) were derived from both the model and the experiments. As mentioned previously, the microbolometer does not have an analogue voltage input and therefore it is not possible to simultaneously record the “lock in” signal, therefore the phase angle was simulated. This was achieved by first creating a simulated “lock in” signal at the loading frequency measured from the test machine, then the phase value that occurred most frequently in the photon detector data was used to adjust the bolometer phase value to match at those points.

The TSA model was used to simulate the DL values from a test specimen with a total crack length of 9.64 mm and a K_I value of 37.599 MPa.m$^{1/2}$, defined as crack length 1. The second model was produced using a total crack length of 17.164 mm and K_I value of 67.708 MPa.m$^{1/2}$, defined as crack length 2. The bolometer experimental results and model results have the noise reduction (NR) facility switched on and the photon detector experimental results have been post processed with motion compensation, using FLIRs random motion software. To allow the software to compensate for the motion three high contrast points are marked on the specimen, in view of the photon detector. On this specimen there are two points above the crack and a single point below.

4.6.1 Crack length 1, $K_I = 37.6$ MPa.m$^{1/2}$

The experimental and simulated mean temperature for the 9.64 mm crack length can be seen in Figures 4.11 and 4.12, for the microbolometer and photon detector respectively. For all of the following figures, the experimental results are the image on the left hand side and the model simulation is on the right. The simulated mean temperature data, T_0 in Equations 4.25 and 4.26, for the microbolometer shown in Figure 4.11 is in the same range as the experimental data, but the heat generated around the crack tip as a result of the cyclic plasticity is shown in the experimental data. It is important to note that the plasticity is not modelled by the linear elastic fracture mechanics approach used for the model. In Figure 4.12 the effect of the plasticity is shown clearly in the experimental data; the model is just showing noise with the increased temperature at the crack-tip resulting from the infinite value given as r tends to zero in Equation 4.25. The indication from comparing the experimental data in Figures 4.11 and 4.12 is that the bolometer is not responding to the cyclic heat generation, possibly as a result of the slow response time.

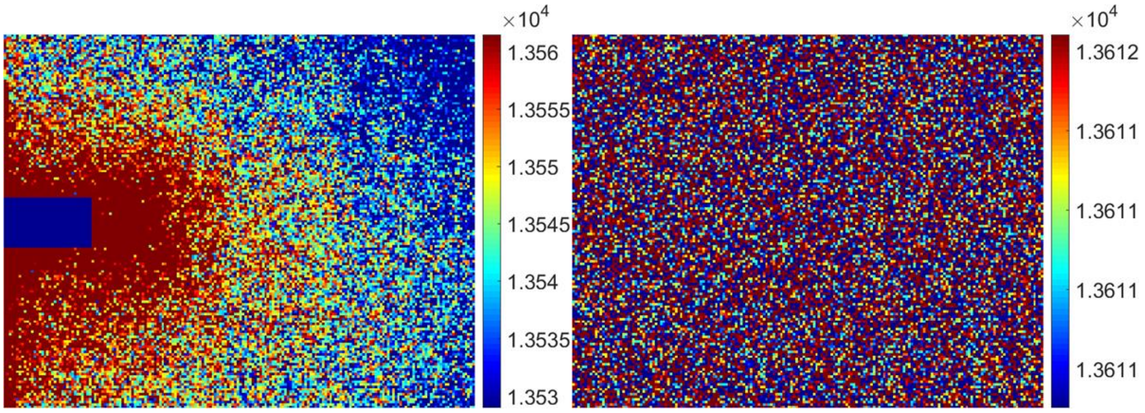

Figure 4.11. Microbolometer mean temperature (DL) for 9.64 mm crack length. Experimental data on the left.

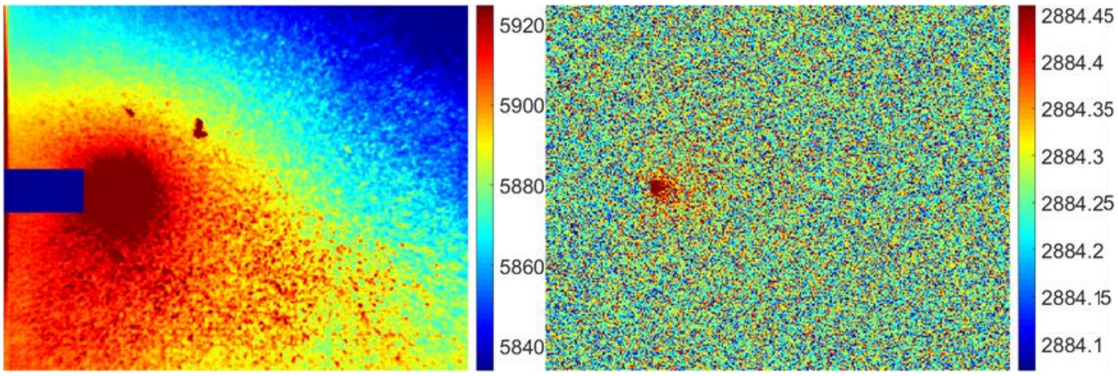

Figure 4.12. Photon detector mean temperature (DL) for 9.64 mm crack length. Experimental data on the left.

The ΔT experimental and simulated results for the microbolometer are shown in Figure 4.13. The experimental data are showing the typical cardioid shape expected in the region of the crack tip [93]. However, the simulated ΔT values are approximately ten times larger than the experimental results. Once again indicating that the microbolometer is not able to respond to the rapid temperature changes occurring in the experiment. Figure 4.14 illustrates the effect, where the temperature response (°C) of a single pixel is plotted against time. Figure 4.14 also includes the identical data from the model for comparison, showing the expected sinusoidal response. This clearly shows that the bolometer raw data cannot be used for TSA.

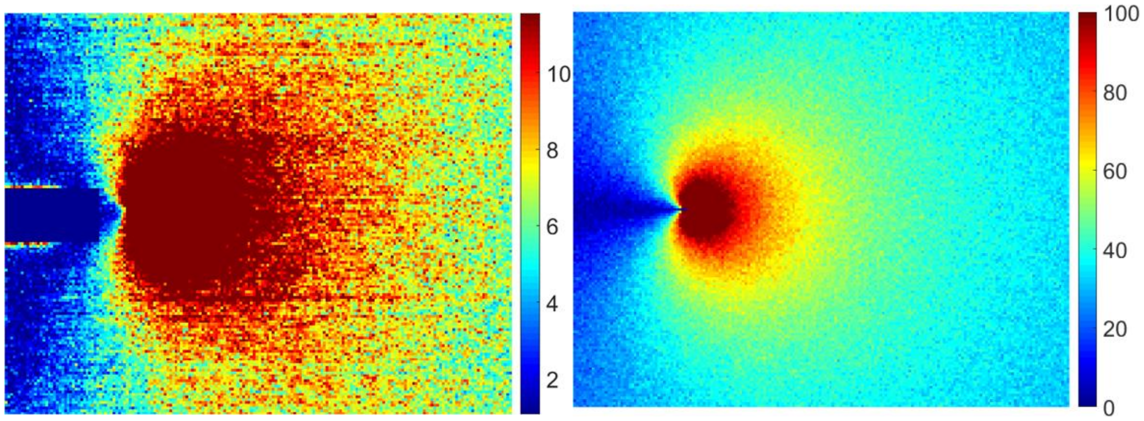

Figure 4.13. Microbolometer ΔT (DL) for 9.64 mm crack length. Experimental data on the left.

To confirm that the experimental results are not responding to the rapid temperature changes, a calculation was undertaken. In this example the maximum *ΔT* recorded by the photon detector was 1.45 K, the specimen loading frequency was 10 Hz, and the microbolometer has a thermal time constant of 0.008 s. *ΔT* is measured between the maximum and minimum stress applied to the specimen (half of a sine wave). For the 10 Hz loading frequency, half of the sine wave takes 0.05 s and the *ΔT* is 1.45 K, giving a temperature change rate of 29 K/s. As the camera was capturing frames at 50 Hz, i.e. one reading every 0.02 ms and according to [79], the detector response time to achieve 99% of the final value is 6 times the time constant, i.e. 0.048 ms, it is clear for a rapidly changing scene the detector does not have time to respond. This is because, the change in temperature over the time constant is 0.232 K and over the response time is 1.39 K, during the time taken to record a temperature reading. This value is almost the same as the maximum ΔT recorded from the specimen and larger than the ΔT recorded over the rest of the specimen. Giving rise to the measurement scatter displayed in Figure

4.14. However, it may be possible to carry out TSA with a bolometer at lower loading frequencies but not where there is significant heat transfer such as at the tip of a crack.

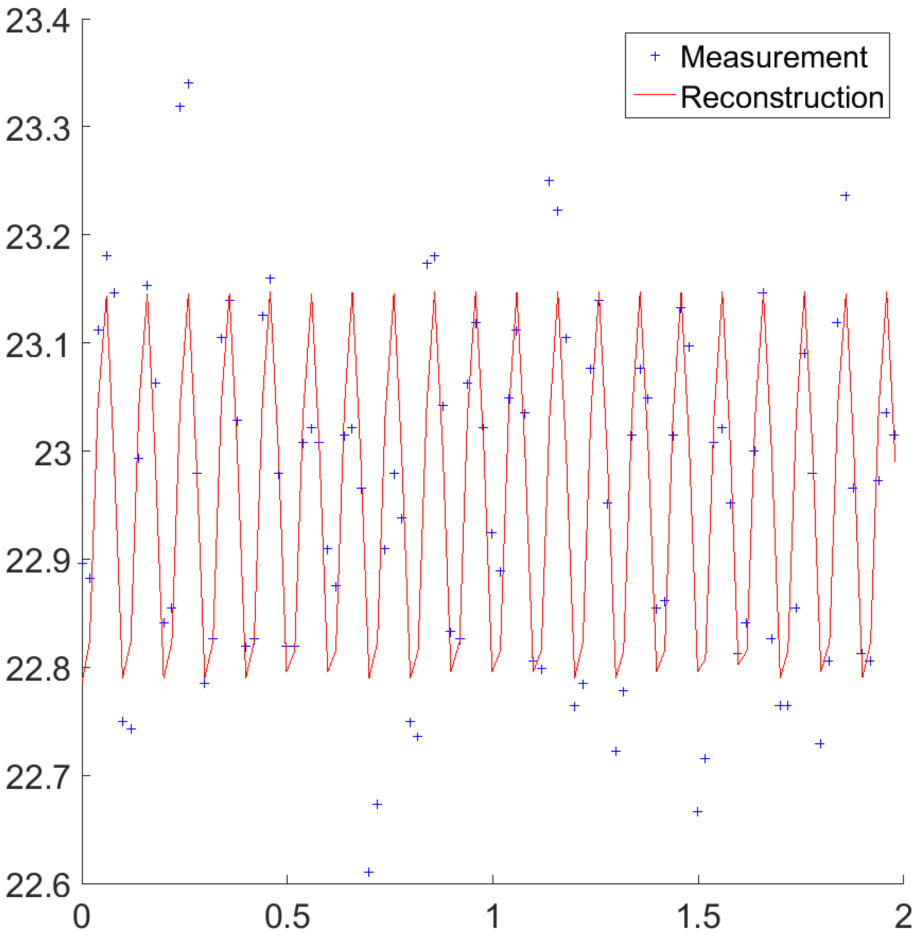

Figure 4.14. Microbolometer temperature (℃) response of a single pixel against time for 9.64 mm crack length

The results from the photon detector show the effect of the plasticity and heat transfer at the crack tip. ΔT from the photon detector (Figure 4.15) is approximately twice that of the simulation. This is because the simulation is based on linear elastic fracture mechanics and assumes adiabatic conditions at the crack tip. Whereas in practice the crack growth contains elastic and plastic loading regions (around the crack tip), contributing to the overall temperature and the change in temperature. Figure 4.16 shows a plot of the simulated ΔT subtracted from the experimental for the photon detector, providing a measure of the temperature change due to plasticity and heat transfer. The maximum difference between the experimental and simulation is 150 DL, at the crack tip, which indicates that the experiment is deviating from the theory significantly in the region of the crack tip. This would be made worst if the loading frequency was reduced causing the thermal diffusion to increase.

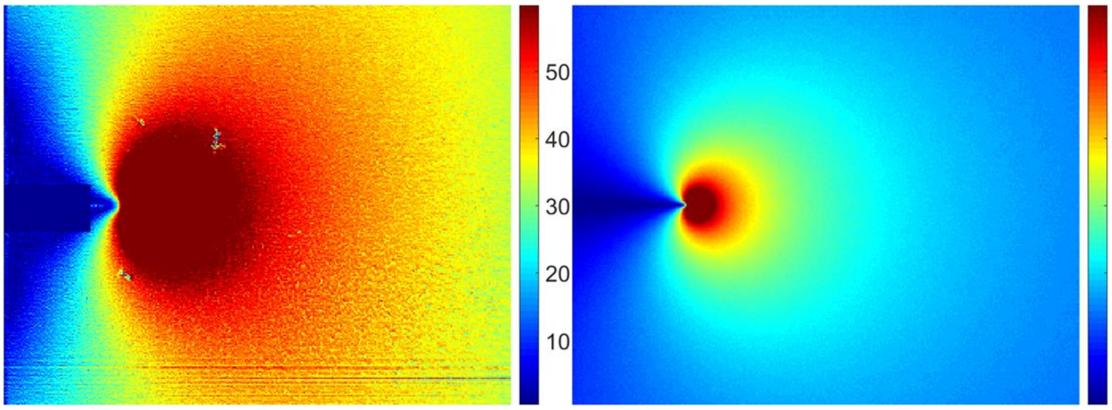

Figure 4.15. Photon detector ΔT (DL) for 9.64 mm crack length. Experimental data on the left.

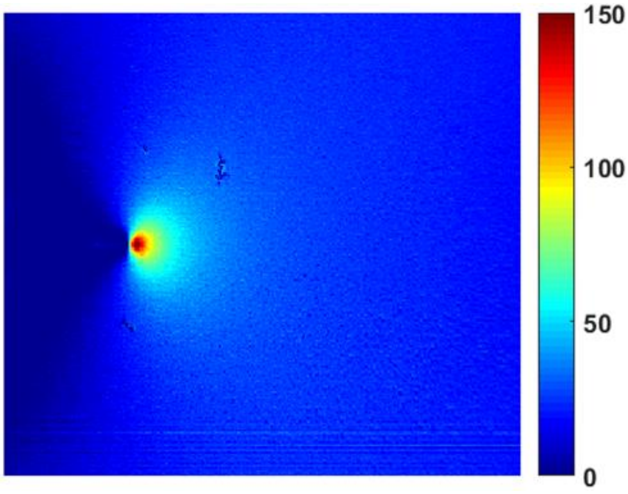

Figure 4.16. Difference between experimental and simulated ΔT (DL) for 9.64 mm crack length using the photon detector.

In Figures 4.17 and 4.18 the phase angles for the microbolometer and photon detector, respectively, can be seen. An out of phase response, indicates areas of non-adiabatic conditions, due to plastic instead of elastic deformation occurring. Both the microbolometer and photon detector, experimental and simulation, display similar values throughout the image, except for the regions around the crack tip. Again this is due to the model assuming only adiabatic/elastic loading conditions.

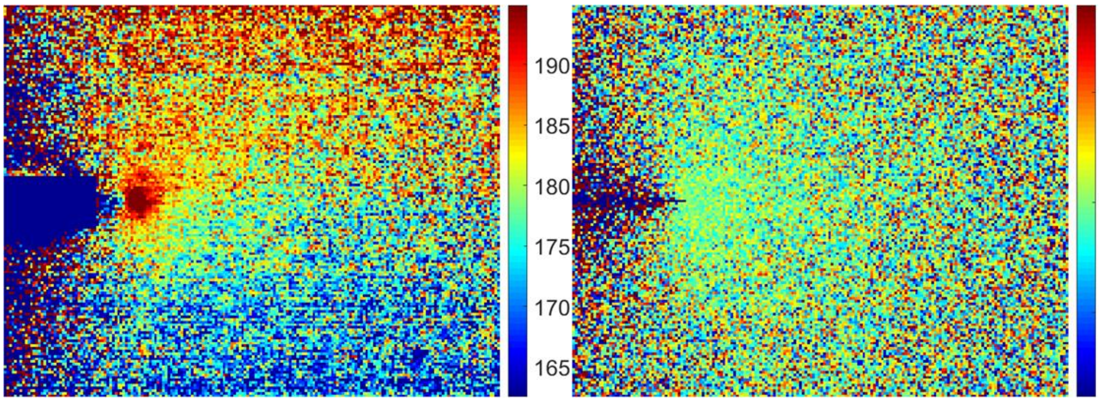

Figure 4.17. Microbolometer Phase angle (°) for 9.64mm crack length. Experimental data on the left.

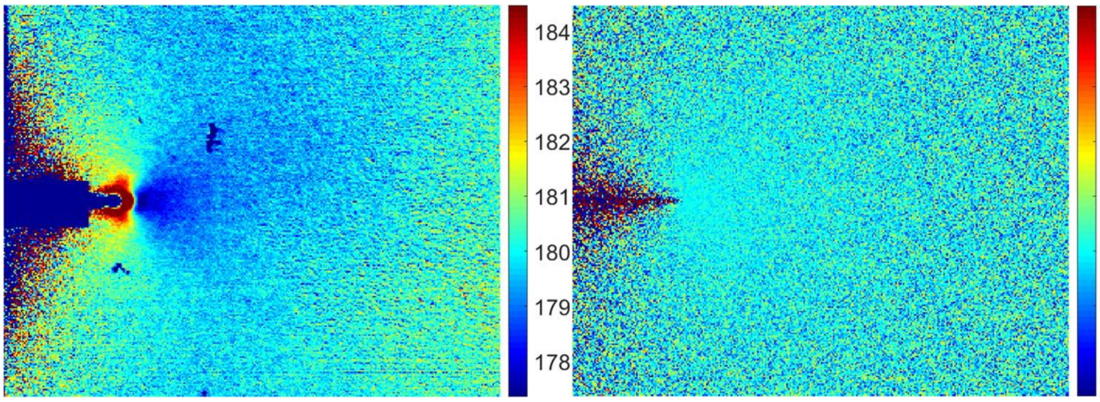

Figure 4.18. Photon detector Phase angle (°) for 9.64mm crack length. Experimental data on the left.

4.6.2 Crack length 2 K_I = 67.7 MPa.m$^{1/2}$

Figures 4.19 and 4.20 show the comparison of experimental and simulated mean temperature for the second crack length of 17.164 mm. As for the first simulated crack length the microbolometer experimental and simulated mean temperature (Figure 4.19) compare favourably. In particular, there is also less heating at the crack tip show experimentally through a reduced hot spot. The simulated and experimental mean temperature plots in Figure 4.20 again show a factor of two difference; clearly indicating the deficiency in the model.

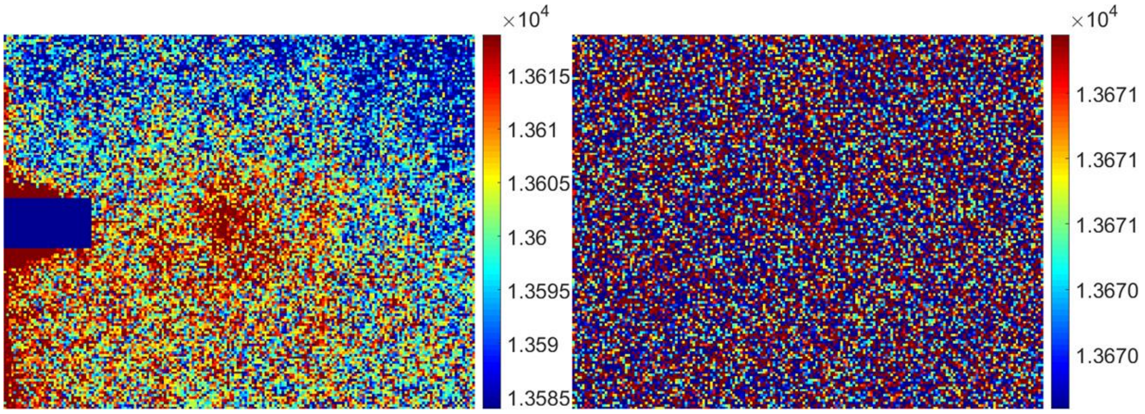

Figure 4.19. Microbolometer mean temperature (DL) for 17.164 mm crack length. Experimental data on the left.

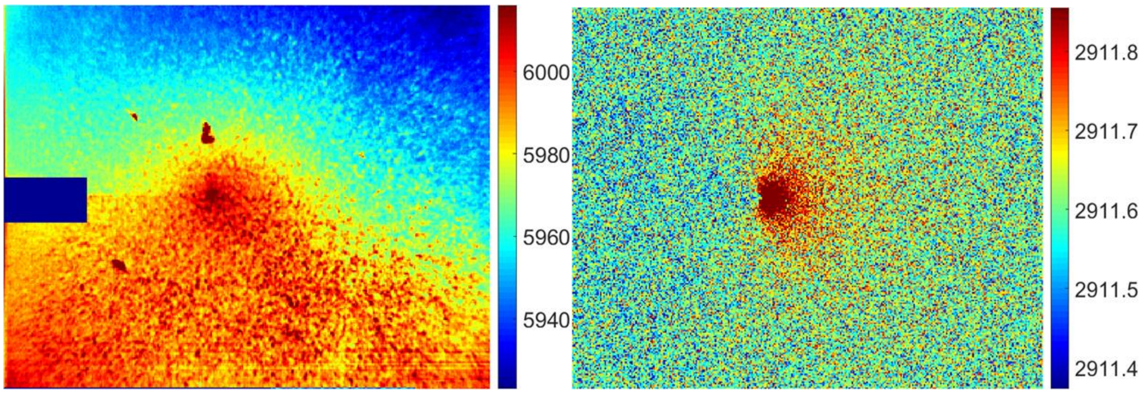

Figure 4.20. Photon detector mean temperature (DL) for 17.164 mm crack length. Experimental data on the left.

Figure 4.21 plots the experimental and simulated ΔT for the microbolometer at the longer crack length. As for the shorter crack length although the basic shape of the data is similar, there is a factor of 10 between the experimental and simulated values. Figure 4.22 shows the ΔT experimentally and simulated for the photon detector at the longer crack length. From a qualitative visual assessment of these plots they are identical, which suggests that at the longer crack length there is little or no plastic deformation. The difference between the two can be found in Figure 4.23, where it can be seen that the maximum DL is approximately 75, half of the

150 DL at 9.64 mm crack length, and over a smaller area. Confirming that at his point of the test, with the reduced loading amplitude, there is little plastic deformation around the crack tip.

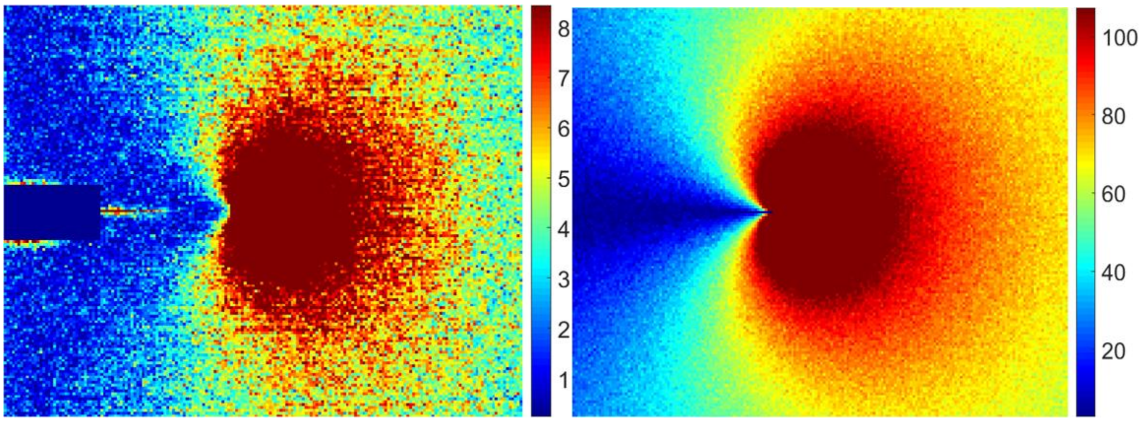

Figure 4.21. Microbolometer ΔT (DL) for 17.164 mm crack length. Experimental data on the left.

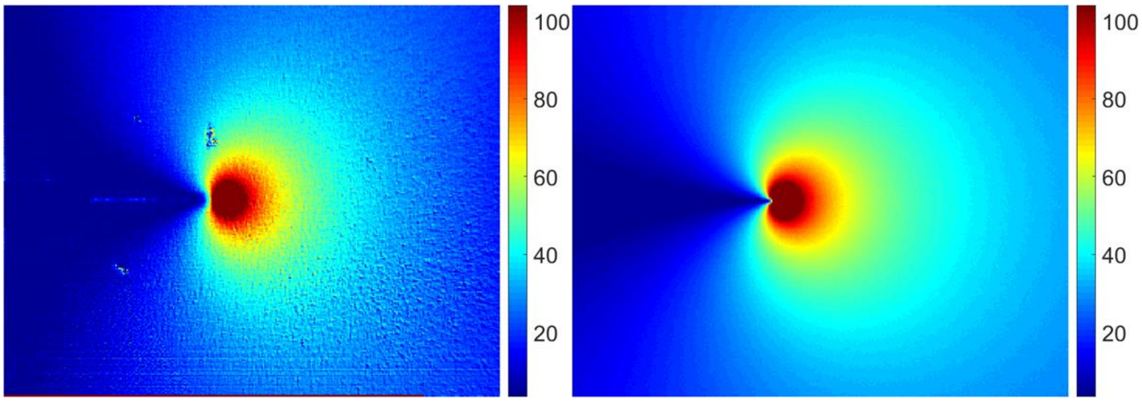

Figure 4.22. Photon detector ΔT (DL) for 17.164 mm crack length. Experimental data on the left.

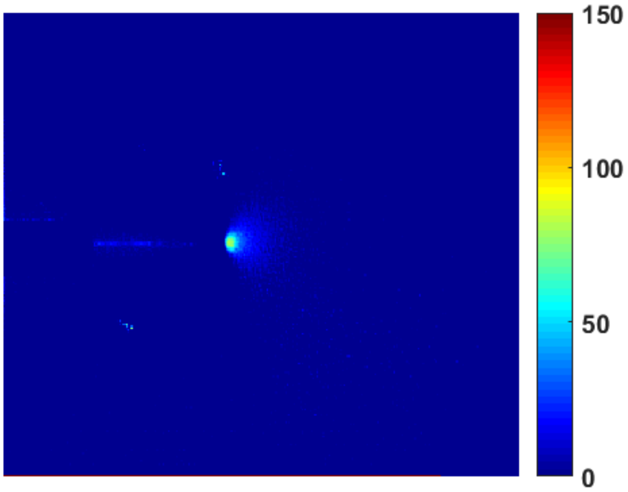

Figure 4.23. Difference between experimental and simulated ΔT (DL) for 17.164 mm crack length using the photon detector.

In Figures 4.24 and 4.25 the phase angle for the microbolometer and the photon detector can be found. As for the 9.64 mm crack length, an out of phase response, indicates areas of non-adiabatic conditions, due to heating and plasticity instead of elastic deformation. Away from the crack tip, and the non-adiabatic conditions, the microbolometer phase images (Figure 4.24) are noticeably different, where the lack of a means to directly record a lock-in signal causes errors in the calculation. Whereas, the photon detectors experimental and simulation images, display similar values throughout the image, except for the regions around the crack tip. Again this is due to the model assuming only adiabatic/elastic loading conditions.

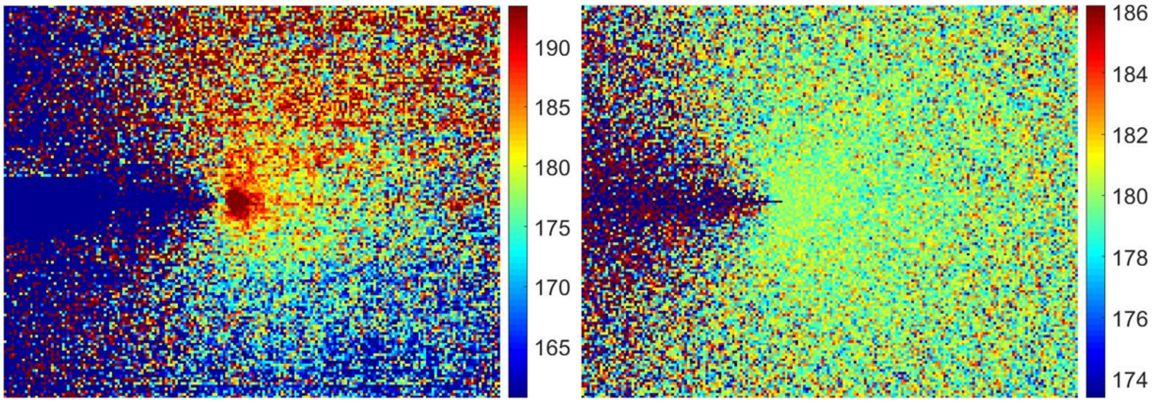

Figure 4.24. Microbolometer Phase angle (°) for 17.164mm crack length. Experimental data on the left.

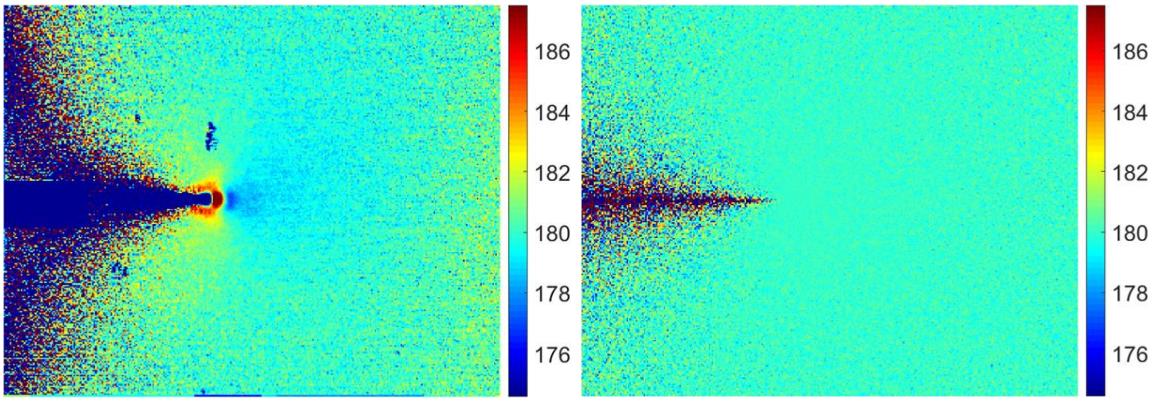

Figure 4.25. Photon detector Phase angle (°) for 17.164mm crack length. Experimental data on the left.

4.7 Conclusions

The test uses fatigue loading to grow a crack from the notch tip which can be monitored using TSA. To investigate the feasibility of using an inexpensive microbolometer to perform these measurements the camera models defined in Chapter 3 have been incorporated into a formulation, to enable the production of simulated TSA data from both the photon detector and microbolometer. The simulations are compared to experimental data for two different crack conditions.

The simulations based on the microbolometer model, produce mean temperature data that compares well to experiments, however the ΔT data is approximately ten times larger than the experimental results. For this experimental set-up it has been discovered that the microbolometers response and noise, make it unsuitable to measure the thermoelastic response of the specimen. It has been shown [94] that a microbolometer can be used for TSA when coupled with a reference load input, using a software called MiTE. Frequencies ranging from 0.5 to 15 Hz were applied to the specimen, but it should be noted that significant post processing was required to account for the thermal time constant and detector response time, and that the specimens were loaded within their linear elastic limit, to prevent damage evolution during recording.

Simulated noise in the temperature data for both the microbolometer and the photon detector, mimics the experimental noise adequately. The simulation of the ΔT for the photon detector captures the temperature distribution around the crack tip accurately, with the exception of the response of plastic deformation particularly evident in the simulation of the shorter crack length. These simulations show the potential for the less expensive microbolometer system to be used in the place of the more expensive photon detector to monitor the crack growth in a metallic SENT test, but not for TSA under these experimental conditions. The full benefit of using TSA to assist in detecting, identifying, and monitoring damage within the specimen can be found in Chapters 5 and 7, for metallic and composite materials respectively.

Chapter 5 Using IRT to detect and monitor crack growth in SENT specimens

5.1 Introduction

The aim of the work in this chapter is to confirm that both types of IR detector, described and evaluated in Chapter 3, can be used to detect and monitor crack growth, in two loading scenarios, and identify any correlation between temperature evolution at the crack tip and the Paris Law [95]. Fatigue cracks in metallic materials follow the fatigue crack growth model called the Paris Law, written as follows:

$$\frac{da}{dN} = C\Delta K^{m} \tag{5.1}$$

where, da/dN is the propagation rate of the crack length a (mm), ΔK is an elastic SIF range (MPa $m^{0.5}$) at the crack tip and C and m are constants.

Figure 5.1 shows the relationship between the change in crack propagation rate and the SIF. Initial crack growth is slow up to ΔK_{th} (threshold SIF), stable crack growth up to ΔK_{Ic}, when the growth becomes rapid and unstable.

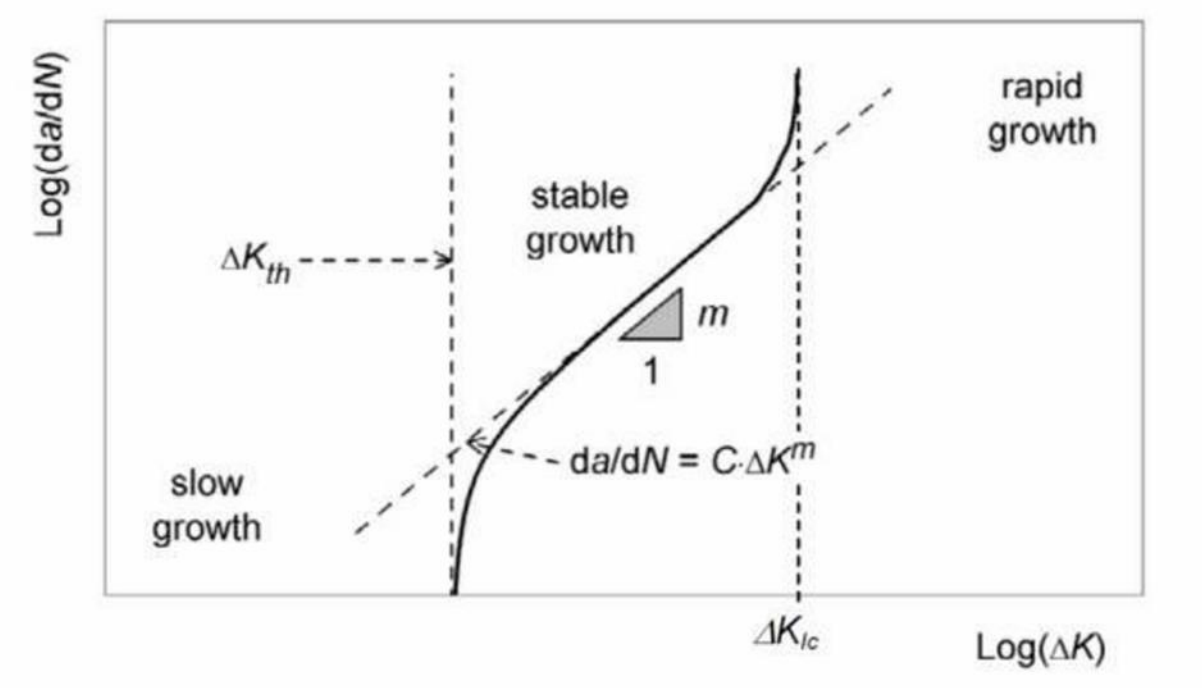

Figure 5.1. Paris Law for crack growth, da/dN as a function of the SIF ΔK [96]*.*

In this chapter it is investigated if infrared thermography can be used to locate and monitor the crack-tip as the crack propagates by using the temperature evolution. The aim is to evaluate if IRT can provide a non-contact approach to monitoring damage evolution. If the position of the crack tip and hence the rate of crack growth can be obtained directly from the temperature measured by the IRT then it establishes if there is an opportunity to use the thermal response as an input to the test machine controller.

Alongside the simple temperature measurement the thermal data is post processed into TSA data in the form of ΔT and phase angle. The position of the crack tip is also identified in this data so the crack length is obtained using just the temperature change, the change in the thermoelastic response and the change in the phase. The SIF is calculated using the crack length and Equation 4.22 and directly by using the ΔT, as described in Chapter 4.

By plotting the crack growth rate (da/dN) and the temperature evolution rate (dT/dN), against the stress intensity factor (ΔK), it is determined if the temperature evolutions follow the Paris model. The first section of this chapter is the test methodology, and is followed by the results section and concludes with a discussion of the results and the suitability of using the IR data to monitor and control crack growth rate.

5.2 Test methodology

The SENT specimens described in Chapter 4 were used throughout this work. Two loading approaches were applied; first the specimens were cyclically loaded at a constant load level, 11.55 kN, +/- 9.45 kN at 10 Hz until significant crack growth was achieved (defined as twice the length of the initial notch); second a 'simulated' controlled crack growth approach was conducted using a series of reductions in load amplitude at specified increases in displacement range defined from the constant load level tests. The constant load level test enables the collection of IRT and TSA data from a crack with a range of SIFs to investigate the capability of the two IR techniques to determine the growth of the crack and the effect on the stress state on the surface of the specimen. The test also determines a level of the change in the test machines displacement range which signifies an acceleration of crack growth and hence a shift from stable to rapid growth, informed by the constant load level test. An explanation of the procedure used for the 'simulated' controlled crack growth test is given in section 5.3.2.

The initial constant load level tests were monitored with the photon detector on the front surface only. This enabled the determination of the change in maximum displacement at which steady crack growth starts to exponentially increase and measure the change in surface temperature at the crack tip. The 'simulated' controlled tests were monitored with the photon detector on the front surface and the bolometer on the rear surface. This provided the opportunity for both, an investigation of the use of IR techniques to assess the growth of the crack and a comparative assessment of the photon detector and the less expensive bolometer. For both tests, the data was recorded every 1000 cycles.

5.2.1 Crack growth measurement

The IR data recorded by the photon detector and the bolometer were both post-processed, in different ways, to determine the crack length, enabling further analysis of the crack growth and calculating the SIF. To measure the crack length, three different approaches were developed for the photon detector. Firstly, the data is post processed into TSA data over the 1000 recording frames. This enabled the location of the maximum mean temperature (T_0), the maximum change in the thermoelastic response (ΔT) and the change in phase angle to be identified. For each data recording run, i.e. every 1000 cycles, 1000 frames were recorded and TSA applied, the X and Y pixel coordinates of the maximum values were extracted manually and recorded in a spreadsheet along with the value of the mean temperature (T_0) and the thermoelastic response (ΔT). Only the pixel coordinates of the phase angle change were recorded and not the actual value of the phase. For the bolometer the maximum temperature value identified in 100 frames of data. Tables of all the results are presented in section 5.3 (see Tables 5.1 and 5.3 to 5.5). The following explains how the crack length was defined using the position coordinates obtained from each approach.

A particular challenge in using the maximum temperature to locate the crack tip, by either method described above, is the potential for ‘hotspots’ occurring within the crack front due to frictional heating as the crack faces run together. Therefore these temperatures were ignored in the analysis. Figure 5.2 displays a typical photon detector mean temperature, where the higher temperatures can be seen on the crack near the notch, and an area of increased temperature around the crack tip. In this example for a specimen loaded at a constant load level after 24,000 cycles, the distance from the edge of the specimen to the hotspot is 12 mm.

Horizontal temperature profiles from the end of the notch to beyond the crack tip (labelled in Figure 5.2) can be found in Figure 5.3. In this example, the maximum temperature (℃) was taken as pixel 90. For all the metallic test specimens the notch length is 7 mm, the distance in pixels from the edge of the specimen to the notch tip is 54 pixels, therefore each pixel is 0.135 mm. For all crack length measurements, a region of interest was defined as a maximum of five horizontal pixel rows either side of the notch tip. These were manually inspected for the maximum temperature. Figure 5.3 displays three horizontal rows centred on the crack tip.

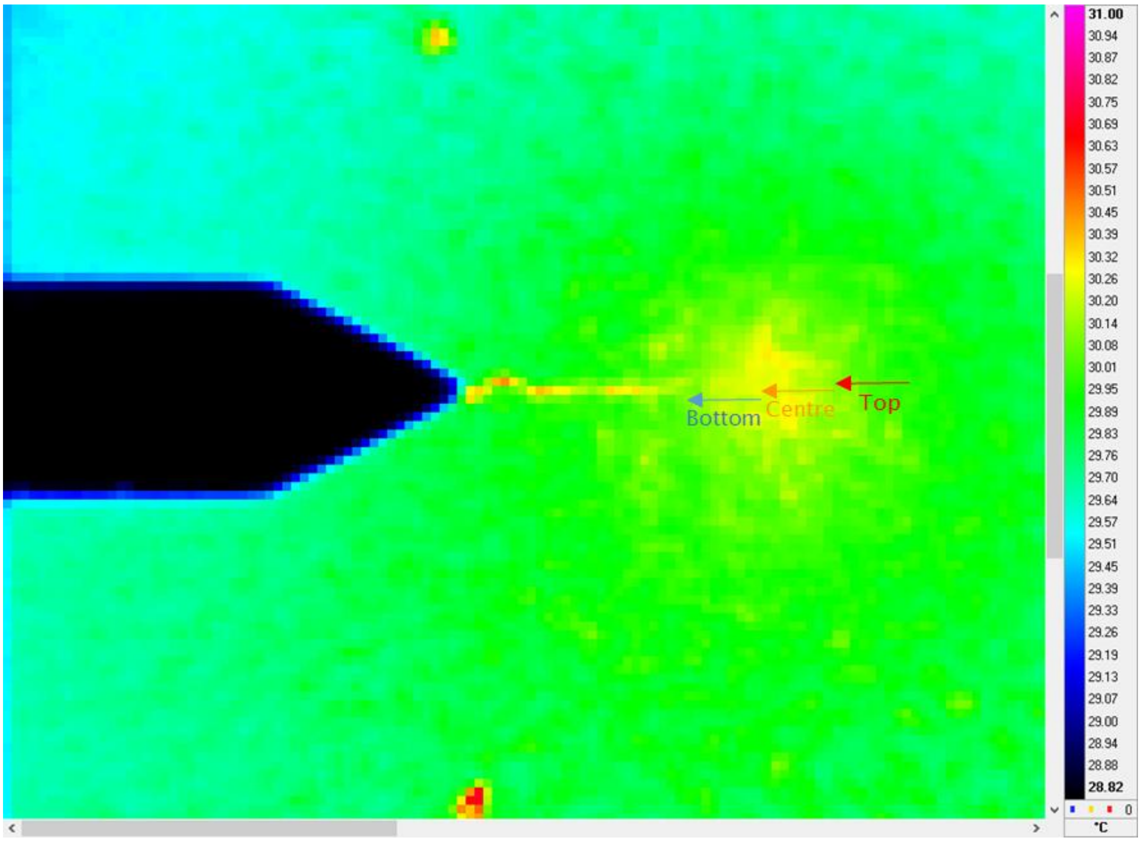

Figure 5.2. A typical photon detector mean temperature, T_0 (℃) image around the specimen crack.

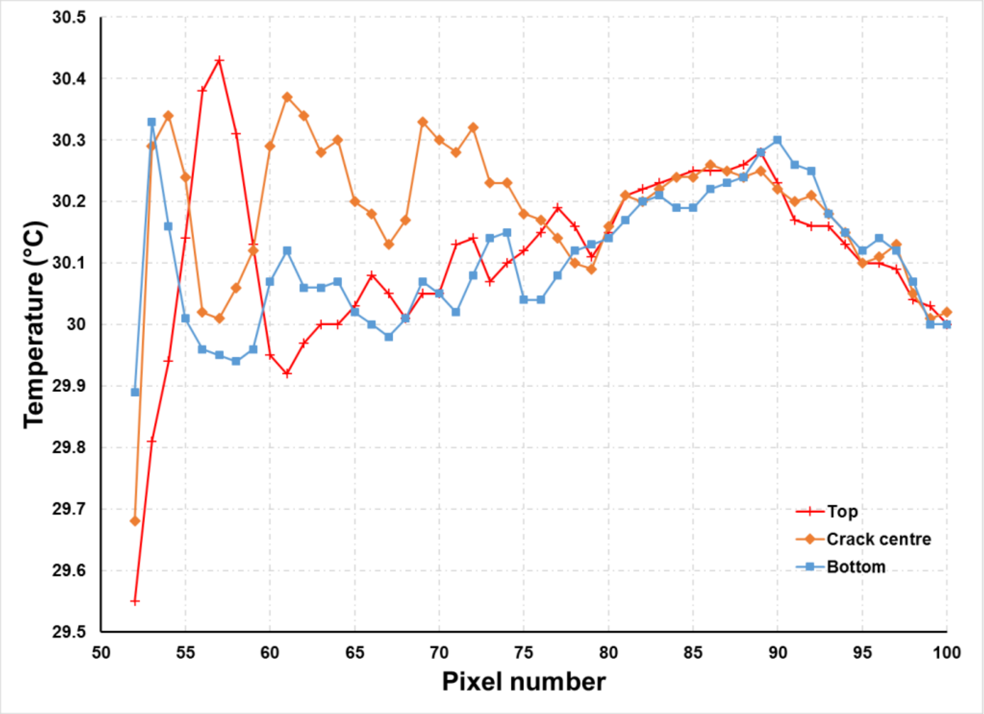

Figure 5.3. Examples of horizontal temperature profiles from the Photon detector plotted from the notch tip.

The second approach to determine the crack length used the thermoelastic response, *ΔT*, from the post processed photon detector data. The maximum value of *ΔT* was determined by scanning the same regions of interest defined in the first approach. Figure 5.4 shows an example of the *ΔT* image around the crack tip, from the same constant load specimen shown in Figures 5.2 and 5.3. For the majority of the images captured there was a single pixel with the maximum *ΔT*. When there were two pixels with the same value, the pixel furthest from the notch was recorded. In the case shown in Figure 5.4 the maximum *ΔT* value was 1.37 °C, at pixel 88, giving a total crack length measurement of 11.725 mm, from the edge of the specimen.

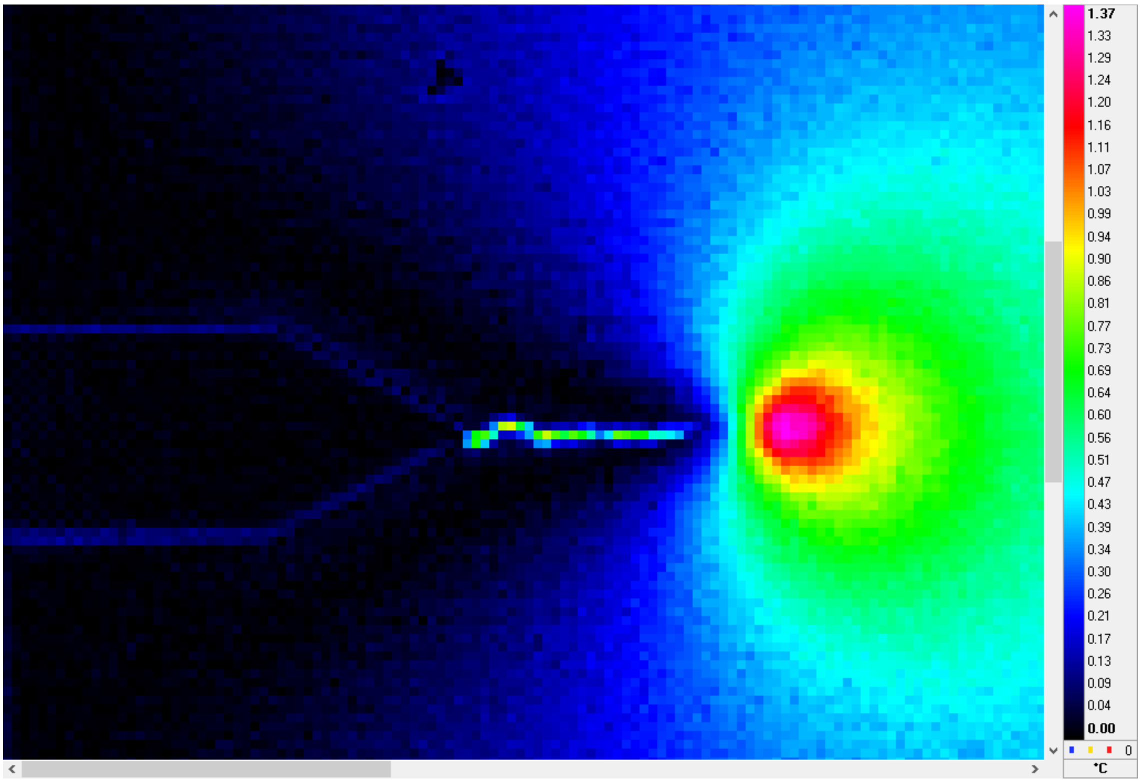

Figure 5.4. A typical photon detector ΔT image around the specimen crack.

The final approach to determine the crack length uses the phase data from TSA applied to images captured by the photon detector. Figure 5.5 shows a typical phase image around the crack tip of the specimen loaded at constant load. To determine the crack length the profile of the phase values along the crack tip (see Figure 5.6) was analysed to find a sudden change in phase. The plastic deformation in ahead of the crack tip leads to an out of phase response, therefore the crack length was determined to be the point before an out of phase curve appears. In the example shown in Figures 5.5 and 5.6 it can be seen that the phase angle along the crack is negative, then swaps to positive, before dropping below 170° at pixel 82, and then behaving non-adiabatically in front of the crack tip. This gives a total crack length of 10.917 mm. The phase crack length measurements were used for all of the SIF calculations requiring crack length, because both the temperature hotspot *(T_0)* and the point of maximum change in temperature *(ΔT)* are in front of the crack tip in the area of most plastic deformation.

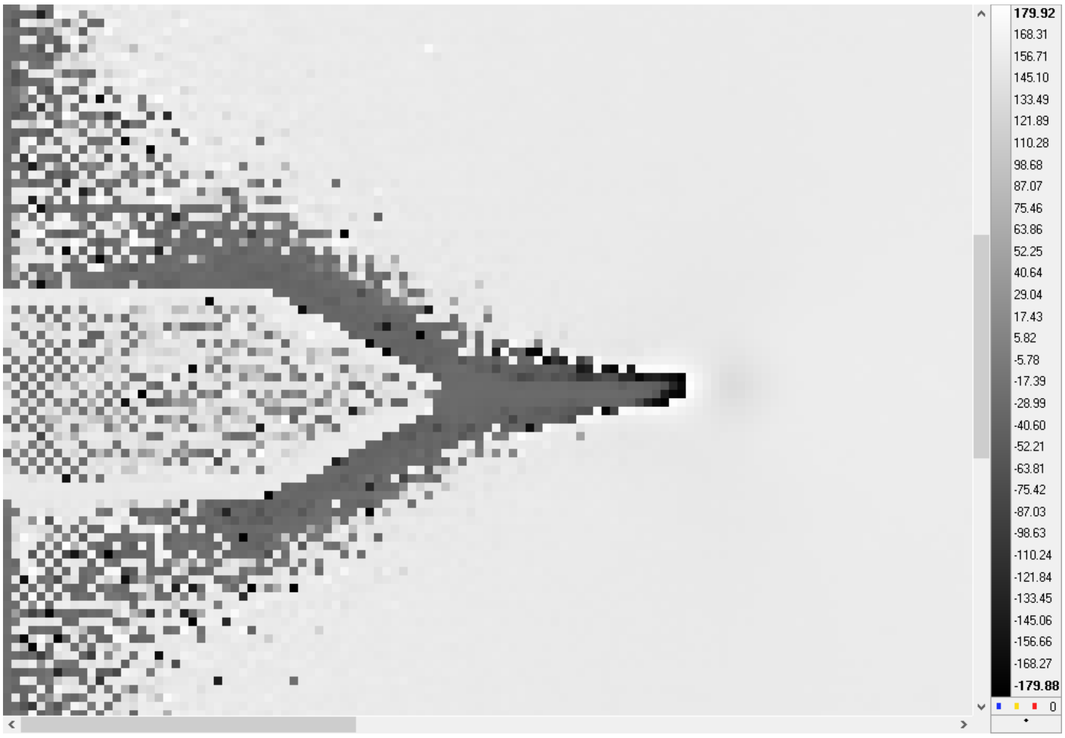

Figure 5.5. Typical photon detector phase image from the specimen loaded at constant load around the specimen crack.

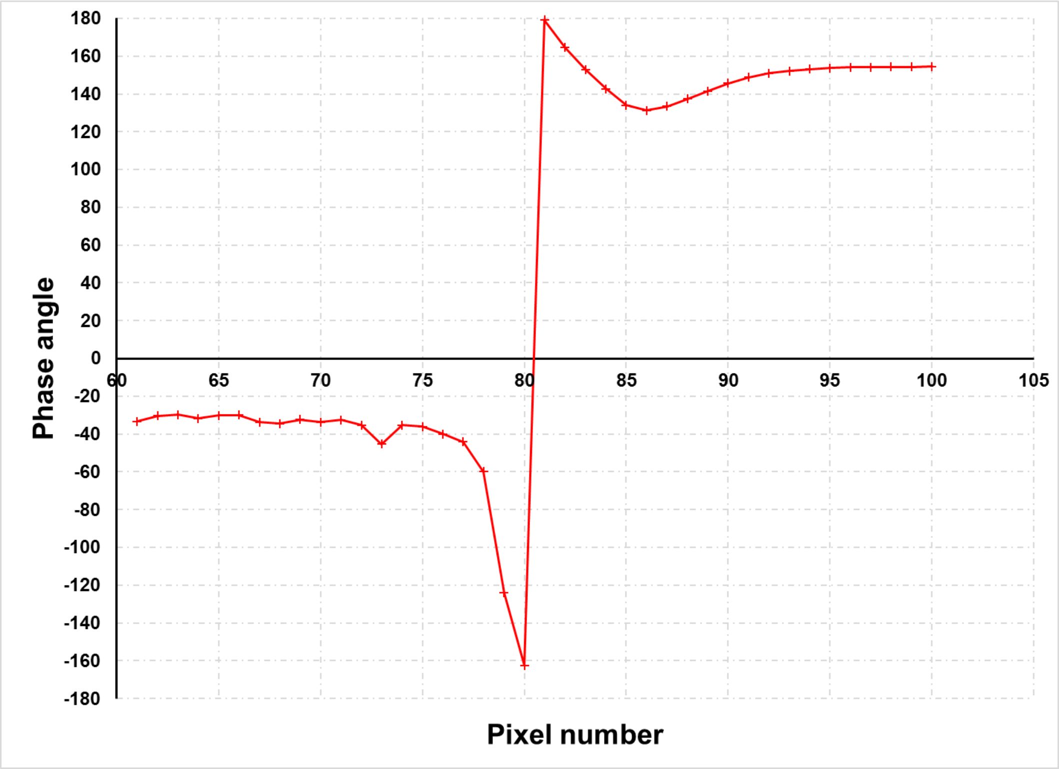

Figure 5.6. Profile showing the phase data along the horizontal line from the notch tip in Figure 5.7.

For the microbolometer, the embedded ResearchIR software was used to find the maximum temperature within a user defined region of interest and the related X and Y pixel coordinates for each image in the temporal sequence. The temporal sequence of maximum temperatures, and coordinates, were manually inspected to find the highest value. The coordinates of the highest maximum temperature within the sequence was defined as the crack tip location.

Figure 5.7 shows a typical temperature image recorded using the microbolometer viewing the rear of the specimen. It should be noted that the notch can be seen on the right of this image as this shows the mirror of the photon detector. The microbolometer also captures the warm housing of the photon detector in the background, the bright circular shape behind the specimen. The red box on the image represents the user selected region of interest which is scanned for the location of the maximum temperature. Figure 5.8 is a magnified view around the notch and crack, with an area of interest selected and the area statistics displayed with the maximum temperature and coordinates. In this image the maximum temperature is 23.8 °C, at pixel coordinates (380, 234). The width of the specimen is 50mm and there are 250 pixels across the specimen, therefore each pixel is 0.2mm wide. A temperature profile plot of area is displayed above the area of interest.

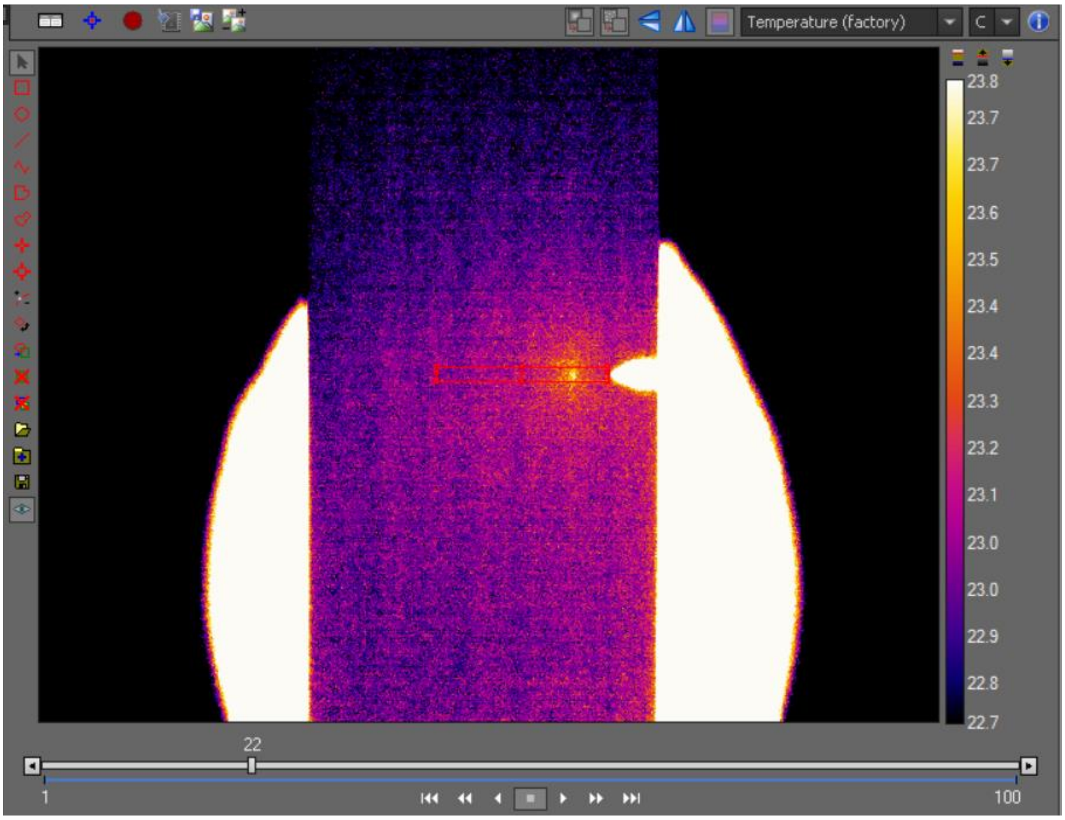

Figure 5.7. A typical Microbolometer temperature, T (°C) image around the specimen crack, also showing the user selected region of interest.

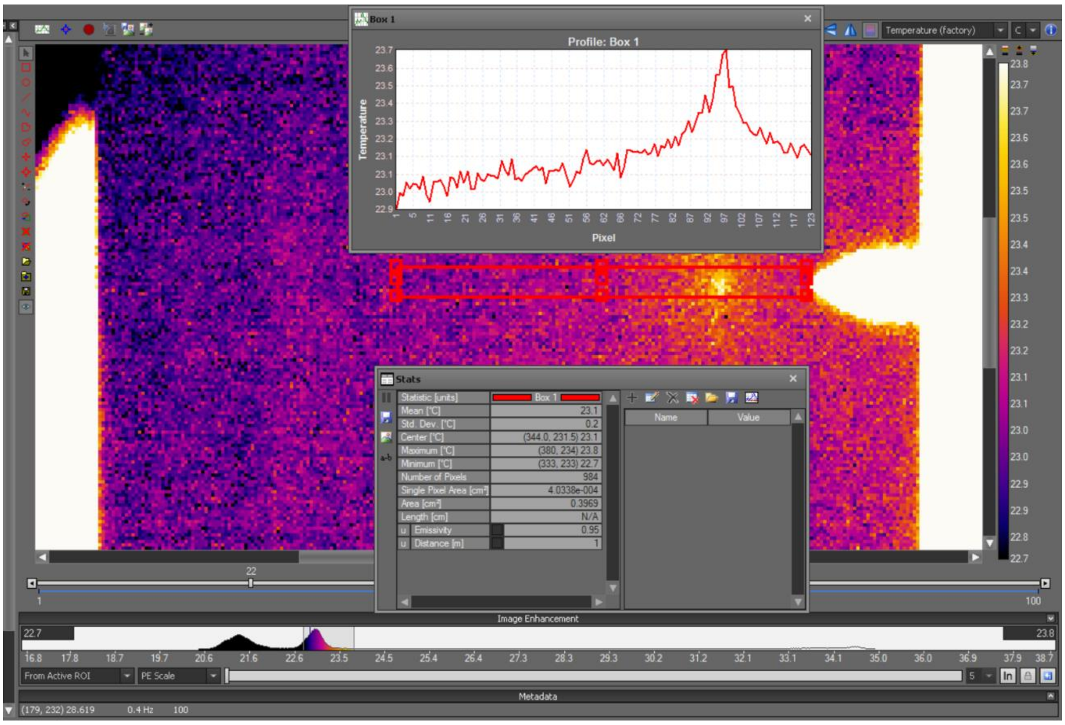

Stats

Statistic [units]	Box 1
Mean [°C]	23.1
Std. Dev. [°C]	0.2
Center [°C]	(344.0, 231.5) 23.1
Maximum [°C]	(380, 234) 23.8
Minimum [°C]	(333, 233) 22.7
Number of Pixels	984
Single Pixel Area [cm²]	4.0338e-004
Area [cm²]	0.3969
Length [cm]	N/A
u Emissivity	0.95
u Distance [m]	1

Figure 5.8. A magnified view of the microbolometer temperature (°C) around the specimen crack, with temperature profile and area statistics.

5.3 Results

In this section detailed results of the IR measurements, post processing, and analysis are presented for a crack growth specimen on a constant load test and a ‘simulated’ controlled growth test. In the figures presented in this section, there are three rows of images. The top row (1) presents the mean temperature (T_0) which are the images that may possibly be used to identify, characterise and quantify the temperature evolution for the test machine feedback and control. Row 2 images are the thermoelastic response (ΔT), post processed images. Finally, the bottom row (3) displays the phase data (Φ). From these sets of three images the maximum temperature and maximum ΔT locations are determined, and the phase crack length is measured. The post processed images in row 2 and 3 are also used for further analysis of the SIF throughout the crack growth experiment.

5.3.1 Constant load crack growth test

A SENT specimen (Specimen 1) was cyclically fatigued in load control at a constant load amplitude. The specimen was subjected to a mean load of 11.55 kN and an amplitude of +/- 9.45 kN, giving an R value of 0.1, and at a frequency of 10 Hz. The aim of this test was to determine how the temperature at the crack tip evolved throughout the test and investigate how controlling the temperature evolution would affect the crack growth rate, therefore the specimen was tested to failure. For this specimen only the photon detector was used to monitor and record the temperature data. 1000 frames were captured every 1000 test cycles.

Figures 5.9 & 5.10 present the three components of the IR data as they evolve during the test, where the temperature hot spot increases in temperature as it also changes location as the crack grows across the specimen during the test, due to the temperature emanating from the plastic deformation ahead of the crack tip. Figure 5.9 shows the IR data for the constant load test at 14,000 and 22,000 cycles, while Figure 5.10 shows the IR data for the same test at 33,000 and 39,000 cycles. These data points were selected to demonstrate how the progression of the crack effects the IR data, with the data at 39,000 cycles representing the final dataset before specimen failure. Table 5.1 lists the maximum T_0, ΔT and Φ values, with the associated pixel locations. For the detector setup in this test the spatial resolution is 0.135 mm/pixel. This was determined by dividing the known notch length, 7 mm, by the number of pixels between the edge of the specimen and the notch tip, 52 pixels. The pixel (0, 0) location is the top left hand corner of the image.

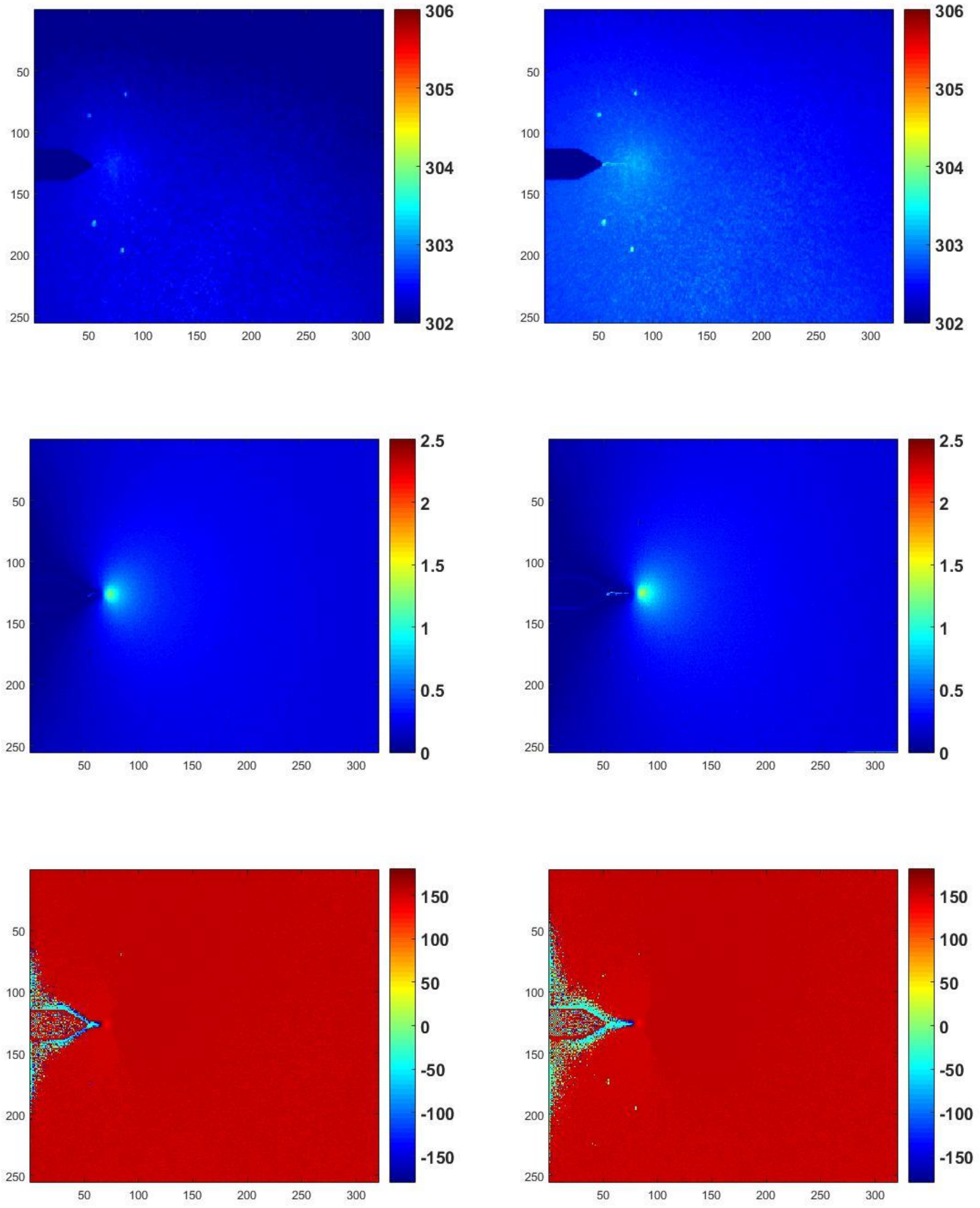

Figure 5.9. Constant load amplitude crack growth test IR component evolution at 14,000 (left hand images) and 22,000 cycles (right hand images). Row 1, T (K). Row 2, ΔT. Row 3, Φ.

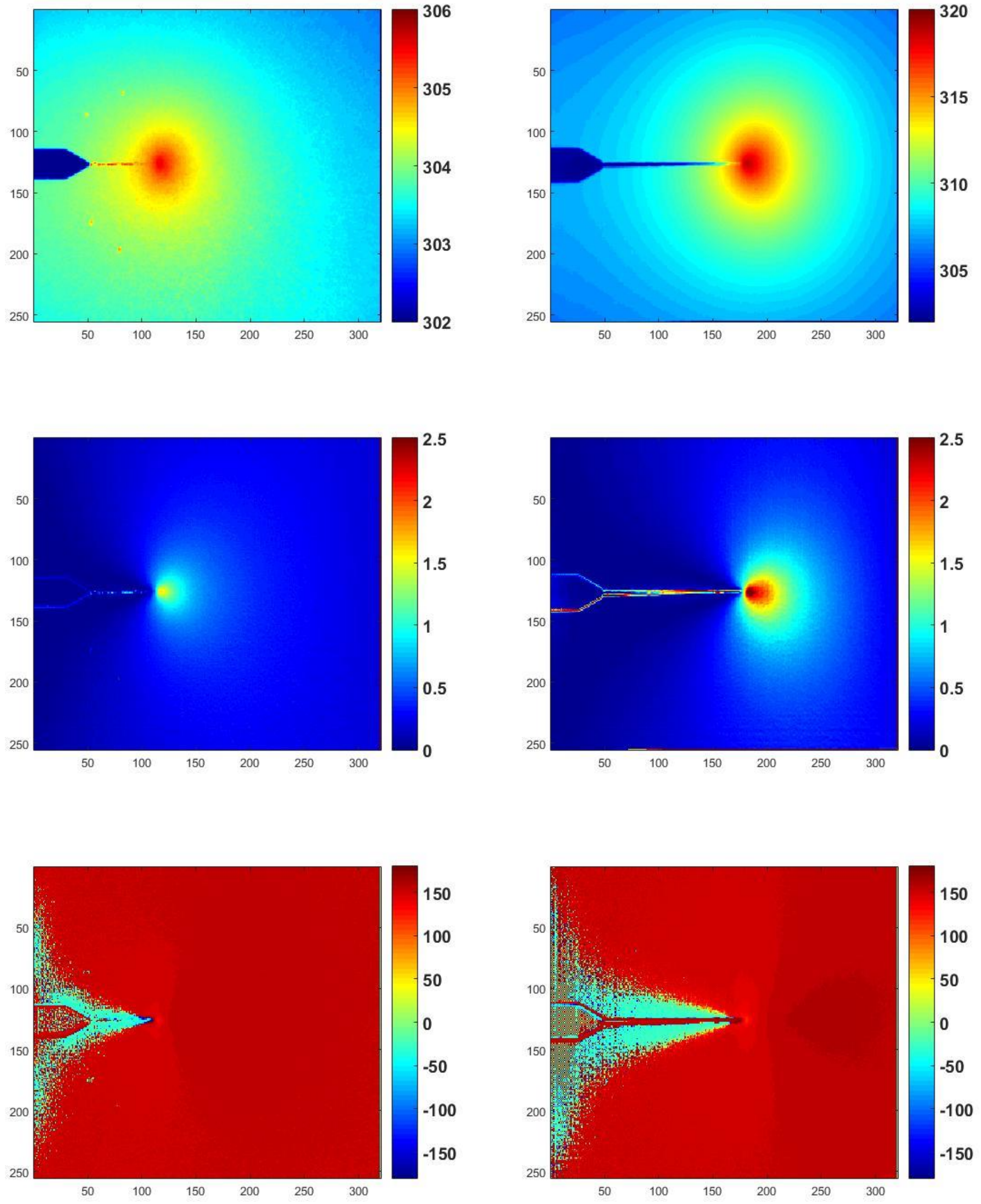

Figure 5.10. Constant load amplitude crack growth test IR component evolution at 33,000 (left hand images) and 39,000 cycles (right hand images). Row 1, T (K). Row 2, ΔT. Row 3, Φ. Note that the mean temperature scale has increased for the 39,000 cycle image.

Table 5.1. Constant load amplitude crack growth test data, Maximum T_0, ΔT, and $\Delta T/T$, with their pixel location, for each dataset.

Run	Cycle count	Crack tip location		Hotspot location					
		Phase		Temperature			Max ΔT location		
		X (px)	Y (px)	X (px)	Y (px)	Temp (°C)	X (px)	Y (px)	Temp (K)
1	500	54	126	56	126	28.51	60	126	1.11
2	1000	54	126	56	125	28.61	60	126	1.12
3	2000	55	126	58	127	28.69	60	125	1.15
4	3000	56	125	58	127	28.80	60	125	1.15
5	4000	56	125	58	127	28.91	62	125	1.17
6	5000	57	126	58	127	28.97	62	125	1.17
7	6000	58	126	58	128	29.02	63	125	1.16
8	7000	59	125	57	127	29.04	65	126	1.18
9	8000	60	125	57	127	29.16	66	125	1.22
10	9000	60	126	64	127	29.27	66	126	1.22
11	10000	61	125	66	128	29.29	68	126	1.22
12	11000	62	125	64	129	29.29	68	125	1.23
13	12000	64	126	72	125	29.39	70	125	1.23
14	13000	65	126	72	125	29.49	71	125	1.22
15	14000	66	126	72	125	29.57	73	126	1.24
16	15000	67	125	72	124	29.59	74	125	1.28
17	16000	69	125	72	124	29.71	75	125	1.30
18	17000	70	126	72	125	29.81	76	125	1.32
19	18000	72	125	74	126	29.84	79	124	1.29
20	19000	73	125	74	126	29.89	79	124	1.33
21	20000	75	125	74	126	30.00	82	125	1.29
22	21000	77	125	72	125	30.08	83	125	1.34
23	22000	78	125	81	125	30.10	85	125	1.35
24	23000	80	124	83	124	30.16	86	124	1.39
25	24000	82	125	90	127	30.30	88	125	1.37
26	25000	85	125	90	127	30.46	91	125	1.40
27	26000	87	125	90	127	30.61	94	125	1.41
28	27000	89	126	92	127	30.81	95	125	1.43
29	28000	92	126	96	126	30.93	98	125	1.49
30	29000	95	125	99	125	31.11	101	125	1.49
31	30000	98	125	103	126	31.30	104	125	1.52
32	31000	102	125	105	125	31.64	109	124	1.56
33	32000	106	125	110	125	31.98	112	125	1.57
34	33000	111	125	115	125	32.40	117	125	1.61
35	34000	117	124	121	124	32.85	123	123	1.68
36	35000	122	124	127	124	33.67	129	125	1.74
37	36000	130	124	134	124	34.63	136	124	1.81
38	37000	140	124	144	124	36.27	147	124	2.00
39	38000	155	124	158	124	39.13	161	124	2.13
40	39000	177	125	180	125	45.75	183	125	2.74

Monitoring the change in actuator displacement, via maximum and minimum actuator position, provides a simple measure of the progress of the crack growth and in particular indicates the point where the crack accelerates and growth becomes unstable. Figure 5.11 plots the evolution of the maximum and minimum actuator position, blue line and orange line respectively, with cycle count and clearly shows they diverge as the crack growth accelerates towards failure at cycle number 39,808. It was hypothesised that monitoring the value of the maximum temperature measured using the IR detector could provide a similar indication of crack growth instability and hence enable test control. The evolution of maximum temperature value, T_0, and maximum thermoelastic response, ΔT, are also plotted in Figure 5.11 represented by the red and yellow line respectively. It can be seen in Figure 5.11, that the maximum temperature closely follows the same trend as the change in maximum and minimum position, throughout the test. This suggests that as the damage growth rate increases, the crack tip temperature also increases, therefore suggesting that if the temperature can be monitored, and adjustments made to the loading to control the temperature evolution, and hence control the crack growth rate. The ΔT value also appears to follow the trend, but with a significantly reduced magnitude, it would be more difficult to discern changes to enable test machine control, and ΔT is a post-processed measurement, making it unsuitable. This hypothesis was further tested using the 'simulated' controlled crack growth (or load drop) experiment, with the results described in Section 5.3.2. The actuator position and temperature data plotted in Figure 5.11 was used to define the procedure for the load drop test. It was determined that there was a steady temperature increase rate until the maximum displacement increased by 0.01 mm, then the rate of change in temperature and maximum displacement increased. Therefore the load amplitude of the load drop test would be decreased when this change in maximum displacement had been achieved.

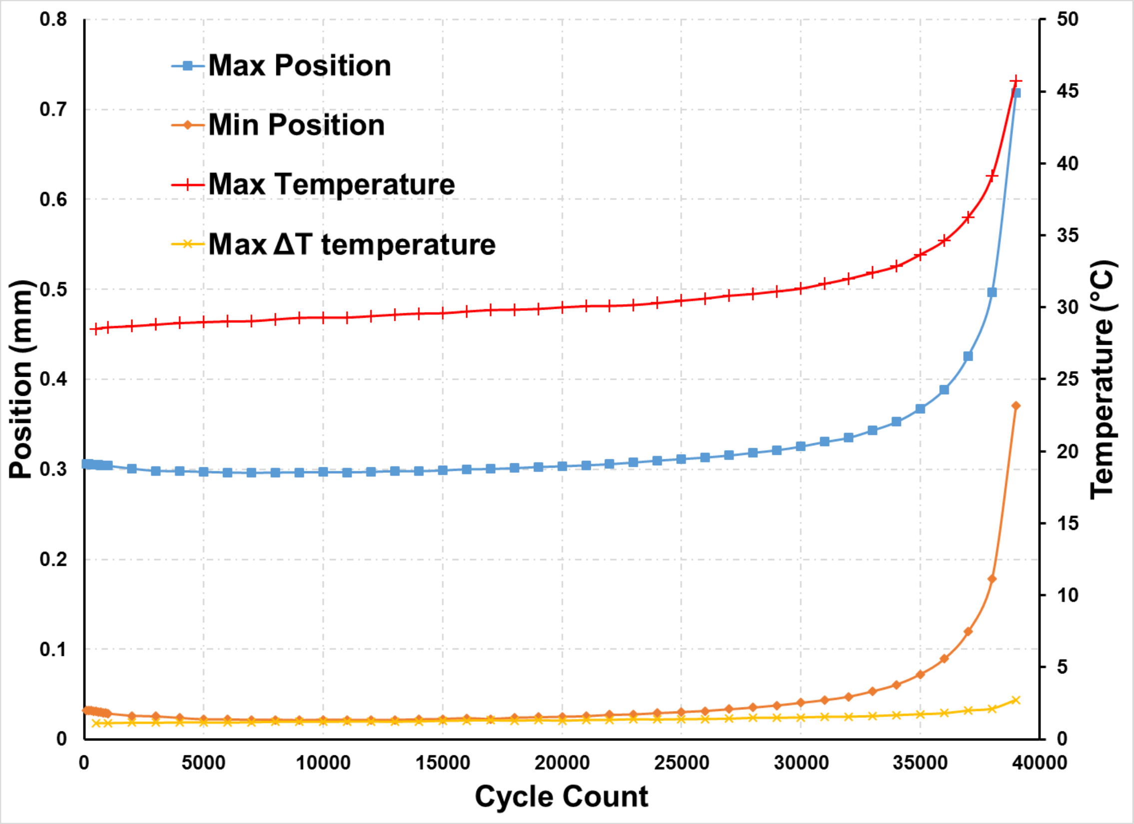

Figure 5.11. Plot showing the evolution of the maximum temperature, T_0 (℃) and maximum and minimum position (mm), with cycle count, for the constant load test.

The crack lengths at each cycle count were then determined using the three approaches described in Section 5.2.3, i.e. maximum temperature location, maximum ΔT location and phase change location. Figure 5.12 plots the increase in crack length with cycle count using the three approaches. All three approaches show a similar crack growth trend, there is a period of relatively steady growth until approximately 25,000 cycles, followed by an almost exponential growth until failure. The crack lengths determined through the phase and maximum ΔT are closely matched and show a clean crack progression, except for the offset caused by difference in the phenomenon that each approach relies on explained in Section 5.2.3. In particular, the maximum ΔT is located ahead of the crack tip in the plastic deformation zone. When the crack length, determined using the maximum temperature location approach, is compared with the other results, it was noted that there was not a steady change in position. This is particularly true in the early stages when the crack growth is small. This was determined to be due to the small changes in temperature at a steady crack growth rate. A smooth increase in temperature only occurred when the crack growth rate started to accelerate around 30,000 cycles and the change in temperature rate also increased.

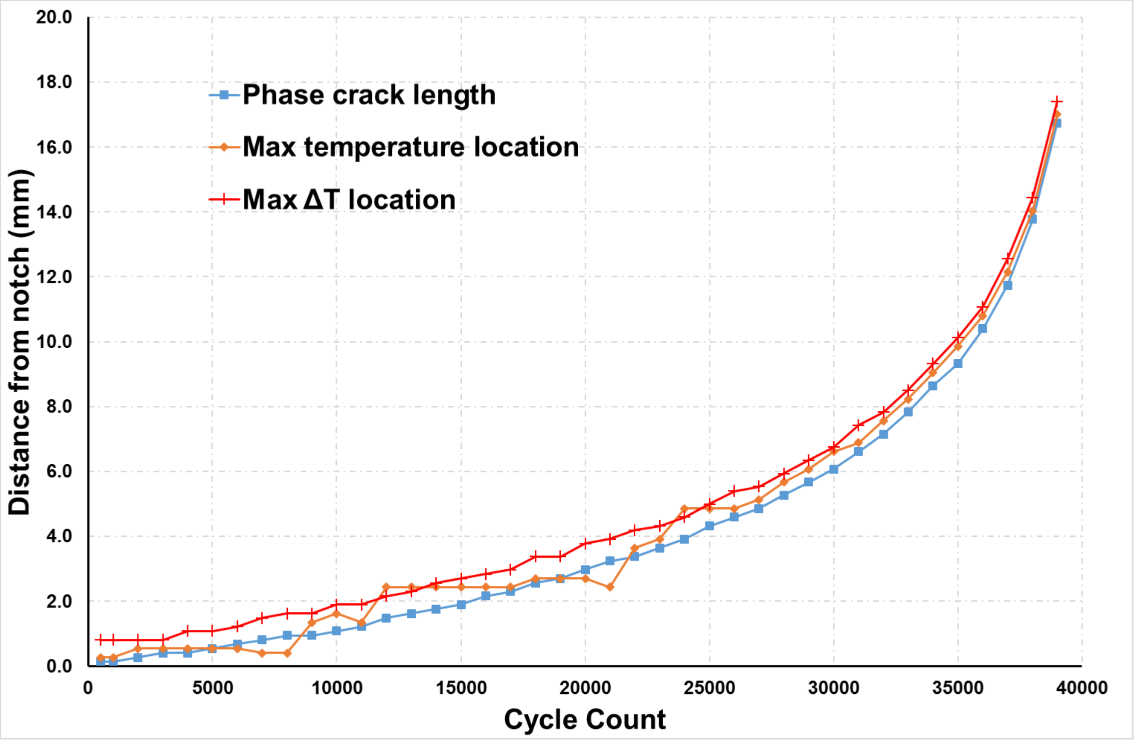

Figure 5.12. Plot showing the crack length evolution, using the three crack length measurement techniques, with cycle count, for the constant load test.

Finally, the crack lengths determined above and the thermoelastic data were used to calculate the SIF as per Section 4.2. Figure 5.13 plots the evolution of the SIF with cycle count for the three crack length approaches; phase, maximum temperature and maximum ΔT in blue, orange and red respectively, and using the thermoelastic response both above and below the crack in purple and green respectively. It can be seen in Figure 5.13, that there is good correlation between the SIFs calculated using all three crack length measurement techniques and the SIFs calculated using the TSA measurement technique, until 29,000 cycles. This is most likely due to the crack growth rate and temperature increase rate accelerating at this point and the assumptions for the suitability of the Westergaard equation no longer being valid. The Westergaard equation assumes linear elastic fracture mechanics and at 29,000 cycles there is a sudden acceleration of temperature generated at the crack tip, due to plastic deformation resulting in a non-adiabatic response.

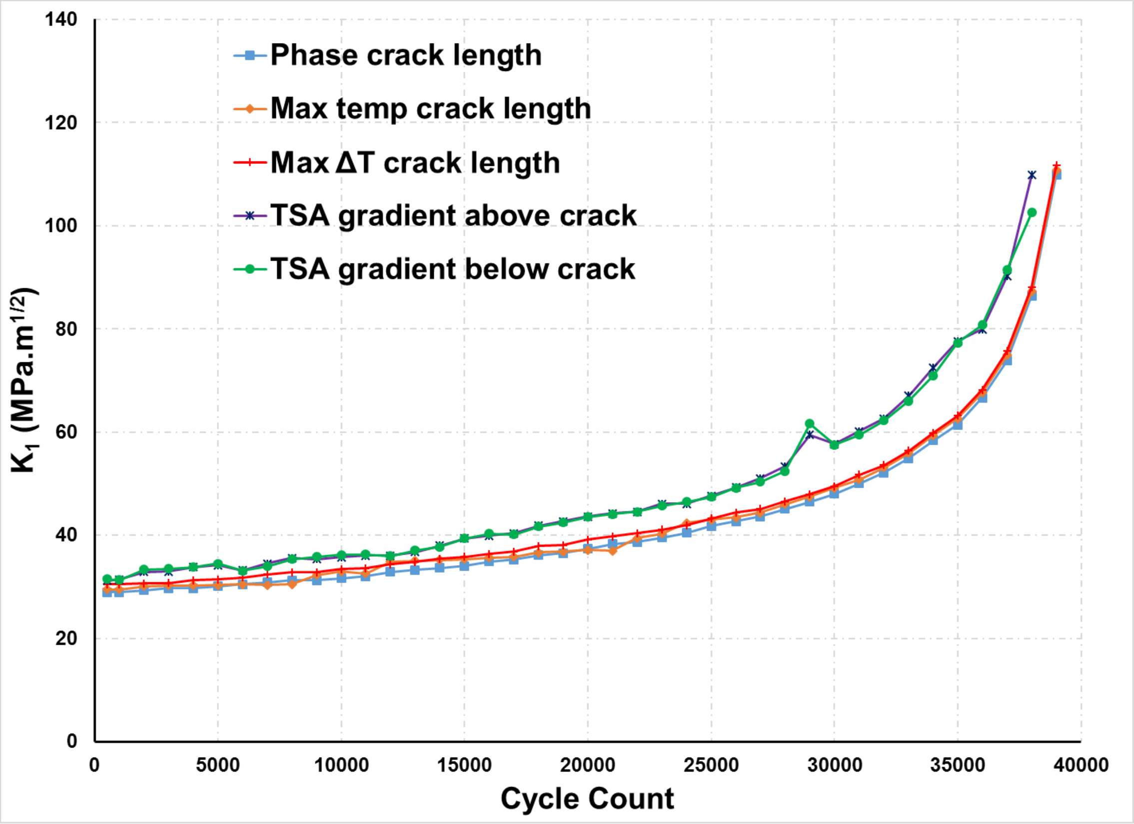

Figure 5.13. Plot of the evolution of SIF with cycle count calculated using the three crack length measurement techniques and from the thermoelastic response, for the constant load test.

Figure 5.14 plots the crack propagation rate, *da/dN*, and temperature evolution rate, *dT/dN*, against the change in stress intensity factor, ΔK, for the constant load test. Linear trend lines for both datasets are also included, with their corresponding equations. The trend line equations give the Paris law parameters *C* (axis intercept point) and *m* (gradient). For the *da/dN* plot;

- $C = 1.48\text{x}10^{-7}$
- $m = 1.20\text{x}10^{-7}$

and the *dT/dN* plot;

- $C = -1.12\text{x}10^{-4}$
- $m = 2.41\text{x}10^{-4}$

Whist it is expected that the intercept values would be different, it is encouraging to note that the rate of temperature evolution is greater than that of the rate of crack propagation. Therefore, suggesting that controlling the crack growth by monitoring the temperature at the crack tip would be easier than by optically monitoring the location of the crack tip, due to the larger changes during the test.

When the Paris law, da/dN against *ΔK*, is calculated and plotted in Figure 5.14 alongside *dT/dN*, despite the sparse data towards the end of the test, indications are there is a good correlation between both plots. The lack of data at the end of the test, where the rapidly growing crack leads to a change in *ΔK* of 8.013 to 26.096 across three data points, reinforces the need for damage evolution control. It should be noted here, that as the crack length is determined from the IR phase data, the minimum resolvable change in crack length is 0.132 mm or a single pixel, which explains some of the initial scatter at the start of the *da/dN* plot in Figure 5.14 as the crack length is changing by subpixel amounts.

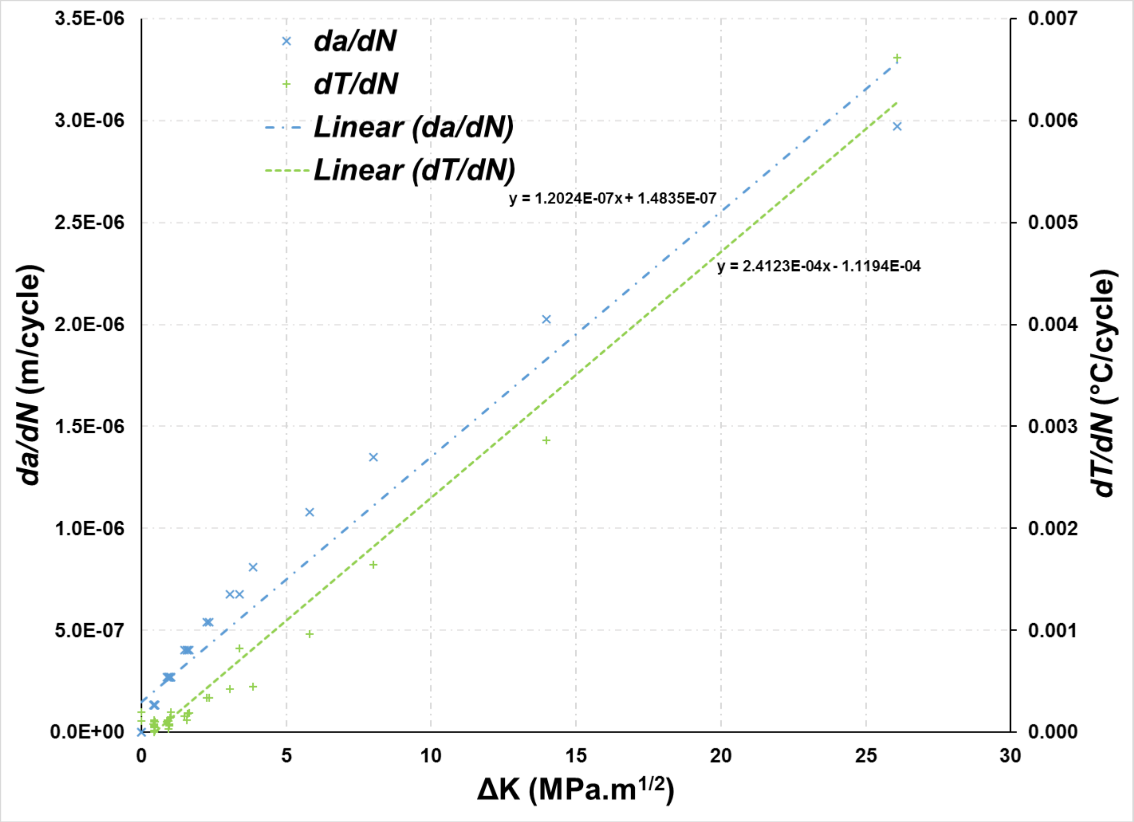

Figure 5.14. Plot of dT/dN and da/dN against ΔK for constant load test.

5.3.2 'Simulated' controlled crack growth test

Both IR detectors were positioned, and the recording parameters set as per section 4.3.2. The spatial resolution for the photon detector on this test was determined as 0.132 mm/pixel. For the microbolometer, there were 250 pixels across the specimen width of 50mm, therefore giving a spatial resolution of 0.2 mm/pixel.

A further SENT specimen (Specimen 2) was cyclically loaded with a stepped decreasing load amplitude to provide a quasi-controlled crack growth and enable an assessment of the influence of changing the maximum stress on the value of the maximum temperature at the crack tip measured using IRT. The point at which to reduce the load amplitude was an increase in the maximum displacement by 0.01 mm, as defined by the constant load amplitude test described in the previous section. 0.01 mm was chosen as it was the displacement at the point the temperature increase rate began to accelerate in the test data. When the change in displacement met the prescribed limit, the loading amplitude was reduced (the mean value remained the same). The specimen continued to be cyclically loaded without interruption. After 100 cycles at the new lower amplitude, a reference maximum displacement was recorded, and the displacement is again monitored for a 0.01 mm increase from the new reference value before a further reduction in load amplitude was applied. This process was repeated four times before the test was stopped. Table 5.2 shows the different mean load, and load amplitude applied during the tests, and the cycle numbers when each were applied. The specimen was initially subjected to a mean load of 11.55 kN and an amplitude of +/- 9.45 kN, giving an initial R value of 0.1, and at a frequency of 10 Hz. The frequency remained constant throughout the test, and the R value reduced.

Table 5.2. 'Simulated' controlled crack growth test, stepped decreasing load amplitude and corresponding cycle numbers.

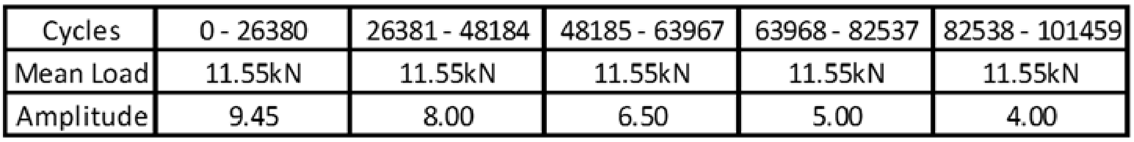

Cycles	0 - 26380	26381 - 48184	48185 - 63967	63968 - 82537	82538 - 101459
Mean Load	11.55kN	11.55kN	11.55kN	11.55kN	11.55kN
Amplitude	9.45	8.00	6.50	5.00	4.00

Tables 5.3 and 5.4 lists the maximum T_0, ΔT and phase values, and their pixel locations from the photon detector. The highlighted yellow rows are the first data points after the stepped load decrease. Table 5.5 shows the maximum T, location and value for the microbolometer for each recorded dataset.

Table 5.3. Data for ‘simulated’ controlled crack growth – Maximum T_0, ΔT, and ΔT/T, with their pixel location and crack length, for each recording run, Part 1.

Run	Cycle count	Crack tip location		Hotspot location					
		Phase		Temperature			ΔT		
		X (px)	Y (px)	X (px)	Y (px)	Temp (°C)	X (px)	Y (px)	Temp (K)
0	1000	54	131	55	130	18.42	56	131	1.19
1	2000	54	130	55	130	18.45	57	130	1.18
2	3000	54	130	55	130	18.51	58	129	1.18
3	4000	54	131	58	130	18.57	58	129	1.19
4	5000	54	131	58	130	18.69	59	129	1.20
5	6000	54	130	58	130	18.74	59	129	1.21
6	7000	55	131	58	130	18.83	60	130	1.23
7	8000	55	131	59	130	18.87	61	130	1.23
8	9000	56	130	59	129	18.94	62	130	1.25
9	10000	57	130	60	130	19.01	62	130	1.27
10	11000	58	130	61	129	19.06	64	129	1.27
11	12000	58	129	64	129	19.16	64	129	1.29
12	13000	59	130	66	131	19.15	65	129	1.30
13	14000	59	130	66	132	19.24	67	130	1.31
14	15000	60	130	66	131	19.26	67	129	1.37
15	16000	61	129	66	131	19.23	68	129	1.36
16	17000	63	129	67	131	19.25	70	129	1.35
17	18000	64	129	67	131	19.27	70	129	1.36
18	19000	65	129	70	131	19.28	72	129	1.42
19	20000	66	129	70	131	19.26	73	129	1.42
20	21000	67	129	71	129	19.27	74	129	1.40
21	22000	68	129	70	131	19.35	76	128	1.42
22	23000	70	129	74	131	19.41	77	130	1.42
23	24000	71	130	77	130	19.40	78	130	1.44
24	25000	72	129	78	128	19.62	80	130	1.44
25	26000	74	130	81	129	19.68	82	129	1.45
26	27000	75	129	81	128	19.32	82	129	1.31
27	28000	75	129	81	129	19.37	82	129	1.30
28	29000	76	130	81	129	19.35	83	129	1.30
29	30000	76	130	81	129	19.30	84	129	1.30
30	31000	77	129	81	129	19.26	84	129	1.30
31	32000	77	130	84	132	19.32	85	129	1.31
32	33000	77	130	84	132	19.34	86	130	1.32
33	34000	78	130	87	132	19.40	86	130	1.34
34	35000	79	129	89	129	19.47	88	129	1.35
35	36000	81	129	89	129	19.48	89	129	1.37
36	37000	82	129	89	130	19.55	90	129	1.39
37	38000	84	129	89	130	19.62	91	129	1.41
38	39000	85	129	89	129	19.58	92	128	1.44
39	40000	87	129	89	129	19.66	93	128	1.43
40	41000	89	129	92	129	19.74	95	129	1.46
41	42000	90	129	94	129	19.69	97	128	1.47
42	43000	92	129	96	129	19.74	99	128	1.48
43	44000	94	129	98	129	19.79	100	129	1.48
44	45000	95	129	100	129	19.95	102	129	1.50
45	46000	97	129	102	129	20.01	103	129	1.53
46	47000	99	129	103	129	20.08	106	128	1.56
47	48000	101	129	107	130	20.27	107	129	1.54
48	49000	102	129	107	130	19.73	109	129	1.34
49	50000	102	129	107	130	19.67	109	129	1.32
50	51000	103	129	107	130	19.60	110	128	1.36

Table 5.4. Data for 'simulated' controlled crack growth – Maximum T_0, ΔT, and $\Delta T/T$, with their pixel location and crack length, for each recording run, Part 2.

Run	Cycle count	Crack tip location		Hotspot location					
		Phase		Temperature			ΔT		
		X (px)	Y (px)	X (px)	Y (px)	Temp (°C)	X (px)	Y (px)	Temp (K)
51	52000	104	129	109	128	19.59	110	128	1.33
52	53000	104	129	109	128	19.56	111	129	1.34
53	54000	104	129	109	128	19.70	112	129	1.35
54	55000	104	129	109	128	19.72	112	129	1.36
55	56000	105	129	109	128	19.75	114	129	1.36
56	57000	106	129	116	129	19.85	115	129	1.39
57	58000	108	129	116	129	19.92	115	129	1.41
58	59000	110	129	116	129	20.01	117	129	1.42
59	60000	112	129	117	129	19.95	118	128	1.45
60	61000	113	129	119	129	20.02	120	129	1.47
61	62000	115	129	125	129	20.09	122	129	1.49
62	63000	117	128	125	128	20.06	123	129	1.51
63	64000	119	129	125	128	20.13	126	128	0.82
64	65000	119	129	125	129	19.73	126	128	1.24
65	66000	119	129	125	128	19.70	127	129	1.25
66	67000	119	129	125	129	19.69	127	129	1.25
67	68000	120	128	125	129	19.64	127	129	1.23
68	69000	120	129	125	129	19.74	127	129	1.23
69	70000	120	129	125	129	19.70	127	129	1.22
70	71000	120	129	125	129	19.71	128	129	1.21
71	72000	120	129	125	129	19.69	129	128	1.23
72	73000	121	129	125	129	19.74	130	129	1.24
73	74000	121	129	125	129	19.71	130	129	1.27
74	75000	121	129	129	128	19.69	131	129	1.28
75	76000	122	129	129	129	19.72	132	129	1.27
76	77000	125	129	134	130	19.79	134	129	1.27
77	78000	126	129	134	130	19.81	134	129	1.31
78	79000	127	129	134	130	19.71	136	129	1.34
79	80000	129	129	135	129	19.82	136	129	1.37
80	81000	130	129	135	129	19.90	138	129	1.36
81	82000	131	129	135	129	19.89	138	128	1.37
82	83000	131	129	135	129	19.74	139	128	1.13
83	84000	132	129	135	130	19.71	140	129	1.12
84	85000	132	129	135	130	19.72	140	128	1.12
85	86000	132	129	138	129	19.77	141	130	1.14
86	87000	133	129	138	129	19.77	141	130	1.15
87	88000	133	129	138	129	19.74	142	128	1.14
88	89000	133	129	139	129	19.83	142	128	1.15
89	90000	134	129	143	130	19.86	142	128	1.16
90	91000	135	128	144	130	19.79	143	128	1.17
91	92000	135	128	144	129	19.82	144	128	1.17
92	93000	136	128	144	130	19.90	145	128	1.20
93	94000	136	128	144	131	19.92	145	128	1.21
94	95000	138	128	144	131	19.86	146	128	1.20
95	96000	139	128	144	131	19.89	147	128	1.20
96	97000	139	128	144	131	19.91	148	128	1.20
97	98000	140	128	144	131	19.88	149	128	1.21
98	99000	141	128	144	131	19.90	149	128	1.23
99	100000	142	128	144	131	19.89	150	128	1.23
100	101000	144	128	144	131	19.88	151	129	1.23

Table 5.5. Data for 'simulated' controlled crack growth – Microbolometers maximum T, with pixel location and crack length, for each run.

Run	Cycle count	Hotspot location		
		Temperature		
		X (px)	Y (px)	Temp (°C)
1	1000	234	234	22.6
2	2000	236	234	22.8
3	3000	234	234	22.8
4	4000	236	234	23.0
5	5000	243	235	23.0
6	6000	234	234	23.2
7	7000	234	234	23.3
8	8000	234	234	22.9
9	9000	236	233	23.1
10	10000	238	231	23.2
11	11000	236	234	23.3
12	12000	238	231	23.2
13	13000	238	232	23.3
14	14000	240	231	23.4
15	15000	241	231	23.3
16	16000	247	235	23.4
17	17000	242	232	23.4
18	18000	242	232	23.3
19	19000	242	235	23.5
20	20000	247	231	23.5
21	21000	247	233	23.5
22	22000	246	231	23.5
23	23000	249	232	23.6
24	24000	250	231	23.5
25	25000	250	233	23.7
26	26000	250	232	23.9
27	27000	250	232	23.4
28	28000	251	234	23.3
29	29000	253	232	23.2
30	30000	250	232	23.3
31	31000	252	232	23.2
32	32000	253	232	23.1
33	33000	251	231	23.3
34	34000	254	232	23.3
35	35000	255	235	23.6
36	36000	255	235	23.6
37	37000	255	235	23.6
38	38000	257	235	23.5
39	39000	258	232	23.6
40	40000	259	232	23.9
41	41000	261	232	23.9
42	42000	261	232	24.0
43	43000	261	232	24.0
44	44000	265	232	23.9
45	45000	265	231	24.3
46	46000	265	232	24.3
47	47000	267	232	24.1
48	48000	268	232	24.3
49	49000	267	230	23.9
50	50000	267	230	23.7
51	51000	270	230	23.8
52	52000	270	231	23.7
53	53000	270	231	23.6
54	54000	270	231	23.8
55	55000	267	231	23.7
56	56000	270	232	23.9
57	57000	272	232	24.0
58	58000	272	232	23.8
59	59000	275	232	23.9
60	60000	274	232	24.0
61	61000	275	232	24.2
62	62000	276	232	24.0
63	63000	277	232	24.0
64	64000	278	232	24.1
65	65000	282	232	23.7
66	66000	279	233	23.6
67	67000	280	234	23.6
68	68000	281	232	23.7
69	69000	282	232	23.7
70	70000	282	232	23.5
71	71000	281	232	23.6
72	72000	281	232	23.7
73	73000	284	231	23.6
74	74000	282	230	23.8
75	75000	281	232	23.7
76	76000	285	232	23.8
77	77000	285	233	23.9
78	78000	286	234	24.0
79	79000	287	234	24.0
80	80000	287	231	23.8
81	81000	288	233	23.9
82	82000	289	231	23.8
83	83000	288	233	23.6
84	84000	288	233	23.6
85	85000	292	233	23.6
86	86000	290	232	23.5
87	87000	290	231	23.6
88	88000	289	233	23.6
89	89000	291	230	23.6
90	90000	291	232	23.7
91	91000	292	231	23.6
92	92000	292	230	23.6
93	93000	292	231	23.5
94	94000	294	231	23.7
95	95000	292	232	23.7
96	96000	293	232	23.9
97	97000	295	233	23.8
98	98000	296	232	23.9
99	99000	295	232	24.0
100	100000	296	233	23.9
101	101000	301	231	23.9

Figure 5.15 plots the evolution of the maximum temperature, from both the photon detector T_0 and microbolometer T, the maximum ΔT from the photon detector, and the maximum and minimum actuator position with cycle count. It should be noted at this point that the photon detector is out of calibration and was reading approximately 4 °C lower than the microbolometer. During this test two K type thermocouples were placed on either side of the specimen to confirm that both sides of the specimen were at the same temperature. The thermocouple readings taken, matched the microbolometer to the first decimal place. The detector were also checked against the blackbody used in Chapter 3, which confirmed the offset.

The maximum actuator position line shown in Figure 5.15 clearly shows the progress of the crack. There is an initial period of specimen stabilisation at the start of the test, then the position starts to increase as the crack length increases. Once the increase in position has reached the 0.01 mm limit set, and the maximum load and stress is reduced, the maximum position shows a significant, and immediate decrease. The new test parameters are allowed to stabilise before the new reference position is recorded. This is repeated for the other three load drops. It can be seen that there is a small acceleration where there is an increase in temperature change rate, measured by both the photon detector and microbolometer, just before each load drop, suggesting that the rapid temperature rate seen in the constant load test (Section 5.3.1) was about to occur. There is also a drop in temperature just after the decrease in the load amplitude which is expected due to the resulting reduced stresses. Whilst the microbolometer temperature follows the general trend of photon detector, there is a reasonable amount of noise, which masks the temperature drops towards the end of the test, when there are smaller changes in the load amplitude therefore making the temperature drops due to the load amplitude decrease, more difficult to discern at the last change. In general it can be noted that controlling the load amplitude, or maximum stress, permits a steady increase in maximum temperature ahead of the crack tip. The next stage is to review the crack growth rate behaviour, due to the test parameter changes.

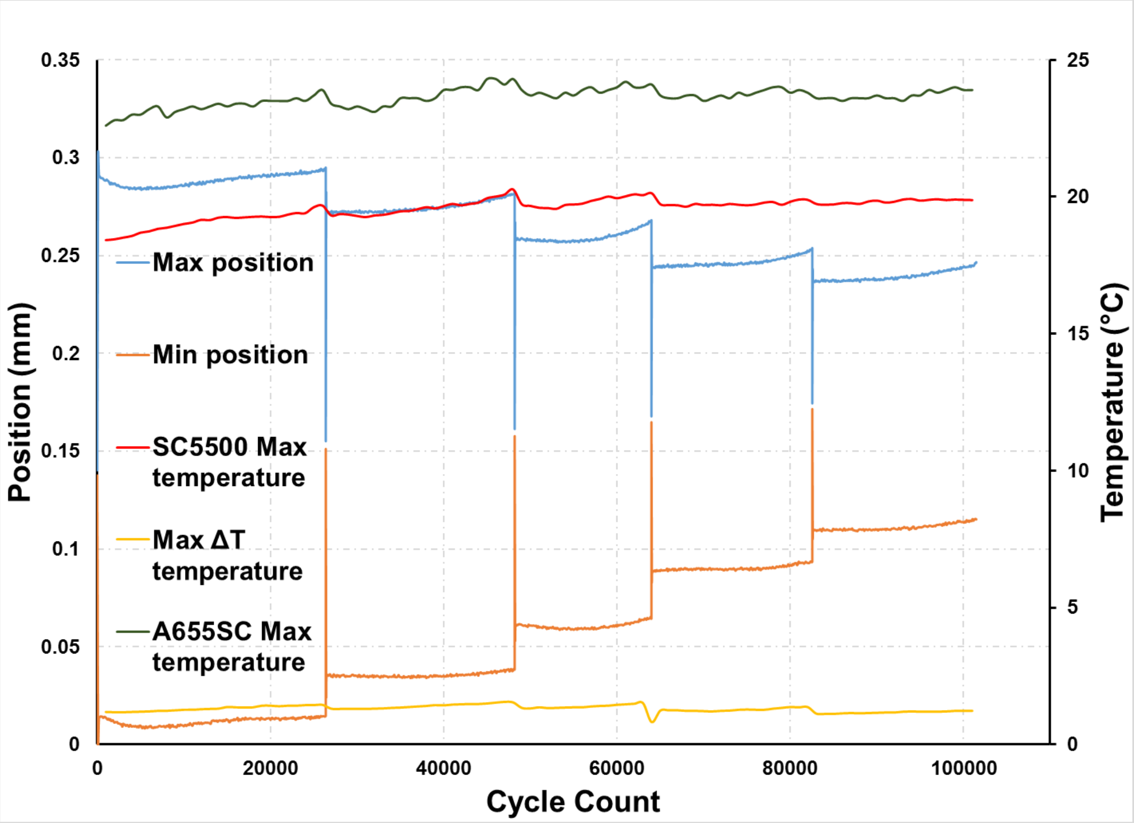

Figure 5.15. Plot showing the evolution of the maximum temperature (°C) and maximum and minimum position (mm), with cycle count, for the 'simulated' controlled crack growth test.

The crack length increase with cycle count are plotted in Figure 5.16, measured using the three approaches described in Section 5.2.1 and an additional measurement using the location of the maximum temperature recorded by the microbolometer. The figure shows the crack length growth rate is controlled and there is a general trend of a steady increase in crack length over the test duration, indicating that, although coarse, the load drops are helping to reduce the unstable crack growth seen for the constant load test case. As before, the phase measured length is the shortest, with the maximum temperature measurements registering consistently ahead of the crack tip, due to the plastic deformation. All of the photon detector measurement follow the same trend of an initial stable plateau at the start of the test and after each load amplitude decrease, before the measurements start to increase. The noise in the temperature data from the microbolometer seen in Figure 5.16 has a detrimental effect on determining the location of the crack tip using the hotspot. The hotspot tends to move around within the hotter region in front of the crack tip leading to scatter in the length measurement.

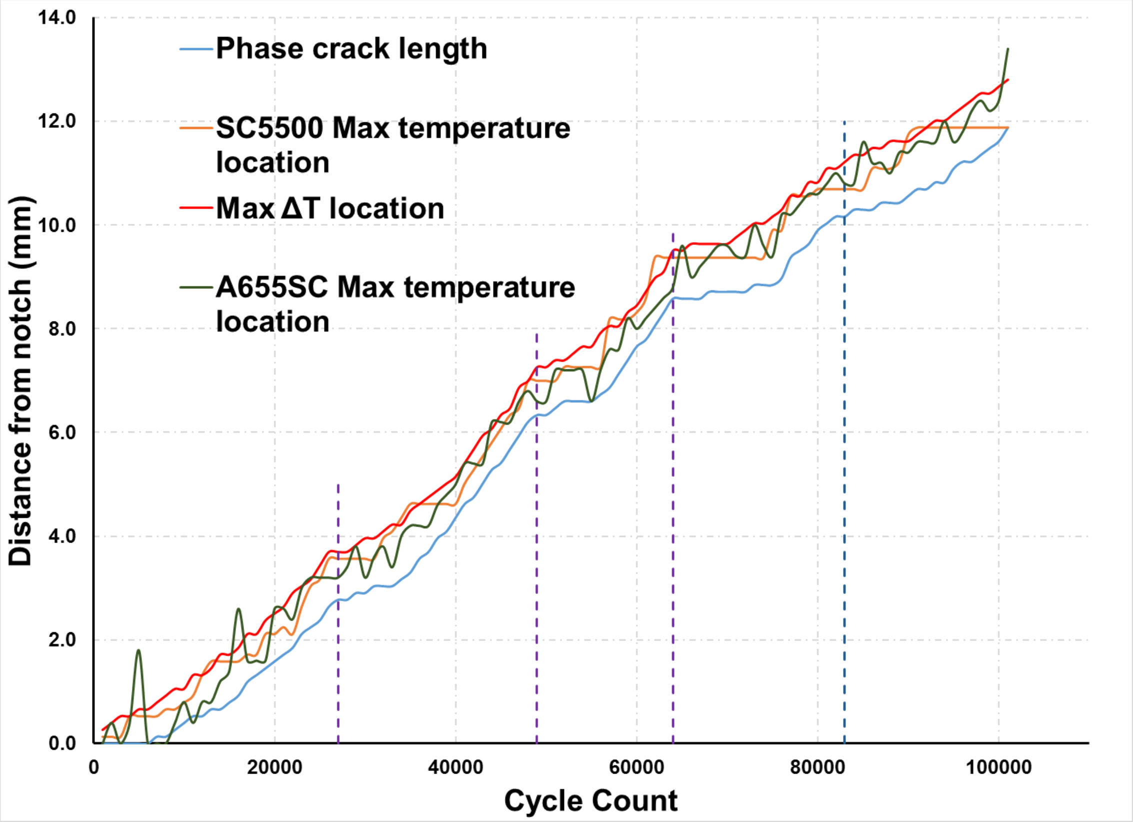

Figure 5.16. Plot showing the crack length evolution, using the three crack length measurement techniques, with cycle count, for the 'simulated' controlled crack growth test.

The evolution of K_I with cycle count is plotted in Figure 5.17 for each of the approaches to determine the crack length. Each of the change in load amplitude cause a sudden drop in the SIF, as expected from Equation 4.22, before it starts to increase again as the crack continues to grow. These drops in SIF also correspond to the drops in recorded maximum temperature shown in Figure 5.15. The drops in SIF and the plateauing of the crack growth rate is primarily due to the course control used in this experiment. When the position limit was reached, the control software moved to the next block with the lower load amplitude. It can be seen that the large load drops at the start of the test incurred the largest plateaus in the crack length and SIF, and the smaller drops at the end of the test incurred the smallest plateaus. This suggests that a large number of small changes in load amplitude/ maximum stress, would control the crack growth rate and temperature increase rate, more smoothly than large changes.

Overall, there is a relatively steady increase in crack growth and SIF throughout the test. Therefore it can be concluded that the crack growth rate in a SENT specimen, may be controlled using the temperature increase rate or the temperature hotspot location.

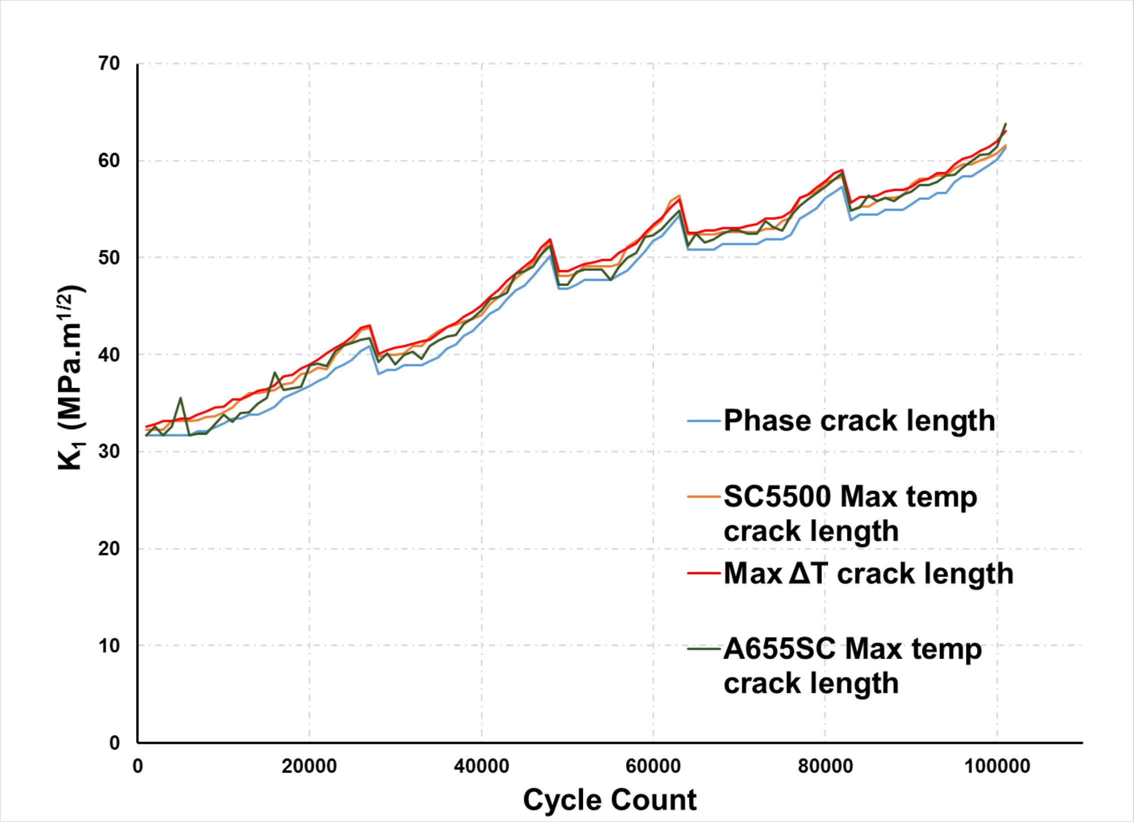

Figure 5.17. Plot of the evolution of SIF with cycle count calculated using the three crack length measurement techniques for the 'simulated' controlled crack growth test.

5.4 Summary

The crack growth in the SENT specimen subjected to cyclic load at a constant load amplitude responded as expected. There was a steady crack growth until accelerating just before total failure, which is mirrored by the increase in maximum actuator position. It was of interest to note that the maximum temperature recorded at the crack tip followed the displacement. The post processed ΔT started to increase at a similar point to the measures, but increased at a much slower rate. Comparing the crack length determined using the phase change and those determined by the hotspot location, it was noted that the phase and maximum ΔT were able to follow the smooth growth of the crack, whereas the T_0 hotspot, did not follow the progression of the crack as smoothly. This suggests that the T_0 hotspot may be detecting frictional heating between the crack surfaces, away from the crack tip.

The SIF was then calculated using the crack lengths obtained by the three the different approaches, described in Section 5.2.1 and using the thermoelastic response as per [89], where it again behaved as expected for a specimen cyclically loaded at a constant load amplitude, in that the SIF increased as the crack length grew. The only exception was to the TSA measured SIF after 29,000 cycles, where the calculated values diverge from the other values. At this point the crack growth rate increased rapidly, along with the temperature, suggesting that there was a significant amount of plastic deformation ahead of the crack tip. As the TSA SIF calculations use the Westergaard equation, which assumes linear elastic behaviour, the deviation from the crack length measured calculations, was to be expected.

For the 'Simulated' controlled crack growth test, with the stepped decreasing load amplitude, it was shown that changing the maximum stress on a specimen affects the temperature increase rate, and the crack growth rate, as expected. In this instance a change in the maximum displacement was used to control the change in load amplitude.

The work in this chapter has demonstrated that IRT has the potential for test machine control with a metallic crack growth specimen. In the next chapter the feasibility of using IRT to detect, monitor and control damage evolution in a composite material is investigated.

Chapter 6 Assessment of damage evolution in Fibre Reinforced Polymer Composites

6.1 Introduction

In chapter 5, it was shown that the temperature hotspot ahead of a crack tip in a metallic test specimen, can be identified and tracked as the crack grows during fatigue loading. One of the objectives of this research is to confirm that an IR detector has the fidelity to detect and monitor damage evolution in composite specimens during fatigue loading. Therefore it is important to assess the use of IRT to monitor the temperature change associated with damage evolution within a composite material. The temperature evolution that occurs in a composite specimen as the damage progresses is sufficient to be detected by both a bolometer and a photon detector. Using the same approach as that applied to the metallic tests in Chapter 5, the temperature response of the composite specimens is captured using IRT and is post-processed to provide TSA data. The thermoelastic response is proportional to stresses and enables the stress redistribution due to damage to be visualised and quantified.

A study by Emery *et al* [6], into the application of TSA to study damage within glass reinforced polymers, shows that TSA can evaluate fibre breakage, matrix cracking and delamination damage. However, the specimens were tested in interrupted steps, where each step included a constant displacement cyclic load for the TSA recording (within the specimens elastic loading region, to prevent damage growth) and then fatigue loading at a higher load than the TSA, for 3000 cycles, in load control, to create damage. It was shown that the damage evolution within the different types of specimen, creating the desired damage mechanisms, was detectable using TSA. Interrupting a fatigue test, to conduct TSA recording or damage inspection, disrupts the temperature evolution due to damage, allowing the specimen to cool, changing the mechanics of the damage evolution. Composite materials are sensitive to temperature increases, so allowing the specimens temperature to fluctuate may cause other material degradation processes. Therefore, the work described in the present chapter will demonstrate that useful data can be obtained from IRT when the specimens are subjected to continuous cyclic loading, preventing the general heating and cooling cycles when the test is stopped.

The work described in this chapter considers damage growth in two different laminate configurations of glass reinforced epoxy specimen. A layup of $(0, 90)_{3S}$ was manufactured, from which on-axis, cross-ply, specimens were machined, generating progressive defects through the fatigue cycle, i.e. matrix cracking, longitudinal splitting, delamination and finally fibre breakage. The second type of specimen was cut at 45° to the fibre directions, in order to generate internal shear damage. The specimens were fatigue tested to failure under a sinusoidal, load-controlled waveform, at a load ratio of R=0.1, during which full-field temperature maps were captured using IR detectors. Additionally, two types of specimen geometry were used, an open hole tension (OHT) specimen and an un-notched rectangular specimen. The OHT specimen localises the region of damage growth, and failure, in a similar way to the metallic SENT specimen used in Chapter 5. This enabled the IR detector, and post-processing, to focus on a smaller region of interest. The fatigue tests on the OHT were initially observed from a single side using only the photon detector, and then further tests used both the photon detector and microbolometer, in the “back to back” experimental set-up. Finally, the “back to back” setup was applied to the plain rectangular specimens to ascertain if IRT could monitor, and measure, damage growth in a sample without a specific damage initiator.

To visually monitor the damage evolution it has been shown that using glass fibre, permits some visual indication of damage area. E-glass specimens have been visually monitored for damage evolution [6] [97], along with S-glass [98]. This allowed the comparison of the visual inspection with the IRT and TSA images for specimens where IRT was only applied to one surface. However where the “back to back” approach was used both surfaces were painted and therefore the visual inspection was not possible.

The test specimen design, experimental arrangement, results from the two specimen types and designs, and a discussion on the relationship between the damage type (from the TSA) and temperature changes measured during damage evolution from the composite specimens.

6.2 Test specimen design

The test specimen had to meet the following design criteria:

- one specimen type to permit internal damage evolution
- one specimen type to have visible surface damage evolution
- concentrate damage evolution in a localised area
- permit a visual inspection of the damage evolution
- fit into an Instron 100 kN servo-hydraulic test machine

It is possible to control the damage location and type in a composite specimen, by selecting certain fibre orientation and ply lay-ups. Previous studies have shown that IRT can be used to detect matrix disbonding and delaminations during fatigue tests on specimens with a (+/-45°) fibre lay-up [99], that matrix cracking is the dominant failure mechanism [6] and that it is possible to use the specimen to identify three stages during fatigue testing [100]. It should be noted that this study is focused on the third stage and damage evolution. The three stages are:

1. A thermoelastic response occurs from the undamaged specimen and the surface temperature of the specimen is at its lowest
2. Small micro-damages occurs in the matrix material and the stresses start to redistribute as the regions start to lose their load carrying capacity
3. The specimen temperature increases due to damage growth and failure.

Visible surface damage evolution can be created by using a lay-up of (0°, 90°). It has been shown [98] that axial cracks and delaminations form during tensile testing, that the specimen fractures orthogonal to the tension axis with 0° fibre failures [99] and that there is axial cracking of the matrix, with internal matrix cracking and delaminations [6].

Composite specimens have a predilection for failure close to the gripped ends of the specimen, unless there is some form of stress concentration, such as manufacturing voids and defects within the composite or artificial concentrations such as tapers, notches and holes. The manufacturing defect locations are difficult to determine, therefore it was decided that the IRT approach would first be assessed on samples with a machined circular hole to create a stress concentration that localises the on-set of damage. Although IRT is a full field monitoring technique, which has the ability to monitor the whole specimen, to improve the resolution of the IRT images, it was decided to focus just on a smaller region of interest local to the hole, with the photon detector [98], [101]. However the full gauge section was observed with the microbolometer [99].

As mentioned in the introduction, it was decided that glass-fibre material should be used. As autoclaved pre-preg material provides the highest quality final product with the least voids and most reproducible material properties it was decided to manufacture the specimens using this approach. Unidirectional glass pre-preg is not used extensively in industry hence choice is limited. A suitable low cost material was identified: E-glass fibre (1062) pre-impregnated with a MTM28-1 resin system material suitable for autoclave consolidation. The manufacturer's designation code for the material is MTM28-1/1062-200-32%RW.

The final consideration was the size of the specimen to fit within an Instron 100 kN test machine. As standard a servo hydraulic test machine has a gripping arrangement that can accept a 50 mm wide specimen and a gripping depth of 50 mm. Generally, the maximum size of specimen would be 300 mm total length (the maximum roll width of the MTM28-1), resulting in 50 mm of grip length at each end and a 200 mm gauge length (distance between the grips). To accommodate the +/- 45 specimens and have a consistent specimen length, a specimen length of 250 mm was used. The width of the specimen is based upon the British standard BS ISO 12817 [26] and BS ISO 14603 [102] for open hole compression of fibre-reinforced plastic composites and open hole tension of continuous fibre ceramic matrix. Both standards use a width ratio of 6d, d being the diameter of the hole, they also suggest a hole diameter of 6 mm, giving a specimen width of 36 mm. A specimen diagram with fibre orientations, can be seen in Figure 6.1. For ease of manufacture, the unnotched specimens used the same specimen geometry, without the drilled hole.

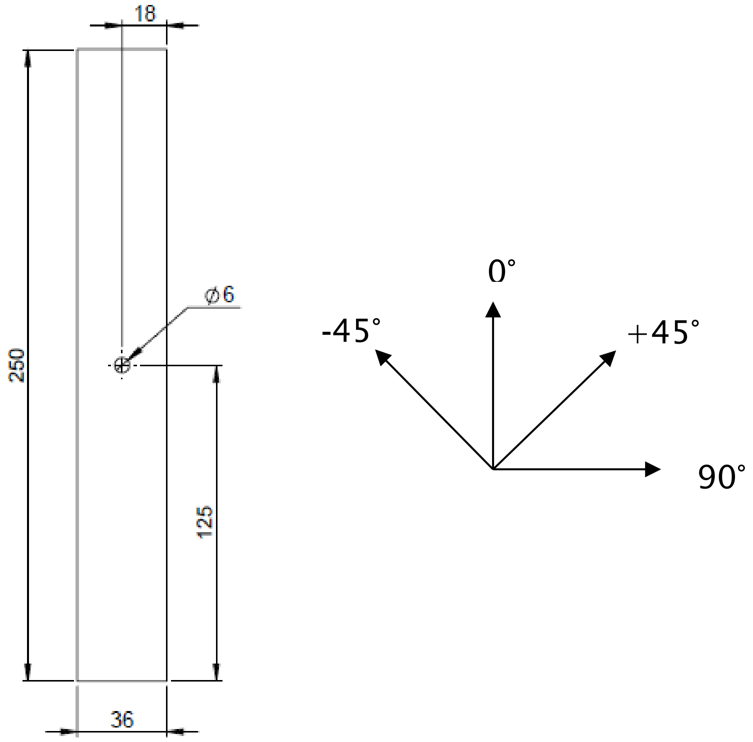

Figure 6.1. Dimensioned drawing of the composite open hole specimen and fibre orientation.

Specimen thickness was an important consideration as the detection of internal damage using IRT becomes more challenging with increasing thickness. It was decided that a 12 ply stacking sequence would be used, giving an approximate thickness of 1.8 mm. Each ply when cured and consolidated, is approximately 0.15 mm thick. This was based on [6], where 13 plies were used successfully for IRT monitoring. Therefore the two laminate stacking sequences chosen are: $(0, 90)_{3S}$ and $(+/-45)_{3S}$.

6.3 Experimental arrangement

The open hole specimens were installed directly into the test machine without the use of bonded end tabs. End tabs are usually bonded onto the gripping area of composite specimens to minimise the stress concentrations when they are clamped in the grips. The concentrations are usually due to serrations on the grip surfaces.

The grips for the machine used for this study were inspected and found to have a knurled gripping surface, rather than serrated teeth. A (0/90) unnotched material offcut was subjected to a quasi-static tensile test to failure, to check that the grips did not initiate specimen damage. The specimen failed away from the grips, towards the centre of the specimen and therefore it was not necessary to bond end tabs to the open hole specimens. End tabs were applied to the unnotched specimens subjected to fatigue loading, as it is known that the cyclic loads can cause premature failure issues at the point of gripping. All end tabs were manufactured from the offcuts of the (+/- 45) specimens, 50mm long and 36 mm wide. An image of the (0, 90) specimens with drilled holes, is shown in Figure 6.2.

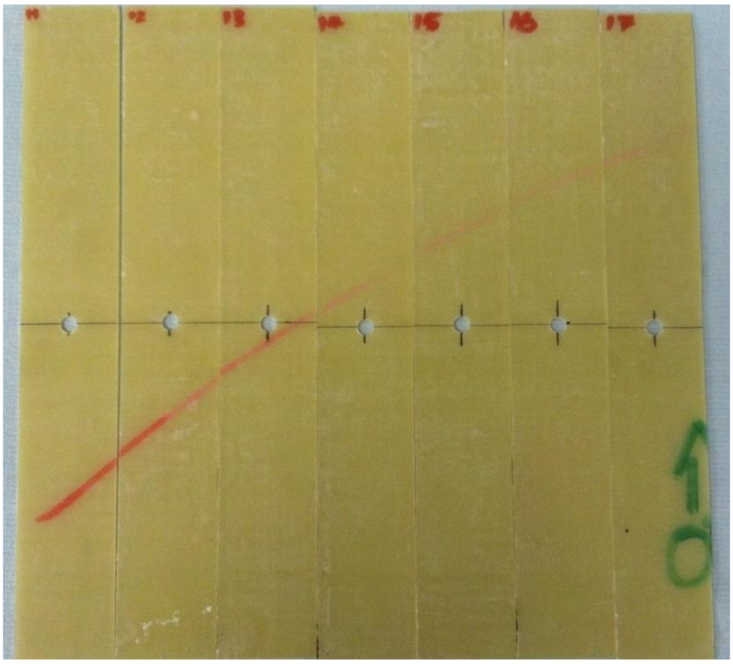

Figure 6.2. (0, 90) specimens after machining and hole drilling.

All specimens were measured for width and thickness using a digital calliper at three points along the specimens gauge length and then averaged. Before the specimens were tested the observed surfaces of the specimens were sprayed with matt black paint to provide a uniform emissivity for the IRT. Due to the roughness of the surface of the specimens, caused by the imprint from the peel ply during manufacture, the paint thickness could not be measured. Peel ply was applied to both sides of the laminate to ensure that the detectors were observing the same surface finish. A typical test setup is shown in Figure 6.3.

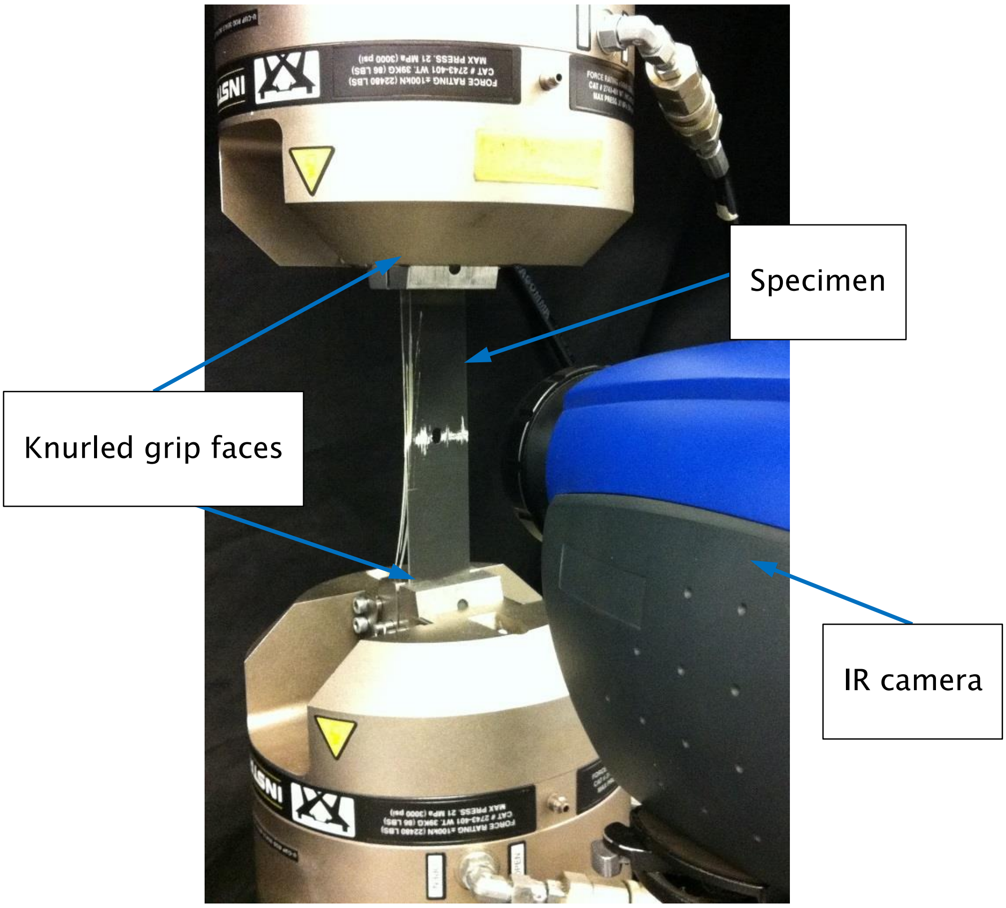

Figure 6.3. Typical test set-up for composite specimens.

6.4 Using a photon detector to monitor/measure the damage growth in an OHT specimen

6.4.1 Specimen dimensions

Table 6.1 presents the specimens gross cross sectional areas (CSA), for the quasi-static test specimens and fatigue specimen monitored with the photon detector.

Table 6.1. Batch one composite specimen dimensions.

Specimen Identification	Specimen type	Test configuration	Width (mm)	Thickness (mm)	Gross CSA (mm^2)
A	+/-45°	Quasi-static	36.06	1.81	65.15
B	+/-45°	Fatigue	36.20	1.81	65.65
C	0/90°	Quasi-static	36.05	1.76	63.45
D	0/90°	Fatigue	36.30	1.78	64.50

6.4.2 Quasi-static testing

One OHT specimen of each layup type were tested quasi-statically to obtain the ultimate tensile stress (UTS) of each type of specimen. Both specimen types were subjected to a tensile ramp rate of 2 mm/min until failure, whilst the FLIR SC5500 photon detector captured images of the front surface at a frame rate of 10 Hz for the duration of the test. The results of the quasi-static testing of both specimen types are shown in Figure 6.4. Figure 6.4 marks the detector recording points shown in Figure 6.5 and Figure 6.7. The off-axis specimen, (+/-45), demonstrates significantly more compliance than the on-axis specimen, (0, 90). This indicates the damage evolution within a (+/-45) specimen slowly evolves and requires more than 10 mm extension to failure, which allows more time for monitoring and feedback. In contrast the test on the (0, 90) specimen type shows a linear response to a brittle failure and the damage evolved to failure within an extension of 2 mm. The UTS for the (+/-45) specimen was 168.5 MPa and for (0, 90) specimen, 277.8 MPa. The area used to calculate the stress was the net CSA (the gross CSA minus the hole CSA).

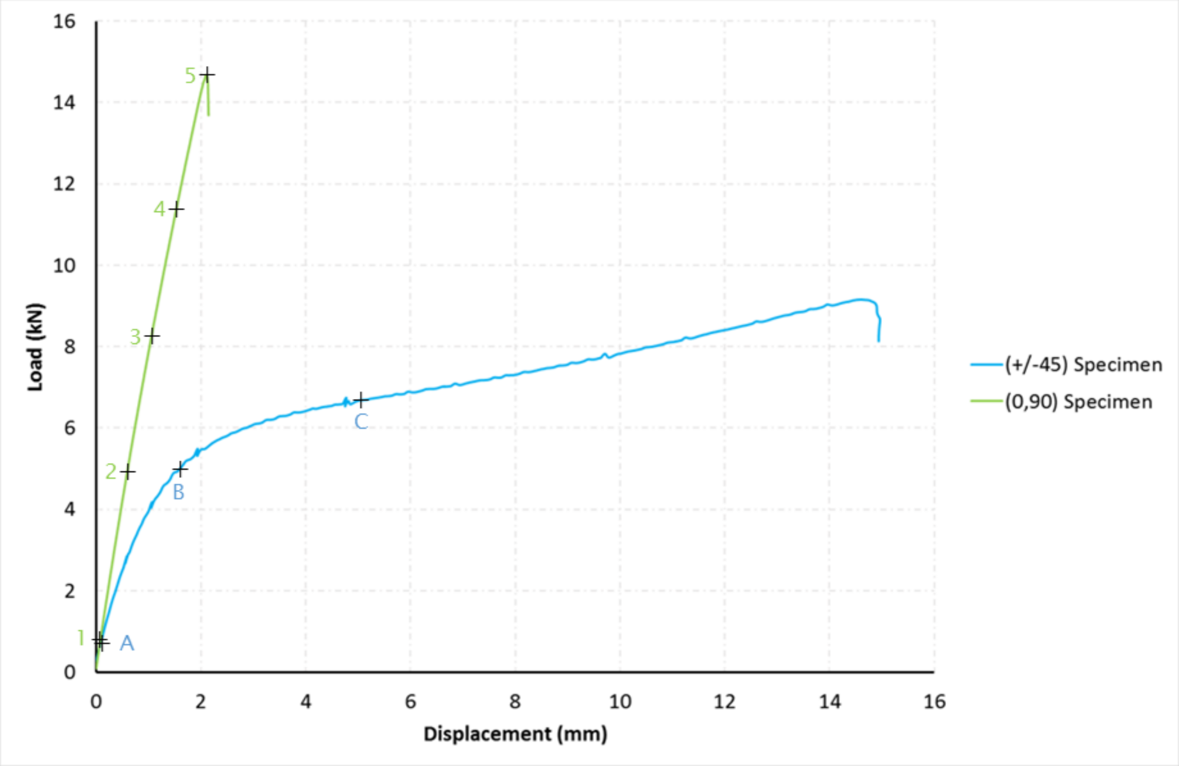

Figure 6.4. Load vs displacement for both specimen types, during quasi-static testing.

Figure 6.5 presents the full-field temperature images from the quasi-static test on a (0, 90) specimen at selected loads as the damage evolves. There is a clearly identifiable temperature increase during testing as the damage evolves In the first image, there are temperature increases at the hole in the 2 and 8 o’clock positions. The second image shows the damage evolves from right hand side (RHS) of the hole first, followed by the left hand side (third image). The damage then grows together on both sides of the specimen (fourth image) until failure (final image). Photographs of the failed specimen are provided Figure 6.6.

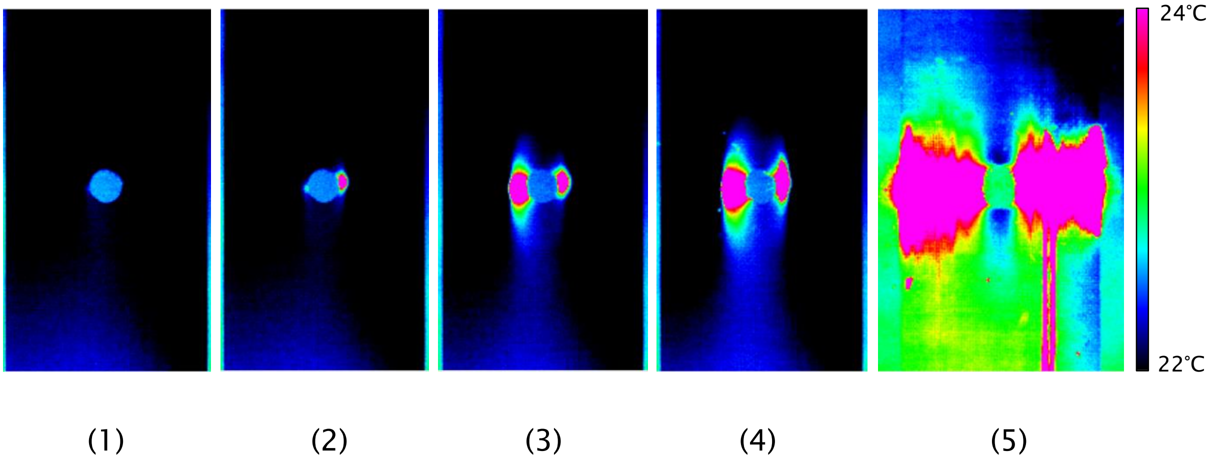

Figure 6.5. Temperature evolution (°C) in (0, 90) Specimen during quasi-static testing.

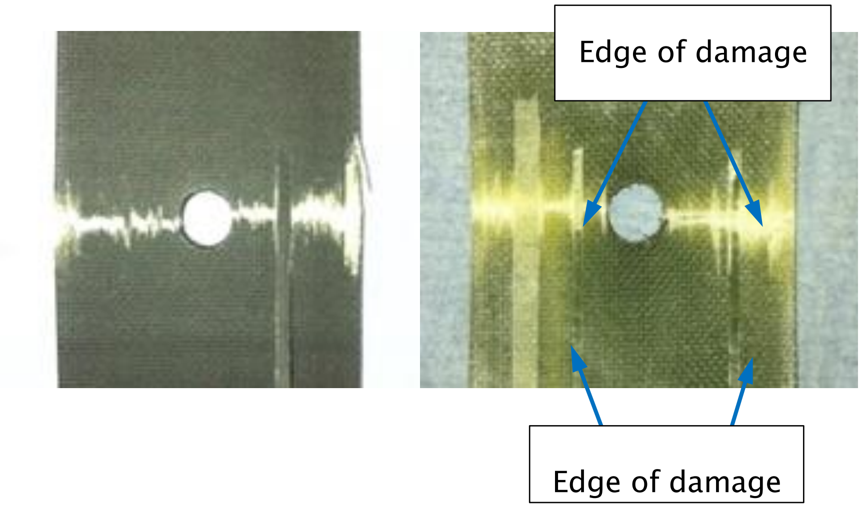

Figure 6.6. (0, 90) Specimen after testing, back face showing damage fanning out from hole

During both tests, the IR detector frame rate was set to 10 Hz for 300 seconds, this meant that the failure of the (+/-45) specimen was not captured. The temperature evolution can be seen in Figure 6.7. Due to the slow rate of extension, the temperature change caused by the damage evolution also increases slowly, with the potential of heat loss through conduction to the surrounding environment. The deformation of the hole is also visible. A photograph of the damaged area within the failed specimen can be seen in Figure 6.8; the lighter green and white areas indicate damage within the specimen.

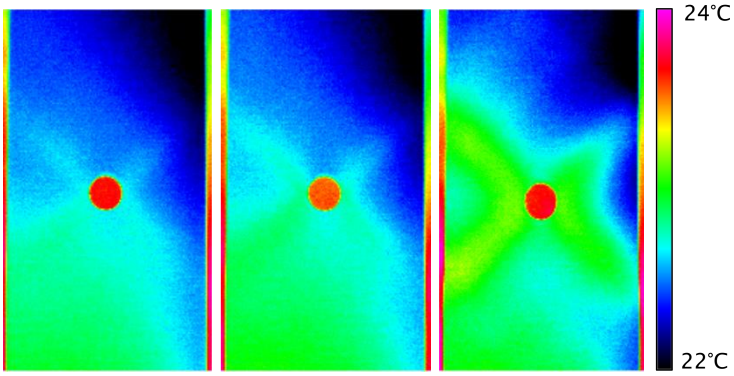

(A) (B) (C)

Figure 6.7. Temperature evolution (°C) in (+/-45) Specimen during quasi-static testing.

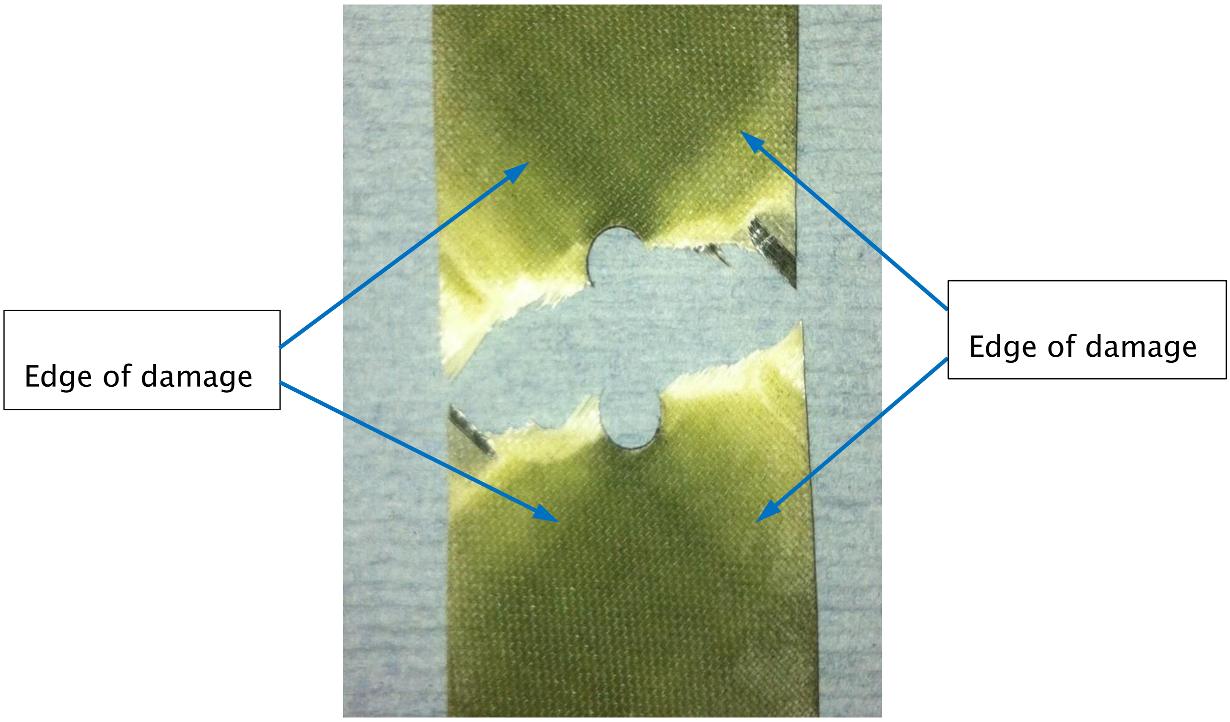

Figure 6.8. (+/-45) Specimen after testing, showing damaged areas.

6.4.3 Fatigue tests on (0, 90) Specimen

The tests were carried out in load control with at a frequency of 5 Hz and an R=0.1. and the (0, 90) specimen was loaded at 70% of the UTS (a load of 5.74 ± 4.70 kN), with full failure occurring at 140,922 cycles. Other higher frequencies were tried, but, due to the deformation of both specimens, 5 Hz was the highest frequency achievable whilst maintaining the required load levels in the servo-hydraulic test machine. Other fatigue loading levels were also tested, but were either too high, so that the specimen failed within a few hundred cycles, too low so the damage evolution stagnated where there was no apparent change after more than 100,000 cycles, or the IR detector was set to record too infrequently and the final stages of damage evolution occurred between the recording points.

Fatigue testing of the composite specimens is being used to assist in the identification, characterisation and quantifying the temperature change associated with different types of composite damage using IRT and TSA. The thermoelastic response, ΔT and $\Delta T/T$ from the (0, 90) specimen is shown in Figures 6.9 and 6.10. In the early parts of the test the temperature did not change, so the data recorded, before 91,000 cycles is not presented. A faint audible crack was heard a few cycles before the 92,000 cycle recording run. This is usually an indication of matrix damage, however this damage mode is not discernible in the IR image in Figure 6.10. The matrix damage is visible in both the ΔT and $\Delta T/T$ images. The initial damage or first ply failure, is found in the 90° plies, for this laminate, whilst this type of damage is not visible in the IR image, it can be seen as the light blue/green horizontal lines in the $\Delta T/T$ images, and is visible from the first data recording at 1000 cycles.

In the 91,000 cycle images, on the RHS of the hole, a small aquamarine area can be seen near the edge of the hole, before the yellow area. This has changed to dark blue in the next set of images. Red arrows indicated the area of change. The dark blue areas with the vertical lines represent the surface longitudinal 0° ply splitting and starting to fracture, with the low thermoelastic response indicating little to no stress is being carried by that portion of the specimen. Between the recording runs at 118,000 cycles and 119,000 cycles audible ‘pinging’ was heard. ‘Pinging’ usually indicates fibre breakage. The speckled region to the lower right hand side of the hole indicated at 119,000 cycles, is a small area of delamination starting to form.

Figures 6.9 and 6.10 show, that when the temperature data were compared there appeared to be little to no change, while, in contrast, the *ΔT/T* images the damage evolution could be clearly discerned.

The last two image sets at 140,750 and 140,900 cycles in Figure 6.10 shows the damage evolution just before failure. The IR image clearly shows an increase in temperature at the damage site. What is more revealing is the *ΔT/T* data which clearly shows how the delaminated areas have grown, forcing the stress to redistribute within the specimen as a result of the damage progression. Local to the hole all load carrying capacity is lost as the delamination progresses away from the hole. The remaining intact material has to carry the load and this is signified by the increased response at the edge of the delamination. Figure 6.11 show the photographs of the front and back of the specimen at the end of the tests. Here the TSA has revealed areas of sub surface damage that are not visible in the photographs. In the second image, showing the back face, the curvature of the delaminated area can be seen on the right hand side of the hole, corresponding with surface damage on the front of the specimen.

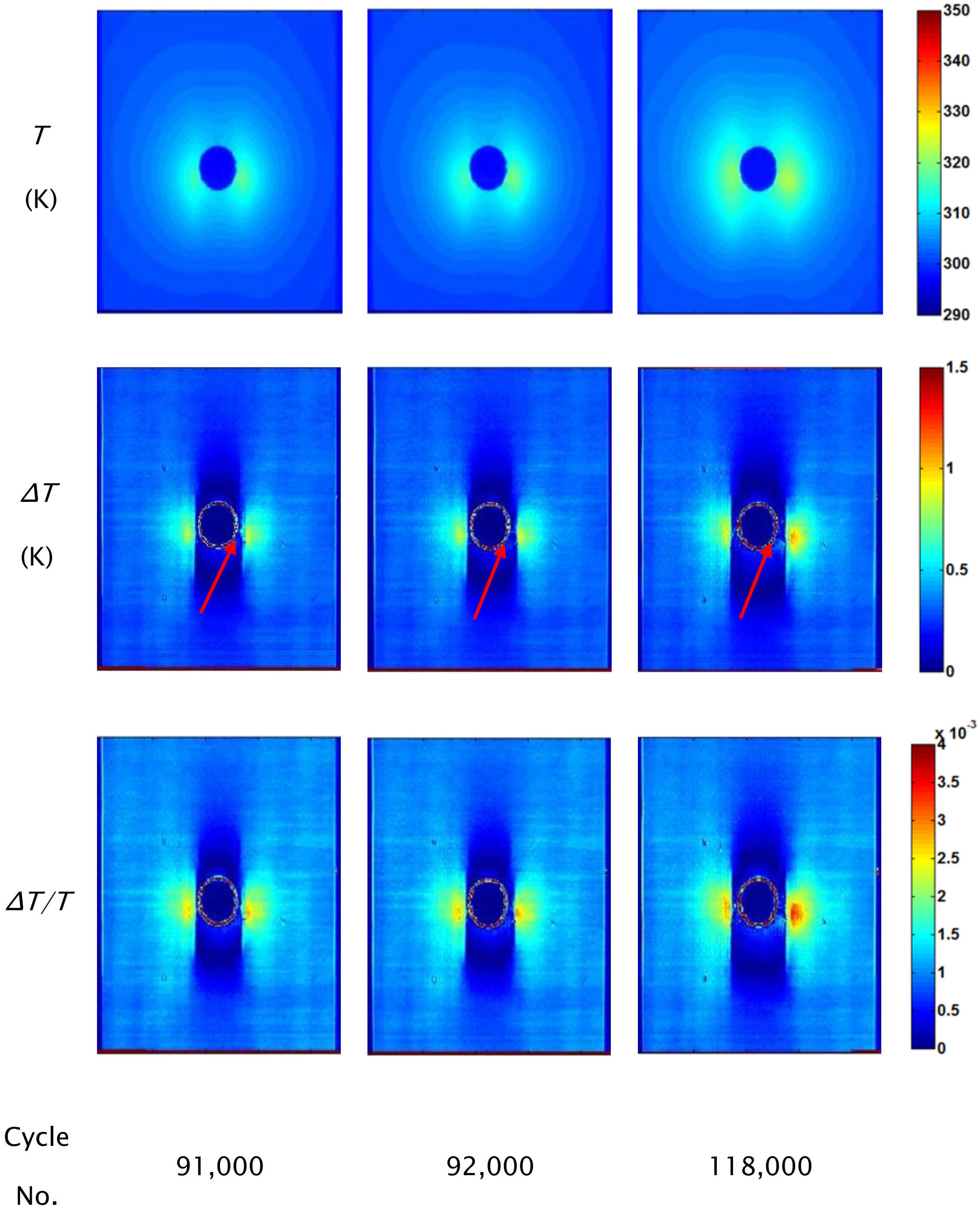

Figure 6.9. (0, 90) Specimen temperature evolution from 91,000 to 118,000 cycles.

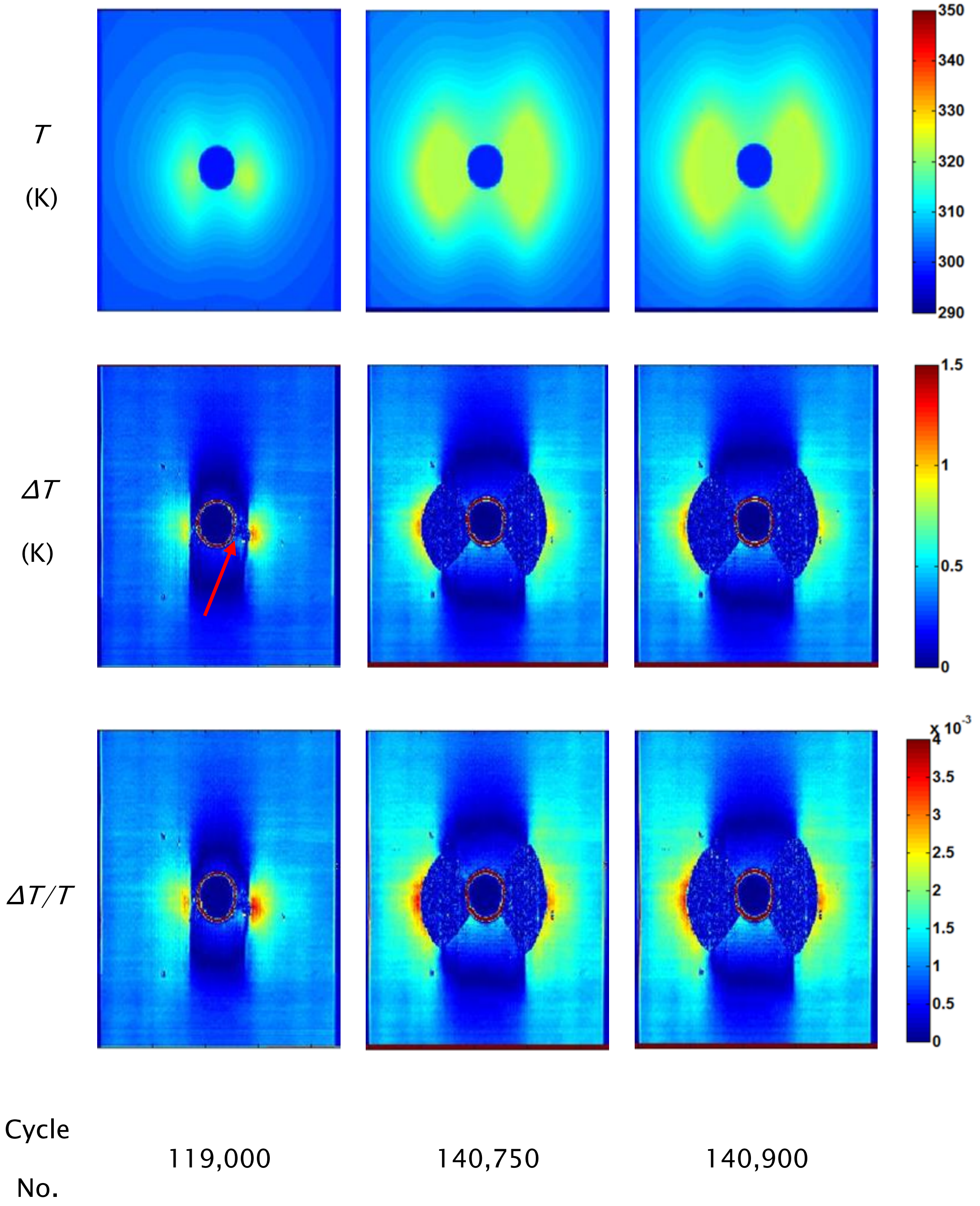

Figure 6.10. (0, 90) Specimen temperature evolution from 119,000 to 140,900 cycles.

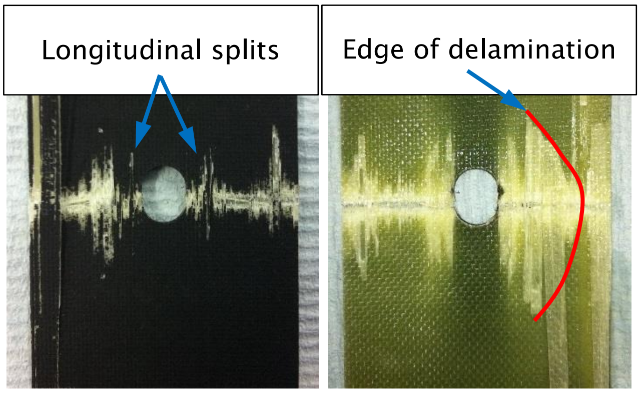

Figure 6.11. Photograph of the failed (0, 90) Specimen, after 140,922 cycles.

6.4.4 Fatigue tests on (+/−45) Specimen

The (+/−45) specimen was fatigue loaded at 55% of the UTS (i.e. a load of 3.35 ± 2.74 kN), before the specimen's full failure occurring at 1291 cycles.

The temperature evolution, ΔT and $\Delta T/T$ of (+/−45) specimen during the fatigue loading is presented in Figures 6.12 and 6.13. Deformation of the hole during the test can be clearly seen, along with deformation along the edge due to the shear coupling. The entire specimen shows an increase in temperature as well as the damaged areas. In the $\Delta T/T$ images, the damage evolution is evident. A crack is growing from the hole signified by the stress concentration, as well as delamination signified by the triangular area shown in images. Figure 6.14 is a photograph of the failed specimen, showing the kink on the right side of the hole, which corresponds well to the damaged regions in the $\Delta T/T$ image. The edge deformation is also clear in the image.

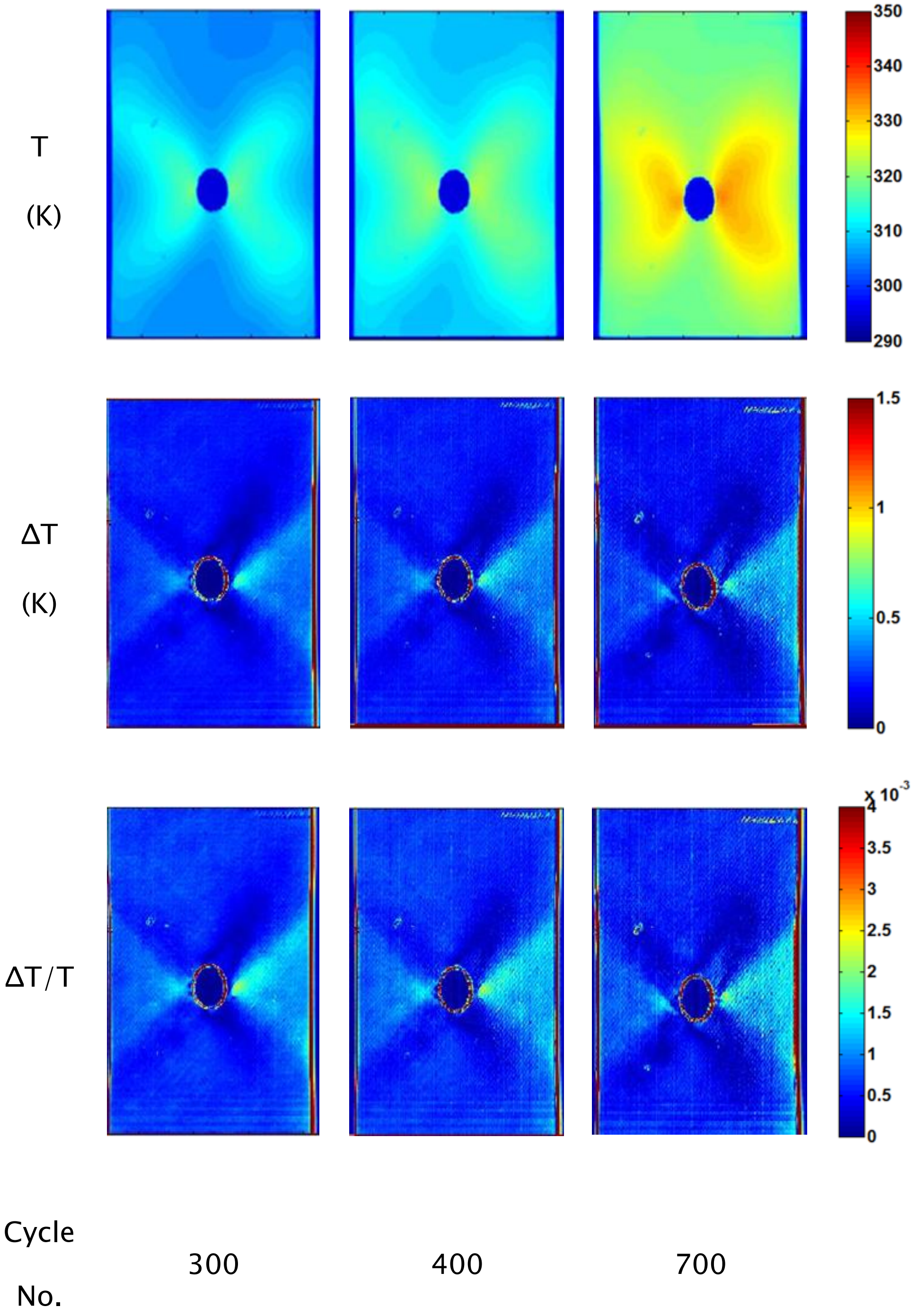

Figure 6.12. (+/-45) Specimen temperature evolution from 300 to 700 cycles.

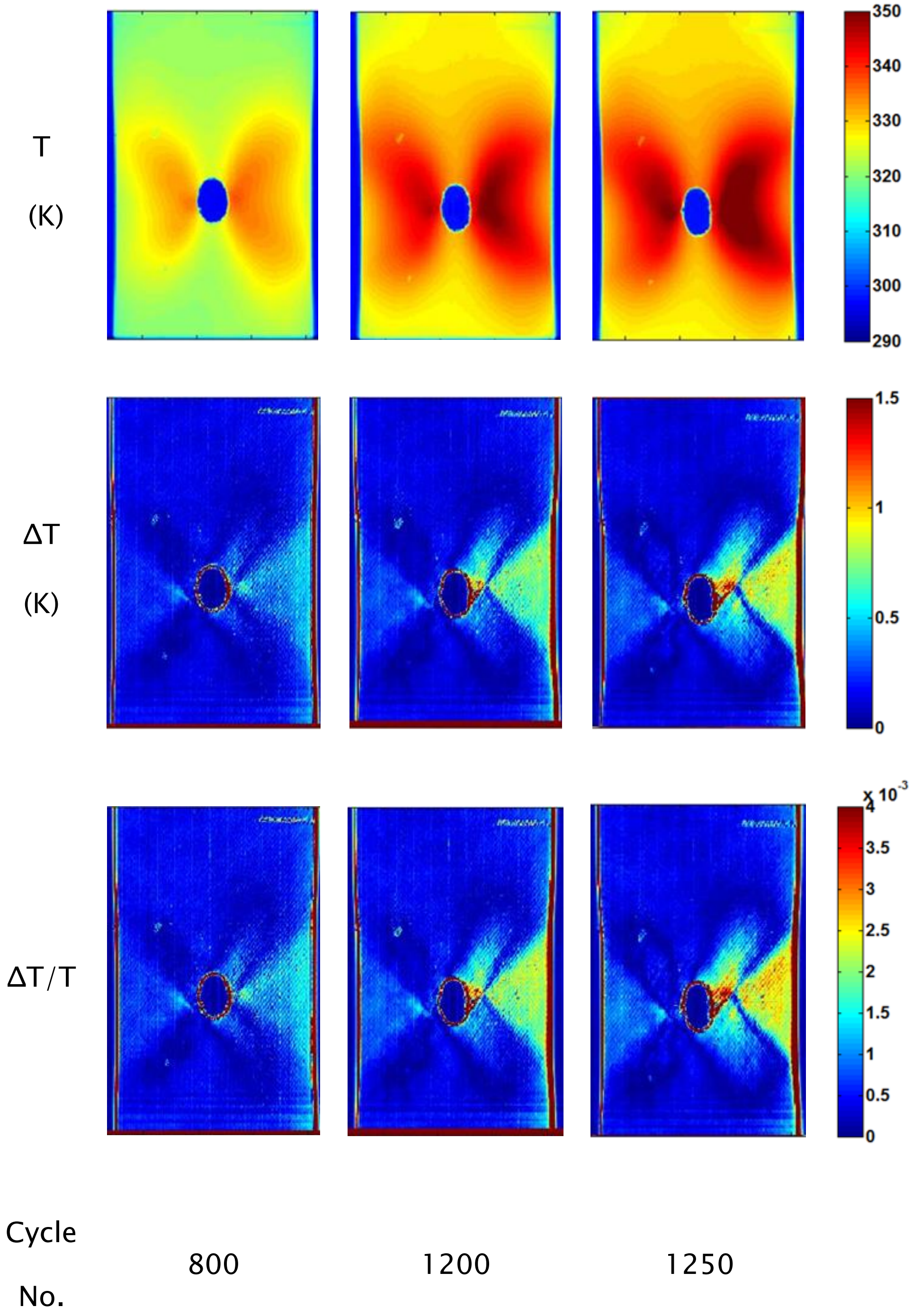

Figure 6.13. (+/-45) Specimen temperature evolution from 800 to 1250 cycles.

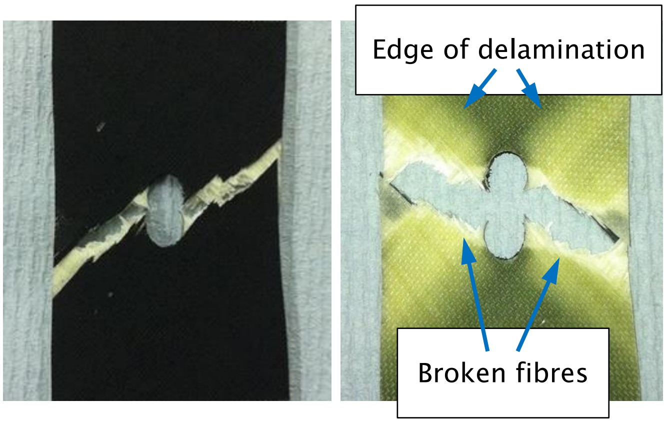

Figure 6.14. (+/-45) Specimen failure image after 1291 cycles.

6.4.5 Summary of initial photon detector tests

It has been demonstrated that the surface temperature changes obtained from an IR detector can monitor damage evolution in a composite material. It is clear from this work that identifying, characterising and quantifying the damage and its severity using the surface temperature change is a difficult proposition. The IR images display similarities in location on the specimen and general shape of the temperature contours, between the specimen types, but the difference in the temperature changes between the (+/-45) specimen and the (0, 90) specimen is as expected as the shearing causes a greater increase in temperature. The temperature difference between delamination, matrix cracking and fibre breakage as seen in the (0, 90) specimen is not detectable. Only by applying the TSA is the actual damage state revealed, therefore it is necessary to link this with the surface temperature data. It is also necessary to link the TSA with the type of damage within the specimen.

The last two sets of ΔT and $\Delta T/T$ images (Figure 6.10) for (0, 90) specimen, 140,750 and 140,900 cycles, appear to show the increasing area of delamination. This was assumed to be a delamination due to the area remaining at temperature in the IR image, but little or no change in the thermoelastic response, ΔT. This suggests that the specimen surface had retained the temperature from the previous damage growth.

6.5 Comparison between the photon detector and the microbolometer performance to monitor damage growth in an OHT specimen

To compare the two different detector types further OHT experiments were undertaken, with the detectors observing “back to back”. The tests were carried out in load control with at a frequency of 5 Hz and an R=0.1. The (+/-45) specimen was fatigue loaded at 53% of the UTS (i.e. a load of 2.79 ± 2.28 kN) and the (0, 90) specimen was loaded at 75% of the UTS (a load of 6.27 ± 5.14 kN). These new load parameters were chosen in an effort to increase the number of cycles before failure for the (+/-45) specimen and decrease the number for the (0, 90) specimen. The specimen dimensions can be found in Table 6.2.

Table 6.2. Batch two composite specimen dimensions.

Specimen Identification	Specimen type	Test configuration	Width (mm)	Thickness (mm)	CSA (mm^2)
E	0/90°	Fatigue	36.38	1.80	65.48
F	+/-45°	Fatigue	36.53	1.85	67.58

6.5.1 (0, 90) Specimen

The temperature evolution of both the front side and back side of the specimen was captured with the photon detector and the microbolometer, respectively, to compare and contrast the differences between the two detector types. The specimen failed after 65,578 cycles, in the area just outside the grips of the specimen, and not at the open hole stress concentration, it is not known what caused the premature failure and as the failure occurred outside of the field of the view of the IR detectors it was not possible to observe the temperature change. Despite the unexpected failure away from the stress concentration sufficient damage growth occurred within the specimen to compare the two detectors.

Comparing the images from the photon detector and the microbolometer at the initial recording at 1000 cycles (see Figure 6.15), it can be seen that the temperature evolution is measurable by both detectors. The photon detector is visible in the field of view of the microbolometer, as well as through the hole, which interferes with the response of the bolometer, making the temperature evolutions difficult to discern, as shown in Figure 6.15. As the temperature evolution increases beyond the detectors external temperature the damage becomes more evident in the later images. (As reported in Chapter 5 the photon detector is out of calibration and was reading approximately 4 °C less than the microbolometer.) For all images in this section, the photon detector images are on the left hand side (viewing 50 mm of the gauge length), and the microbolometer full field images on the right (viewing approximately 130 mm of the gauge length).

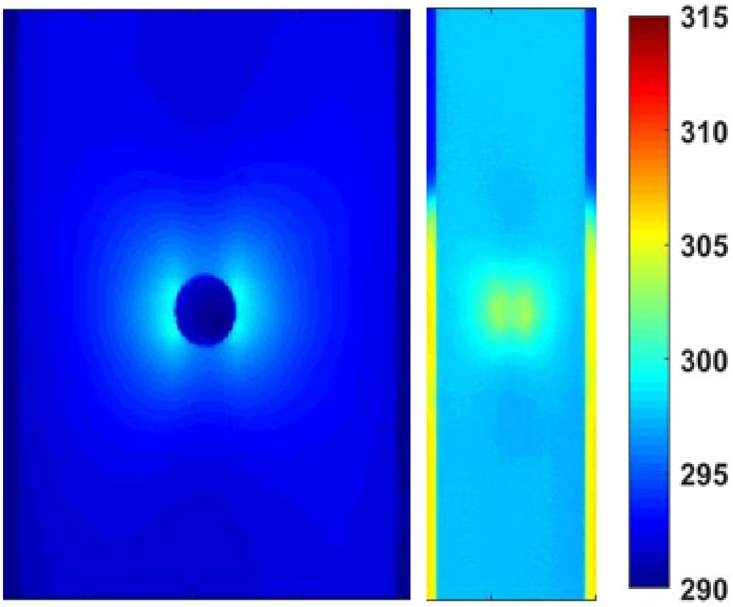

Figure 6.15. (0, 90) Specimen E, temperature comparison after 1000 cycles.

As the damage and temperature evolve around the hole it should be noted that the shape of the temperature evolution is similar between both surfaces, see Figure 6.16. IRT is considered to a surface measurement only, yet in this instance there is a correlation between the two surfaces. Suggesting that the temperature increase due to damage, either diffuses through this type of specimen, or the damage is through the specimen thickness.

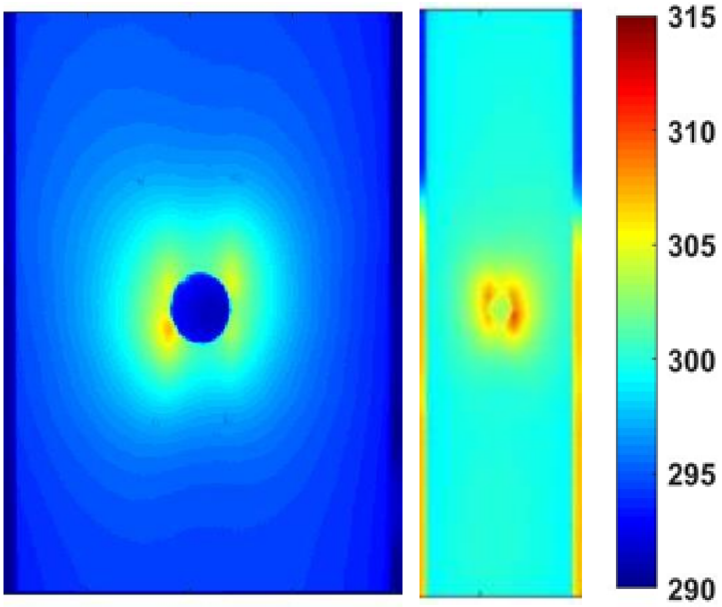

Figure 6.16. (0, 90) Specimen E, temperature comparison after 20,000 cycles.

The temperature evolution throughout the test is mirrored on both side of the specimen and can be seen in Figure 6.17, after 40,000 cycles, and Figure 6.18, after 65,000 cycles, just before failure. Comparing this specimen's temperature evolution, with the previous, single sided test, suggests that the surface longitudinal 0° plies are splitting and beginning to break and delaminate. The mirroring of the temperature demonstrates that the microbolometer has the capability to detect and monitor damage evolution within this type of specimen.

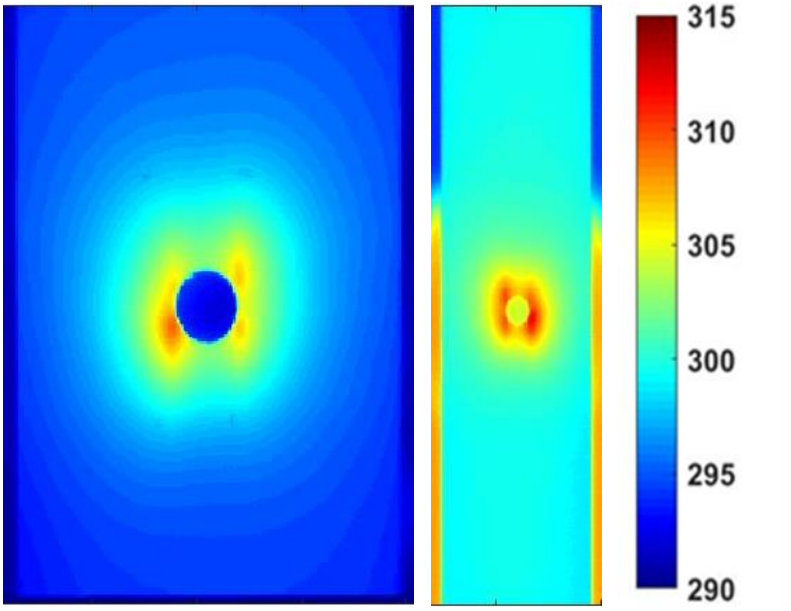

Figure 6.17. (0, 90) Specimen E, temperature comparison after 40,000 cycles.

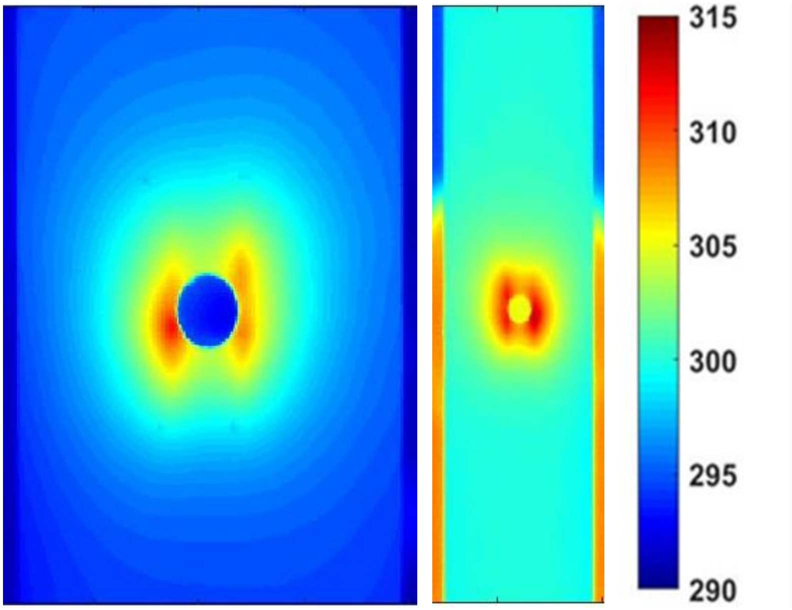

Figure 6.18. (0, 90) Specimen E, temperature comparison after 65,000 cycles.

6.5.2 (+/- 45) Specimen

Specimen F was installed into the test machine, so that the detectors has the same field of view as the previous test, 50 mm and 130 mm for the photon detector and microbolometer, respectively. The specimen was cycled for 110,000 cycles, before the test was stopped manually. Figure 6.19, displays the detectors' temperature images after 20,000 cycles, where it can be seen the temperature is evolving more on the left hand side of the specimen, when viewed from the photon detector, which is mirrored in the microbolometer image. Throughout the test the temperature evolution of the photon detector images is mirrored in the microbolometers output. This evolution can be found in Figures 6.20 and 6.21, at 70,000 cycles and 110,000 cycles, respectively.

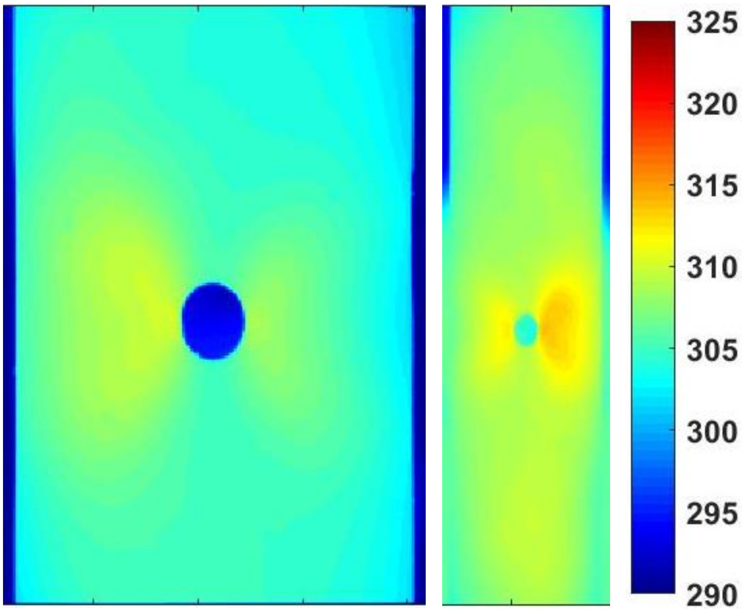

Figure 6.19. (+/-45) Specimen F, temperature comparison after 20,000 cycles.

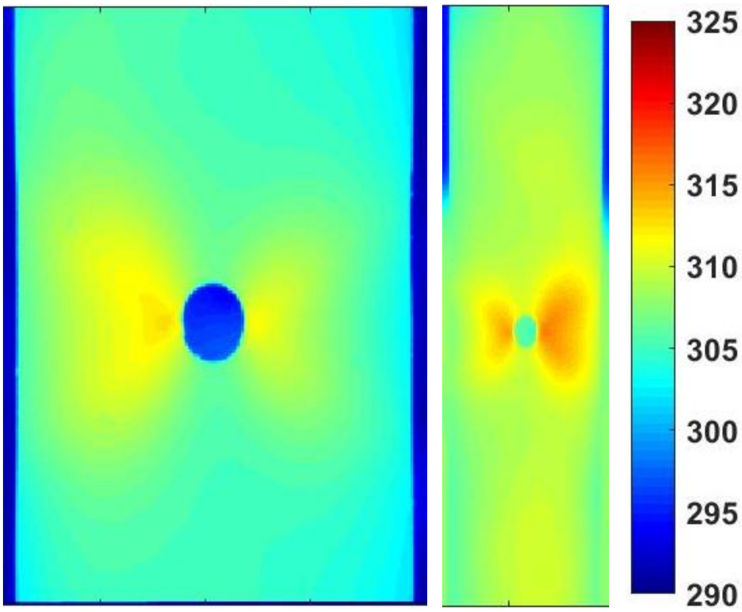

Figure 6.20. (+/-45) Specimen F, temperature comparison after 70,000 cycles.

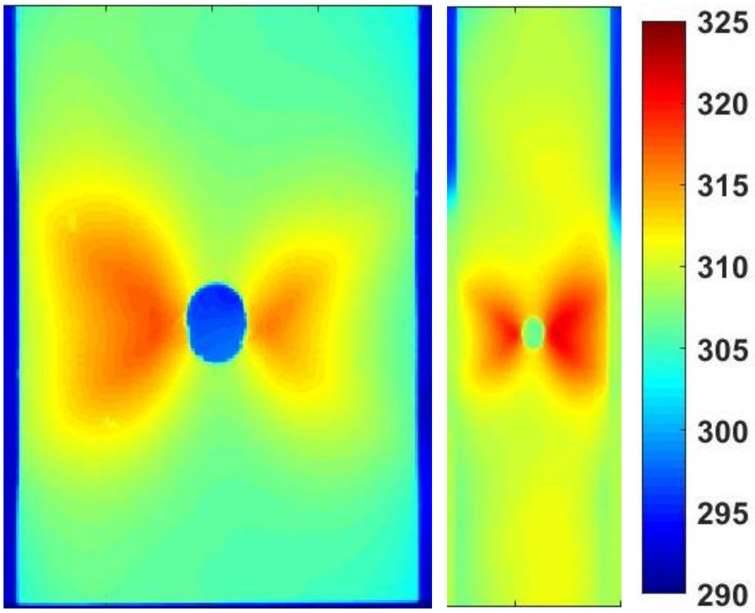

Figure 6.21. (+/-45) Specimen F, temperature comparison after 110,000 cycles.

6.6 Using IR detectors to assess damage growth in an un-notched composite specimen

For this test an un-notched (0, 90) specimen was manufactured without a central hole and had end tabs applied, to minimise the stress concentration at the edge of the grips. An alternative E-glass fibre pre-impregnated epoxy resin system RP-528, was used to manufacture the specimen, with an autoclave consolidation, to the same layup as the previous tests. The only variability was the overall thickness of the material. Table 6.3, displays the specimens' dimensions. The test was carried out in load control with at a frequency of 5 Hz, an R=0.1, and the specimen was loaded at 65% of the UTS (a load of 17.59 ± 14.39 kN).

Table 6.3. Rectangular un-notched composite specimen dimensions.

Specimen Identification	Specimen type	Test configuration	Width (mm)	Thickness (mm)	CSA (mm^2)
G	0/90°	Fatigue	36.73	2.77	101.74

The first indication of damage was seen at 71,000 cycles by the microbolometer, with the 130 mm view of the specimen gauge length. Figure 6.22, displays the microbolometers temperature image on the left hand side. A red arrow points to the corresponding surface damage on the failed specimen. The increased temperature at the bottom of the specimen is partially due to the heat transferring from the hydraulic actuator, through the grips to the specimen. It is also the location that the specimen finally failed.

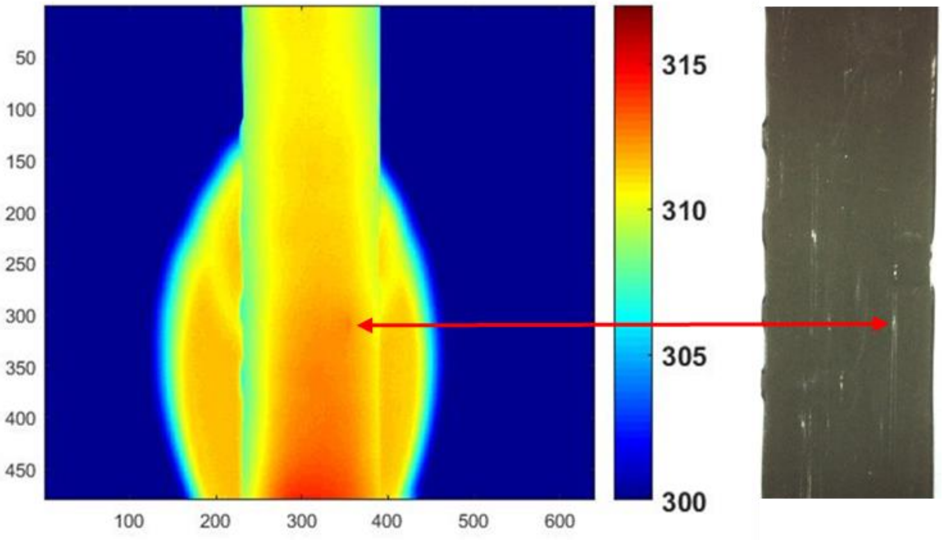

Figure 6.22. (0, 90) Specimen G, initial surface damage after 71,000 cycles.

Damage and temperature evolution continued within the single hotspot until 110,000 cycles, when other hotspots began to evolve, see Figure 6.23. Two of the new hotspots occurred within the photon detectors field of view, 50 mm about the specimens centre point. As with the open hole specimen, the damage on the back face was detected on the front, with the photon detector.

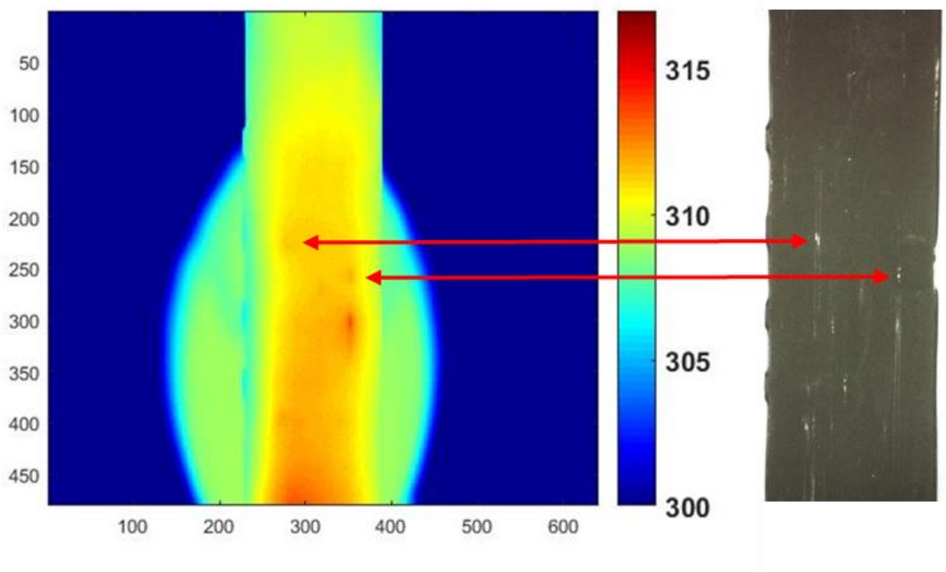

Figure 6.23. (0, 90) Specimen G, second stage surface damage after 110,000 cycles.

A comparison between the two detectors at 120,000 cycles can be found in Figure 6.24. Where it can be seen that the temperature created by the damage on the back face has just begun to have an effect on the through thickness temperature of the specimen. The photon detector image is on the top, and the arrows indicated the back to back point temperature increases. At this point there were no visual indications of damage on the front face, but it was visible on the back (white marks in the black paint), see Figure 6.25.

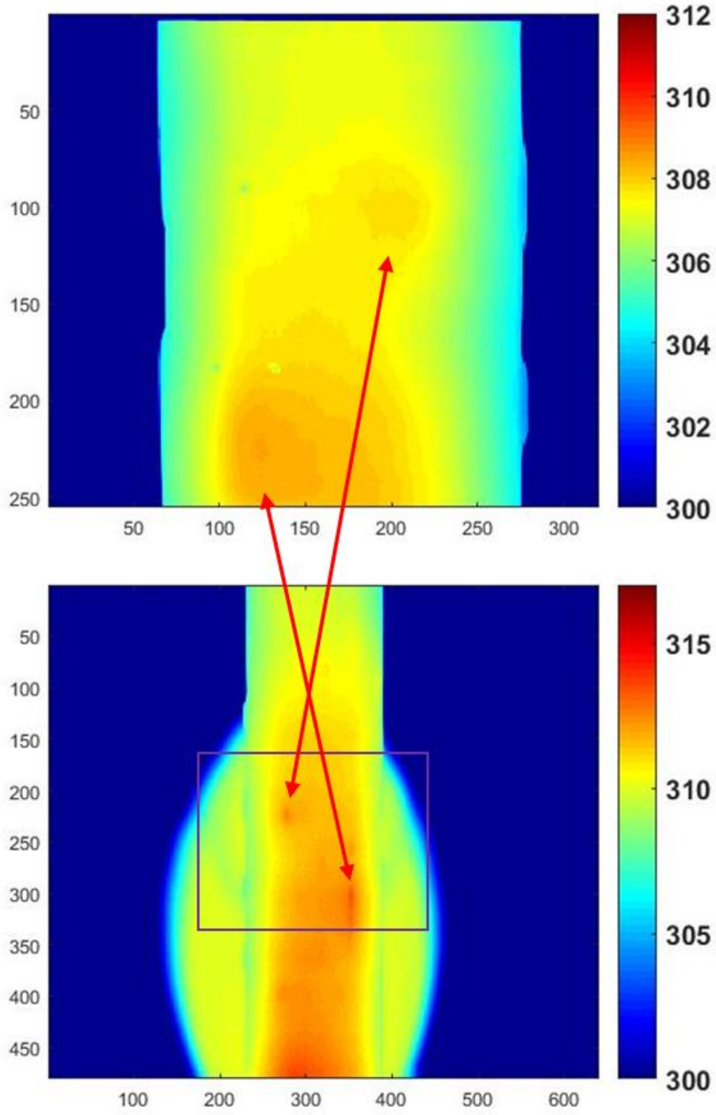

Figure 6.24. (0, 90) Specimen G, temperature comparison after 110,000 cycles. The purple box outlines the photon detectors field of view, on the microbolometer image.

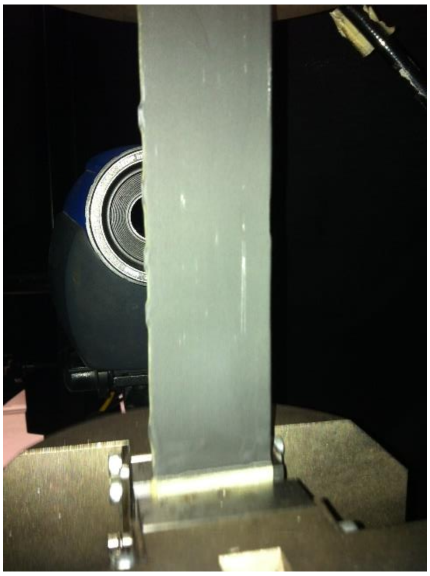

Figure 6.25. (0, 90) Specimen G, photograph of back face damage after approximately 110,000 cycles.

As the temperature and damage evolves, the temperature evidence on the front face also evolves. Figure 6.26 displays the temperature of both faces, just before failure at 160,000 cycles. It is evident that the surface damage on the back face is detectable on the front face, without any visual cues. From the two initial hotspots detected on the front face, only the upper spot evolved further, whereas the lower hotspot to the edge of the specimen, evolved slower that another hotspot towards the centreline of the specimen. When these two lower spots are compared in the microbolometer image, they appear to be of a similar temperature, which would indicate that there is damage at a point within the thickness of the specimen, closer to the front face than the back. The final failure point, above the lower grip, is just visible at the bottom of the microbolometer image.

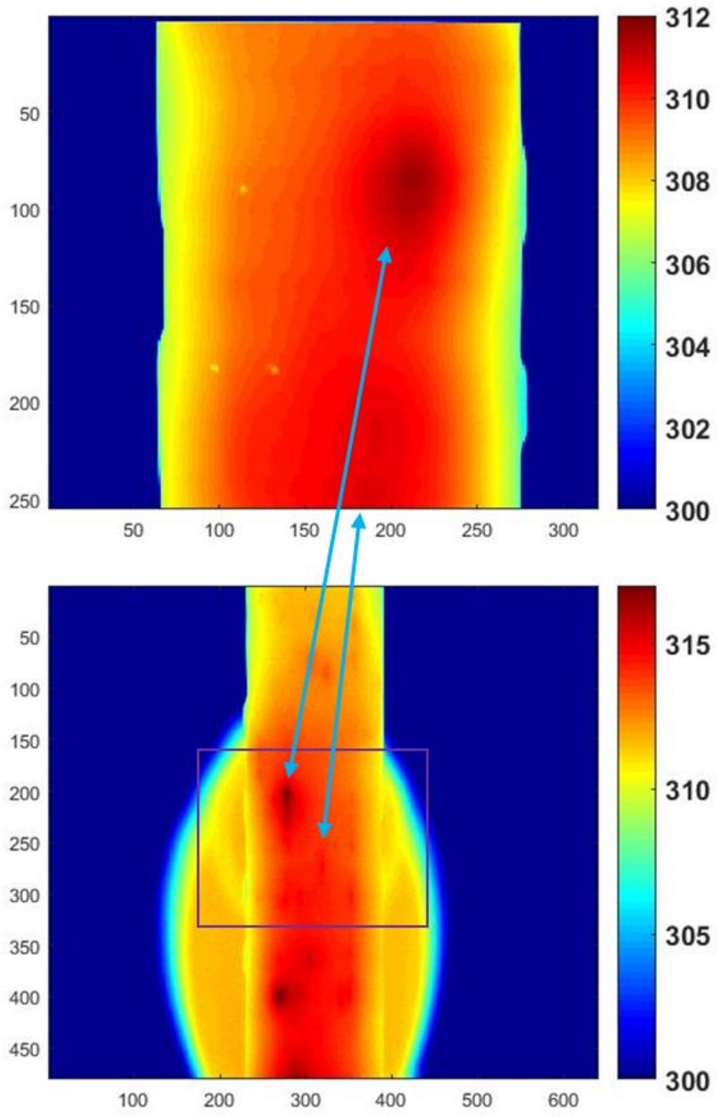

Figure 6.26. (0, 90) Specimen G, temperature comparison after 160,000 cycles. The purple box outlines the photon detectors field of view, on the microbolometer image.

Photographs of the front and back faces of the specimen can be seen in Figure 6.27. The white areas of surface damage can be determined on the back face image. With the long fibre splitting, thin white lines, creating a small and noticeable temperature increase, the areas of fibre breakage, the white spots, generate a significant temperature increase. On the front face no white areas are visible. The only observed marks are those created during the failure event toward the end tab, and the pencil marks used for motion compensation and marking the detectors field of view.

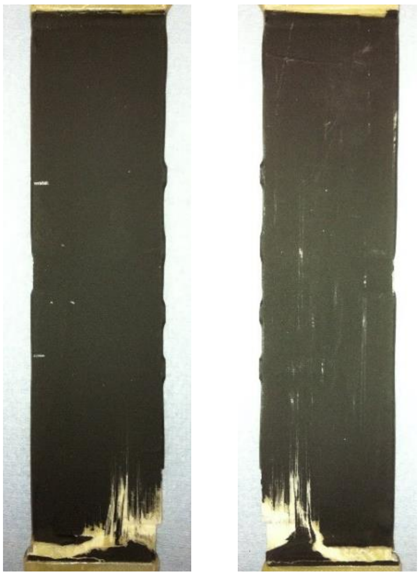

Figure 6.27. (0, 90) Specimen G, photograph of both faces after failure.

6.6.1 Summary of application of IR to damage growth in an un-notched specimen

The un-notched specimen experiment has shown that this microbolometer has the capability to detect and monitor damage created within an unnotched specimen, and that temperature increases due to internal damage can diffuse through the composite to the surface to be detected. Why the damage appeared on one side of the specimen, was investigated, and was due to the manufacturing technique. When composite materials are autoclave consolidated, the laminate has one side against the mould surface, and for these specimens a layer of peel ply between the laminate and the mould. On the other side there is another layer of peel ply, a perforated release film, and a layer of breather cloth. When the laminate is cured under pressure, some of the epoxy resin flows into the peel ply, through the perforated release film and into the breather cloth. On the mould side of the laminate, the resin can only flow into the peel ply, so has a resin rich surface, when compared with the other side. It was found that the surface damage appeared on the breather cloth side of the laminate, where there was a thinner surface layer of resin.

6.7 Conclusions

The photon detector and microbolometer have the capability to use IRT to monitor and assess damage evolution in a composite material, through the use of IRT, as temperature evolves on the surface of the specimen in both a quasi-static and cyclically loaded experiments. Distinguishing the type of damage, from the temperature evolution and cyclic variation, requires the use of a photon detector to post process the results for TSA. The ability to detect subsurface damage in this type of specimen was unexpected, due to the general temperature insulating properties of epoxy resin systems. This information may prove useful, after further study, as a method of characterising the type of damage.

To quantify the damage evolution, creating a temperature envelope, with predetermined temperature limits, appears possible. If the lower temperature limit is just above the specimens temperature when it is cycled close to the materials elastic limit, and the upper limit 5 K to 10 K above that. This would create a measurable temperature band around the damaged area. As the damage grows and the temperature envelope increases, the band would lengthen to enclose the damage evolution. Then, the change in area between the two limits or the number of pixels, would be measured or counted. Controlling the test machine would then use an area increase rate (mm^2/min) or pixel number increase rate (pixel/min).

In conclusion, damage within a composite material can be identified by an increase in temperature. Quantifying the damaged area is feasible with the IRT measurement technique, which will be refined to accommodate the characterisation outcome. Leading into the next chapter, Chapter 7 Strategies to integrate IRT into test machine control.

Chapter 7 Strategies to integrate IRT into test machine control

7.1 Introduction

In Chapters 5 and 6 it was demonstrated that by using IRT to monitor the surface temperature of around a crack tip in a SENT specimen and at damage in composite materials it is possible to obtain an indicator that correlates with the damage evolution. It was also shown that such measurements could be made with both a state-of-the-art photon detector, and a less expensive microbolometer. This would potentially allow the approach to be more widely considered by the testing community. In this chapter, the approaches are considered to use the results of the work in Chapter 5 to control a test machine during a fatigue type test. Next, four possible implementation strategies to control the test machine, using the IR detector, are discussed. The chapter concludes with two proof of concept trials, using microbolometers.

The control methods overviewed in Chapter 2, all require the measurement of a global physical change within the specimen, whereas the PhD project investigates controlling the damage evolution rate in materials, which may not exhibit a global physical change. Measuring the specimen’s change in compliance, will indicate that damage has occurred, but its location or size within the component would not be known. Therefore using IRT, that can monitor temperature changes due to damage evolution, and then feedback the data to the test machine control, would be beneficial.

To implement the new damage evolution control strategy it is necessary interface the IR system with the test machine controller. The purpose of the chapter is to identify an appropriate implementation strategy. Four possibilities are described in the next section and based on an evaluation of the benefits and limitations of each approach the most appropriate strategy of interfacing the detector system with the test machine controller is established. From the four possible implementation strategies, two were chosen for further study. The results of the study and feasibility trial are reported in sections 7.3 and 7.4.

7.2 Implementation Strategies

7.2.1 Implementation Strategy 1 (IS1): External waveform control

External waveform control uses a single computer to run the imaging system's software, monitor the data output and generate a waveform with an analogue signal output. The signal is then passed to the test machine via an analogue input, commanding the actions of the test machine. An example of the successful application of this method, is a system designed and manufactured by Dirlik Controls Ltd.'s [103]. In this instance the crack length within a metallic specimen is measured and monitored by DCPD, whilst being subjected to a spectrum loading regime, generated within the same computer. The test is stopped when the crack reaches a prescribed length.

With the specific external control strategy proposed for test control using IR imaging, a single computer commands the test machine and monitors the damage evolution of the specimen. The computer generates the required waveform and the digital signal is converted to an analogue output of ±10 V by a digital to analogue converter (DAC) for input into the 8800 controller. The 8800 controller is setup as a slave unit, so the voltage input is proportional to the required load or displacement. It should be noted that the load and displacement limits can be set on the 8800 controller as an outer safety limit, to stop the test. Outputs of the achieved load and displacement are then fed back using the controllers' outputs via an analogue to digital converter (ADC) to the computer. The computer has its own PID controller that compensates for errors. The specimen is loaded as specified and any damage evolution is monitored. In this instance the IR detector outputs a voltage corresponding to the chosen damage evolution parameters, which is fed back into the computer, where a PID controller runs the tests program as required. Figure 7.1 illustrates the monitoring and control process.

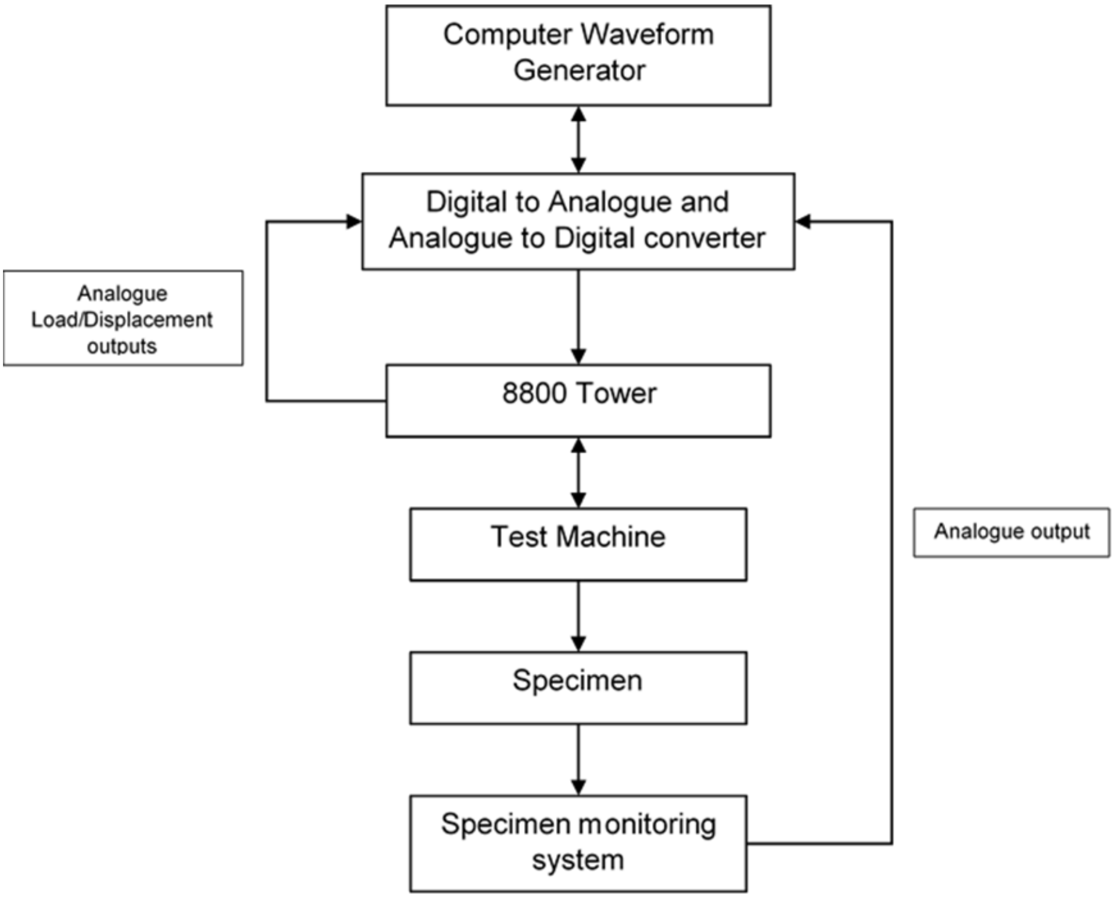

Figure 7.1. Schematic of external waveform control and data processing.

The benefits of this type of monitoring and control system include:

- Adaptability to be used on any test machine that can accept a ±10 V analogue input, with analogue outputs of the test machines load and displacement values.

- Direct digital connection between the imaging software and the control software, minimising communication time between them.

The drawbacks of this system include:

- Not using the full capabilities of the Instron digital controller, such as their extensively developed PID and amplitude control algorithms.
- A new feedback and PID control system needs to be produced, developed and trialled.
- The multiple digital to analogue and analogue to digital conversions can introduce errors into the control and feedback system. An analogue signal is continuous whereas a digital signal works at a specified frequency, therefore an ADC will miss some of the signal if the digital sampling frequency is not high enough and a DAC will have steps in the output, with the size depending on the digital frequency.

7.2.2 Implementation Strategy 2 (IS2): External trigger

Optris PI connect and FLIR's Altair software for microbolometer and photon detectors respectively, have the ability to produce an analogue or digital trigger signal when certain parameters are met. The Instron 8800 digital controller can accept an analogue or digital trigger input. This strategy connects these two options together. The test setup requires two computers, one running the Instron software, the second running the camera system software. Both the Instron and camera operate as normal.

A test is started using the Instron software with the IR camera running. The software allows a region on the specimen to be monitored within the IR sensor array. When a prescribed temperature value is achieved a trigger signal is generated into the 8800 controller. The digital trigger inputs are limited to stopping the test using the standard limit action options, or continuing the test and logging the event. Figure 7.2 outlines the set-up.

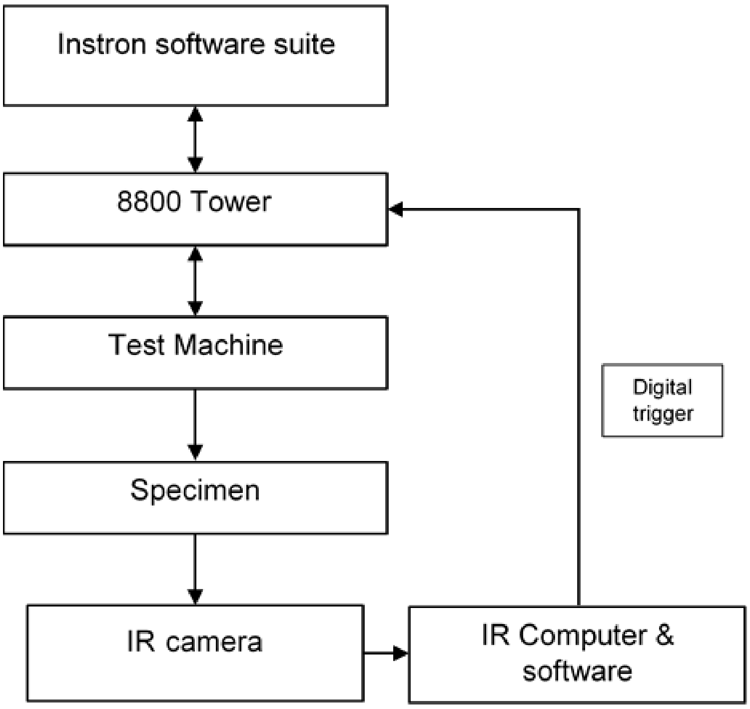

Figure 7.2. Schematic of camera monitoring and trigger control.

The benefits of using this system are:

- The FLIR software has the limit and trigger actions already installed and available.
- The Instron 8800 controller has the digital trigger inputs as standard.
- Standard Instron software can be used to run the test sequence.

The drawbacks of the system are:

- The 8800 controllers limit actions are restricted in their capabilities, only capable of safely stopping the test or recording that it has received a trigger. Ideally to control the test machine with the imaging techniques, an action changing the waveform is required.

- The two computer systems are operated separately, therefore they would have to be linked or synchronised together, to start and finish simultaneously.
- Two computers are required to operate the systems

7.2.3 Implementation Strategy 3 (IS3): External imaging

Two computers are used to run the Instron software suite and the imaging techniques separately. This strategy connects the two computers via a network, allowing the transfer of the camera systems digital output data, to the Instron control software. A diagram of this connection strategy can be seen in Figure 7.3. The Instron software operates the test regime as required and the imaging system monitors the specimen. The data output from the imaging system, a live output from the IR system or a delayed post processed output from the TSA system is passed to the Instron computer via a network or other connection.

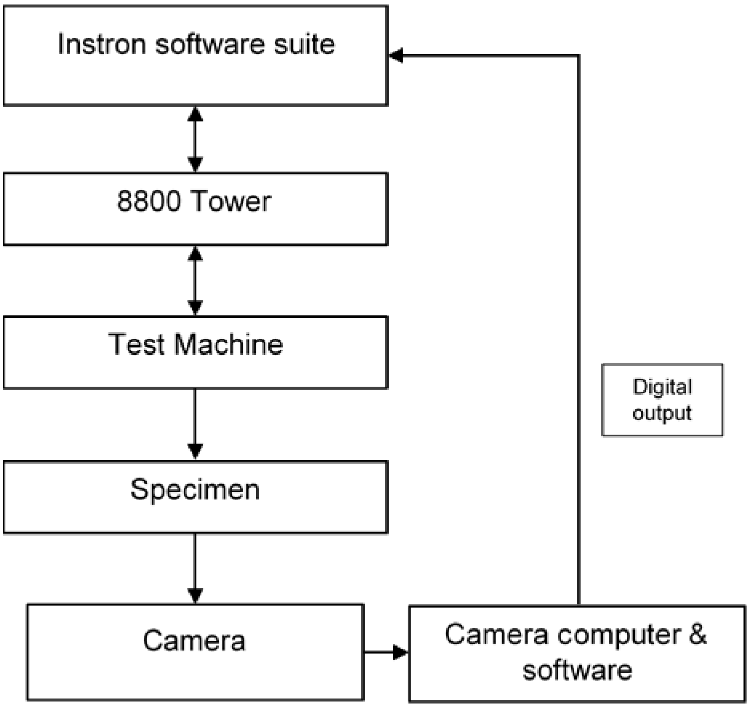

Figure 7.3. Schematic of computer communication and control.

The digital data passed to the Instron computer will require processing, into a form suitable for the Instron software suite. Temperature outputs from the IR and TSA systems will require software for this conversion. Parameters will have to be specified on how the data is monitored, including temperature and strain/displacement limits, and the actions to be taken. Test machine control actions should include, changing the speed, frequency and amplitude of the command waveform. Instron's specimen self-heating control [14] (SSHC) is the type of software package required, and has been described earlier in this chapter.

The benefits of this strategy include:

- Digital to digital communication eliminates the need for DAC and ADC conversions and the output errors generated.
- The digital inputs are direct data outputs from the imaging software, not a trigger signal.
- The two computers can be synchronised to start and stop the test simultaneously.
- The test machine and the imaging system remain separate, allowing the imaging system to be used away from the test machine.

The challenges to develop this system include:

- Additional software is required to process the camera systems output into a form the Instron software can utilise.
- The software requires a definition of the damage evolution parameters and limits.
- Actions, when the damage evolution parameters and limits are reached, will require defining, on how the command waveform is changed.

7.2.4 Implementation Strategy 4 (IS4): Software communication

Software to software communication between the imaging system and test controller requires the two software packages to be operated on the same computer. This allows digital to digital communication between the two. The control process requires the Instron software suite to control the test waveform. The imaging technique monitors the specimen for damage evolution. The digital output data from the imaging system is passed to the Instron software, via software that processes the camera output data into an Instron compatible form. When a damage evolution event is detected outside of specified temperature, and strain/displacement limits, the Instron software adjusts the test control parameters. Figure 7.4 demonstrates this strategy. It is predominantly the same as the computer to computer communication, but without the network connection.

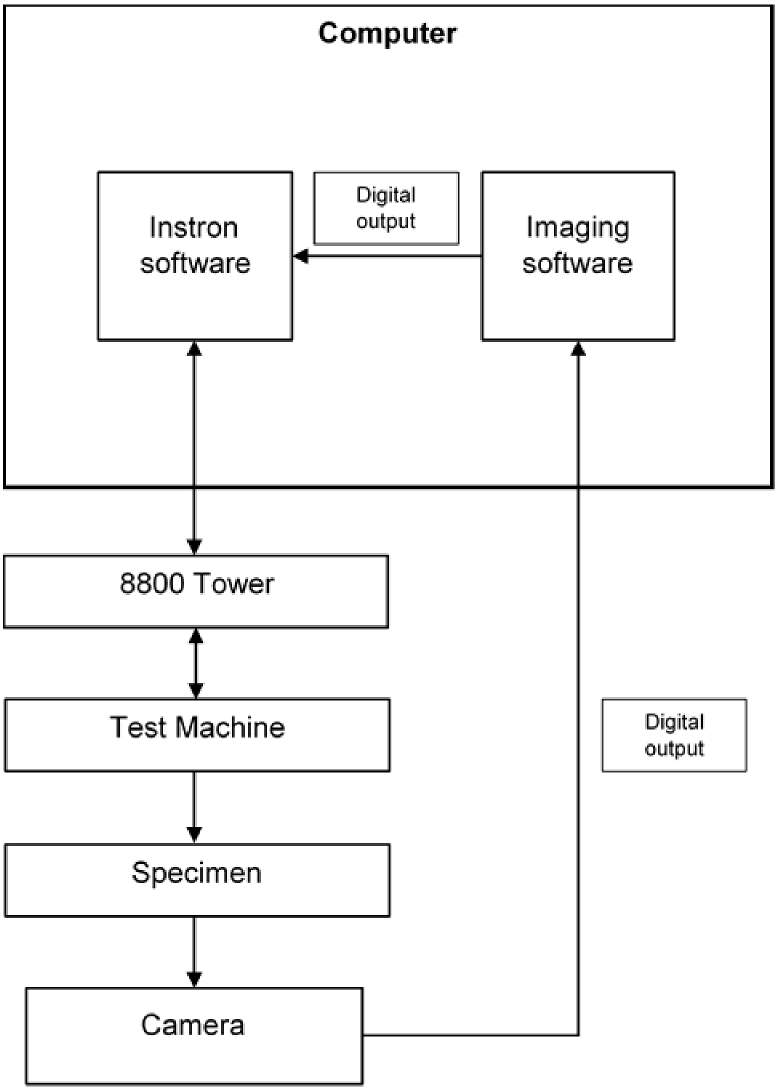

Figure 7.4. Schematic of software to software monitoring and control.

The benefits of using this strategy include the following points:

- Digital communication between the imaging technique system and the Instron control system, removing the DAC and ADC conversion errors.
- Increased communication speed between the software packages, no communication through network cards.
- Synchronised data from the test machine and imaging system.
- A single computer reduces test set-up complexity.

The challenges of this system include:

- Computer limitations. Can the computer run both software packages together without software conflicts and capacity limitations?
- Additional software will be required to process the camera systems output into a form the Instron software can utilise.
- The software will need to define the damage evolution parameters and limits.
- Actions, when the damage evolution parameters and limits are reached, will require defining, on how the command waveform is changed.

7.2.5 Implementation Strategies Summary

Four implementation strategies have been presented to enable the communication and interaction of imaging systems with test machine control. These strategies are:

IS1: External waveform control

IS2: External trigger

IS3: External Imaging

IS4: Software communication

All four of the strategies have different challenges to address prior to implementation. IS1: External waveform control, is a technique that has been proven to work, for DCPD monitoring of spectrum loaded fatigue tests, but it slaves the Instron controller, not utilising the well-developed Instron control and feedback systems. There are also the error sources associated with the DAC and ADC communication signals, and the development of a new PID control system.

IS2: External trigger, using the digital input connections on the 8800 controller, limits the actions available to control the test waveform. The actions are predominantly safety features to stop the waveform and return the specimen to a safe position. The alternative actions just record that the trigger was activated, and the test waveform continues until completion.

IS3: External imaging isolates the imaging system from the Instron test machine, allowing the imaging technique to be used on different test machines or even without a test machine.

IS4: software to software communication requires the software for the imaging system to be run on the same computer as the Instron software suites, but the processing requirements for each software package and the processing capabilities of the computer require investigation, along with communication protocols between the software packages.

A summary of the evaluation of the four Implementation strategies can be seen in Table 7.1. The four strategies are listed down the left hand side of the table, and their requirements are listed across the top. In the table “Yes” signifies that it is a requirement. The three colours indicate if the requirement introduces errors into the control system (Red), the statement requires additional processes to operate efficiently (Amber) or the requirement is beneficial to the project (Green). The two options that warranted further investigation are, IS2 and IS4. A version of IS2, utilising an analogue input, communicating to the WaveMatrix software, has undergone a feasibility trial. The outcome of the trial with an Optris PI450 microbolometer is described in the section 7.3. IS4, using an IR camera to monitor and control the temperature evolution has been studied and implemented using LabVIEW to control the camera as described 7.4. Some suggestions as to how to integrate IR cameras into the test machine control systems are provided in the future work section.

Table 7.1. Summary of the Implementation Strategies

Implementation Strategy	Analogue input required	Digtal input required	ADC or DAC conversions	Instron PID control	PID control development	Additional computer required	Off the shelf software	Custom software development	External triggering or control
IS1	🟧 Yes	🟧 No	🟥 Yes	🟥 No	🟥 Yes	🟧 Yes	🟥 No	🟥 Yes	🟧 Yes
IS2	🟧 Yes	🟥 Yes	🟧 Yes	🟩 Yes	🟩 No	🟧 Yes	🟩 Yes	🟩 No	🟧 Yes
IS3	🟩 No	🟥 Yes	🟩 No	🟩 Yes	🟩 No	🟧 Yes	🟩 Yes	🟧 Yes	🟧 Yes
IS4	🟩 No	🟩 No	🟩 No	🟩 Yes	🟩 No	🟩 No	🟧 No	🟧 Yes	🟩 No

🟥 Items that introduce errors
🟧 Items that can be worked around
🟩 Items that are beneficial to project

7.3 Analogue temperature input trial

An Optris PI450 IR camera was available during the placement at Instron, so it was decided that it should be used as a trial of IS2, External trigger, and replicate a simple version of the SSHC software. IS2 uses the IR detector to measure the surface temperature of the test specimen and send an analogue temperature output to the test machine controller. The benefits of an analogue signal are; WaveMatrix can be used to set the limits (keeping all of the control parameters within the same software package) and the temperature can be logged during the test. This section is split into five parts. The first, Section 7.3.1 outlines the test set-up, describing the equipment used and their communication connections. The next two sections describe the use of the analogue signal to trigger the test machines control limits (Section 7.3.2) and the WaveMatrix software control limits (Section 7.3.3), including the test outcomes and observations. Section 7.3.4 uses the camera control software to record images during a test sequence. The results of the trial are described and discussed.

7.3.1 Test setup

The Optris PI450 is a microbolometer, with the specification as given in section 3.3.3. For this trial a standard lens was used, giving a field of view (FOV) of 38° x 29°. The camera was connected to a laptop, running the Optris PI connect software and a process interface (PIF) cable connected the camera to the 8800 digital controller. Figures 7.5 & 7.6, show the trial set-up on an Instron E1000 ElectroPuls test machine, located at Instron UK’s headquarters. The specimen used was a matt black painted dog bone specimen, manufactured from glass filled nylon, cyclically loaded with a mean load of 500 N, an amplitude of 400 N and a frequency of 10 Hz.

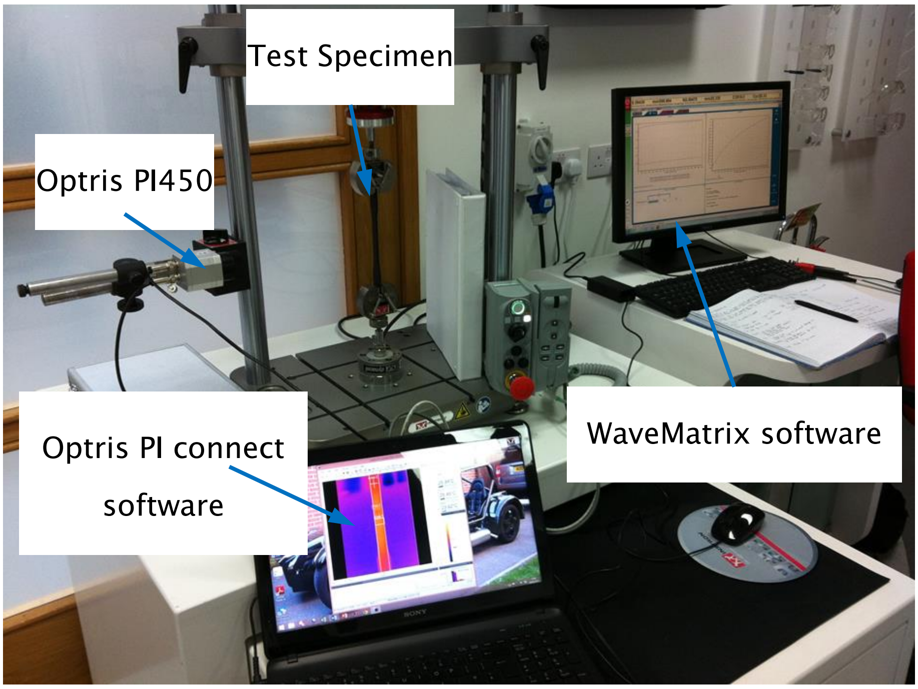

Figure 7.5. Trial set-up for Optris PI450 Microbolometer.

Figure 7.6. Trial set-up for Optris PI450 Microbolometer.

The camera is connected to the test machine via the PIF cable, which allows the transmission of a single temperature output from one of the measured areas previously specified. A strain channel was used to connect the PIF cable to the test machine controller. The PIF’s analogue output and shield were connected to pin numbers 1 and 14 respectively on the 24 pin D-type connection. A 15 volt supply from the test machine controller, via the connector, is used to power the PIF cable. The use of the strain input allows a user defined transducer to be setup, using the calibration wizard. Output from the cable is a voltage ranging from 0 to 10 volts. To increase the voltage output to temperature resolution, the working range for the voltage output was reduced from the camera’s full scale. Therefore the lower temperature range limit was set at 20°C for an output of 0 volts. The upper temperature range limit was set at 40°C for an output of 10 volts, giving a scale of 2°C per volt. The user defined transducer channel in WaveMatrix was set to convert the voltage back into temperature, allowing its use as a control parameter.

7.3.2 Machine control limit trial

Initial trials consisted of testing the test machine control limits, using the temperature input, with the undamaged specimen. The temperature input chosen, from pre designated areas (Section 3.3.3) was the average temperature over the gauge section of a matt black painted dog bone specimen, manufactured from glass filled nylon. The upper limit was set at approximately 0.5°C above the specimen’s ambient temperature. Once the limit was reached, the test machine was set to stop the fatigue cycle and unload the specimen. To cyclically load the specimen a sine wave was created using the waveform generator. Triggering the limits, using the temperature measured by the camera, was successful in stopping the test machine, but it was noted that there was a lag between the temperature registered by the Optris software and the test machine. An audible alarm had been set on the Optris software, at the same temperature trigger limit in the test machine software. The audible alarm was heard three or four times before the test machine stopped the test, suggesting that the test machine had not received the previous peaks in temperature, possibly due to DAC and ADC creating a lag in the system. It is not known how this lag can be overcome, to improve the response time.

7.3.3 WaveMatrix control limit trial

This trial was to recreate a simple SSHC. Instead of the specimen's frequency being reduced to decrease the specimen temperature, the test was paused to allow the specimen to cool, before restarting the cyclic loading.

For these trials a WaveMatrix program was created, with the following steps.

- Step 1: Switch from displacement to load control and ramp the specimen to the mean load of the fatigue cycle.
- Step 2: cyclically load the specimen for 10,000 cycles, with the maximum temperature set just above the specimen's ambient temperature. When the temperature limit is reached or the 10,000 cycles are completed the fatigue cycle was stopped at the mean load and progressed to the next step.
- Step 3: Hold the mean load for 1 minute to allow the specimen to cool. A lower temperature limit was set so that when the specimen had cooled the controller looped back to the start of the fatigue cycle step 2, or the 1 minute was completed.
- Step 4: The number of loops was set at 5, then the test was stopped and unloaded.

A variety of load levels and frequencies were trialled. The majority of which were successful in stopping mid step when the temperature limit was exceeded and moving to the next step or looping around to start at step 2. The unsuccessful trials were due external influences affecting the test.

7.3.4 Optris software image recording

In addition to the analogue temperature output, the Optris software has the ability to record moving images, so the possibility of using the cameras temperature output to control the test and also record images at various points during the test was investigated.

For the next set of trials the specimen was fatigued at a variety of frequencies and images were recorded at the fastest frame rate of 80 Hz. During this batch of tests the specimen was damaged with an approximate 1 mm notch, cut along the specimen centre line, at its edge. The frame rates tested were 10, 5, 2 and 0.5 Hz and the recording time set 5, 10, and 20 seconds. Temperature measurement areas and analogue output, were the same as the previous tests.

Upon review of the recorded images it was noted that all of the temperature measurement areas had significantly shifted towards the left hand side of the images. The measured areas were no longer on the specimen. It was also noted that at one, or occasionally two random points in the recording the image froze, yet the time counter continued to run. When the recording was replayed the freezing was at the same point, suggesting that the problem occurred during the recording and not the playback.

The frame rate was then reduced to 40 Hz from the initial 80 Hz and the starting and stopping of the recording was operated manually. Also, the test was held at the mean load, the recording was started, and then the fatigue cycling was started. During these trials the recording did not freeze, but it was noted that when scrolling manually through each frame the time counter did not scroll through smoothly. The time between each frame ranged from 0.01 seconds to 0.04 seconds. For 40 Hz a frame should be taken every 0.025 seconds.

When the software is recording or a snapshot is taken the output from the PIF drops to zero volts. This also happens when any other tabs or control buttons are pressed within the software. Therefore, recording or adjustment of the camera parameters should not done, whilst the test machine is using the temperature output as a control or limit. This limits the possible uses of this camera in monitoring and recording test temperature evolution, for later processing.

7.4 Digital input trial

After consultation with Instron UK's software development team, the decision was made to use National Instrument's LabVIEW, system design software. The Instron software currently uses LabVIEW, therefore allowing the data output to be integrated into the WaveMatrix software. During consultations with the software development team during the secondment, it was confirmed that two channels of data, created from the LabVIEW output, could be used in the 'User-Defined Channel Calculations' module in WaveMatrix.

The calculations module is an optional feature within WaveMatrix, which allows calculations to be made during the test sequence. The standard calculations available include acceleration, velocity, Young's modulus, and frame compliance correction calculations [104]. The User-Defined Channel Calculation allows the operator to write a calculation in the programming language C#, using two data inputs, resulting in an additional output channel. A WaveMatrix channel is a measurement output from the test machine, i.e. load or displacement, or from an additional Instron sensor, such as extensometers, crack opening displacement (COD) gauges and temperature, or a calculation output channel. The output channel can either be configured as a peak and trend channel providing a single data point per cycle or as a tracking channel that provides continuous data. As standard within WaveMatrix, these two options allow the data from the channel to be recorded and displayed graphically during testing or used as a data logging trigger. After consultation with Instron, it was confirmed that the User-Defined Channel Calculation output, may be used to adjust the test parameters, in a similar method to the SSHC [14].

When using infrared thermography (IRT) to monitor damage evolution, there is a variety of measurement parameters available. Therefore, the measurement parameter inputs into the calculation channel required for detecting and monitoring damage evolution in a SENT metallic specimen are the temperature of the hotspot and the hotspots X and Y pixel coordinates.

7.4.1 Development of LabVIEW programme

The FLIR A655SC microbolometer, was used to trial the use of LabVIEW, to monitor and control an IR detector, controlled through the GenlCam™ protocol via an Ethernet cable and the cameras GigE™ Vision interface. For this trial a laptop was used to run the camera and software. Using this protocol the temperature of each pixel can be monitored using LabVIEW. FLIR produce a software development kit (SDK) for this camera, giving access to components of the ResearchIR software.

National Instrument's LabVIEW is a graphically based programming language, used for building test, measurement and automation applications. To use LabVIEW to monitor and output the required data, a Virtual Instrument or VI has to be created. Here the objective is to find the maximum and minimum values of digital level (DL) in a data array obtained from a thermal image. As an initial trial, to confirm that a LabVIEW program could communicate with the detector. First a 'Front Panel' had to be designed. For this trial, a live display (Image Out) from the FLIR A655SC was created as shown in Figure 7.7. The Front Panel also displays the maximum (Max) and minimum (Min) digital level, and their co-ordinates (index(es)) within the image.

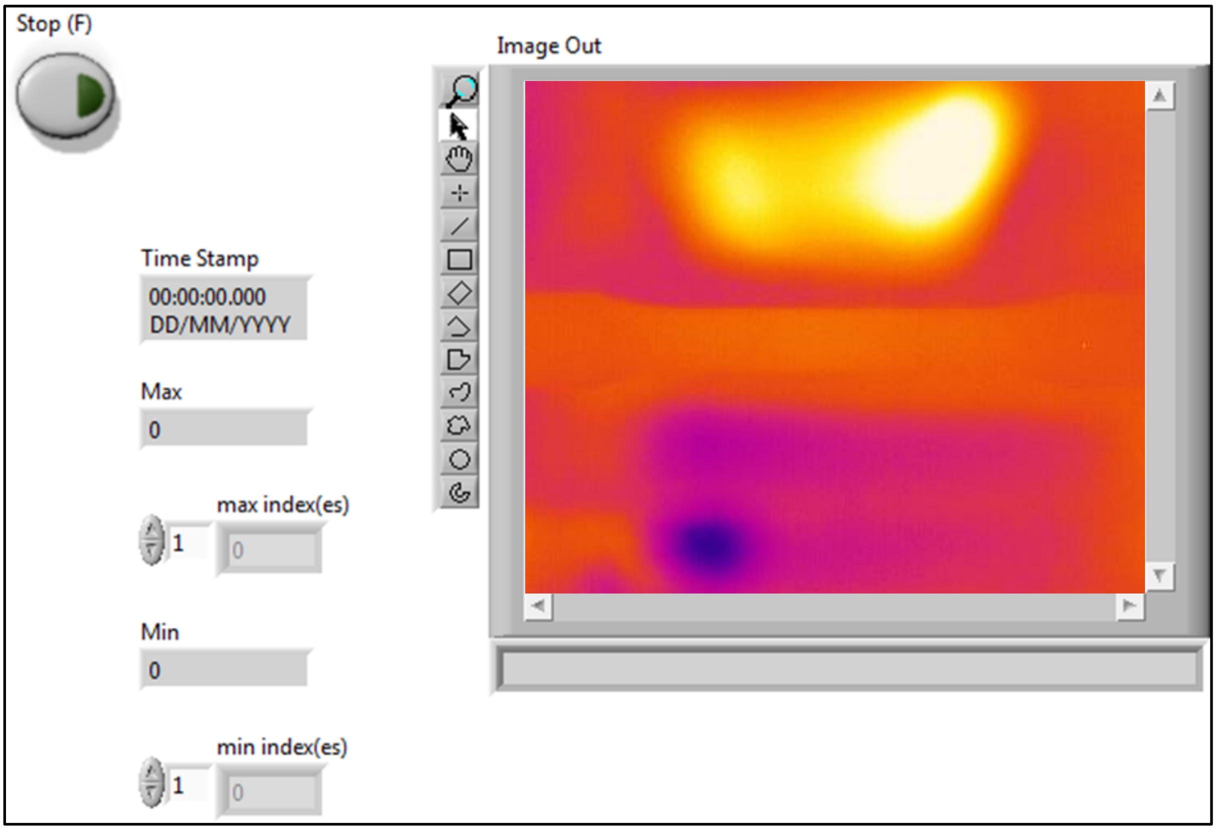

Stop (F)

Image Out

Time Stamp
00:00:00.000
DD/MM/YYYY

Max
0

max index(es)
1 0

Min
0

min index(es)
1 0

Figure 7.7. LabVIEW front panel.

It was then necessary to create a LabVIEW block diagram, to connect and convert the camera output to the required information. The block diagram developed is shown in Figure 7.8. Starting from the left hand side of the image, the first block creates the ‘Image out’ portion of the front panel, and is the live display from the camera. The second block contains the camera input via an Ethernet cable. The third and final block takes the image from the camera and outputs the max and min digital levels and their locations. From the camera output the data is input to the IMAQ create block and IMAQdx Open camera VI. These two blocks are instructing the program that the incoming data is a digital image acquisition. The next block is for the program to take a snapshot of the live data (when the stop button is pressed). The image is then transferred to the next block where it is converted to a data array, and then to a block that searches for the max and min values within the array. Finally the max, min and location values are identified and displayed in the appropriate boxes on the front panel.

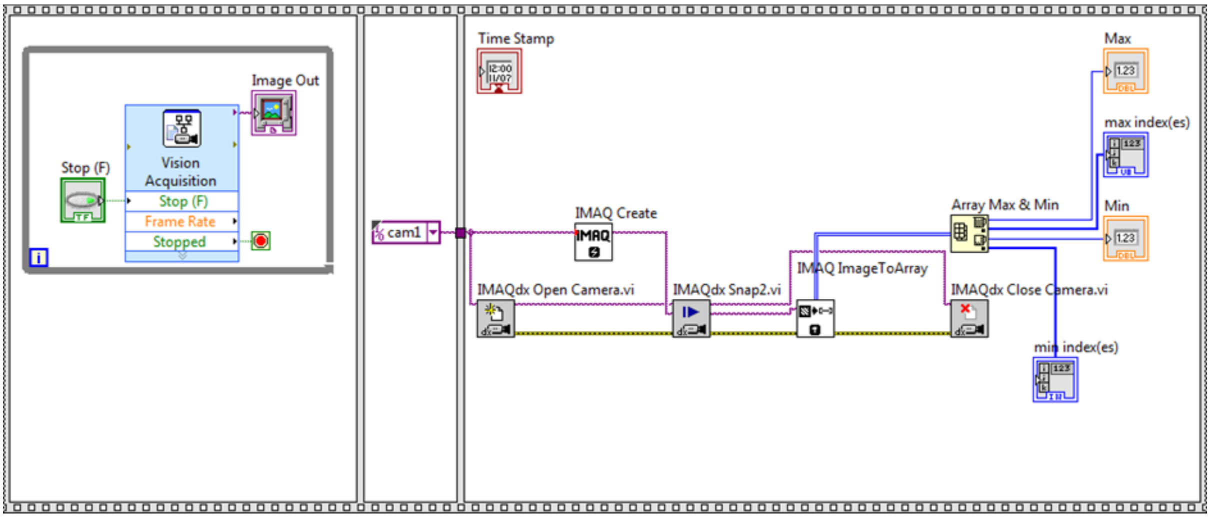

Figure 7.8. LabVIEW block diagram.

The LabVIEW program developed using the GenICam™ protocol was used to monitor the cameras output and record the maximum and minimum digital level and their respective locations. Tracking of the maximum and minimum locations was successful and the location was given in the indexes 0 and 1 (X and Y co-ordinates), by selecting the scroll key to the left hand side of the output. Unfortunately, the significant problem with this camera and its digital level output, was that the camera rescaled the digital levels, whenever the image changed. The hottest point in the image was always 65536 and the coldest point 0. Therefore monitoring a temperature increase was not possible. A live digital output and location program was tested. Replacing the Snap block with a play (or continuous) block, but this program suffered from significant lag and instability, only working on some occasions. Therefore, FLIR's ThermoVision SDK is required to convert the digital levels to a calibrated temperature, define a region of interest within the image, and output the maximum temperature, with the hotspots X and Y pixel coordinates.

7.4.2 FLIR's ThermoVision LabVIEW software development kit

FLIR's ThermoVision SDK is a comprehensive VI package containing everything required for the user to connect the IR detector to LabVIEW, adjust the detectors configuration parameters, calibrate the detector using the inbuilt or user defined calibration files, and generate a calibrated temperature image. From this point additional VI's would need to be created to replicate the Research IR's ability to select an area of interest on the test specimen and then display the maximum temperature, and the X and Y pixel coordinates within the "Stats" box. Then, this information would be converted into the required format for the Instron software.

The use of the SDK was investigated, and programs created using suitable VI's. Unfortunately, none of the programs created was successful in outputting a calibrated temperature image. Various fixes, ranging from different software versions, in LabVIEW, windows, and drivers Pleora and eBus, were trialled, but all were unsuccessful. The program strategy, using the SDK, starts with connecting the computer to the microbolometer, and configure the test parameters, including frame rate and sensor window size. An image is recorded in DL, converted to temperature using the calibration files, and then output a calibrated temperature image. This sequence would be repeated at the required frame rate, to create a 'live' image of the test specimen. Onto the live image, an area of interest is defined, and the image converted into an array of temperature values. From the array temperature values the maximum value and its X and Y coordinates within are displayed. These values would be refreshed at the detector frame rate. Another algorithm has to be developed to ignore any temperature hotspots occurring within the crack, due to frictional heating, as discussed in section 5.2.1.

7.5 Summary

The four implementation strategies all have their own benefits and challenges, but they all have the ability to control a test machine from IR data. IS2 has been demonstrated with the Optris PI450 microbolometer, outputting the temperature of a region of interest, specified on the specimen, via the PIF cable, connected to the test machines analogue input. From the analogue input, the voltage was converted back to a temperature value, and used to successfully control a fatigue test. IS4 was investigated, and has been shown that an image from an IR detector can be interrogated to produce a maximum value and its X and Y coordinates. Further development must be undertaken to produce a robust and reliable calibrated temperature output, in a format suitable for software to software communication. Leading into the next chapter, Chapter 8 Thesis summary and areas for future study.

Chapter 8 Conclusions and future work

In Chapter 2 literature review, current methods of damage, detection, monitoring and control in metallic and composite materials were described. The full field monitoring techniques of DIC, IRT, and TSA were also described along with their suitability and damage detection and control methods. It was concluded that DIC and TSA were not suitable processes for ‘live’ test machine control due to the data post processing requirements. It was concluded that:

- IRT showed promise as a possible technique that could be integrated into test machine control system but required further investigation and validation. It was decided to combine TSA and IRT as TSA could be used to identify the damage types in composite materials.
- As the photon detectors used for IRT inspections are very expensive a lower cost means of monitoring was required and bolometer systems should be investigated for their suitability as a means of monitoring and for TSA.

Therefore, Chapter 3 described the two different types of IR detector, and evaluated their performance across a range temperatures and detector settings, using a temperature controlled black body. The results from the experimental trials were input into a Matlab camera model and confirmed that the photon detector had greater sensitivity and less noise than the microbolometer. It was concluded that:

- The bolometer systems had sufficient sensitivity to be used for monitoring purposes and that an evaluation was required to investigate if such systems could be used for TSA, to evaluate the damage type after post processing the IRT data.

Chapter 4 used the camera models to develop a simulation of the thermoelastic response from both the bolometer and the photon detector. To validate the models it was necessary to select a specimen with a known stress field. Therefore the SENT specimen was chosen, as the stress field in the region of a crack-tip under mode 1 opening, can be described by linear elastic fracture mechanics. Therefore a relationship between the known stress change in the SENT specimen and the camera response was identified and input into the camera model. Chapter 4 described the experimental arrangements to conduct IRT on the SENT test specimen. It was described how the SIF could be determined simply by measuring the crack length and directly from the thermoelastic response. Data was captured at two “snap shots” with different crack lengths and SIF’s the experimental output compared to the camera model for the same conditions. It was concluded that:

- The microbolometer had a very slow response and hence for the loading frequencies used in the experimental work, is unsuitable for TSA.
- The microbolometer could be used to detect and monitor crack growth in a SENT specimen.

The SENT specimen experimental results are presented in Chapter 5, with a description of how the crack length was obtained from TSA data from the photon detector and the temperature from the microbolometer. The results presented included a test using a constant load amplitude and a ‘simulated’ controlled crack growth, with stepped load amplitude reductions. It was concluded that:

- Both the photon detector and microbolometer were able to detect and monitor crack growth.
- The SIF derived directly from the thermoelastic response correlated virtually exactly with the SIF’s obtained from the crack length measurements.
- The temperature increase rate correlated well with the Paris crack growth law.
- The temperature evolution at the crack tip temperature could be used as a parameter to control the test machine.

Chapter 6 moves the work onto composites and reports the results from notched and unnotched specimens in the form of OHT and rectangular coupons with two material lay-ups. It was concluded that:

- Both the photon detector and microbolometer could successfully detect and monitor damage evolution in both specimen types.
- TSA could identify the different types of damage.
- TSA could detect the subsurface damage, despite the insulating properties of epoxy resin system.
- To use IRT to control damage evolution in a composite material is feasible if the temperature profile at inception of damage can be determined, and the temperature at which damage occurs can be defined.

Finally Chapter 7 suggests four strategies to integrate IRT into test machine control. The strategies are External waveform control (IS1), External trigger (IS2), External imaging (IS3) and Software communication (IS4). It was concluded that:

- IS2 could be used by confirming that an analogue temperature output from an IR detector, could be successfully integrated into the WaveMatrix test control software.
- IS4 was feasible that an image from an IR detector can be interrogated to produce a maximum value and its location within the image.
- Further development is necessary on the detectors calibration and control software to fully realise the potential of software to software communication.

In summary, the objectives outlined in Chapter 1 have been met and it has been successfully demonstrated the IRT can be used to detect and monitor damage evolution in both metallic and composite materials. The detector modelling approach used to assess the performance of the photon detector and microbolometer, and create a simulated thermoelastic response of a SENT specimen, established that, for the experimental parameters trialled, the microbolometer was not suitable for TSA. The ability to integrate an IR detector into the control system of a mechanical test machine has been demonstrated. More importantly it has been shown that a low cost bolometer has sufficient sensitivity for the task of test machine control.

Areas of further work that have been identified for further development in the integration of IRT into test machine control are:

- Study a range of composite laminate configurations to identify temperature profiles at the inception of damage, which can be defined and used as a test control parameter.
- Develop software that can integrate with a microbolometer and extract the temperature calibration data and control parameters, or software that communicates directly with a detectors temperature output, removing the need for an ADC.
- Automate the TSA measurement of SIF, as an alternative control method to temperature increase rate, or maximum temperature location, in metallic crack growth specimens.
- Investigate the suitability of using a microbolometer for TSA using different test parameters to those used in this thesis, and the MiTE software, that incorporates a ‘lock in’ signal.

Appendix A

Bolometer TSA Matlab script

```
classdef TSA_FLIR_A655SC < handle
    % TSA_FLIR_A655SC class
    %
    %   How to use:
    %
    % % initialise TSA_FLIR_A655SC object with
    % %   * a file path to the SEQ file
    %       bol = TSA_FLIR_A655SC(fullfile(fold,'Run25.seq'));
    %
    % % load the images
    %       bol.ReadImages();
    %
    % % specify load
    % %   can be specified by the acqusition frequency and load values (synchronisation lost)
    %       bol.SetLoad(ld_freq,l);
    % %   can be specified by the acqusition time as vector and load values (synchronisation lost)
    %       bol.SetLoad(t_v,l);
    % %   can be specified by the time as matrix (synchronisation maintained)
    %       bol.SetLoad(t_m,l);
    %
    % %convert bolometer into TSA
    %       tsa = bol.GetTSA();
    %
    % %analyse load (extract frequency and phase)
    %       tsa.AnalyseLoad()
    %
    % %run lock-in algorithm
    %       [T,dT,p] = tsa.RunLockIn();
    %
    % 2017 - modexpeng ltd - modexpeng@gmail.com

    %% class: properties
    properties (SetAccess = public, GetAccess = public)
    end

    % Protected properties (user can get but not set)
    properties (SetAccess = protected, GetAccess = public)
    end

    % Dependent properties which are not stored.
    properties (SetAccess = private, GetAccess = public, Dependent = true)
        NbRows
        NbCols
        NbFrames
    end
```

```
    % Dependent properties which are not stored.
    properties (SetAccess = private, GetAccess = public)
    end

    % Private properties
    properties (SetAccess = private, GetAccess = private)
        FMR = [];
        info = struct();
        % Picture data
        pi_d = zeros(0,0,0); % pictures
        pi_t = zeros(6,0); % times
        % Loading data
        lo_d = zeros(1,0); % data
        lo_t = zeros(6,0); % times
    end


    %% METHODS
    %% class get.variable methods for Dependent
    methods

        function v = get.NbFrames(obj)
            v = size(obj.pi_d,3);
        end
        function v = get.NbCols(obj)
            v = size(obj.pi_d,2);
        end
        function v = get.NbRows(obj)
            v = size(obj.pi_d,1);
        end

    end

    % class public methods
    methods(Access = public)

        % constructor
        function obj = TSA_FLIR_A655SC(fp)
            % Constructs the object
            obj.FMR = FlirMovieReader(fp);
            obj.info = obj.FMR.info;

obj.pi_d(obj.info.height,obj.info.width,obj.info.numFrames) = 0;
            obj.pi_t(1,obj.info.numFrames) = 0;
        end

        function SetUnit(obj,unit)
            % Sets units to read data
            if ~ismember(unit,obj.info.availableUnits)
                error('TSA_FLIR_A655SC:SetUnit:InvalidUnit','The
desired unit is not available.')
            end
            obj.FMR.unit = unit;
        end

        function ReadImages(obj)
```

```
            % Load images into memory
            for a = 1:obj.NbFrames
                obj.pi_d(:,:,a) = obj.FMR.step(a-1);
                dat = obj.FMR.getMetaData();
                tm = cellfun(@(c)
str2double(c),strsplit(dat.Time,':'));
                obj.pi_t(:,a) =
datevec(tm(1)+datenum(2016,0,0,tm(2),tm(3),tm(4)));
            end
        end

        function SetLoad(obj,tm,ld)
            % Set load data.
            %   * tm: following sizes are allowed
            %       - 1x1: acquisition frequency (Hz)
            %       - 1xn or nx1: time vector (sec)
            %       - 6xm or mx6: time matrix ([year month day
hour minute second]xm)
            %   * ld: following sizes are allowed
            %       - 1x1: loading frequency (Hz)
            %       - 1xn or nx1: vector storing load data
            if all(size(ld)~=1)
                error('TSA_FLIR_A655SC:SetLoad:InvalidLoad','ld
should be a vector')
            end
            obj.lo_d = reshape(ld,1,[]);
            if size(tm,2)==6
                tm = tm';
            elseif size(tm,2)==1
                tm = reshape(tm,1,[]);
            end
            obj.lo_t = tm;
        end

        function tsa = GetTSA(obj)
            % Create and return TSA object.
            lo_t_ = obj.lo_t;
            pi_t_ = obj.pi_t;
            if size(lo_t_,1)==6 && size(pi_t_,1)==6
                id = find(lo_t_(:,1)==pi_t_(:,1),1,'last');
                lo_t_(1:id,:) = lo_t_(1:id,:) -
lo_t_(1:id,1)*ones(1,size(lo_t_,2));
                pi_t_(1:id,:) = pi_t_(1:id,:) -
pi_t_(1:id,1)*ones(1,size(pi_t_,2));
                lo_t_ = 24*60*60*datenum(lo_t_')';
                pi_t_ = 24*60*60*datenum(pi_t_')';
            elseif size(lo_t_,1)==6
                lo_t_ = 24*60*60*(datenum(lo_t_')-
datenum(lo_t_(:,1)'))';
            elseif size(pi_t_,1)==6
                pi_t_ = 24*60*60*(datenum(pi_t_')-
datenum(pi_t_(:,1)'))';
            end
            tsa = TSA(pi_t_,obj.pi_d);
            tsa.SetLoad(lo_t_,obj.lo_d);
        end
```

```
        function im = GetIm(obj,i)
            % Return image.
            im = obj.pi_d(:,:,i);
        end

    end

    % class private methods
    methods(Access = private)

    end

    % class protected methods
    methods(Access = protected, Hidden = true)

    end

    % class static methods
    methods(Access = protected, Hidden = true, Static)

        % recursive file finder
        function ret = find_file(fold,pattern)
            ret = 
struct('name',{},'date',{},'bytes',{},'isdir',{},'datenum',{});
            for f = dir(fold)'
                if ismember(f.name,{'.','..'})
                    continue
                end
                f.name = fullfile(fold,f.name);
                if f.isdir && numel(regexp(f.name,pattern))>0
                    tmp = 
TSA_FLIR_A655SC.find_file(f.name,pattern);
                    ret = [ret ; tmp];
                elseif ~f.isdir && numel(regexp(f.name,pattern))>0
                    ret(end+1,1) = f;
                end
            end
        end

    end

end
```

Appendix B

TSA gradient calculator Matlab script

```
function [data] = Tsareadandgrad(pxmm,cracktip)

for i=1:40
    if i < 100
        if i <10
            a = num2str(i);
            filename=strcat('DTN00',a);
            filename2=strcat('TN00',a);
        else
            a = num2str(i);
            filename=strcat('DTN0',a);
            filename2=strcat('TN0',a);
        end
    else
        a = num2str(i);
        filename=strcat('DTN',a);
        filename2=strcat('TN',a);
    end
    data.DT{i}=evalin('base',filename);
    data.T{i}=evalin('base',filename2);
end

for i=1:40;
    data.T{i}=data.T{i}+273.15;
    data.DTT{i}=data.DT{i}./data.T{i};
end

for i=1:40
    [data.M{i},I] = max(data.DTT{i},[],2);
end

for i=1:40
    for j=1:255
        data.M1{i}(j,1)=(j-cracktip)*-pxmm;
    end
    data.M1{i}(:,2) = 1./(data.M{i}.^2);
end

for i=1:40
    [c1 index1] = min(abs(data.M1{i}(:,1)-3));
    [c2 index2] = min(abs(data.M1{i}(:,1)-5));

data.alpha{i}=polyfit(data.M1{i}(index2:index1,1),data.M1{i}(index
2:index1,2),1);
end

end
```

List of References

[1] P. Broberg, "Surface crack detection in welds using thermography," *NDT & E International,* vol. 57, pp. 69-73, 2013.

[2] L. Toubal, M. Karama and B. Lorrain, "Damage evolution and infrared thermography in woven composite laminates under fatigue loading," *International Journal of Fatigue,* vol. 28, no. 12, pp. 1867-1872, 2006.

[3] S. Bagavathiappan;, B. B. Lahiri, T. Saravanan, J. Philip and T. Jayakumar, "Infrared thermography for condition monitoring - A review," *Infrared Physics & Technology,* vol. 60, pp. 35-55, 2013.

[4] M. J. Riedl, Optical Design Fundamentals for Infrared systems. Second edition, Bellingham: SPIE Press, 2001.

[5] R. C. Waugh, J. M. Dulieu-Barton and S. Quinn, "Modelling and evaluation of pulsed and pulse phase thermography through application of composite and metallic case studies," *NDT&E,* vol. 66, pp. 52-66, 2014.

[6] T. R. Emery and J. M. Dulieu-Barton, "Thermoelastic stress analysis of damage mechanisms in composite materials," *Composites: Part A,* vol. 41, pp. 1729-1742, 2010.

[7] N. Rajic and D. Rowlands, "Thermoelastic stress analysis with a compact low-cost microbolometer system," *Quantitative InfraRed Thermography,* vol. 10, no. 2, pp. 135-158, 2013.

[8] R. B. Vieira, G. L. Gonzales and J. L. Freire, “Thermography applied to the study of fatigue crack propagation in polycarbonate,” *Experimental Mechanics,* 2017.

[9] British Standards, “BS ISO 12108 Metallic Materials. Fatigue testing. Fatigue crack growth method,” 2012.

[10] British Standards, “BS EN 3873 Aerospace series. Test methods for metallic materials. Determination of fatigue crack growth rate using corner-cracked (CC) test specimens,” 2010.

[11] L. C. Overgaard, E. Lund and O. T. Thomsen, “Structural collapse of a wind turbine blade. Part A: Static test and equivalent single layered models,” *Composites: Part A,* vol. 41, pp. 257-270, 2010.

[12] M. Leong, L. C. Overgaard, O. T. Thomsen, E. Lund and I. M. Daniel, “Investigation of failure mechanisms in GFRP sandwich structures with face sheet wrinkle defects used for wind turbine blades,” *Composite structures,* vol. 94, pp. 768-778, 2012.

[13] J. Jones, S. P. Brookes, M. T. Whittaker and R. J. Lancaster, “Non-invasive temperature measurement and control techniques under thermomechanical fatigue loading,” *Materials Science and Technology,* vol. 30, no. 15, 2014.

[14] Instron, “WaveMatrix-Specimen-Self-Heating-Control,” [Online]. Available: http://www.instron.co.uk/wa/library/streamFile2.aspx?sdoc=1508.

[15] M. Naderi, A. Kahirdeh and M. M. Khonsari, “Dissipated thermal energy and damage evolution of Glass/Epoxy using infrared thermography and acoustic emission,” *Composites: Part B,* vol. 43, pp. 1613-1620, 2012.

[16] Instron, “8802 Servohydraulic Fatigue Testing System,” [Online]. Available: http://www.instron.co.uk/wa/product/88028803-Floor-Model-fatigue-Systems.aspx. [Accessed 3 December 2014].

[17] Y. Li, K. H. Ang and G. C. Chong, “Patents, software and hardware for PID control: an overview and analysis of the current art.,” *IEEE Control Systems magazine,* vol. 26, no. 1, pp. 42-54, 2006.

[18] ASTM international, “ASTM E647-13ae1 Standard Test Method for Measurement of Fatigue Crack Growth Rates”.

[19] British Standards, “BS ISO 13003 Fibre-reinforced plastics. Determination of fatigue properties undr cyclic loading conditions.,” 2003.

[20] ASTM international, “ASTM D3479/D3479M Standard Test Method for Tension-Tension Fatigue of Polymer Matrix Composite Materials.,” 2012.

[21] British Standards, “BS EN ISO 17640 Non-destructive testing of welds. Ultrasonic testing. Techniques, testing levels, and assessment.,” 2010.

[22] British Standards, “BS EN ISO 5579 Non-destructive testing. Radiographic testing of metallic materials using film and X-ray or gamma rays.,” 2013.

[23] ASTM international, “ASTM E2580 Standard Practice for Ultrasonic Testing of Flat Panel Composites and Sandwich Core Materials used in Aerospeca Applications,” 2012.

[24] ASTM international, “ASTM E2662 Standard Practice for Radiographic Examination of Flat Panel Composites and Sandwich Core Materials used in Aerospace Applications,” 2015.

[25] W. R. Broughton, M. R. Gower, M. J. Lodeiro, G. D. Pilkington and R. M. Shaw, “An experimental assessment of open-hole tension-tension fatigue behaviour of a GFRP laminate,” *Composites: Part A,* no. 42, pp. 1310-1320, 2011.

[26] British Standards, “BS ISO 12817:2013 Fibre-reinforced plastic composites. Determination of open-hole compression strength,” British Standards, 2013.

[27] ASTM international, ASTM D7136/D7136M Standard Test Method for Measuring the Damage resistance of a Fiber-Reinforced Polymer Matrix Composite to a Drop-Weight Impact Event, 2015.

[28] Airbus Industrie, *AITM 1.0010 Fibre Reinforced Plastics. Determination of compression strength after impact.,* 1994.

[29] O. J. Nixon-Pearson, S. R. Hallett, P. J. Withers and J. Rouse, “Damage development in open-hole composite specimens in fatigue. Part 1: Experimental investigation,” *Composite Structures,* no. 106, pp. 882-889, 2013.

[30] A. Bilel, M. K. Philen and S. W. Case, “Progressive damage assessment of centrally notched composite specimens in fatigue,” *Composites: Part A,* no. 74, pp. 47-59, 2015.

[31] N. Blanco, D. Trias, S. T. Pinho and P. Robinson, “Intralaminar fracture toughness characterisation of woven composite laminates. Part 1: Design and analysis of a compact tension (CT) specimen,” *Engineering Fracture Mechanics,* no. 131, pp. 349-360, 2014.

[32] N. Blanco, D. Trias, S. T. Pinho and P. Robinson, “Intralaminar fractur toughness characterisation of woven composite laminates. Part II: Experimental characterisation,” *Engineering Fracture Mechanics,* no. 131, pp. 361-370, 2014.

[33] M. Ueda and A. Todoroki, “Delamination monitoring of CFRP lminate using the two-stage electric potential change method with equivalent electric conductivity,” *Engineering Fracture Mechanics,* vol. 75, pp. 2737-2750, 2008.

[34] J. M. Dulieu-Barton, “Thermoelastic stress analysis,” in *Optical Methods of Solid Mechanics*, Weinheim, Wiley-VCH, 2012, pp. 345-366.

[35] W. Harizi, S. Chaki, G. Bourse and M. Ourak, “Mechanical damage assessment of Polymer-Matrix Composites using active infrared thermography,” *Composites: Part B,* vol. 66, pp. 204-209, 2014.

[36] W. Harizi, S. Chaki, G. Bourse and M. Ourak, “Mechanical damage assessment of Glass Fiber-Reinforced Polymer composites using passive infrared thermography,” *Composites: Part B,* vol. 59, pp. 74-79, 2014.

[37] F. Libonati and L. Vergani, “Damage assessment of composite materials by means of thermographic analyses,” *Composites: Part B,* vol. 50, pp. 82-90, 2013.

[38] C. Goidescu, H. Welemane, C. Garnier, M. Fazzini, R. Brault , E. Peronnet and S. Mistou, “Damage investigation in CFRP composites using full-field measurement techniques: Combination of digital image stereo-correlation. infrared thermography and X-ray tomography,” *Composites: Part B,* vol. 48, pp. 95-105, 2013.

[39] R. Usamentiaga, P. Venegas , J. Guerediaga, L. Vega and I. Lopez, “Automatic detection of impact damage in carbon fiber composites using active thermography,” *Infrared Physics & Technology,* vol. 58, pp. 36-46, 2013.

[40] V. P. Vavilov, “Modeling and characterizing impact damage in carbon fibre composites by thermal/infrared non-destructive testing,” *Composites: Part B,* vol. 61, pp. 1-10, 2014.

[41] R. Steinberger, T. I. Valadas Leitao, E. Ladstatter, G. Pinter, W. Billinger and R. W. Lang, “Infrared thermographic techniques for non-destructive damage characterization of carbon fibre reinforced polymers during tensile fatigue testing,” *International Journal of Fatigue,* vol. 28, pp. 1340-1347, 2006.

[42] M. L. Pastor, X. Balandraud, M. Grediac and J. L. Robert, “Applying infrared thermography to study the heating of 2024-T3 aluminium specimens under fatigue loading,” *Infrared Physics and Technology,* vol. 51, pp. 505-515, 2008.

[43] J. Fan, X. Guo and C. Wu, “A new application of the infrared thermography for fatigue evaluation and damage assessment,” *International Journal of Fatigue,* vol. 44, pp. 1-7, 2012.

[44] C. Garnier, M.-L. Pastor, B. Lorrain and O. Pantale, “Fatigue behaviour of impacted composite structures,” *Composite Structures,* vol. 100, pp. 443-450, 2013.

[45] J. Montesano, H. Bougherara and Z. Fawaz, “Application of infrared thermography for the characterization of damage in braided carbon fiber

reinforced polymer matrix composites," *Composites: Part B,* vol. 60, pp. 137-143, 2014.

[46] W. Thompson, "On the Thermoelastic, Thermomagnetic and Pyro-electric Properties of Matters," *Philosophical Magazine,* vol. 5, pp. 4-27, 1878.

[47] P. Stanley and W. K. Chan, "The application of thermoelastic stress analysis to composite materials," *Journal of Strain Analysis,* vol. 20, no. 3, pp. 129-137, 1988.

[48] R. A. Tomlinson and E. J. Olden, "Thermoelasticity for the analysis of crack tip stress field," *Strain,* no. May, pp. 49-55, 1999.

[49] D. P. Myriounis, E. Z. Kordatos, S. T. Hasan and T. E. Matikas, "Crack-Tip Stress Field and Fatigue Crack Growth Monitoring Using Infrared Lock-in Thermography in A359/SiCp Composites," *Strain,* vol. 47, pp. 619-627, 2011.

[50] B. V. Farahani, P. J. Tavares and P. M. G. P. Moreira, "SIF Determination with Thermoelastic Stress Analysis," *Procedia Structural Integrity 2,* pp. 2148-2155, 2013.

[51] F. A. Diaz, E. A. Patterson, R. A. Tomlinson and J. R. Yates, "Measuring stress intensity factors during fatigue crack growth using thermoelasticity," *Fatigue and Fracture of Engineering Materials and Structures,* vol. 27, no. 7, pp. 571-783, 2004.

[52] O. Plekhov, T. Palin-Luc, N. Saintier, S. Uvarov and O. Naimark, "Fatigue crack initiation and growth in a 35CrMo4 steel investigated by infrared thermography," *Fatigue & Fracture of Engineering Materials & Structures,* vol. 28, pp. 169-178, 2005.

[53] D. P. Myriounis, E. Z. Kordatos, S. T. Hasan and T. E. Matikas, “Crack-tip stress field and fatigue crack growth monitoring using infrared lock-in thermography in A359/SiCp composites,” *Strain,* vol. 47, pp. 619-627, 2011.

[54] N. Rajic and C. Brooks, “Automated crack detection and crack growth rate measurement using thermoelasticity,” *Procedia Engineering,* vol. 188, pp. 463-470, 2017.

[55] L. Krstulovic-Opara, B. Klarin, P. Neves and Z. Domazet, “Thermal imaging and Thermoelastic Stress Analysis of impact damage of composite materials,” *Engineering Failure Analysis,* vol. 18, pp. 713-719, 2011.

[56] A. K. Hussain, J. Mahmud and R. A. Tomlinson, “Detecting microscopic defects in aged thermoplastic using thermoelastic technique,” *IEEE Business Engineering and Industrial Applications Colloquium (BEIAC),* pp. 822-826, 2013.

[57] E. Fagerholt, E. Ostby, T. Borvik and O. S. Hopperstad, “Investigation of fracture in small-scale SENT tests of welded X80 pipeline steel using Digital Image Correlation with node splitting,” *Engineering Fracture Mechanics ,* vol. 96, pp. 276-293, 2012.

[58] S. Vanlanduit, J. Vanherzeele, R. Longo and P. Guillaume, “A digital image correlation method for fatigue test experiments,” *Optics and Lasers in Engineering,* vol. 47, pp. 371-378, 2009.

[59] LaVision, *StrainMaster product manual for strain calculation dialog (DaVis 8.1.0),* 2012.

[60] Y. Yuan, J. Huang, J. Fang, F. Yuan and C. Xiong, "A self-adaptive sampling digital image correlation algorithm for accurate displacement measurement," *Optics and Lasers in Engineering,* vol. 65, pp. 57-63, 2015.

[61] J.-q. Zhao, P. Zeng, L.-p. Lei and Y. Ma, "Initial guess by improved population-based intelligent algorithms for large inter-frame deformation measurement using digital image correlation," *Optics and Lasers in Engineering,* vol. 50, pp. 473-490, 2012.

[62] B. Pan, L. Yu, D. Wu and L. Tang, "Systematic errors in two-dimensional digital image correlation due to lens distortion," *Optics and Lasers in Engineering,* vol. 51, pp. 140-147, 2013.

[63] T. Hua, H. Xie, S. Wang, Z. Hu, P. Chen and Q. Zhang, "Evaluation of the quality of a speckle pattern in the digital image correlation method by mean subset fluctuation," *Optics and Laser Engineering,* vol. 43, pp. 9-13, 2011.

[64] P. Lava, S. Coppieters, Y. Wang, P. Van Houtte and D. Debruyne, "Error estimation in measuring strain fields with DIC on planar sheet metal specimens with a non-perpendicular camera alignment," *Optics and Lasers in Engineering,* vol. 49, pp. 57-65, 2011.

[65] Instron, "DIC Replay," [Online]. Available: http://www.instron.co.uk/wa/product/DIC-Replay.aspx.

[66] X. Fayolle, S. Calloch and F. Hild, "Controlling testing machines with digital image correlation.," *Experimantal Techniques,* vol. 31, no. 3, pp. 57-63, 2007.

[67] X. Fayolle and F. Hild , “Controlling Stress Intensity Factor Histories with Digital Images,” *Experimental Mechanics,* no. 54, pp. 305-314, 2014.

[68] G. Tao and Z. Xia, “A non-contact real-time strain measurement and control system for multiaxial cyclic/fatigue tests of polymer materials by digital image correlation method,” *Polymer Testing,* vol. 24, pp. 844-855, 2005.

[69] R. Wu, C. Kong, K. Li and D. Zhang, “Real-Time Digital Image Correlation for Dynamic Strain Measurement,” *Experimental Mechanics,* no. 56, pp. 833-843, 2016.

[70] E. Durif, J. Rethore, A. Combescure, M. Fregonese and P. Chaudet, “Controlling Stress Intensity Factors During a Fatigue Crack Propagation Using Digital Image Correlation and a Load Shedding Procedure,” *Experimental Mechanics,* no. 52, pp. 1021-1031, 2012.

[71] E. Fagerholt, E. Ostby, T. Borvik and O. S. Hopperstad, “Investigation of fracture in small-scale SENT tests of a welded X80 pipeline steel using Digital Image Correlation with node splitting,” *Engineering Fracture Mechanics,* no. 96, pp. 276-293, 2012.

[72] J. D. Carroll, W. Abuzaid, J. Lambros and H. Sehitoglu, “High resolution digital image correlation measurements of strain accumulation in fatigue crack growth,” *International Journal of Fatigue,* no. 57, pp. 140-150, 2013.

[73] F. Laurin, J. S. Charrier, D. Leveque, J. F. Maire and P. Nunez, “Determination of the properties of composite materials thanks to digital image correlation measurements,” *Procedia IUTAM,* vol. 4, pp. 106-115, 2012.

[74] M. A. Caminero, M. Lopez-Pedrosa, C. Pinna and C. Soutis, “Damage Assessment of Composite Structures using Digital Image Correlation,” *Applied Composite Materials,* no. 21, pp. 91-106, 2014.

[75] S. Giancane, R. Panella, R. Nobile and V. Dattoma, “Fatigue damage evolution of fibre reinforced composites with digital image correlation analysis,” *Procedia Engineering,* vol. 2, pp. 1307-1315, 2010.

[76] G. P. Battams and J. M. Dulieu-Barton, “Data-rich characterisation of damage propagation in composite materials,” *Composites: Part A,* vol. 91, pp. 420-435, 2016.

[77] R. K. Fruehmann, J. M. Dulieu-Barton, S. Quinn and J. P. Tyler, “The use of lock-in amplifier to apply digital image correlation to cyclically loaded components,” *Optics and Lasers in Engineering,* vol. 68, pp. 149-159, 2015.

[78] FLIR Systems Inc., “Knowledge Base,” FLIR Systems Inc, [Online]. Available: http://www.flir.com/cvs/cores/knowledgebase/index.cfm?view=35726. [Accessed 31 January 2018].

[79] H. Budzier, V. Krause, S. Bohmer, G. Gerlach and U. Hoffmann, “Fast microbolometer based infrared camera system,” DIAS Infrared GmbH-Publications-No 20.

[80] Xenics nv, “LWIR uncooled bolometer cores,” [Online]. Available: http://www.xenics.com/en/application/lwir-uncooled-bolometer-cores. [Accessed 5 February 2016].

[81] FLIR systems Inc, “MWIR Camera cores, Photon HRC,” [Online]. Available: http://www.flir.com/cores/display/?id=51957. [Accessed 30 January 2016].

[82] FLIR Systems Inc., “FLIR SC5000 Series,” [Online]. Available: http://www.flir.com/cs/emea/en/view/?id=42577. [Accessed 8 December 2014].

[83] R. Fruehmann, D. Crump and J. M. Dulieu-Barton, “Characterization of an infrared detector for high frame rate thermography,” *Measurement Science and Technology,* vol. 24, no. 105403, 2013.

[84] FLIR Systems Inc. , “Altair,” [Online]. Available: http://www.flir.com/cs/emea/en/view/?id=42413. [Accessed 08 December 2014].

[85] FLIR Systems Inc., “FLIR A655SC Infrared Camera,” [Online]. Available: http://www.flir.com/science/display/?id=46802. [Accessed 11 July 2017].

[86] FLIR Systems INC., “FLIR ResearchIR Software,” [Online]. Available: http://www.flir.com/science/display/?id=51371. [Accessed 11 July 2017].

[87] Optris GmbH, “Infrared camera optris PI400 / PI450,” [Online]. Available: http://www.optris.com/thermal-imager-pi400. [Accessed 31 January 2016].

[88] H. L. Ewalds and R. J. H. Wanhill, Fracture Mechanics, London: Edward Arnold, 1986.

[89] P. Stanley and W. K. Chan, “The determination of stress intensity factors and crack tip velocities from thermoelastic infra-red emissions,” *Proc. of*

International Conference on Fatigue of Engineering Materials and Structures, vol. C262, pp. 105-114, 1986.

[90] A. F. Robinson, J. M. Dulieu-Barton, S. Quinn and R. L. Burguete, “Paint coating characterization for thermoelastic stress analysis of metallic materials,” *Measurement Science and Technology,* vol. 21, 2010.

[91] L. Bodelot, L. Sabatier, E. Charkaluk and P. Dufrenoy, “Experimental setup for fully coupled kinematic and thermal measurements at the microstructure scale on an AISI 316L steel,” *Materials Science and engineering: A,* vol. 501, no. 1, pp. 52-60, 2009.

[92] Fine Tubes Ltd, “Alloy 316L, UNS S31603,” Ametek.com, [Online]. Available: http://www.finetubes.co.uk/products/specialist-tube-materials/stainless-steel-tubes/alloy-316l-uns-s31603/. [Accessed 1st March 2016].

[93] P. Stanley and J. M. Dulieu-Smith, “The detemination of crack-tip parameters from thermoelastic sata,” *Experimental techniques,* vol. 20, no. 2, pp. 21-23, 1996.

[94] N. Rajic and D. Rowlands, “Thermoelastic stress analysis with a compact low-cost microbolometer system,” *Quantitative Infrared Thermography Journal,* vol. 10, no. 2, pp. 135-158, 2013.

[95] P. Paris and F. Erdogan, “A Critical Analysis of Crack Propagation Laws,” *Journal of Basic Engineering,* vol. 85, no. 4, pp. 528-533, 1963.

[96] K. Kuhn, “Figure 33 Paris law for crack growth,” ResearchGate, [Online]. Available: https://www.researchgate.net/figure/278726933_fig8_Figure-

33-Paris-law-for-crack-growth-dadN-as-function-of-the-stress-intensity-factor. [Accessed 7th February 2016].

[97] M. Quaresimin, “Damage evolution under cyclic multiaxial stress state: A comparative analysis between glass/epoxy laminates and tubes,” *Composites: Part B,* vol. 61, pp. 282-290, 2014.

[98] R. M. O'Higgins, M. A. McCarthy and C. T. McCarthy, “Comparison of open hole tension characteristics of high strength glass and carbon fibre-reinforced composite materials,” *Composites Science and Technology ,* vol. 68, pp. 2770-2778, 2008.

[99] C. Goidescu, “Damage investigation in CFRP composites using full-field measurement techniques: Combination of digital image stereo-correlation, infrared thermography and X-ray tomography,” *Composites: Part B,* vol. 48, pp. 95-105, 2013.

[100] C. Colomboa, “Fatigue behaviour of a GFRP laminate by thermographic measurements,” *Procedia Engineering,* vol. 10, pp. 3518-3527, 2011.

[101] L. Toubal, M. Karama and B. Lorrain, “Damage evolution and infrared thermography in woven composite laminates under fatigue loading,” *International Journal of Fatigue ,* vol. 28, pp. 1867-1872, 2006.

[102] British Standards, “BS ISO 14603:2012 Fine ceramics (advanced ceramics, advanced technical ceramics). Test method for open-hole tension of continuous fibre-reinforced ceramic matrix composites at room temperature,” British Standards, 2012.

[103] Dirlik Controls Ltd, “Spectrum or flight loading,” [Online]. Available: http://www.dirlik.co.uk/spectrum-or-flight-loading.html.

[104] Instron, “Chapter 9 – Setting up WaveMatrix Calculations,” in *WaveMatrix Software – V1.8 Onwards. M22-16102-EN Revision D*, 2013.